Doctoral Thesis

Novel Technologies for Mitigation of Flow Accelerated Corrosion of the Secondary Side of Pressurized Water Reactors

Seunghyun Kim

Department of Nuclear Engineering

Graduate School of UNIST

2019

Novel Technologies for Mitigation of Flow Accelerated Corrosion of the Secondary Side of Pressurized Water Reactors

Seunghyun Kim

Department of Nuclear Engineering

Graduate School of UNIST

Novel Technologies for Mitigation of Flow Accelerated Corrosion of the Secondary Side of Pressurized Water Reactors

A thesis
submitted to the Graduate School of UNIST
in partial fulfillment of the
requirements for the degree of
Doctor of Philosophy

Seunghyun Kim

12. 03. 2018

Approved by

Advisor
Ji Hyun Kim

Novel Technologies for Mitigation of Flow Accelerated Corrosion of the Secondary Side of Pressurized Water Reactors

Seunghyun Kim

This certifies that the thesis of Seunghyun Kim is approved.

12. 03. 2018

signature

Advisor: Ji Hyun Kim

signature

In Cheol Bang

signature

Soon-Yong Kwon

signature

Chi Bum Bahn

signature

Young-Jin Kim

ABSTRACT

Secondary side of pressurized water reactors undergo severe erosion-corrosion (E-C) under high-temperature flowing water, and one of the most damaging phenomenon is flow accelerated corrosion (FAC). Due to FAC, many failures of the secondary system occurred which threatened the safety and the integrity of nuclear power plants. In this study, novel technologies, which include development of FAC resistive coatings and alloys, are proposed and their performance was evaluated in various FAC conditions. As the resistive coatings, Ni-P/TiO_2 nanocomposite and Fe-based amorphous metallic coatings (AMCs) were deposited on carbon steel substrate. Since they are known to possess outstanding corrosion and erosion resistance. In case of FAC resistive alloys, low alloy steels with different Cr and Mo contents were developed since Mo could be substituted by higher Cr contents according to Ducreux's equation. Also, Nakamura's crack susceptibility model and manufacturing costs of the alloys were considered. As a product, FAC resistive alloys (FRAs) are manufactured via vacuum arc melting method. And, the performance of the FAC resistive coatings and the alloys have been experimentally demonstrated by employing various FAC instruments.

At first, their electrochemical properties under seawater have been evaluated using linear sweep voltammetry and electrochemical impedance spectroscopy. Ni-P/TiO_2 coating shows excellence corrosion resistance due to the anodic protection for Ni-P matrix by spatially dispersed TiO_2 nanoparticles and the stability of NiO. However, Fe-based AMC shows susceptibility in seawater corrosion due to intrinsic surface morphology, defects, and surface area. In case of FRAs, the corrosion behavior in seawater condition has similar trend indicating that Mo could be substituted by high Cr. Electrochemical behavior of Ni-P and Ni-P/TiO_2 coatings under simulated secondary water chemistry is also evaluated. Compared to Ni-P coating, Ni-P/TiO_2 coating is less activated where FAC is favored i.e., 150 ºC. However, the effect of spatially dispersed TiO_2 nanoparticle is vanished at 125, 175 and 200 ºC but still the coating can suppress the corrosion.

To evaluate FAC resistive performance, secondary water chemistry control system and an autoclave system is prepared. At temperature range 125 to 200 ºC, FAC simulation performance of the coatings and the alloys have been tested under deaerated water with pH 9.3, which is controlled by ethanolamine. In case of the coatings, Ni-P/TiO_2 coating effectively suppress the corrosion by the galvanic coupling compared to Ni-P. Fe-based AMC also shows remarkable corrosion resistance since FAC is a complex phenomenon of corrosion and erosion. Instead of weight loss, slight weight gain is observable for Fe-based AMC. In case of FRAs, the oxide morphology is two-layer structure. The outer oxide layer is composed of Cr-rich amorphous oxide and the inner oxide is Cr-substituted magnetite according to their crystal structure. The corrosion rates of the alloys are in good agreement with Ducreux's model.

Finally, FAC tests at 5.7 m/s of flow were carried in the test facilities. To test FAC performance of the coatings, coated 90° elbows were prepared and their thickness is measured by ultrasonic thickness technique. In case of A106 Gr.B carbon steel, significant thickness reduction is observable at intrados due to localized acceleration of flow velocity while A335 P22 keeps its thickness for 21 days of immersion. Ni-P/TiO_2 coating also shows significant thickness reduction at intrados and surface and cross section morphologies confirms that the coating is detached. However, Fe-based AMC does not show thickness reduction but slight increased thickness is observable due to the formation of thick oxide.

Thus, it can be concluded that: Ni-P/TiO_2 coating is good corrosion resistive coating under corrosive condition but not effective under erosion condition; Fe-based AMC is susceptible to seawater corrosion but highly effective under erosion-corrosion condition; Mo-free FRA is available option for the substitution of commercial low alloy steel.

CONTENTS

LIST OF FIGURES

LIST OF TABLES

ABBREVIATIONS

AECL	Atomic Energy of Canada Ltd.
AMC	Amorphous Metallic Coating
AVT	All Volatile Treatment
BWR	Boiling Water Reactor
CANDU	Canada Deuterium Uranium
CE	Cavitation Erosion
ClSCC	Chloride Induced Stress Corrosion Cracking
CODAP	Common Online Data Analysis Platform
CPE	Constant Phase Element
CS	Carbon Steel
CX	Cross Section
DCPD	Direct Current Potential Drop
DH	Dissolved Hydrogen
DIW	Deionized Water
DO	Dissolved Oxygen
DP	Diffraction Pattern
E-C	Erosion-Corrosion
ECP	Electrochemical Corrosion Potential
EDF	Electricite De France
EDS	Energy Dispersive Spectroscopy
EIS	Electrochemical Impedance Spectroscopy
ENP	Electroless Nickel Plating
ETA	Ethanol Amine
FAC	Flow Accelerated Corrosion

FFT	Fast Fourier Transformation
FIB	Focused Ion Beam
E-C	Flow Induced Materials Degradation
FRA	E-C Resistive Alloy
HRTEM	High Resolution Transmission Electron Microscopy
HVOF	High-velocity Oxygen Fuel
LAS	Low Alloy Steel
LDIE	Liquid Droplet Impingement Erosion
LSV	Linear Sweep Voltammetry
MFRA	Mo-free E-C Resistive Alloy
NPP	Nuclear Power Plant
PHWR	Pressurized Heavy Water Reactor
PTFE	Polytetrafluoroethlyene (Teflon)
PWHT	Post Weld Heat Treatment
PWR	Pressurized Water Reactor
Re	Reynolds Number
SCE	Saturated Calomel Electrode
SEM	Scanning Electron Microscopy
SHE	Standard Hydrogen Electrode
SS	Stainless Steel
STEM	Scanning Transmission Electron Microscopy
STXM	Scanning Transmission X-ray Microscopy
TEM	Transmission Electron Microscopy
UHV	Ultra-High Vacuum
UT	Ultrasonic Testing

UTS	Ultimate Tensile Strength
VAR	Vacuum Arc Re-melting
XAS	X-ray Absorption Spectroscopy
XPS	X-ray Photoelectric Spectroscopy
XRD	X-ray Diffraction
YS	Yield Strength
YSZ	Yttria Stabilized Zirconia

I. Introduction

1.1. Materials Degradation in Secondary System of PWRs

Nuclear energy now becomes reliable baseload electrical source as clean energy from past few decades of history. In worldwide, nuclear energy meets 13 % of the electrical demand [1]. And, in Korea, 12 % of the electrical demand is provided by nuclear energy. There are 24 operating NPPs in Korea and the predominant reactor type is PWRs. Thus, understanding and mitigating the materials degradation in PWRs is an essential to enhance the materials integrity and safety of operating NPPs. Commercial PWRs consist of two systems: primary and secondary system. The schematic diagram of commercial PWRs is given in Figure 1.1. The purpose of primary system is to transport heat from nuclear fuels to steam generator and that of secondary system is generate electricity by the steam. After passing the turbines, the steam is condensed by cooling water. As the steam is cooled, it condenses back into feedwater system and recirculated the system. Thus, main components of secondary system such as steam generators, moisture separators, high- and low-pressure turbines, condensers, re-heaters, and they are connected by pipelines are exposed to high-temperature and pressure flowing water. Due to the susceptibility of materials in this environments, the materials undergo severe degradation, so called E-C, and many studies have been reported its mechanism, forms, some important accidents, and available countermeasures [2-5].

In terms of corrosion and erosion, the unique features of secondary system are high-temperature and pressure, alkaline water chemistry, low DO concentration, and fast flow velocity of coolant. In this condition, Fe based alloys will undergo severe corrosion and/or erosion as shown in Figure 1.2. In deaerated alkaline water, half-cell reactions of Fe corrosion are known as follows (Figure 1.2(a)) [6]:

$$\text{Anode: } Fe \rightarrow Fe^{2} + 2e^{-} \quad (1.1)$$

$$\text{Cathode: } 2H_2O + 2e^{-} \rightarrow H_2 + 2OH^{-} \quad (1.2)$$

Here, half of the dissolved Fe^{2+} ions transform into Fe_3O_4, and the others dissolved into the flowing water. Besides the destructive electrochemical reaction involving dissolved materials of the liquid itself, mechanical hydrodynamic and physical effects have to be considered to investigate the interactions between a flowing water and a solid wall [6]. Temperature determines the phase stability and solubility of Fe_3O_4 [7-10]. And, flowing water make impacts on mass transport and concentration gradient of soluble species. Or, if there is drastic pressure drop, accelerated liquid droplet or bubbles will make a severe damage to metallic substrate (Figure 1.2(b)). Due to the continuous dissolution of soluble species

and wear of the substrate, wall-thinning, leaks, and failure of pipelines and components occurs and eventually catastrophic accidents [11]. In the next section, various type of E-C in various NPPs type will be reviewed.

1.2. Types of E-C and Related Accidents

Representative E-C phenomena in secondary system are CE, FAC, and LDIE as shown in Figure 1.3. Their occurrence is usually distinguished by the phase of water. CE occurs at single-phase and LDIE occurs at two-phase flow only. FAC is observable in both phases. The schematic of the mechanism of each phenomenon is displayed in Figure 1.4.

CE involves the repeated formation and collapse of vapor bubbles and this collapse causes the generation of shock waves that cause material deformation and removal [2, 5, 12]. It is the deep localized degradation, which is frequently observed in pumps, downstream of internals, and valves, caused by cavitation. That is, violent collapse of stream bubbles in water flow near solid parts is governed by physical fluid and material properties (Figure 1.4(a)). As a result of CE, surface damage is rapidly propagated and increased due to constant collapse of bubbles [13]. Cavitation factor can be defined as follow:

$$C = \frac{\Delta P}{p_0 - p_v(T_0)} \tag{1.3}$$

Where ΔP is the pressure drop across the component, p_0 is the static pressure within the component, $p_v(T_0)$ is the saturated pressure at the fluid temperature within the component. A cavitation factor of less than 0.2 indicates the likelihood of cavitation. CE is generally found at an orifice downstream but recently there was wall-thinning observed at 90° elbow pipeline [12].

FAC is the continuous dissolution of Fe_3O_4 due to the destructive chemical reaction of Fe oxidation and Fe_3O_4 dissolution, and the mass transport into the flowing water (Figure 1.4(b)). Since there is an equilibrium between the oxidation and the dissolution in Fe_3O_4, continuous wall thinning occurs. The role of flow in FAC is enhancing concentration gradient of ion concentration and mass transport of soluble ions between oxide/water interface and bulk water. Among many kinds of FAC models, Sanchez-Caldera suggested the following model [3]:

$$\text{FAC Rate} = \frac{\theta(T)\cdot \mathbf{C_{eq}}}{1/\mathbf{K}+(1-f)\cdot\left[\frac{\delta}{D}+\frac{1}{\mathbf{h}}\right]} \quad (1.4)$$

Where θ(T) is the porosity in cm^2 of open area of metal, C_{eq} is the equilibrium concentration of Fe species, K is the reaction constant, f is the fraction of oxidized metal converted into magnetite at the interface, δ is the magnetite thickness, D is the diffusion coefficient of Fe cations in water, and h is the mass transfer coefficient. FAC appears not only where pipeline and components is exposed high-temperature flowing water but also where vigorous pressure drop is, such as an orifice [14].

LDIE is the erosion of metallic components by the accelerated liquid droplets (Figure 1.4(c)) [15]. It has been defined earlier as continuing material loss of a solid target material due to continued exposure to impacts by liquid drops. As a result of the collision of droplets at these surfaces, the oxide film is removed and the bare metal, which is now exposed to steam or liquid, is corroded to generate a new oxide film [16]. Repeating the events of oxide film rupture and recovery enhances local wall thinning. High hardness materials tend to be more resistible to LDIE. The acceleration occurs where drastic pressure drop is, such as orifice, reducer, etc. [5]. While FAC is the dissolution of oxides layer by chemical reaction, LDIE is the destruction of metallic substrate due to mechanical damage. The velocity will increase and act to decrease the static pressure

$$\Delta P = \frac{\rho}{144}\left(\frac{v_2^2 - v_1^2}{2g}\right) \quad (1.5)$$

Where ΔP is the pressure difference through a component, ρ is the fluid density, v_2 and v_1 is the flow velocity.

Also, LDIE can be quantified as following equation:

$$\dot{m}'' = \frac{C\cdot\rho_f\cdot\dot{m}_{tot}\cdot(1-x)\cdot V_d^4\cdot F_e\cdot F_h\cdot\rho_{ox}}{(P\cdot\varepsilon_c)^2\cdot A_C} \quad (1.6)$$

Where $\dot{m}''$ is the wear rate per unit area, C is the wear coefficient derived empirically, ρ_f is the fluid density, m_{tot} is the total mass flow rate, x is the flow quality, V_d is the droplet velocity, F_e is the entrained fraction, F_h is the fraction impacting surface, ρ_{ox} is the oxide density, P is the indentation hardness, ε_c is the critical strain to fracture, A_C is the characteristic wear area. LDIE on the turbine blades is a typical

pattern of LDIE, which is often mitigated by improving surface hardness. Air vent lines of feed water heaters are often damaged by LDIE, which shows a typical pattern of LDIE for high velocity steam and a typical pattern of LDIE for low velocity steam [17].

1.3. Failures in NPPs due to E-C

From the history of operating NPPs, many accidents related E-C have been reported in various reactors types: PWR, BWR, and PHWR (CANDU) in worldwide [18, 19]. Also, as NPPs in Korea age, it has also experienced piping E-C related accidents including thinning in the downstream straight pipe of a check valve in a feedwater pump line, the downstream elbow of a control valve in a feedwater flow control line, and failure of the straight pipe downstream of an orifice in an auxiliary steam return line [20, 21]. Table 1.1 enlists representative cases of the E-C related failures. Some failures induces not only break or rupture of components but also human casualties. Figure 1.5 displays the catastrophic destruction of pipelines and components of NPPs due to E-C. The recently observed FAC of CANDU outlet feeders cooperates a texturing of the corroding surface in morphology of scalloping that is typical surface shape of FAC [18]. Feeder pipe of Rajasthan NPPs from India was investigated by Singh [22]. Massive wall-thinning of the feeder had occurred downstream and close to the weld in 32.75 mm inner diameter elbows.

In 2014, Common Online Data Analysis Platform (CODAP) integrates the number of accidents due to E-C and susceptibility of key components of secondary system as shown in Figure 1.6. In Figure 1.6(a), the number of E-C related accidents is displayed according to plant types: PWR, BWR, and PHWR(CANDU). The statistics shows that PWR is the highest rank among the plants type but this is also contributed from the total number of PWR in the world. In 2005, the number of accidents at PWR exceeds 60 and this is due to the aging of PWRs over few decades. According to the Figure 1.6(b), the most susceptible components to E-C is external steam line followed by feed water. These two components are the regions of two-phase and single-phase flow, respectively. Thus, it can be concluded that the corrosion and erosion will frequently occur in this region due to FAC and LDIE.

1.4. Key Parameters on the E-C Behavior

Generally, key parameters of E-C can be categorized in three: thermal-hydraulic, water chemistry, and materials as shown in Figure 1.7. Predominant thermal-hydraulic parameters are temperature, pressure drop, flow rate and velocity, and geometry of pipelines and components. These factors result in characterization of hydrodynamic factors such as Re, mass transfer coefficient, surface shear stress, intensity of turbulence, freak energy density, etc [3]. Temperature determines solubility,

reaction rate constant, diffusion coefficient, and mass transfer constant during the electrochemical reaction of Fe and Fe oxides [23]. Fe solubility is important because hydrolysis reactions of the ferrous ions, the dissolution equilibria of corrosion products including Fe_3O_4, FeO, and $Fe(OH)_2$, and the number of electrons in the chemical reaction , which determine E-C rate of CS, is highly dependent on it [8]. Pressure drop determines localized flow profile. Geometry is highly related to the flow profile [24]. Turbulence in the flow enhances FAC rate by increases the flow rate at localized regions [25]. And, there is a critical shear stress which can mechanically remove protective layers which depends on the local velocity [26]. In two-phase flow condition, Reynold number is given as follow:

$$Re = \frac{Q}{S \cdot \rho_L} \frac{(1-X)}{(1-\alpha)} \frac{d}{v_L} \tag{1.7}$$

where Q is the mass flow rate, S is the pipe cross-section area, ρ_L is the density of liquid, X is the steam quality, α is the void fraction, d is the pipe diameter, v_L is the kinematic viscosity. Since in the given condition, Q, S, ρ_L, d, and v_L is fixed. Thus,

$$Re \propto \frac{(1-X)}{(1-\alpha)} \tag{1.8}$$

This equation shows that the relationship between Re and X is reciprocal. Thus, in high quality steam, Re would decrease thus FAC rate follows when void fraction is not changed.

In terms of water chemistry, DO concentration, pH, and its controller are known as to be seriously involved in E-C behavior of the alloys [27-29]. In high DO concentration, oxygen excessive condition is formed, thus ECP of the system shifts to positive direction. Eventually, steels form more protective and compact oxides such as Fe_2O_3 [30]. pH is also strong parameters that determine corrosion rate of steels. In low pH, stable form of Fe is known as to be Fe^{2+}. Thus, current secondary system keeps pH over 9.3 to reduce the corrosion rate of steels. Also, in the early history of PWR operation, phosphorous water chemistry was used but currently NH_3, ETA, and morpholine water chemistry is used as a part of AVT. Some research has been carried out to investigate the correlation between the types of pH controller and the corrosion rate of steels in secondary water chemistry. Computational results for liquid film pH at 90% steam quality suggests that ETA provide the sufficient protection while NH3 induces pH drop at very high steam quality [27]. Combination of ETA and NH_3 was more effective than ammonia alone with comparison of Korea NPPs field data and laboratory data [28].

Various studies have been reported that increase in alloy contents greatly reduces corrosion and erosion rate of steels in secondary water chemistry [31]. By addition of small amount of Cr in steels, protective Cr-rich oxide is formed at the interface. Fujiwara found that the Cr addition results in the formation of the stable $FeCr_2O_4$ in the oxide film and that $FeCr_2O_4$ prevents the diffusion of Fe in the oxide film [23]. Generally, it is considered that oxygen injection to feed water stabilizes Fe_2O_3 and reduces the Fe solubility [32]. However, Moon reported that P11 and the P22 possesses the coexistence of both Fe_3O_4 and Cr_2O_3 in their oxide [33]. Similar trend was also reported by Cheng [34, 35]. He studied electrochemical behavior of various steels with different Cr contents. Microstructure affects E-C behavior. According to the Nam's study, ferrite is less susceptible than bainite or ferrite-cementite to E-C due to galvanic coupling between the metal and the carbide [15].

In 1984, as a counter measure for Surry accidents, EPRI developed CHEC® program to predict FAC rate [36]. Most tests were run in the CIROCO loop, in which, at that time, the stream was directed toward the specimens rather than flowing inside them as is done nowadays [37]. More generally, the state of the loop was quite different at the time, compared to nowadays. In the program, Ducreux's model on FAC was employed as follows (Figure 1.8(a)):

$$\text{Relative FAC Rate} = 1/(83[\text{Cr}]^{0.89}[\text{Cu}]^{0.25}[\text{Mo}]^{0.2}) \quad (1.9)$$

where [Cr], [Cu], and [Mo] is the alloy contents of Cr, Cu, Mo in an alloy, respectively. The model is developed based on experimental results from BRT CICERO loop tests at pH 9.0, flow velocity 1.3 – 60 m/s, 180 ºC single-phase flow.

In early 1990, Huijbregt developed FAC model to predict the corrosion rate in two phase flow as follows (Figure 1.8(b)) [36]:

$$\text{Relative FAC Rate} = 1/(0.61 + 2.43[\text{Cr}] + 1.64[\text{Cu}] + 0.3[\text{Mo}]) \quad (1.10)$$

The model was developed by employing 100 hrs of experiments for alloys with different alloy contents.

And, in middle 1990, Bouchacourt developed theoretical model. It describes both the Cr content effect and the time dependency of the FAC rate of carbon steel under single-phase flow [37]. In this model, the relative FAC rate drastically decreased as Cr contents exceed 0.05 wt.%. And, the FAC rate decrease as time increases. This is supposedly due to: Progressive oxide porosity decrease over time as the oxide chromium concentration increases, as for the Ducreux model; reduction of the

solubility of the oxide over time and as the oxide gets enriched in chromium, as for the Ducreux model; increase of the oxide thickness over time (not considered by the Ducreux model).

Kastner model, which is used in WATHEC codes of Siemens, added molybdenum contents as a material factor [36]. At 180 ºC, compared to Mo-free alloy, the result was more conservative than that of Ducreux's.

Thus, carbon steel (e.g., A106 Gr.B) pipelines and components have been substituted by low alloy steel (e.g., A335 P22). However, the fundamental role of Cr in E-C resistance is not clearly investigated and those of Mo and Cu is not known yet.

1.5. Mitigation of E-C by Employing New Materials

From the previous sections, the mechanism of E-C, and key parameters of E-C behavior of alloys are investigated. The key to mitigate or prevent E-C is the obstruction of electrochemical interaction at metal/oxide/water interface. Since the modification of thermal hydraulic condition and/or water chemistry is highly restricted due to the consideration of the compatibility with other metals and alloys and the fundamental design of NPPs. In this study, as new materials, coatings and new alloys will be exploited as shown in Figure 1.9.

Coatings for corrosion and erosion resistance are one of the most classical field of research in assorted science and engineering societies since application of coatings into used material is cost-effective and time-saving compare to replacement of alloys. In NPPs, claddings, linings, and barrier coatings are used to enhance structural and materials integrity. However, the application in pipelines and components of secondary system is barely reported. Therefore, it is essential to evaluate thermodynamic properties of coating materials, and their compatibility with secondary water chemistry. Thus, in this study, E-C resistive materials will be developed based on mechanistic model of E-C rate and addition of small amount of alloy elements. Candidates materials will be introduced in the following sections.

Table 1.1. Remarkable E-C accidents inducing failures in various type of NPPs

No.	Year (or RFPY)	Plant Name (Type)	Component	Operating Condition
1	2004 [3]	Mihama (PWR)	SG tube inlet with orifice d/d_0 = 3.28	- Temperature = 155 °C - Velocity 2.2 m/s - pH = 9.1 – 9.4 - DO concentration = 2 ppb - Tube diameter = 15.6 mm - Re = 2×10^5
2	1986 [3]	Surry (PWR)	Condensate water pipe after orifice d/d_0 = 1.612	- Temperature = 140 – 142 °C - Velocity = 5.5 m/s - pH = 8.6 – 9.3 - DO concentration < 5 ppb - Pipe diameter = 540 mm - Re = 5.8×10^6
3	1991 [6]	Millstone (PWR)	Reheater drain tank line elbow	- Temperature = 239 °C - Velocity = 2.3 m/s - NH_3 and N_2H_4 water treatment - Single-phase flow
4	2013 [21]	Korea (PWR)	1” Pipe after plate-type orifice	- Outer diameter = 1” - Schedule = 80 - Temperature = 293.3 °C - Pressure = 74.3 atm - Steam Quality = 0.975 - Flow Rate = 9.72 kg/hr
5	(15.67) [22]	Rajasthan (CANDU)	Feeder Pipe	- Diameter = 1.25” – 2” - Flow Rate = 7.62 – 15.24 m/s - Temperature = 280 – 290 °C
6	Not Available [20]	Korea (PWR)	Straight pipe on the downstream of the motor in feedwater system	- Thickness = 1.5” to 1.161”
7	1978 [6]	Oyster Creek (BWR)	Feedwater and drain condensate downstream of feedwater pump	- General electric BWR - Location: 200 × 350 mm reducer

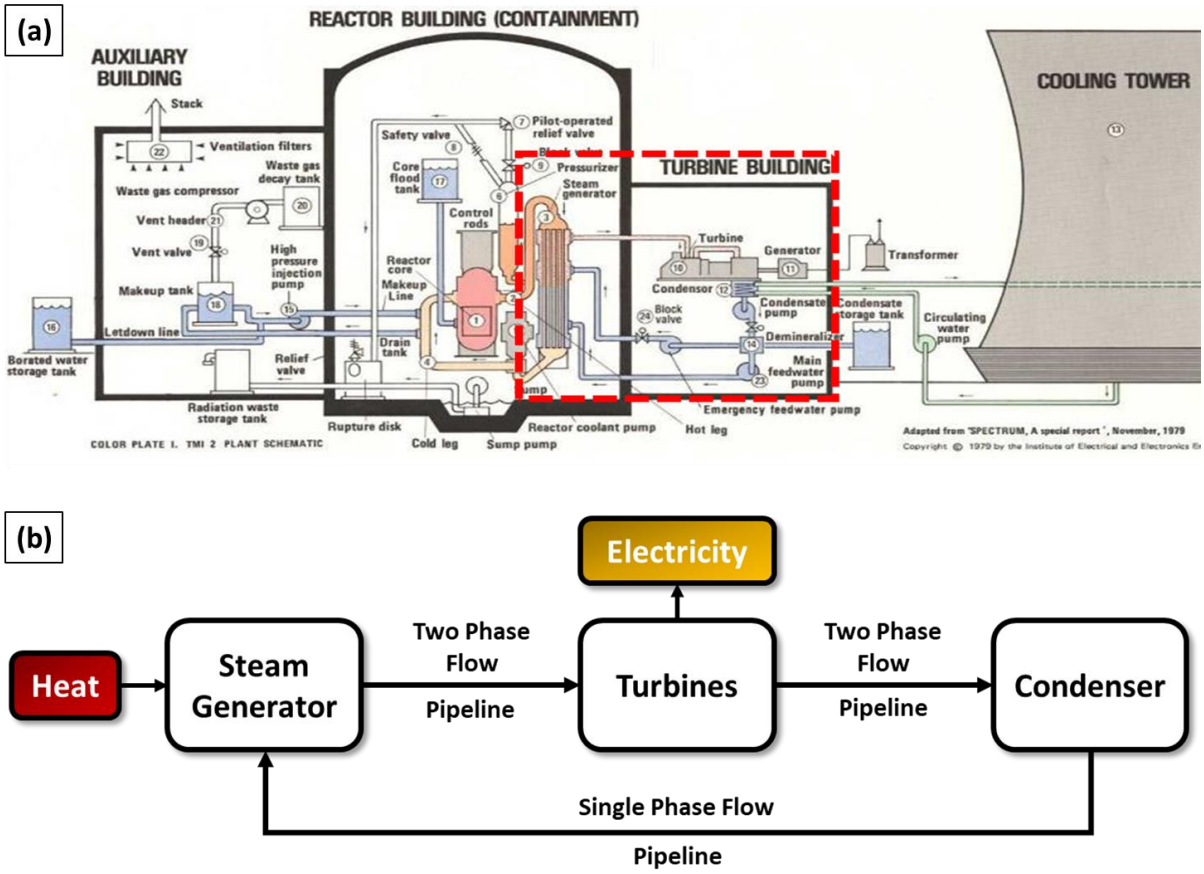

Figure 1.1. Schematic diagram of (a) PWRs and (b) the role and water phase in main components and pipelines of secondary system of NPPs

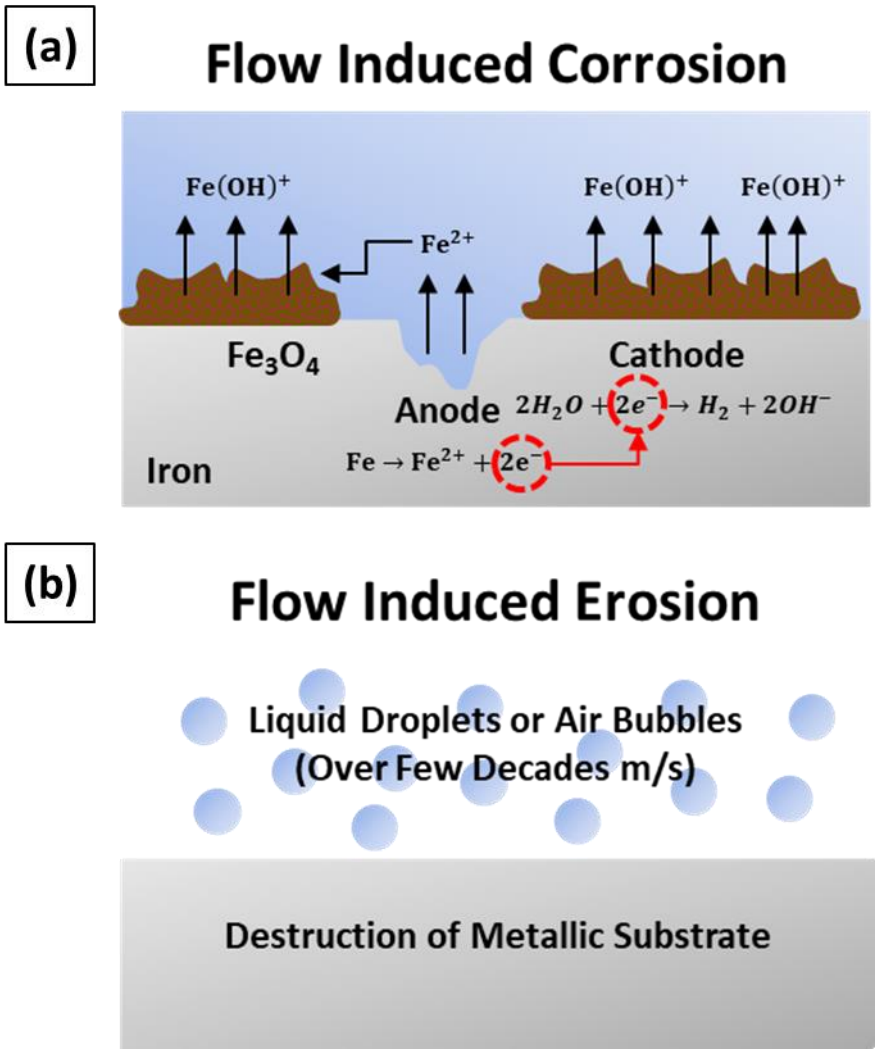

Figure 1.2. Schematic diagram of (a) corrosion and (b) erosion of Fe in high-temperature flowing water

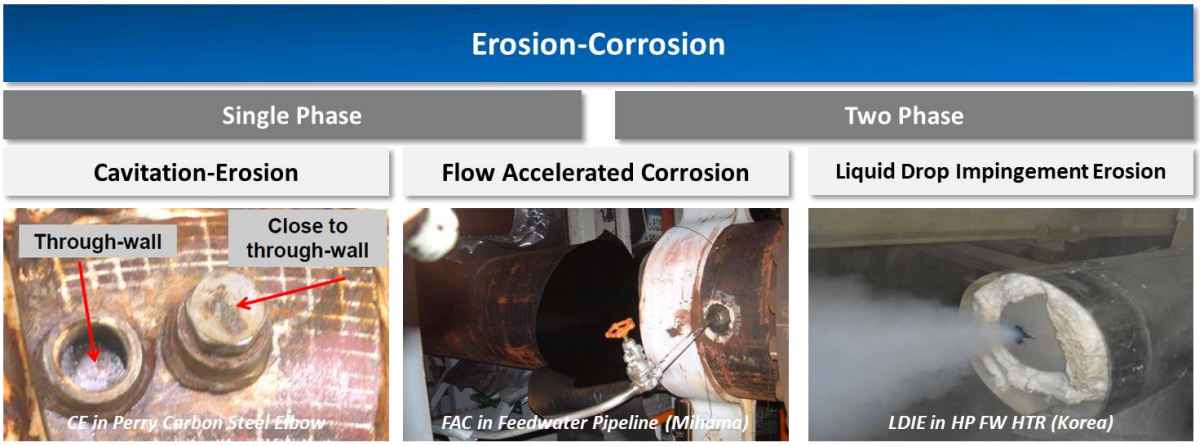

Figure 1.3. Categories of E-C in terms of phase of coolant and examples of representative accident cases [6, 15]

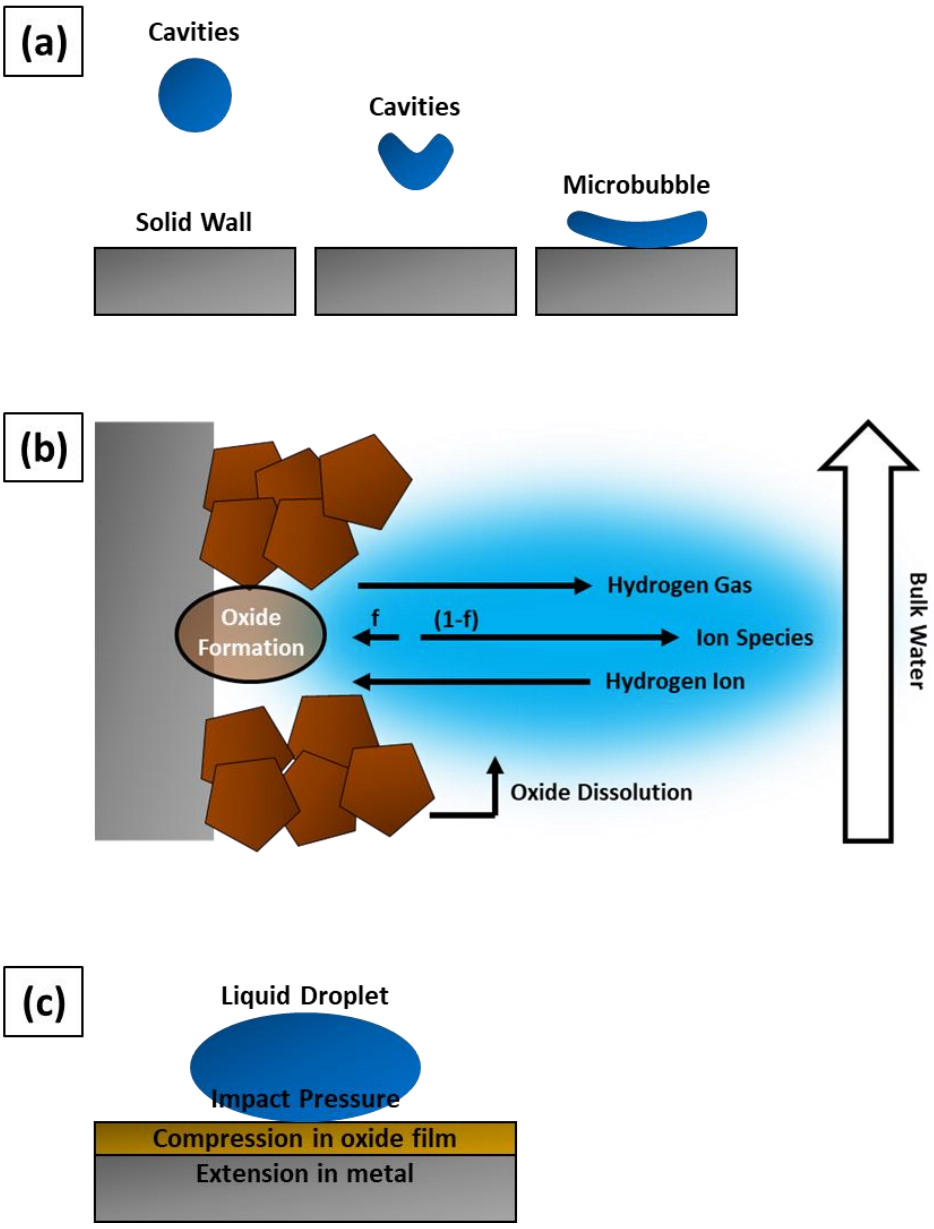

Figure 1.4. Schematic diagrams of mechanism of (a) CE, (b) FAC, and (c) LDIE

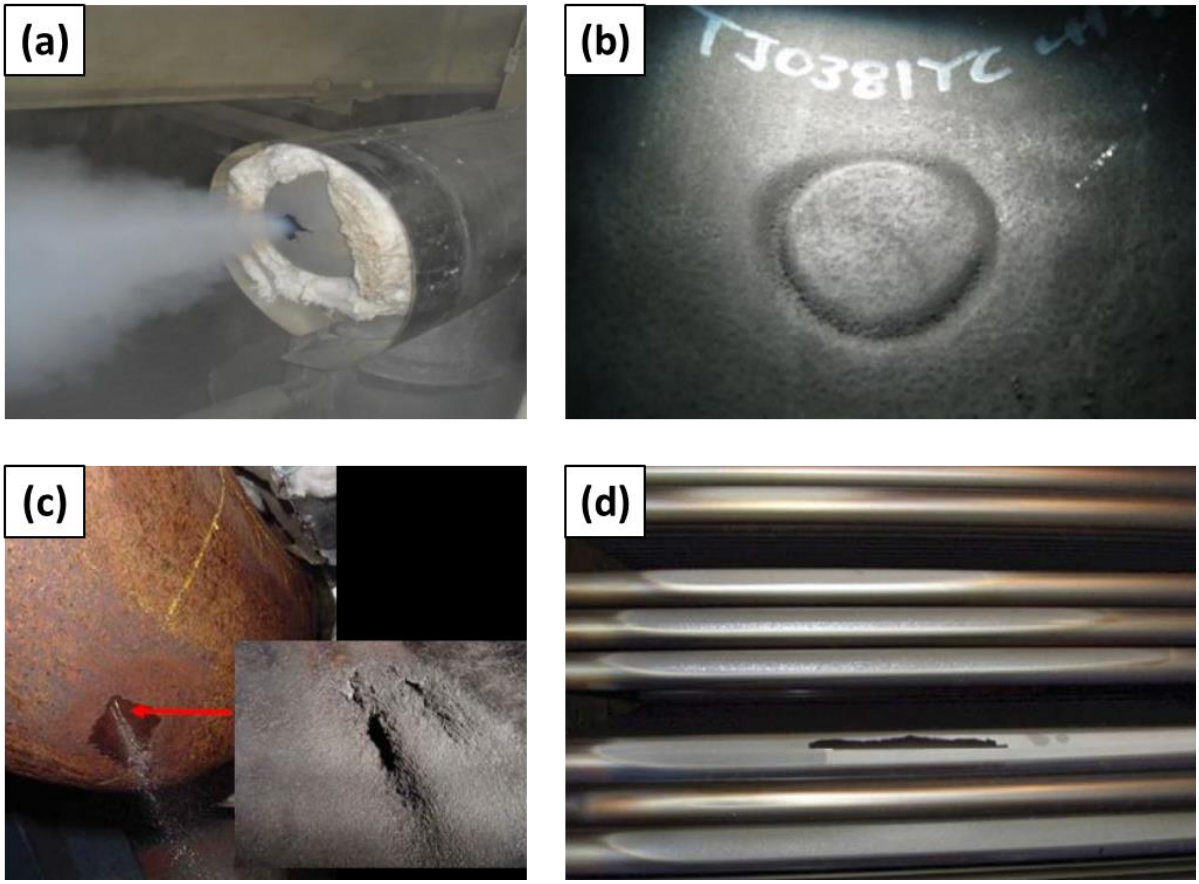

Figure 1.5. LDIE induced failures of pipelines and components of NPPs: (a) Korea Unit Y #2, (b)Korea Unit W #1, (c) Belgium Tihange Unit #1, (d) CANDU feeder pipe [3, 15]

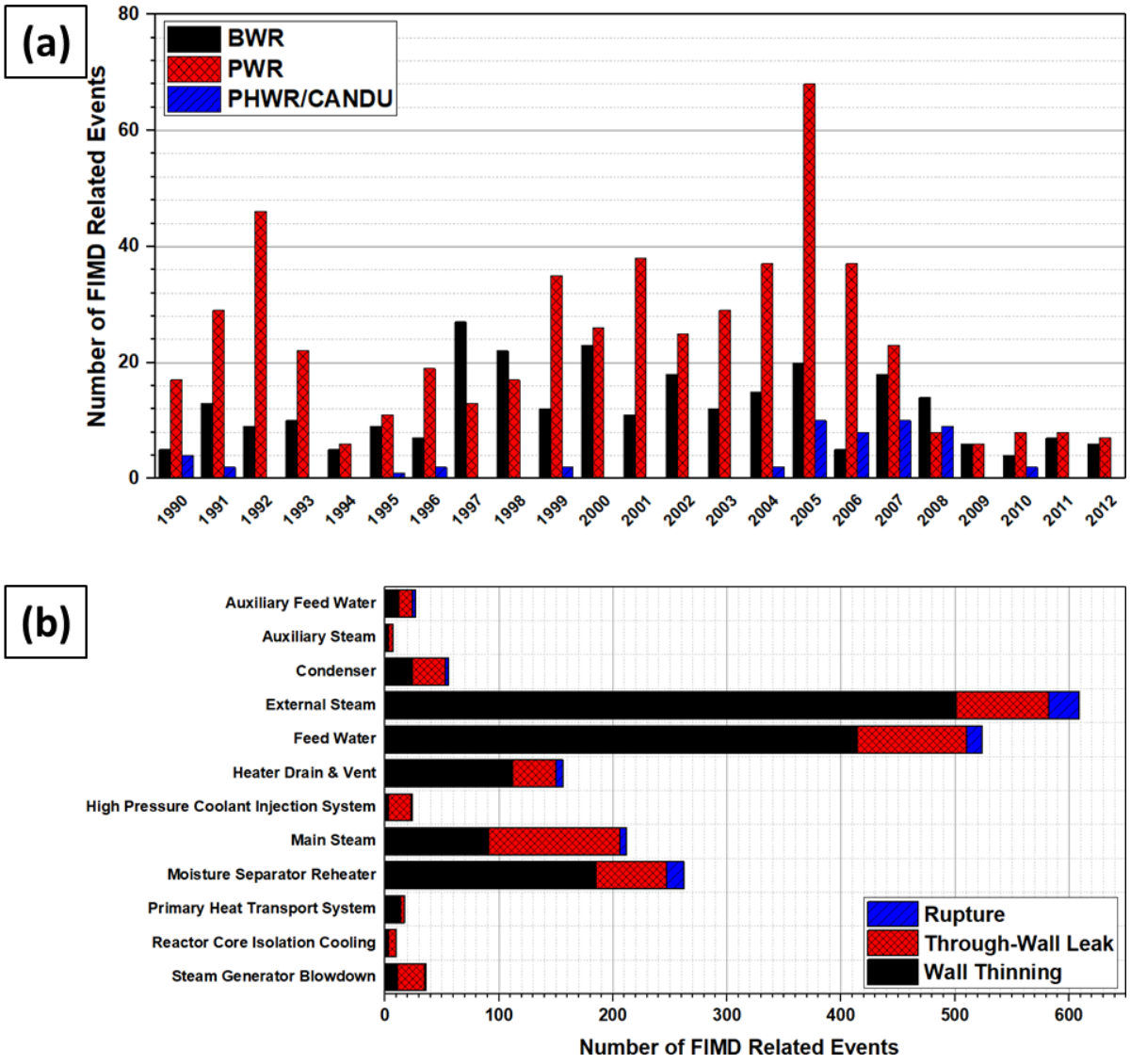

Figure 1.6. CODAP report on the number of E-C related events in (a) various types of NPPs and (b) components of NPPs

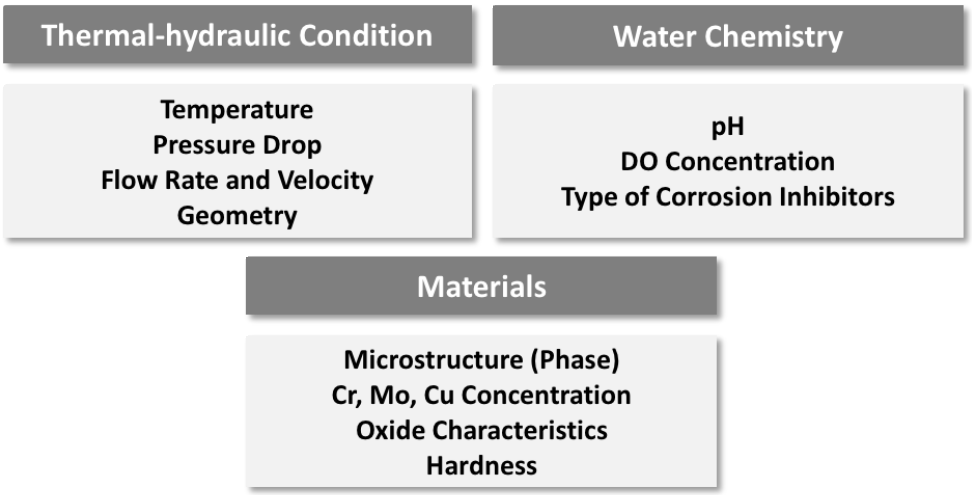

Figure 1.7. Key parameters of E-C categorized by thermal-hydraulic, water chemistry, and materials parameters

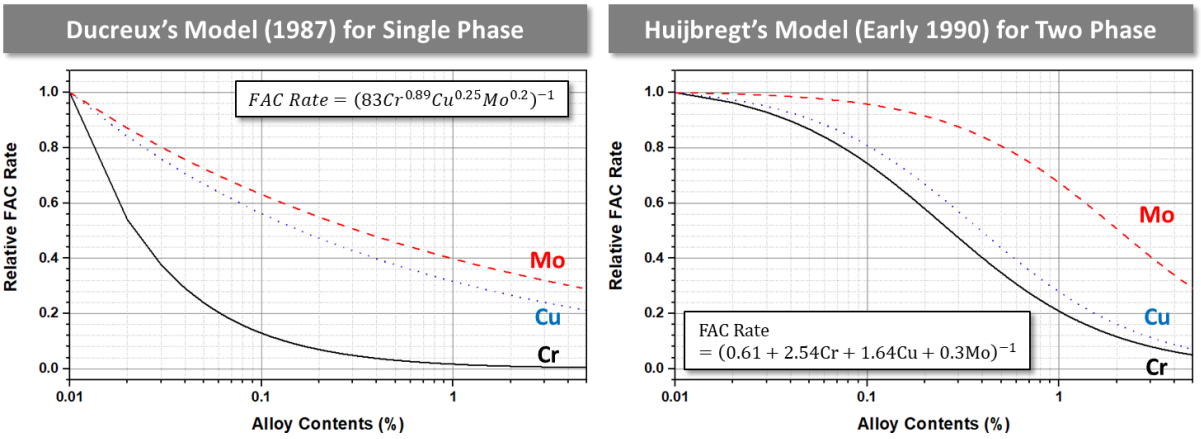

Figure 1.8. Effects of Cr and Mo contents on the E-C behavior of LAS: Ducreux's and Huijbregt's models on relative FAC rate and alloy contents in single- and two-phase flow condition, respectively

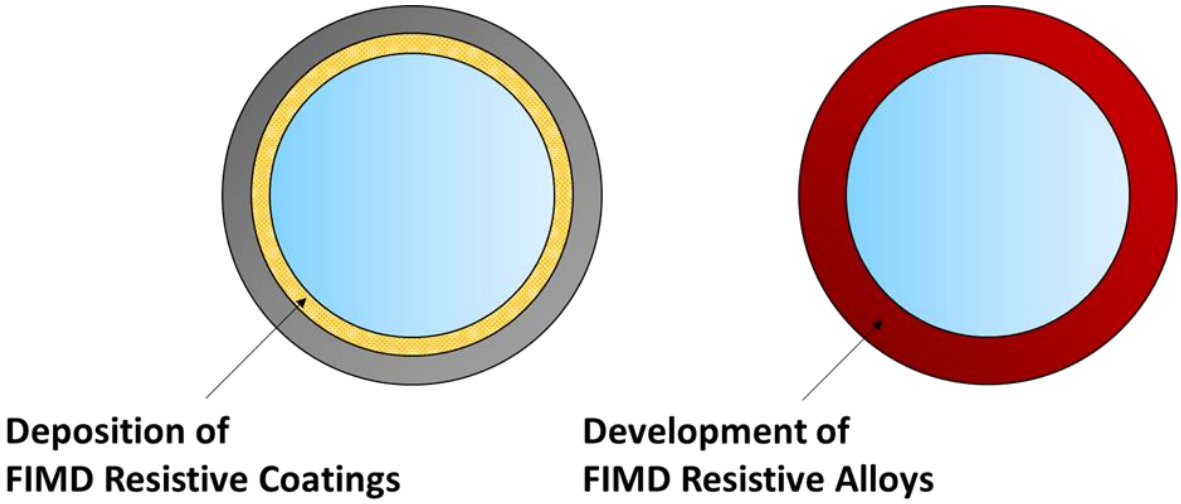

Figure 1.9. Schematic diagram on the concept of mitigation of E-C by the development of the resistive coatings and alloys

II. PROBLEM DEFINITION

2.1. Monitoring and Predicting of E-C in NPPs

Wall-thinning and corrosion of pipelines and components of NPPs is managed by various non-destructive evaluation techniques such as UT tests [38]. Those in-service tests are strictly managed by worldwide operating companies. However, due to complexity in geometry, human factors, and intrinsic errors in the measurement, many alternative techniques have been being developed. Zhang suggested array electrode to monitor corrosion of pipeline materials and those results were compared to computational results [39]. In their results, the maximum corrosion rate appears at innermost side of the elbow, i.e., the location with the maximum flow velocity and shear stress, while the minimum corrosion rate appears at outermost side of the elbow, the location with minimum flow velocity and shear stress. Series of works from Ryu suggests DCPD technique for monitoring wall-thinning in pipelines since management of E-C by current NDE is in lack of reliability [40-42]. Subramanian suggest thin-layer activation method to trace FAC of CS and those results were compared to Sanchez-Caldera model [43]. However, prediction of E-C rate is still in development due to complexity of the system [44, 45]. And, monitoring techniques is unable to fundamentally solve E-C problems in pipelines and components of NPPs. Thus, many research has been carried out to develop adequate countermeasure for the mitigation of E-C as discussed in the very following sections.

2.2. Mitigation of E-C by Water Chemistry Modification

Water chemistry parameters is one of the dominate parameters in the rate of E-C in CS and LAS. Thus, there were tremendous efforts to control E-C by modification in parameters of water chemistry including pH and its control agent, DO concentration. In the early stage of operation of PWRs, phosphorous chemistry was employed. However, the phosphorous water chemistry has been substituted by AVT due to the wastage. Conventionally, NH_3 is used as control agent to rasie pH at boiler, feedwater, and condensate [27]. High pH water chemistry reduces the solubility of Fe_3O_4 thereby reduces E-C rate. The usage of NH_3 requires high purity water and still enhances the corrosion of any Cu that might be present in a two-phase flow region. Furthermore, due to more volatility of NH_3 than that of water, two-phase flow region offers limited protection to corrosion. However, ETA, an alternative pH controller, possess less volatility than that of NH_3 thus the two-phase region offers better corrosion protection. Because NH_3 is corrosive to Cu, ETA can also be a better alternative for systems where multiple alloys exist. ETA have been applied in NPPs for decades and some guidelines are available for their application in these systems.

The high-pH chemistry made the system very sensitive to DO concentration. A concentration

of 1 – 2 ppb was sufficient to stifle FAC, apparently via a front of oxide based on Fe_2O_3 that progressed downstream [30]. In BWR, O_2 water chemistry is applied by injecting amount of O_2 into feedwater system to obtain high ECP. It has proven to be a powerful countermeasure to FAC [46]. The threshold level of O_2 to prevent carbon steel corrosion under neutral conditions is very different from that under high pH conditions. 20 ppb level of DO concentration is known to be the threshold level under neutral conditions. However, high O_2 water chemistry is not applicable for PWR due to compatibility with Ni base alloys especially steam generator tubes made of Inconel 600 [1]. From many literatures, it has been reported that high DO concentration stimulate PWSCC initiation and growth [47].

2.3. Mitigation of E-C by Materials Modification

Due to susceptibility of CS in a E-C favored condition, LAS replaces the most damaged parts of secondary system as shown in Figure 2.2. While main steam lines still use CS (e.g., A106 Gr.B) as pipeline materials, the other steam and water lines employ LAS (e.g., A335 P22) as an alternative. As shown in Figure 2.3, as Cr contents increases, resistance in corrosion and erosion of pipeline greatly reinforced. Decision was initially made to replace some severely corroded CS pipelines and fitting system with LAS [17]. When Cr contents in the material is increased from 0.03 to 0.5 wt.%, FAC rate of the alloy reduces to one tenth. The surface oxide changes from Fe_3O_4 to $FeCr_2O_4$ with addition of Cr in carbon steel. Similar result was reported by Fujiwara [32] but his study was based on calculation results rather than experimental approach.

Regardless of its effectiveness, degradation mechanism of LAS in high-temperature flowing water is partially and qualitatively investigated. In 2003, EPRI reported FAC rate and amounts of Cr contents in steels [48]. The reports assembled all known information concerning the effects of chromium on the rate of FAC. In particular, laboratory papers were assembled and reviewed. FAC model of Ducreux, Huijbregts, Kastner, and AECLwere introduced. Plant data from Diablo Canyon, Dominion Power, Callaway, Wolf Creek, San Onofre, Dukovany, and other miscellaneous data were also integrated. However, the report concluded that still the reliability of the data is questionable. In 2006, EPRI also described an experimental investigation for quantitatively determining the effect of Cr content on the rate of FAC of carbon steel [37]. The results were in good agreement with the Ducreux model ranging between 0.04 to 0.12 wt.% indicating threshold Cr contents under which there is no effect from the Cr could be lower than 0.04 wt.%. The relative FAC rate for the specimen containing 0.15 wt.% Cr was lower than that predicted by Ducreux model. Thus, the model may be conservative for relatively higher Cr contents. Time-dependent FAC rate on specimens shows that the FAC rate measured on specimens containing less than 0.15 wt.% Cr showed no significant decrease with time for test durations up to 1000 hours which is consistent with AECL. As the FAC rates obtained in this work

did not show any decrease with time, they could not account for the difference between the Ducreux model (based on short tests) and the field results. This was to be expected as the chromium contents of most of the tested specimens were quite low and the test durations relatively short compared to operating durations.

As Cr greatly enhances E-C resistance, SSs would be possible alternate replacement materials for CS as these are significantly less susceptible to FAC due to high Cr contents [17]. But the replacement with austenitic SSs need to be considered with additional engineering aspects. They have a 1.4 times greater thermal expansion rate than that of CS. Also, they are susceptible to Cl-SCC with the Cl contaminants in thermal insulation. The replacement with SS was initially considered for PHWR in some advanced reactors (under design) but has not been implemented yet.

And, among the alloy elements in LAS, the role of Mo is not fully understood. The role of Mo in steels are increases the resistance to both uniform and localized corrosion, increases mechanical strength, strongly promotes a ferritic microstructure [49-51]. However, enhances the probability for the formation of secondary phases in ferritic, duplex, and austenitic steels and in martensitic steels it increases the hardness at higher tempering temperatures due to its effect on carbide precipitation. Thus, in view point of corrosion, Mo is effective alloy elements for localized corrosion such as pitting. Since FAC is categorized as general corrosion, the addition of Mo in LAS is needed to be debated. According to Galvele's study, high concentration of Cl ions is observed in the passive layer, which is formed in HCl solution according to Auger analysis [52]. The anodic reaction occurred in this alloy appears to be the formation of a dissolving salt layer ($CrCl_3$) at the surface. The results suggest that Mo exerts its influence by reducing the dissolution rate of the salt layer. Sugimoto's study on the corrosion behavior of Ni-Cr-Mo and Fe-Mo alloys showed that Mo is only effective against corrosion when Ni and Cr presence and there was no electrochemical differences in Fe-xMo alloys [51]. The results from Newman was in good agreement with those of Sugimoto [53]: Mo enhances passivation especially in terms of pitting corrosion resistance only when it co-exists with Cr and/or Ni. Based on these studies, early conjecture can be mad that Mo can be substituted by Cr in terms of E-C resistance is established.

Recently, weldability and PWHT issues in LAS arise. In general, hydrogen cracking is a general mechanism hindering the weldability of CS and LAS with high strength levels. Also, reheat cracking a general problem in ferritic LAS containing Cr, Mo, V, and W. Thus, crack susceptibility of LAS is quantified by Nakamura as shown in following equation [54]:

$$Crack\ \ Susceptibility = \%Cr + 3.3 \times (\%Mo) + 8.1 \times (\%V) - 2 \quad (2.1)$$

Cracking occurs along the prior austenite grain boundaries of heat affected zone, as shown in Figure 2.4, that shows the microstructure of A335 P22 subjected to Gleeble thermal weld and stress [54]. The stress was continued during cooling and reheating process at an elevated temperature. During the weld process for HAZ near the fusion line, the temperature was high enough to dissolve pre-existing Cr, Mo, and V carbides in the austenite phase field. Following rapid cooling was fast enough to not alloy reprecipitate of the carbides. When the coarse-grained heat affected zone is reheated to elevated temperature for stress relieving, carbon precipitations formed at dislocations of prior austenite grain interiors and strengthen them before stresses are relieved. Since interior of the grain is much more strengthened than grain boundaries, stress are not relieved thus cracking can occur along the grain boundaries.

Furthermore, even if corrosion resistive coatings might be promising solution for E-C, their application in high-temperature flowing water has been barely reported. Table 2.1 enlists corrosion and erosion resistive coatings for various metallic substrate. One of the promising corrosion resistive coatings that can be applied to secondary water chemistry is ENP since it has excellence corrosion and wear resistance when it is incorporated with noble nanoparticles. Thermodynamic stability and phase transformation of Ni species in alkaline water chemistry is reviewed some previous studies [55]. Tremaine reviewed the solubility of Ni and its corresponding oxide and hydroxide from 423 to 523 K using flowing instrument [56]. In his study, solubility constant for multiple Ni base oxides and hydroxides have been derived such as $NiOH^+$, $Ni(OH)_2$, and $Ni(OH)^{3-}$. Zeller found out the effect of P contents in ENP in 50 wt.% NaOH solution by exploiting electrochemical technique [57]. In his work, the interface chemistry of $Ni(OH)_2$/NiO in 50 wt.% NaOH solution was studied using a concept of P-depleted zone. Work from Kang revealed the different behavior of ENP and pure Ni in KOH solution based on some X-ray and electrochemical technique [58]. Recent work from Ziemniak gave comprehensive understanding on the solubility of NiO in various hydrothermal condition and this enables understand the corrosion behavior of Ni and Ni-base alloys in simulate secondary water chemistry [59]. In this work, the effects of temperature on the hydrolysis of NiO was studied in detail. Finally, Medway made a synchrotron X-ray diffraction study for the characterization of hydrolysis in Ni electrodes in alkaline water chemistry. He found a formation of multiple layer structure (e.g., Ni/NiO/$Ni(OH)_2$ and NiOOH) at the electrode surface [60]. Regardless of their efforts, it is hard to directly apply their findings in E-C behavior of Ni based materials.

Bulk metallic glasses are attracting tremendous interest from various industrial and academic research groups because of its numerous physical and chemical properties [61-63]. They exhibit outstanding corrosion resistance due to the homogenous chemical composition and the absence of crystal imperfection such as dislocation, point defects, second phases and precipitations [62-66]. Among these amorphous alloys, the Fe-based AMC provides impressive surface protection and can be used in

place of more expensive Co or Ni based alloys [64, 65, 67, 68]. Therefore, the corrosion resistance and tribological properties of AMC in aggressive environments have been widely studied. Zheng studied the erosion–corrosion behavior of Fe-based AMC in 3.5 wt.% NaCl using potentiostatic polarization, XPS, and Mott–Schottky analysis [69]. He investigated the electrochemical and chemical properties of passive films, which were formed under various applied potential, during the erosion–corrosion tests. In addition, Wang compared the performance of HVOF and HVAF sprayed Fe-based AMC [70]. The superior erosion–corrosion resistance of HVAF AMC compared to that of the HVOF AMC could be related to the mechanical properties due to its more compact structure. Regardless of these advantages, their application in high-temperature flowing water is very rare. Even though some coating techniques, such as flame, arc, plasma thermal spray, are applied to the power plants, application in the secondary side of the PWRs is rare.

2.4. Experiments on E-C

Variety of studies have tried to fundamental aspects of E-C by laboratory scale or facility scale experiments because simulation of E-C requires high flow velocity with drastic pressure drop.

For LDIE tests, conceptual design of the impingement test system was based on ASTM standard method, named ASTM method G73-10. In the standard, three types of test method are suggested for LDIE: high-frequency vibratory method, water-jet method, and rotating machine method. The vibratory method is suitable for bubble induced corrosion but it is not relevant to LDIE in secondary system. Water-jet method can easily simulate LDIE damage but control of droplet size and distribution is complex. The rotating machine method is suitable for simulating LDIE and it has advantages in controlling test conditions including droplet speed and size [15]. By this method, Nam studied LDIE behavior of various Fe-based materials but his study is limited due to water chemistry: since corrosion and erosion in secondary system of PWR occurs in alkaline condition, acidic water chemistry would accelerate the corrosion.

Due to the limitations in setting up experimental instruments and facility, computational simulation method is often adopted in E-C studies. Furthermore, some simulation results have been combined with experimental results. Study from El-Gammal have investigated flow profile, hydrodynamic factors, and wear surface morphology in an elbow pipe [71]. And, some advanced corrosion monitoring techniques have been employed to qualitatively and quantitatively evaluate E-C behavior of pipeline materials. It is generally acknowledged that FAC is an electrochemical reaction that is accelerated by flow. Regardless of importance in measuring electrochemical properties such as ECP, only few studies have been focused on it [72]. In 2001, Uchida reported FAC behavior of pipeline materials by exploiting electrochemical monitoring and oxide composition especially Fe_2O_3 and Fe_3O_4

[73]. He found that higher oxidizing power (i.e., higher ECP) was key to reduce FAC rate.

Table 2.1. Some corrosion and erosion resistive coatings

No.	Coating		Tests and Environments	Ref.
	Method	Material		
1	Electroless Ni plating	Ni-P/ZrO_2	- Hardness - Salt spray - Corrosion in 5 wt.% NaCl	[74]
2	Electroless Ni plating	Ni-Cu-P/PTFE	- Hardness - Friction tests	[75]
3	Electroless Ni plating	Ni-P	- Friction performance - Corrosion in 10 wt.% NaOH	[76]
4	Electroless Ni plating	Ni-P/TiO_2	- Wear - Hardness	[77]
5	Rapid thermal annealing	Graphene	- Corrosion in 3.5 wt.% NaCl	[78]
6	Electroless Ni plating	Ni-P/TiO_2	- Hardness - Friction tests	[79]
7	Electroless Ni plating	Ni-P/TiO_2	- Hardness - Corrosion in 3.5 wt.% NaCl	[80]
8	Electroless Ni plating	Ni-P/TiO_2	- Corrosion in 3.5 wt.% NaCl	[81]
9	Electroless Ni plating	Ni and Ni-P	- Corrosion in 6 M KOH	[58]
10	HVOF	Fe-based AMC	- Erosion in 3.5 wt.% NaCl	[69]
11	HVOF	Fe-based AMC	- Erosion in sand-containing 3.5 wt.% NaCl	[68]
12	HVOF	Fe-based AMC	- Erosion in 3.5 wt.% NaCl	[82]

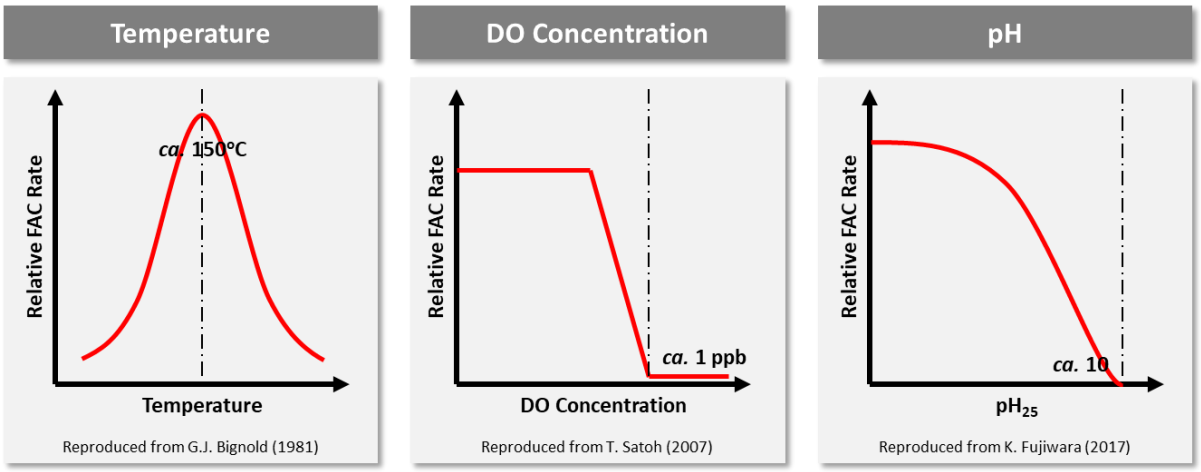

Figure 2.1. Effects of water chemistry on the E-C behavior of the alloys: (a) temperature, (b) DO concentration, (c) pH, and (d) pH control agents

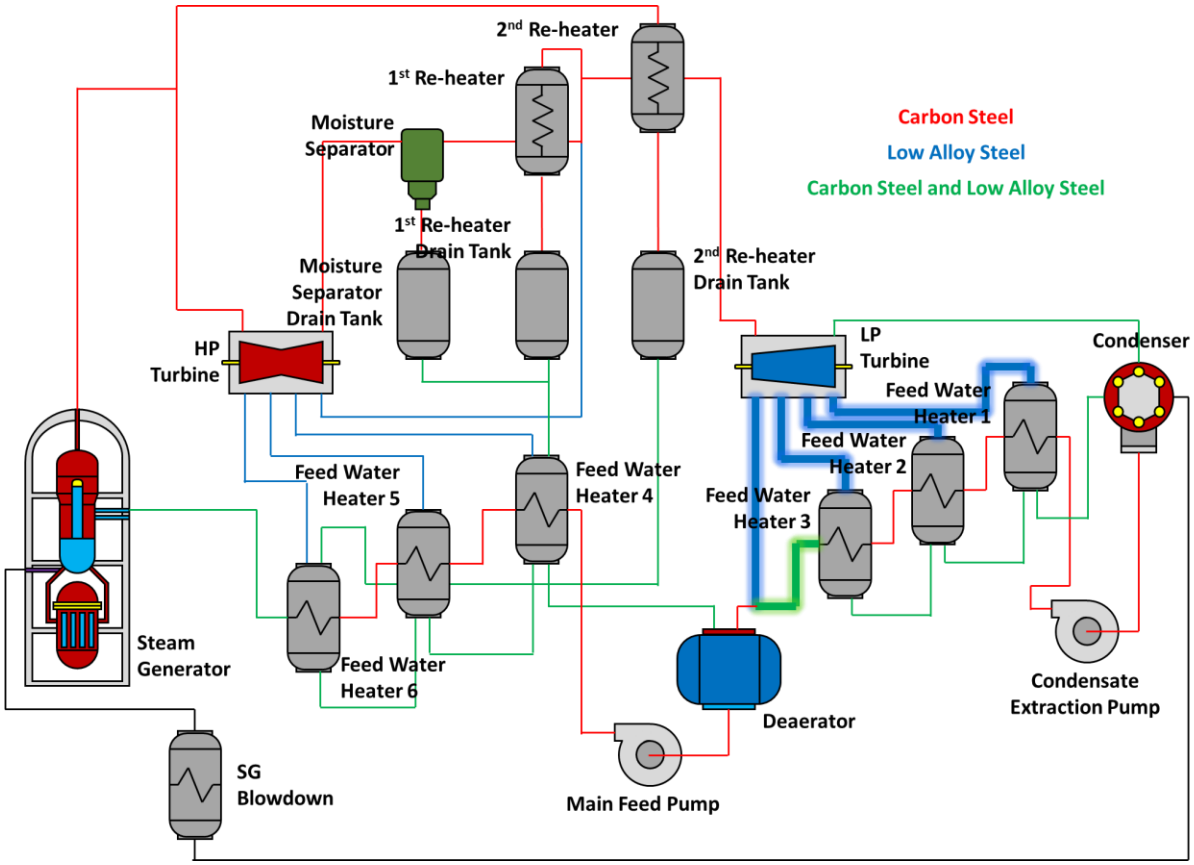

Figure 2.2. Atals of Materials in secondary system of NPPs: Red is CS, blue is LAS, and green is combined region and those glowing lines are recently replaced lines from CS to LAS

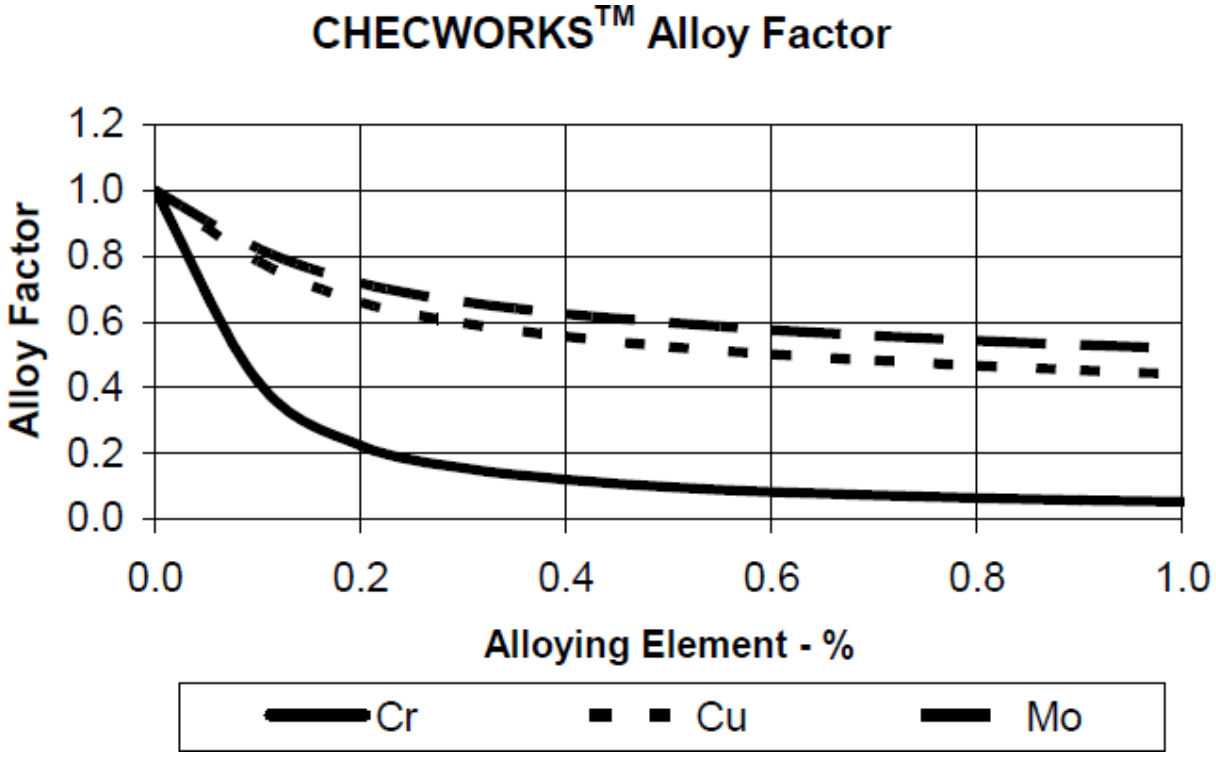

Figure 2.3. Effects of alloy contents on alloy factor in CHECWORKS™ [37]

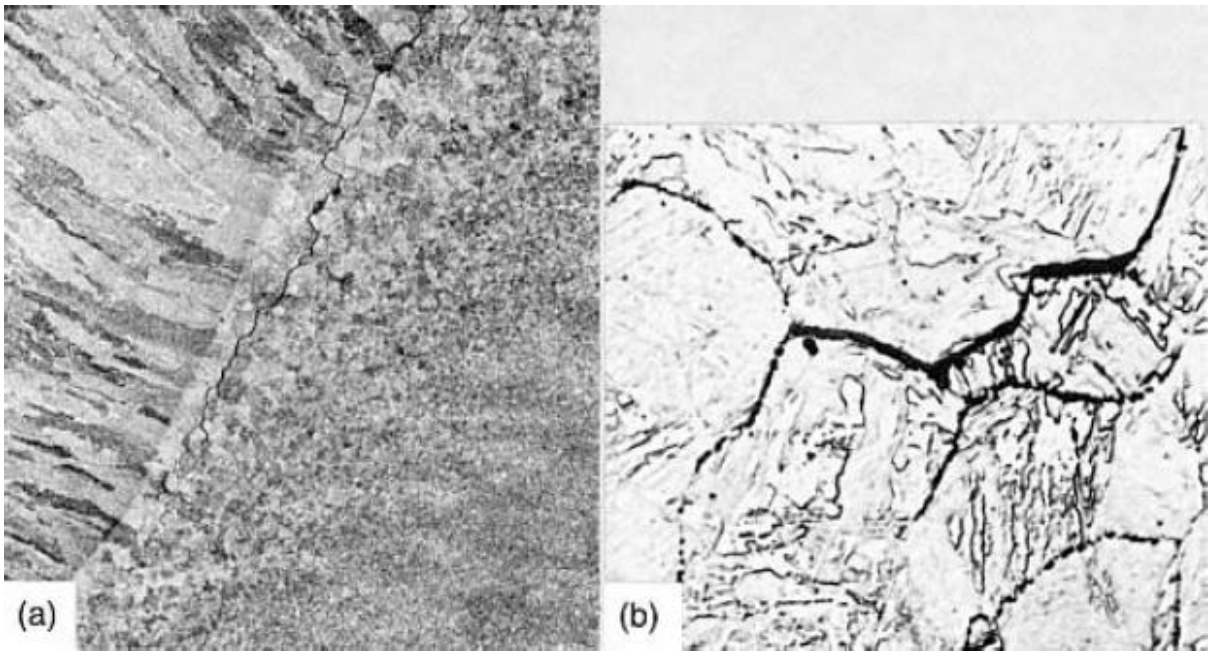

Figure 2.4. Reheat cracking behavior of CrMoV steels in different magnification: (a) ×35, (b) ×1000 [54]

III. APPROACH AND GOAL

3.1. Development of E-C Resistive Coatings

3.1.1. Requirements for E-C Resistive Coatings

As previously discussed in the previous sections, CS is known as to be susceptible to E-C since they possess poor passivity due to the lack of alloy contents. Thus, E-C resistive coatings should provide sufficient thermodynamic stability, electrochemical robustness, and long life-time as shown in Figure 3.1. Electrochemical properties in high-temperature alkaline water of base material should be verified. Also, the method of coating should be applicable to pipeline with complicated geometry. Wettability of the material also should be considered. The water wettability of the Fe and Ni is known to be almost same according to Faghri's study. Their contact angle is 40 and 34°, respectively. Since FAC is an interaction between metal and water, small difference in the contact angle may not introduce any negative effects [83]. Also, porosity of the coatings should be considered as it determines electrochemical active area of the metals. Plus, mechanical properties such as hardness and toughness of the materials are considered. Even though FAC is highly related to the corrosion process, its erosive behavior may make an effect on the coating surface. Thus, high hardness materials would be beneficial.

3.1.2. Candidate Materials

As candidate materials, electroless Ni-P/TiO_2 plating, which possess spatially dispersed TiO_2 nanoparticle in Ni-P matrix (Figure 3.2(a)), and HVOF sprayed Fe-based AMC (Figure 3.2(b)) are selected.

The electroless Ni-P plating has been widely used in assorted industrial fields where corrosion and wear resistance is required such as marine, heavy, automobile industries [84, 85]. Moreover, spatially dispersed nanoparticles are known to enhance the corrosion and wear resistance of Ni-P plating. By adding noble nanoparticles including oxides and carbides, electrochemical and tribological properties of the coating becomes better [86, 87]. TiO_2 [77, 79-81, 88-94], ZrO2 [74, 95, 96], SiO_2 [97], Al_2O_3 [98, 99], SiC [100-103], PTFE [75, 104], carbon based materials such as graphene [105-107] nanoparticles have been introduced to significantly improve corrosion and wear resistance. Among them, TiO_2 nanoparticles exhibit excellent thermodynamic phase stability in alkaline water chemistry at ambient and elevated temperature. Furthermore, the spatial dispersion of TiO_2 nanoparticles does not affect the orientation of Ni crystallites. Thus, Ni-P/TiO_2 coating can be a good countermeasure for E-C. However, the performance of ENP in high temperature flowing water is barely investigated [108, 109]. And, the effect of flow on the corrosion resistance in Ni-P/TiO_2 coatings is barely investigated.

Fe-based AMC is one of the promising coating material where corrosion and erosion resistance

is required. The coating is usually deposited on substrates by thermal spray technique. As one of them, HVOF accelerates melted particle over ultrasonic velocity into substrate. Thus, HVOF sprayed Fe-based AMC is expected to be effective against E-C since they possess excellent corrosion and wear resistance in corrosive environments

3.2. Development of E-C Resistive Alloys

3.2.1. Strategy to Develop E-C Resistive Alloys

In the development of E-C resistive alloys, three criteria are considered: E-C resistance in terms of alloy contents, crack susceptibility, and price. E-C resistance is calculated based on Decruex's relative FAC model as previously discussed in Equation 1.7 Secondly, the crack susceptibility during welding and reheat cracking is considered based on Nakamura's crack susceptibility model (Equation 2.1). Finally, the price of the alloy based on the original price of each ingot is considered. The price of the ingot of Fe, Cr, and Mo is considered.

3.2.2. Candidate Materials

Based on three criteria, the chemical composition of E-C resistive alloy is determined: 2.25Cr-1Mo (FRA 1, hereafter), 3.2Cr-0.5Mo (FRA 2, hereafter), and 4.2Cr (MFRA, hereafter). The relative quantity of three criteria is given in Figure 3.3. Compared to commercial alloys, FRA 1 has same quantities, FRA 2 has decreased relative FAC rate, crack susceptibility, and price, and MFRA has similar FAC rate but decreased crack susceptibility and one of third price.

3.3. Enhancement in Nuclear Safety and Materials Integrity of NPPs

The ultimate objective of this study is enhancement of nuclear safety and materials integrity of NPPs by adopting advanced corrosion resistive materials based on coating and alloy development. Recently, the safety of NPPs has been threatened by severe accident such as the Fukushima accident. The accident broke out due to hydrogen evolution and explosion in zirconium fuel cladding thus many research has been carried out to develop accident tolerant material. In other words, enhancement in materials integrity is directly related to the nuclear safety. Even though the Fukushima accident brings about huge social impacts on nuclear accident within a decade, it is important to focus on E-C since it continuously appears during operation of NPPs, and in some accidents lead to not only failure of secondary system but also human casualties. Thus, it is expected that this study will contribute to the integrity of secondary system, and finally materials integrity in NPPs.

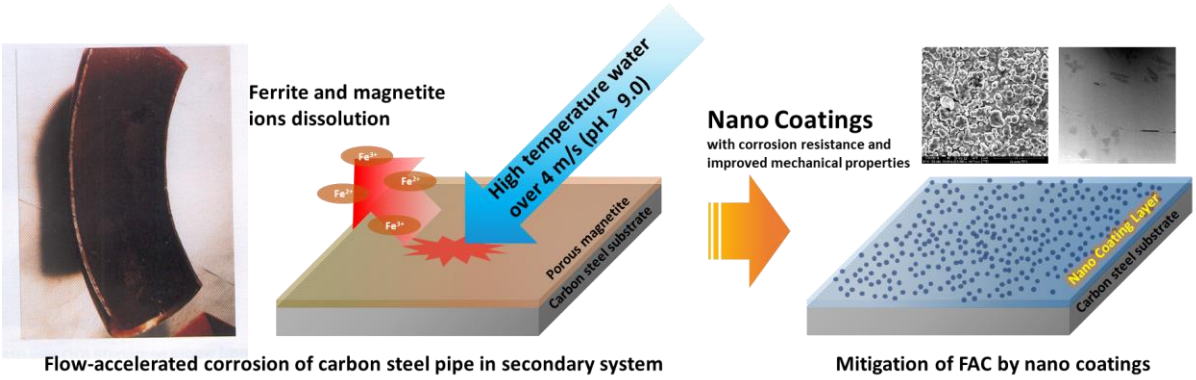

Figure 3.1. Schematic diagram on the concept of the mitigation of E-C by the deposition of nano-structured coatings on CS surface

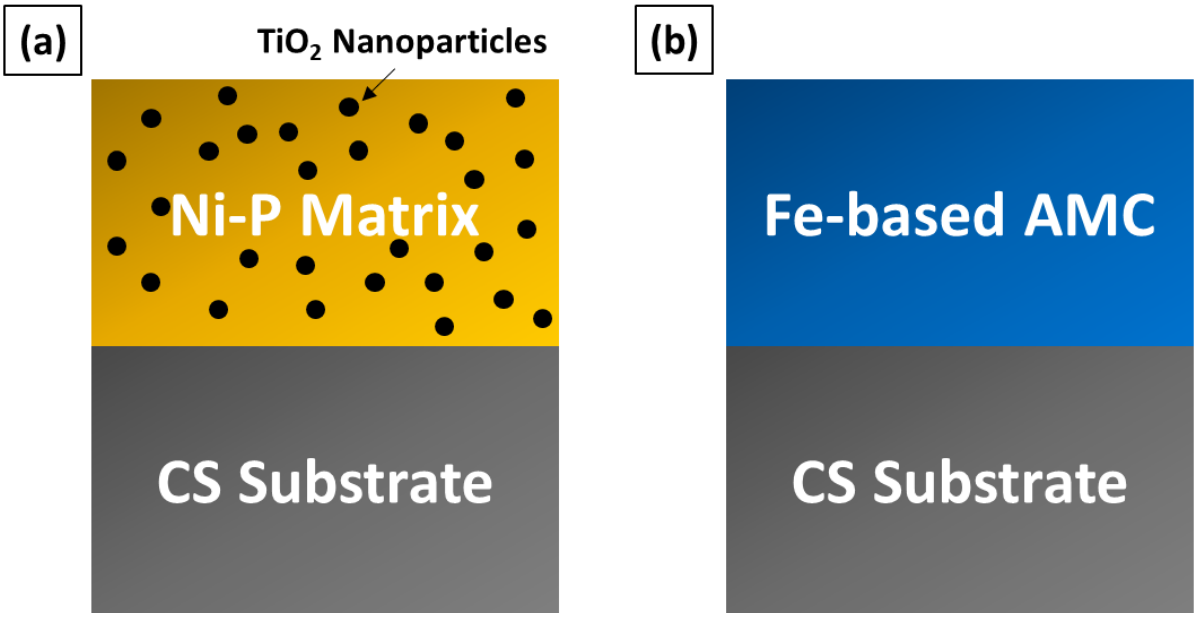

Figure 3.2. Schematic diagrams on the CX of (a) Ni-P/TiO_2 and (b) Fe-based AMC coatings for E-C resistance

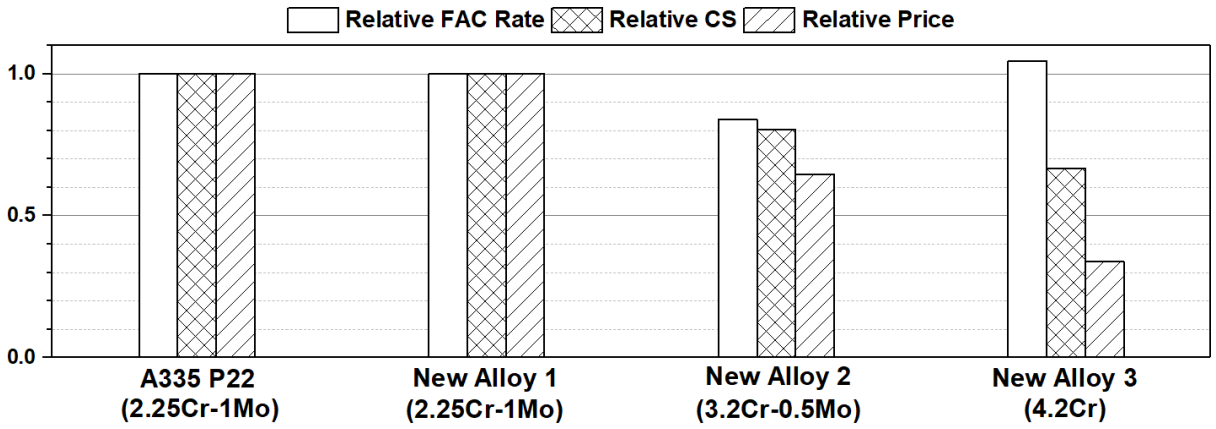

Figure 3.3. Relative quantities of E-C resistive alloys in terms of single phase FAC rate, crack susceptibility, and price

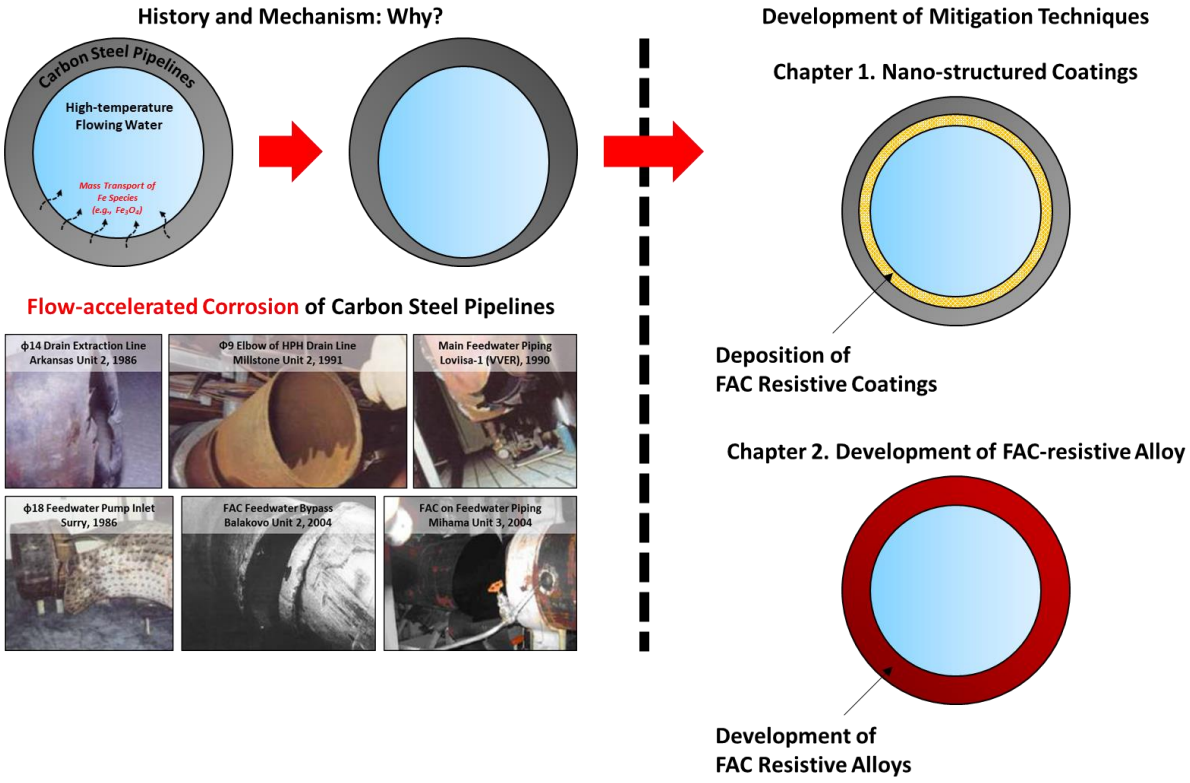

Figure 3.4. Enhancement in nuclear safety and materials integrity of NPPs by the developments of coatings and alloys for pipelines and components of NPPs

IV. MATERIALS AND METHODS

For this study, three commercial alloys were prepared as substrate or a comparison: A516 Gr.60, A106 Gr.B and A335 P22. The chemical composition of the alloys is enlisted in Table 4.1. A516 Gr.60 is used as a plate substrate instead of A106 Gr.B since A106 Gr.B is only manufactured in a seamless pipe.

4.1. Preparation of the E-C Resistive Coatings

4.1.1. Electroless Ni-P/TiO_2 Coatings

A516 Gr.60 CS with a size of 20 mm × 20 mm × 5 mm were prepared as substrates. They are mechanically polished by 320, 400, 600, and 800 Grit SiC papers and cleaned with acetone, ethanol, and DIW in ultrasonic bath. Afterwards, the substrates were degreased in 1 M NaOH and pickled in 8 vol% H_2SO_4 solution for 20 s. Then, the samples were immediately immersed into the two ENP bathes, as listed in Table 4.2. 2 g/L of TiO_2 nanoparticles (Figure 4.1) with size less than 21 nm and 1 g/L of sodium dodecyl sulfate ($NaC_{12}H_{25}SO_4$) were added to deposit Ni-P/TiO_2 coatings, and ultrasonically agitated using a magnetic stirrer to acquire homogenously dispersed nanoparticle suspension. To obtain the minimum zeta potential, the pH of the bathes were adjusted to 9 by adding drops of 1 M NaOH solution. After the plating, heat treatment at 400 ^oC in air condition was conducted for the mitigation of hydrogen embrittlement and the crystallization to Ni_3P, and the pre-passivation. Therefore, two coatings were prepared: Ni-P and Ni-P/TiO_2. To manufacture coated elbows (A106 Gr.B elbow), a loop system was constructed. To circulate plating bath into the elbow, a reservoir tank and a pump was prepared. The elbow is immersed in ultrasonic bath to agitate the nanoparticles.

4.1.2. Fe-based AMCs

For the experiments, Fe-based AMC was prepared by HVOF spray process. A gas atomized feedstock powder, SHS7574 (NanoSteel Co.), was purchased from NanoSteel. The as-purchased powder has a diameter of 25-40 μm (Figure 4.2). Effects of the powder size on the coating quality of HVOF is reported in elsewhere but due to high vaporization temperature of Fe, Cr, W, Mo, Mn, and Si, it is expected that the size effect would be negligible [110]. The chemical composition of the feedstock powder is given in Table 4.1, and the spray parameters and conditions are summarized in Table 4.3. The spray process was done in Castolin Eutectic. The feedstock powder was sprayed onto the samples using H_2 as the ignition gas with 1034 kPa of O_2 pressure. The distance between the gun and the substrate was 200 mm. Sheets of A 516 Gr.60 with dimensions of 20 mm × 20 mm × 5 mm were prepared as substrates, which were sequentially ground using 320, 400, 600, and 800 SiC papers; then, the substrates

were rinsed with acetone, ethanol, and DIW. Finally, the substrates were sandblasted with SiC powders. The sprayed samples were cleaned with acetone, ethanol, and DIW to remove non adherent contamination from the surface.

4.2. Preparation of the E-C Resistive Alloys

4.2.1. Design of Alloy Contents

Chemical composition of the E-C resistive alloys is determined by Ducreux's model. The Cr and Mo contents of P22 is 2.25Cr-1Mo and according to the model, the contents can be substituted by 4.2Cr. Thus, the alloy contents in the E-C resistive alloys are set as shown in Table 4.1. Here, FRA 1 is the model alloy for P22 since the effects of other elements such as Si, Mn should be excluded during the corrosion experiments. FRA 2 is the model alloy to examine the effects of Cr and Mo. MFRA is the Mo-free alloy which substituted Mo in P22 by Cr.

4.2.2. Manufacturing Process

The manufacturing process of the E-C resistive alloys is given in Figure 4.3. Prior to the process, the phase diagrams of the alloys were calculated using ThermoCalc as shown in Figure 4.4. Regardless of chemical composition, the phase diagrams of the alloys show similar trends. The range of austenite stabilized temperature was approximately 850 ~ 1410 ^{o}C for all alloys. Thus, hot rolling and normalizing was processed in this temperature range. For manufacturing of the alloys, VAR methods were employed. In vacuum environments, feedstock materials (>99.9 % Fe, Cr, Mo, and C) were prepared (Figure 4.5(a)), and the plasma arc melted the feedstock materials (Figure 4.5 (b) and (c)). After furnace cooling, the manufactured ingots had a size of 100 mm in diameter and 15 mm in thickness (Figure 4.5. (d)). Then the ingots were hot rolled until the thickness reaches less than 3 mm and air cooled (Figure 4.5 (e) and (f)). The hot rolled ingots finally normalized and tempered in 970 ^{o}C for 30 min and 675 ^{o}C for 10 min, respectively. After the normalizing and the tempering, the ingots were air cooled approximately -10 ^{o}C/sec until it reaches 300 ^{o}C. The cooling temperature profiles were obtained and the CCT diagrams for each alloy is calculated using JMatPro as shown in Figure 4.6. The CCT diagrams shows that the expected microstructure of the alloy is bainite.

4.3. Microstructure and Chemical Analysis

4.3.1. Optical, Electron Microscopy and X-ray Photoelectric Spectroscopy

The microstructure characterizations of the materials were carried out using OM, SEM (Quanta 200, FEI, US) and TEM (JEM-2100F, JEOL, Japan). And the chemistry was analyzed by the attached EDS instruments. For the fabrication of TEM samples in size of 6 × 6 μm, dual beam FIB (Helios 450, FEI, US) was employed. The electron DPs from TEM images were analyzed by FFT analysis software (GATAN Microscopy Suite 3) and those results were compared to the credible references (JCPDS database). The chemical composition was analyzed along the depth profile before and after the erosion–corrosion testing using XPS (K-alpha, ThermoFisher Scientific, US) and compared with XPS database and other credible references. During the depth profiling, Ar^+ ions were used as the sputtering source. All spectra were calibrated to the adventitious carbon peak at 284.8 eV. The backgrounds were subtracted based on the Shirley background.

4.3.2. Synchrotron STXM and XAS

Prior to the STXM and XAS experiments, the samples were process by dual-beam FIB in size of 6 × 6 μm with < 100 nm thickness. The experiments were performed at Pohang Light Source 10A STXM beamline. Schematic, photographs, and sample preparation procedure of the beamline are displayed in Figure 4.7. Spatial resolution of X-ray was 20 – 30 nm and monochromator energy range was 120 – 2000 eV. As shown in Figure 4.7(a), incident X-ray (with intensity, I) penetrate a central stop and a zone plate and eventually focused at the sample after a pin hole. Some X-ray might be absorbed by metallic species (i.e., Fe, Cr) then non-absorbed X-ray (with intensity, I_0) was able to be detected. Here, optical density can be defined as $\log10(I_0/I)$. By moving the sample in x- and y-axis direction (co-axial to width and height direction of the sample, respectively), STXM images can be obtained. Figure 4.7(b) is the photograph of the sample holder. Figure 4.7(c) is the ultra-high vacuum (UHV) chamber for the synchrotron X-ray experiments since soft X-ray can be easily captured by air. From STXM images, XAS spectrum were collected. The reference spectrum of Fe and Cr in various oxidation states were compared to credible references.

4.4. Mechanical Properties

The tension testing and the hardness measurement were conducted for the manufactured ingots. For the tension testing, the plate-type specimens were prepared according to ASTM E8/E8M – 16a. Strain rate was set to 0.3375 fraction/min. For the hardness measurements, 10 points were in the center region of the specimens based on Vickers hardness.

4.5. Corrosion and Erosion Experiments

4.5.1. Electrochemical Experiments in Seawater

Corrosion behavior of the material in seawater was investigated by LSV and EIS using PAR 273A potentiostat (Princeton Applied Research, US) and Solartron 1260A impedance analyzer (Solartron Analytical, US). For seawater tests, 3.5 wt% NaCl solution was prepared as an electrolyte. Pt mesh and SCE were used as counter and reference electrodes, respectively. ECP were measured for 1 h to obtain steady-state conditions. EIS measurements were performed over the frequency range from 10^{-2} to 10^{6} Hz with a DC potential of 0 V versus the ECP and the AC amplitude was set to 10 mV. Fittings of the Nyquist and Bode plots were performed using Z-view®. The best-fit model parameters were found based on a trial-and-error approach and verified through chi-square statistics. LSV curves were measured, with a scan rate was set to 0.5 mV/s and the Tafel's plots were fitted using CorrWare®.

4.5.2. Water Chemistry Control System

For the following experiments under thermal-hydraulic conditions, a recirculation loop system was prepared as shown in Figure 4.8. The loop has of the reservoir water tanks, the feed water system and high-pressure pumps, the water chemistry sensors (DO, pH, and in-let and out-let conductivity), the autoclave, the condensers, and the ion exchanger. As solution, ETA solution with pH 9.3 was prepared to simulate secondary water chemistry. The design temperature of the system was maximum 250 °C. Pressure was controlled by the high-pressure pumps recirculating the water in 4 L/hr of flow rate. The water chemistries parameters were controlled by following system: high-purity Ar continuously supplied and purged the water to eliminate DO in the water (< 1 ppb); the pH sensor was interlocked to chemical injection pumps so if pH_{25} dropped under 9.3, high-pH (150 ppm ETA solution) water was injected into the system until it reached pH_{25} 9.3. Corrosion products were demineralized by an ion-exchanger. The test conditions for the high-temperature and pressure experiments are enlisted in Table 4.4.

4.5.3. Electrochemical Experiments in High-temperature and Pressure Water

Corrosion behavior of the materials in high-temperature water were also investigated LSV and EIS. Ar-saturated 15 ppm ETA solution was prepared in the electrochemical system as shown in Figure 4.9. During experiments, the temperature, pressure, pH, and DO concentration were maintained at 125, 150, 175 °C, 80 bar, 9.3±0.2, and < 1 ppb, respectively. In the corrosion test cell, a three-electrode system was installed with 0.1 M KCl-filled Ag/AgCl electrode and a Pt mesh, which are the reference and counter electrodes, respectively. The reference potential of the electrode were calculated with the following equation [111]:

$$E_{Ag/AgCl}\ \ (mV\ \ vs\ \ SHE)) = 288 + 3.0 \times 10^{-6}\Delta T^3 - 2.40 \times 10^{-3}\Delta T^2 - 0.749\Delta T \quad (4.1)$$

where $E_{Ag/AgCl}$ is the reference potential of the reference electrode against SHE and ΔT is the difference between target temperature and room-temperature. Working electrodes were electrically insulated with a PTFE stage and the contact area was ca. 0.384 cm^2. ECP were measured for 2 h to obtain steady-state conditions. EIS measurements were performed over the frequency range from 10^{-2} to 10^6 Hz with a DC potential of 0 V versus the ECP and the AC amplitude was set to 10 mV. Fittings of the Nyquist and Bode plots were performed using Z-view®. The best-fit model parameters were found based on a trial-and-error approach and verified through chi-square statistics. LSV curves were measured, with a scan rate was set to 0.5 mV/s and the Tafel's plots were fitted using CorrWare®.

4.5.4. FAC Simulation Experiments

FAC simulation was conducted in a rotating cage system as shown in Figure 4.10. The samples were installed at the rotating cage which is co-axially fixed to the shaft of the magnedrive. The cage was rotated at 1500 RPM which could be converted to approximately 5 m/s of flow velocity. The tested samples were sequentially cleaned by acetone, ethanol, and DIW in ultrasonic bath to detach corrosion products, then weight changes were recorded using a balance. The average and standard deviation was calculated based on 4 samples per kind.

4.5.5. FAC Experiments

FAC experiments for 90-degree elbows, made of A106 Gr.B and A335 P22, were conducted in the loop system as shown in Figure 4.11. The system, located at FNC Technology Co., Ltd., is composed of the two sets of the high-pressure pumps, the feed pump, the reservoir water tanks, and the water chemistry sensors. The temperature of the test sections was set to 150 ºC, and the water chemistry of the system was: pH_{25} = 9.3, DO concentration < 1 ppb. Temperature was controlled by a set of heaters, and pH was controlled by ETA. The thickness of the samples was measured by UT (PT-878, General Electric, US) with attached dual elements transducer. The measuring error was 5 % and frequency was 1 – 20 MHz, which is typically used for pipe thickness measurement.

Table 4.1. Chemical composition of the commercial alloys and Fe-based materials

Materials	Chemical Composition (wt.%)															
	Fe	**Cr**	**Mo**	**Cu**	**Ni**	**W**	**Mn**	**Al**	**Si**	**Nb**	**Ti**	**V**	**B**	**C**	**P**	**S**
A516 Gr.60	Bal.	0.3	0.08	0.3	0.3		0.95	0.02	0.4	0.01	0.03	0.02		0.18	0.015	0.008
A106 Gr.B	Bal.	0.4	0.15	0.4	0.4		1.06		0.1			0.08		0.3	0.035	0.035
A335 P22	Bal.	2.25	1				0.3		0.5						0.025	0.025
Fe-based AMC	Bal.	18	14			6	2		1				3			
FRA 1	Bal.	2.25	1											0.1		
FRA 2	Bal.	3.2	0.5											0.1		
MFRA	Bal.	4.2												0.1		

Table 4.2. Chemical composition of the plating bathes and parameters [55]

Chemical or Parameters	Quantity		Unit	Note
$NiSO_4 \cdot 6H_2O$	32.5		g/L	Nickel source
$NaH_2PO_2 \cdot H_2O$	26		g/L	Reducing agent
$Na_3C_6H_5O_7 \cdot 2H_2O$	13		g/L	Complexing agent
H_2NCH_2COOH	32.5		g/L	Brightening agent
$(NH_4)_2SO_4$	35		g/L	pH buffer
Anatase TiO_2	0	2	g/L	Nanoparticles
$NaC_{12}H_{25}SO_4$	0	1	g/L	Anionic surfactant
pH	9			
Temperature	80		^oC	
Agitation	300, 2		RPM, hr	
Time of plating	2		Hr	

Table 4.3. Spraying parameters and condition of the HVOF process

Parameters (Unit)	**Condition**
Air Pressure (kPa)	620
O_2 Pressure (kPa)	1034
LPG Pressure (kPa)	655
Powder Velocity (kPa)	255
Gun-Sample Distance (mm)	200
Powder Transport Gas	N_2
Ignition Gas	H_2

Table 4.4. Test conditions, methods, samples of E-C experiments

Tests	Methods	Samples	Temperature (^{o}C)	pH_{25}	Test Duration
Electrochemical Experiments	LSV, EIS	CS	125, 150, 175	9.3 (ETA Injection)	2 hr
		Ni-P			
		Ni-P/TiO_2			
FAC Simulation Experiments	Rotating Cage Corrosion (v = 5 m/sec)	CS	125, 150, 175, 200	9.3 (ETA Injection)	14 days
		P22	150		
		Ni-P	125, 150, 175, 200		
		Ni-P/TiO_2	125, 150, 175, 200		
		Fe-based AMC	125, 150, 175, 200		
		FRA 1	150		
		FRA 2	150		
		MFRA	150		
FAC Experiments	2'' Elbow Pipe (R = 150mm, v = 5.7 m/sec)	CS	150	9.3 (ETA Injection)	30 days
		P22	150		
		Ni-P/TiO_2	150		
		Fe-based AMC	150		

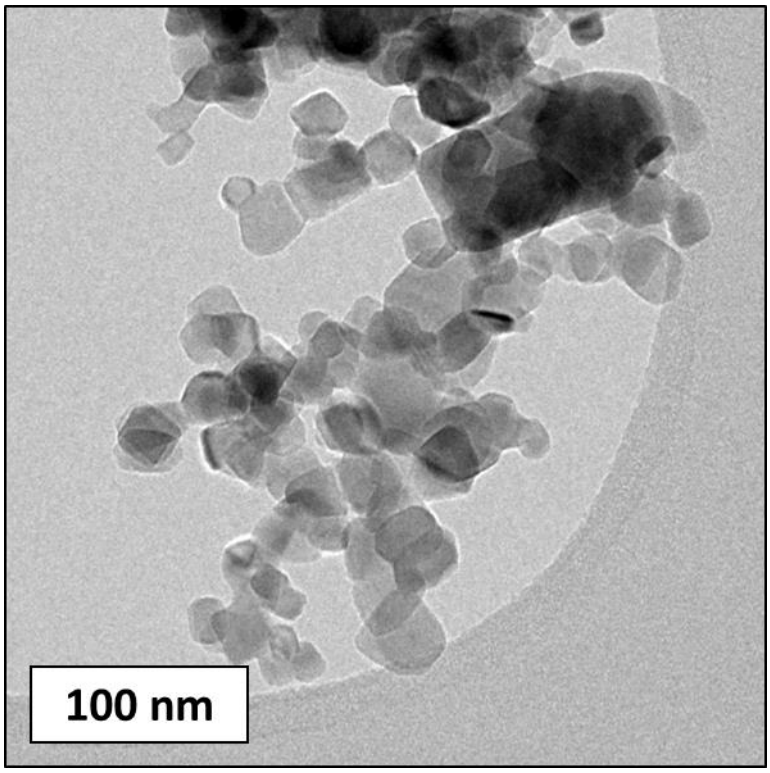

Figure 4.1. TEM morphology of TiO_2 nanoparticles dispersed in ethanol solution

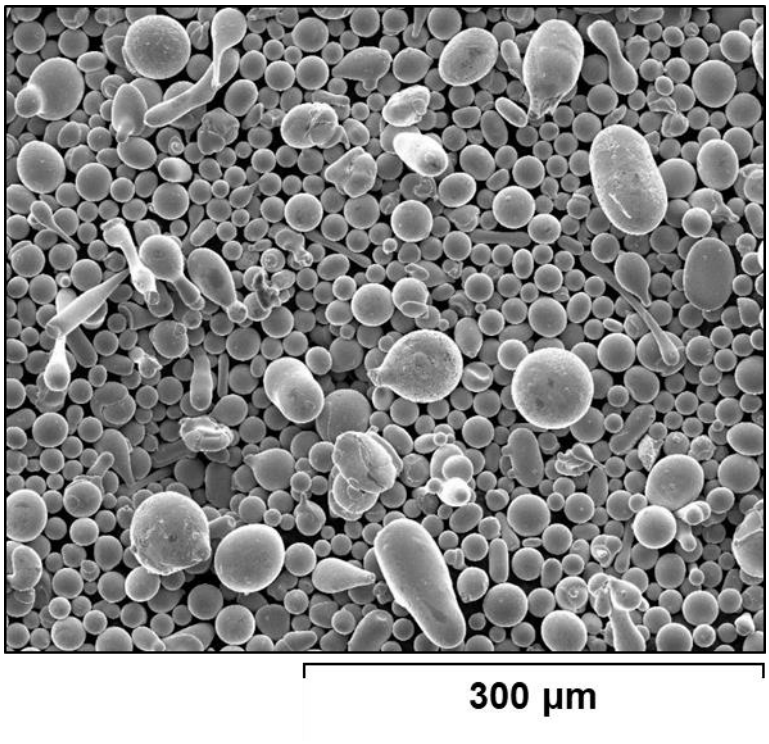

Figure 4.2. SEM powder morphology of Fe-based AMC feedstock powder

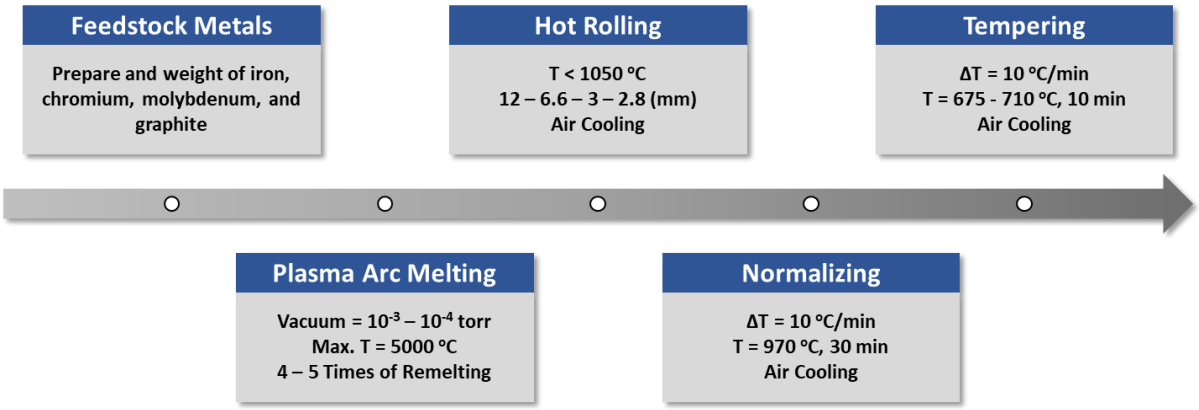

Figure 4.3. Manufacturing process of the E-C resistive alloys and parameters

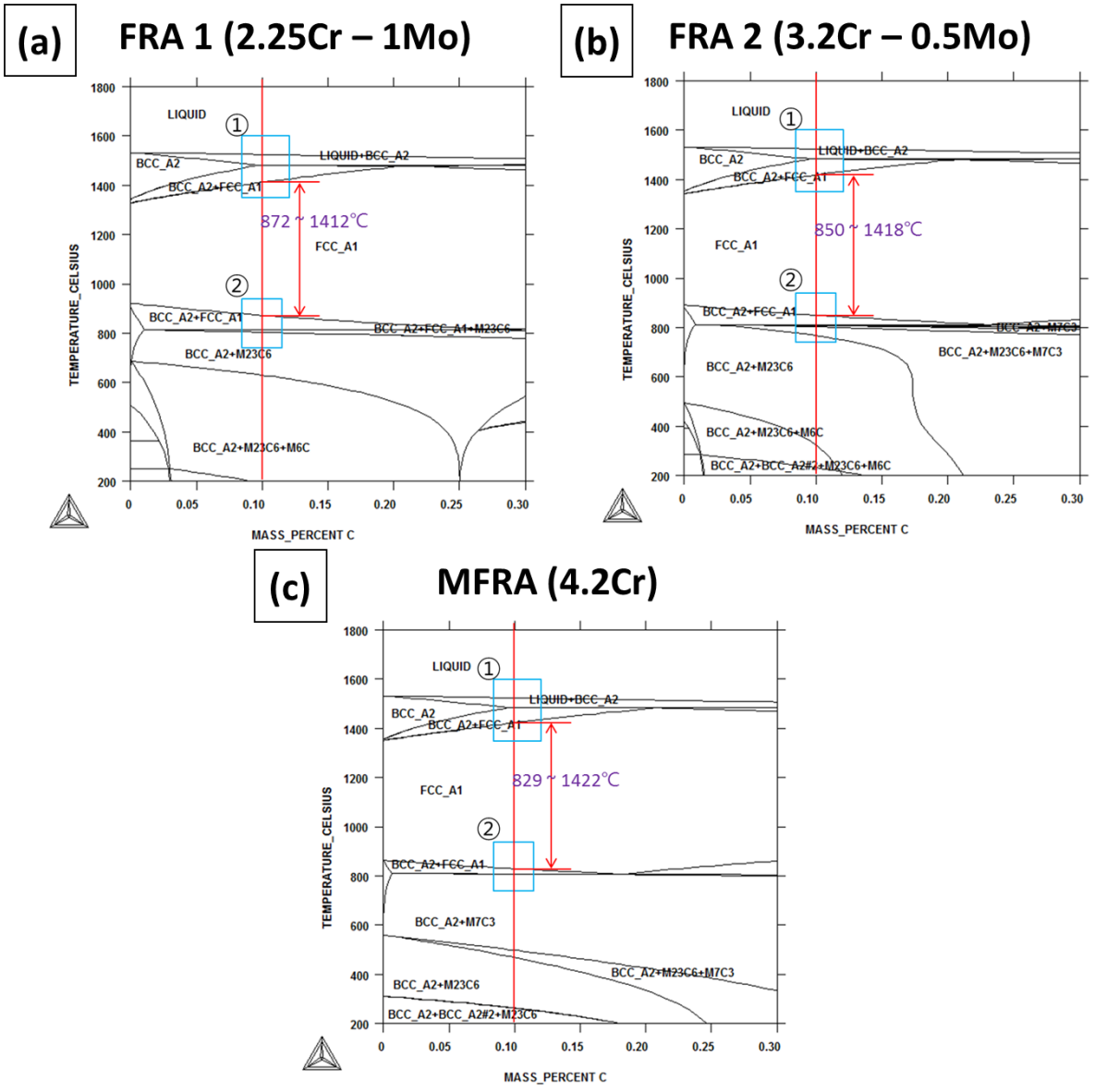

Figure 4.4. Phase diagram of (a) FRA 1, (b) FRA 2, and (c) MFRA for the determination of hot rolling and heat-treatment conditions constructed by ThermoCalc

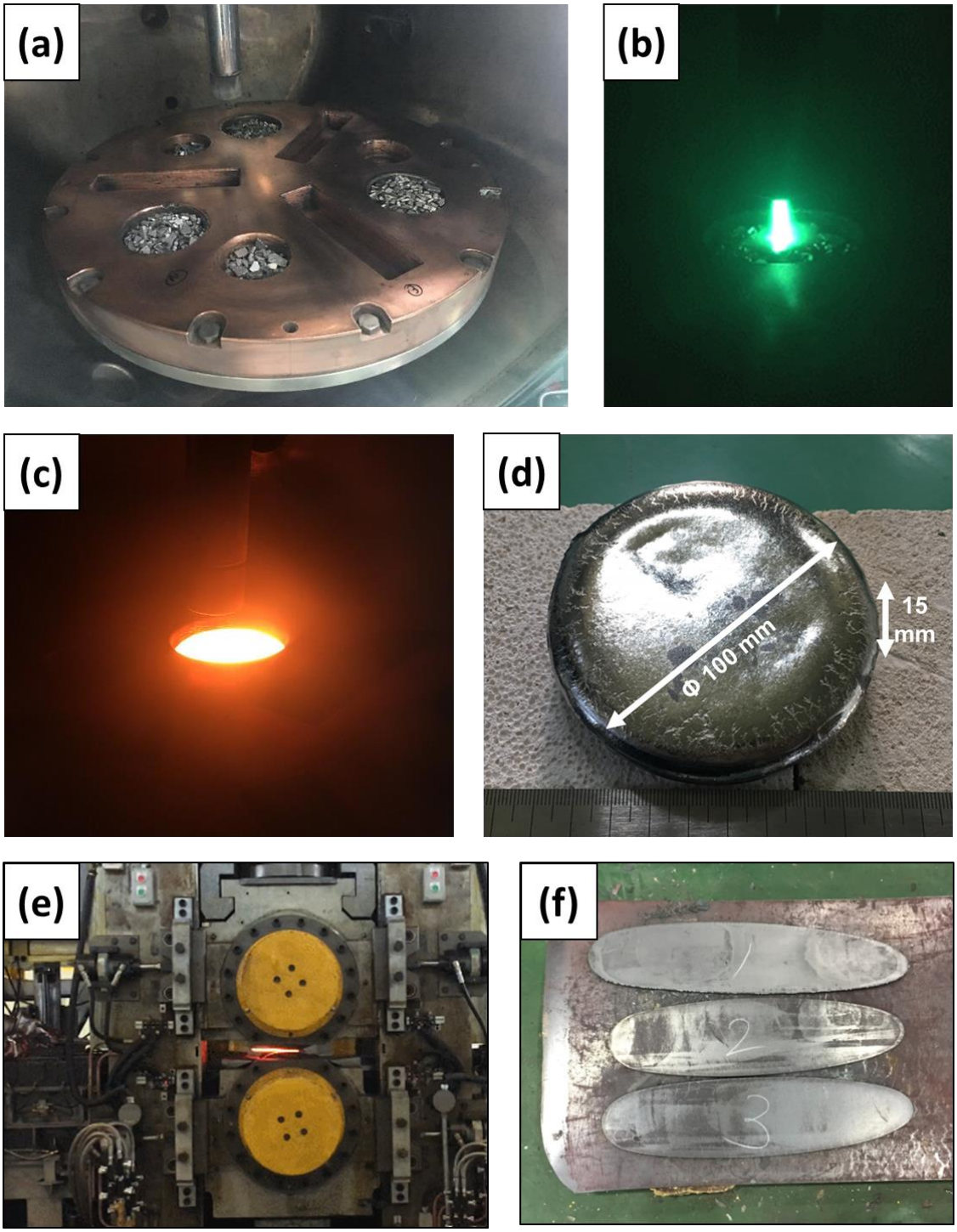

Figure 4.5. Photography of the manufacturing process: (a) prepared feedstock metals on Cu crucible, (b) morphology of arc, (c) a melted and (d) a manufactured ingot, (e) hot rolling process, and (f) hot rolled plate]

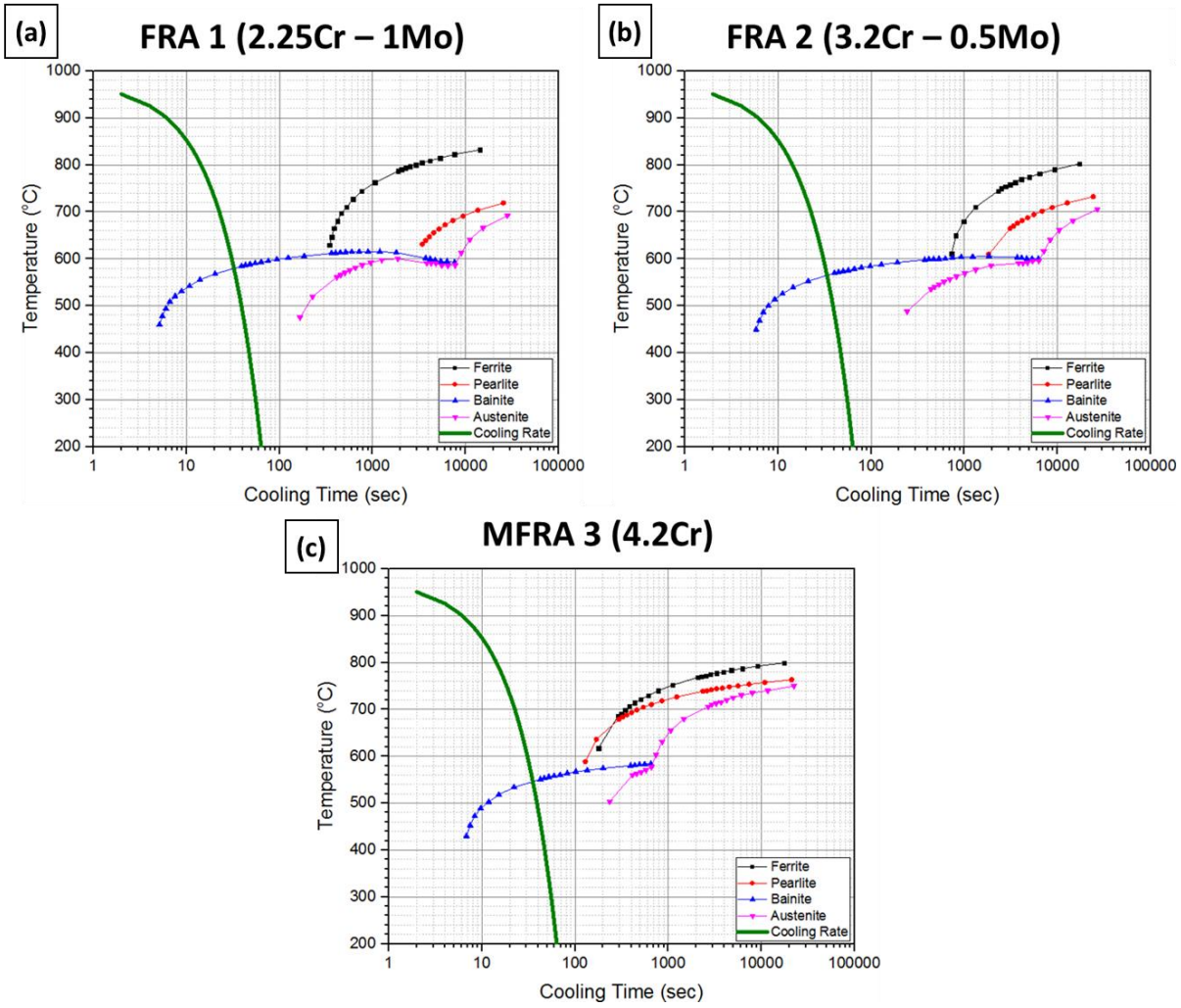

Figure 4.6. CCT diagrams and measured cooling rate of the alloys: (a) FRA 1, (b) FRA 2, and (c) MFRA

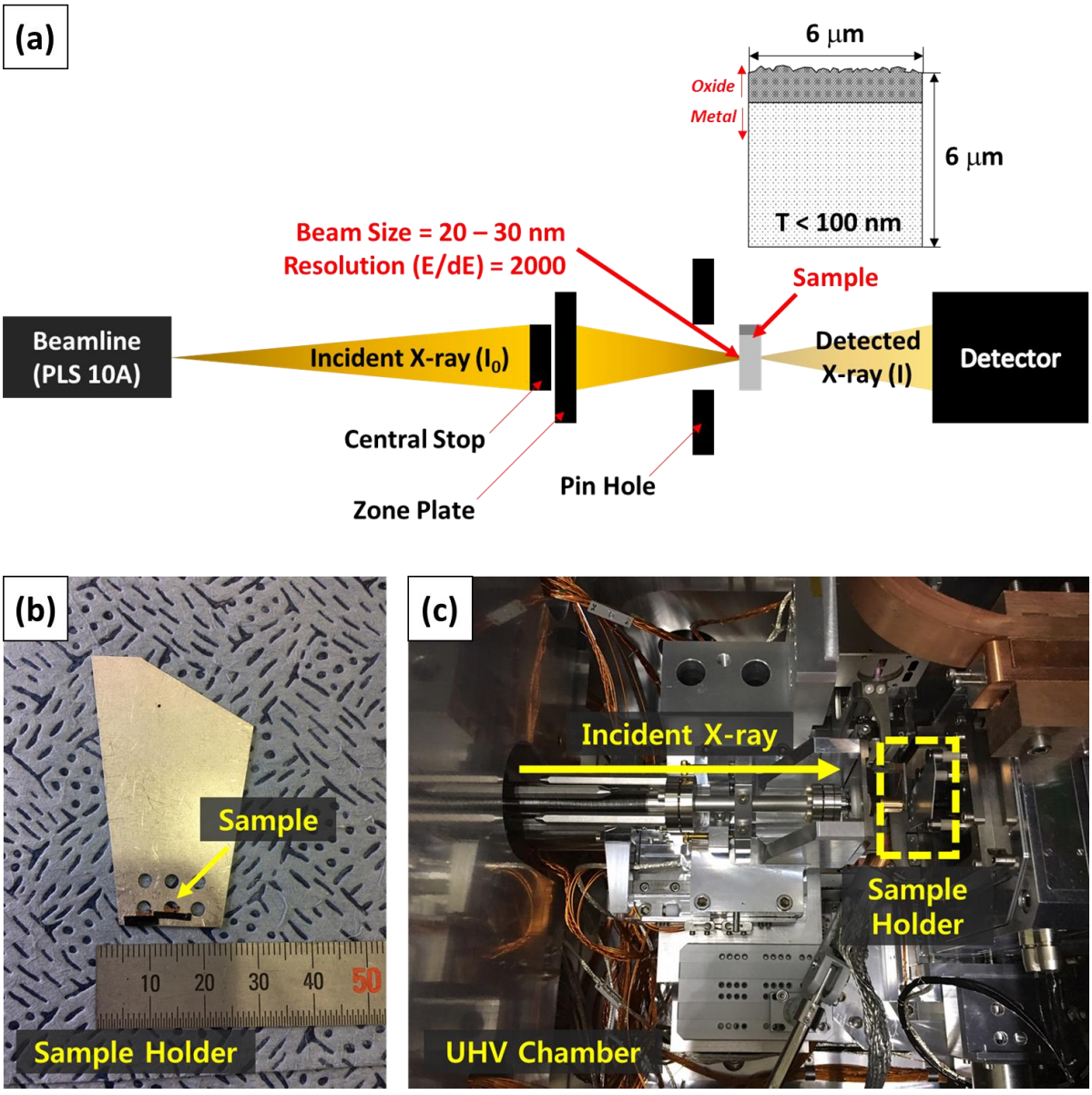

Figure 4.7. (a) Schematic diagram of the experimental parts of the PLS 10A STXM beamline and photography of (b) installed sample and (c) UHV chamber for STXM and XAS experiments

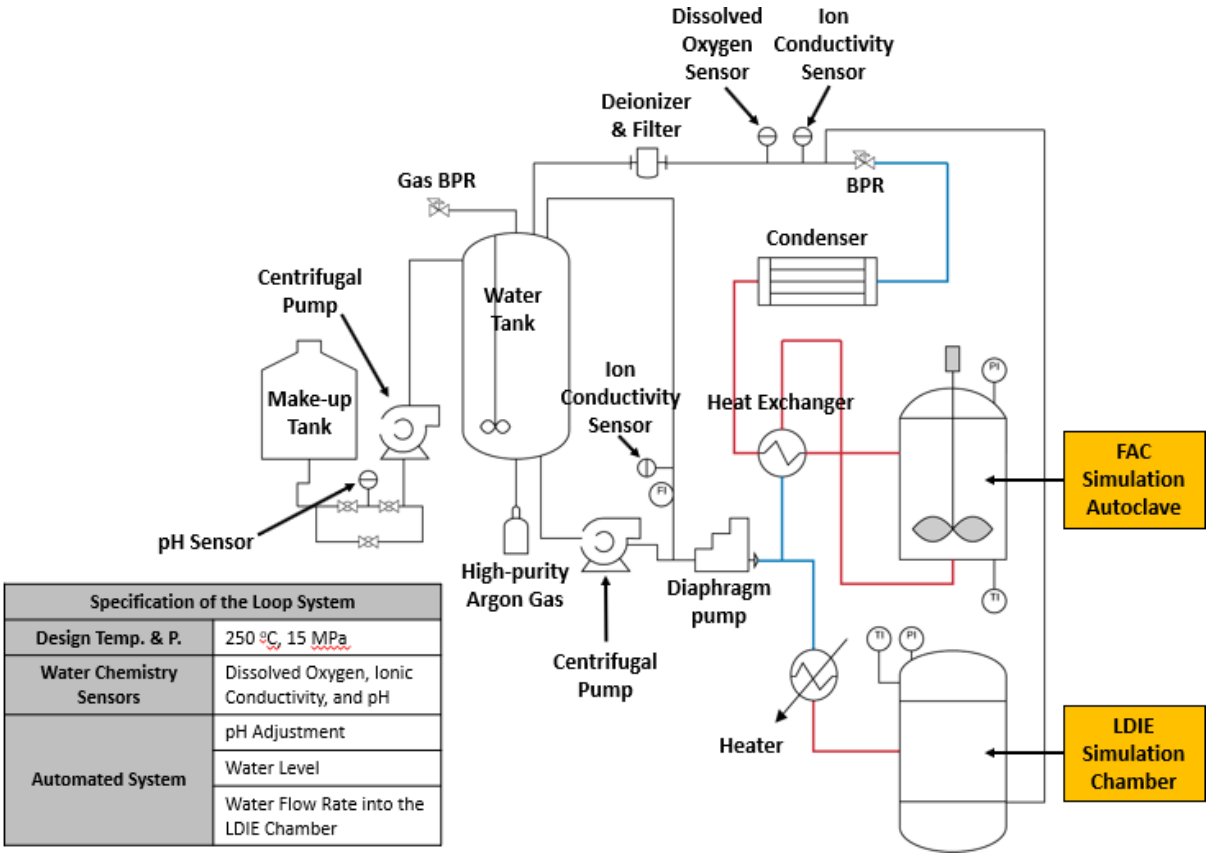

Specification of the Loop System	
Design Temp. & P.	250 °C, 15 MPa
Water Chemistry Sensors	Dissolved Oxygen, Ionic Conductivity, and pH
Automated System	pH Adjustment
	Water Level
	Water Flow Rate into the LDIE Chamber

Figure 4.8. Schematic diagram of the water chemistry control system, test chambers, and specification for FAC simulation and LDIE simulation tests.

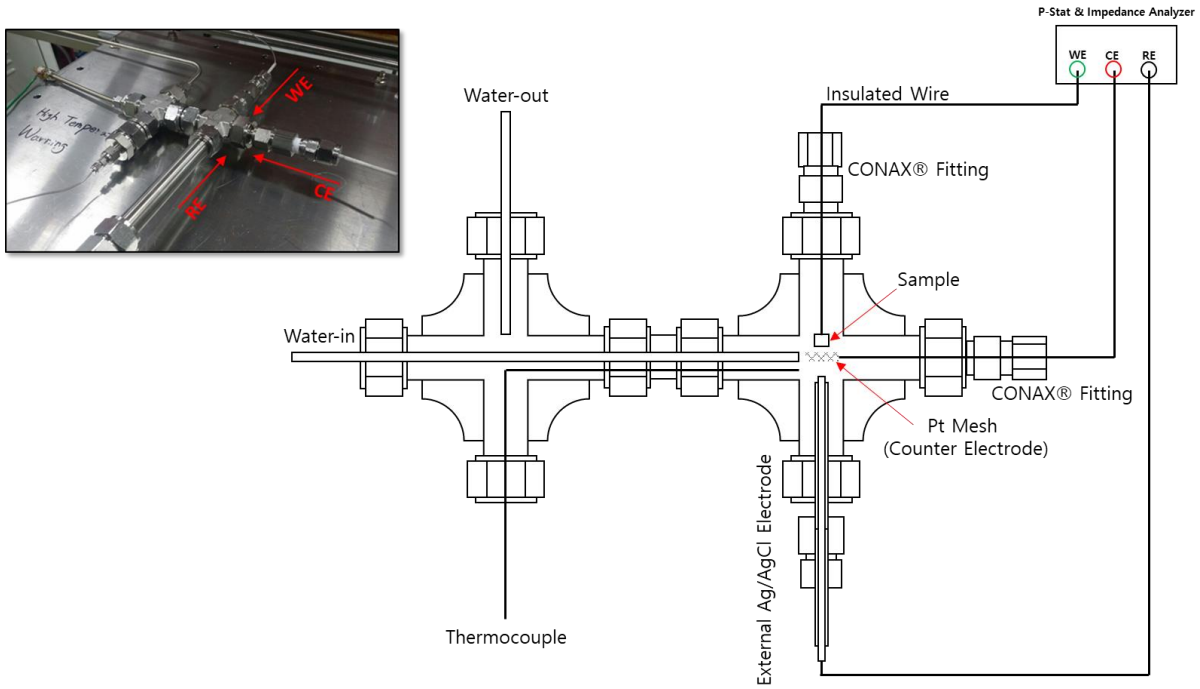

Figure 4.9. Photography and schematic diagram of three-electrode system for high-temperature and pressure condition

Figure 4.10. FAC Simulation autoclave system with a magne-drive, a shaft, and a sample cage

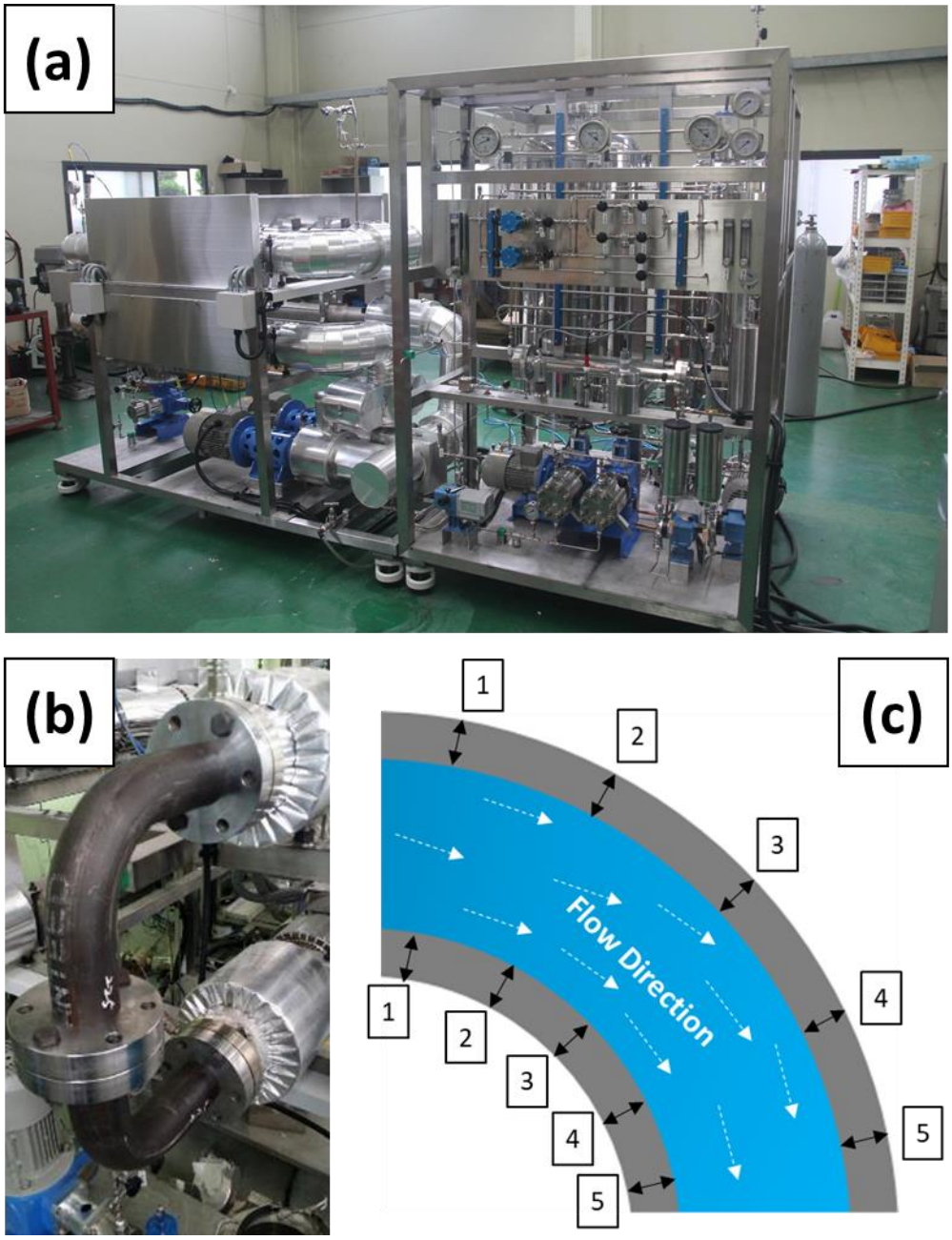

Figure 4.11. FAC tests facilities for the performance evaluation of the coated CS elbows: (a) overall photography, (b) installed coated 2” CS and LAS elbows with radius 150mm, and (d) UT position

V. RESULTS AND DISCUSSION

5.1. Performance of the E-C Resistive Coatings

5.1.1. Microstructure and Chemical Analysis

Microstructure characterization using SEM surface, TEM CX morphologies, and EDS results of Ni-P and Ni-P/TiO_2 coatings are displayed in Figure 5.1. The surface morphologies of the coatings reveals homogeneity without any porosity and cracking. This indicates that the plating parameters are well optimized for both coatings. As shown in Figure 5.1(a), microstructure of Ni-P coating is composed of multiple Ni-P clusters with a size of approximately 5 μm. TEM CX morphologies confirms the presence of thin NiO film at the surface, which is formed during the heat treatment procedure. On the other hand, the morphology of Ni-P/TiO_2 coating is distinguishable from Ni-P coating. While Ni-P coating possess relatively regular shape and size of Ni-P grains, Ni-P/TiO_2 has 1–8 μm size grains (Figure 5.1(b)). This is originated from that TiO_2 nanoparticles probably provided the nucleation site for Ni^{2+} during the plating process [112]. Like to Ni-P, Ni-P/TiO_2 also possess thin NiO film at the surface which is formed during the heat treatment. The chemistry of TiO_2 nanoparticles is confirmed by electron DP, that d-spacing equal to 0.352 and 0.189 nm which mall matches with JCPDS reference data. Furthermore, the heat treatment also induces the segregation of P into the cluster boundaries according to Hentschel [113] and Hur [114]. When the concentration of P exceeds a certain amount, BCT Ni_3P is formed.

SEM morphologies of Fe-based AMC is illustrated in Figure 5.2. In Figure 5.2(a), the feedstock powder has a homogenous size (25–40 μm) distribution of in spherical shape. Figure 5.2 (b), (c) reveal the surface and CX morphologies, respectively. The surface morphology reveals some roughness with a collection of splats. The higher magnification image of the surface in Figure 5.2 (b) shows that the surface consists of both flat and pit regions. In the cross-sectional morphologies, a compact coating layer approximately 350 μm thick is deposited. Furthermore, large and small pores are observed. The large pores located between flattened droplets are mainly caused by the loosely packed layer structure or the gas porosity phenomenon, while the small pores are attributed to shrinkage porosity, as displayed in Figure 5.2 (d) [68-70, 115]. Yellow arrows indicate small pores, and white arrows indicate large pores, which appear between droplets near the surface. In Figure 5.2(e), the chemical composition of the coating is displayed as marked in Figure 5.2(c). The amorphous coating layer approximately 320 μm thick can be verified with a homogenous chemical composition without exhibiting unexpected second phases. The cross-sectional morphology of the coating agrees well with observations in other studies [68-70, 115].

Figure 5.3 shows the TEM images and an electron-diffraction pattern image of the coating layer. In Figure 5.3(a) and (b), a boundary of an amorphous and nanocrystalline phase region can be

distinguished. Nanocrystalline structures are known to form during the rapid heating and quenching process of the feedstock powder [115]. The nanocrystalline phases exhibit the forms of both polygons and particles, as shown in Figure 5.3(a). The halo-ring pattern is assigned to the amorphous matrix layer, while the electron DP reveals that it consists of various oxides, carbides, and borides such as Fe_2C, Cr_7C_3, $M_{23}C_6$, Cr_2B, and some other oxides that are known as to be formed by self-annealing and/or adiabatic re-coalescence in the deposited layers [115]. In this investigation, the nanocrystalline phase was identified as Cr_7C_3 according to the electron DP.

The XPS spectra of the as-sprayed coatings are displayed in Figure 5.4 with the alloy elements Fe, Cr, and Mo. The spectra are listed from bottom to top with sputtering times of 0, 20, 330, 660, 1000, 2000, 3000, 4000, 5000, and 6000 secs, respectively. The reference spectrum of each element is extracted from credible references and the NIST XPS database. For Fe (Figure 5.4 (a)), the peak of Fe_2O_3 (709.8 eV) is present until the sputtering time reaches 660 s. Analogous to that of Fe, the Cr peak (574.2 eV) is dominant after 1000 s, while the Cr_2O_3 peak (576.8 eV) is present until 660 s (Figure 5.1.1.4(b)). It is known that un-sputtered Cr_2O_3 exhibits a sharp structure, which is directly located on the right side of the $Cr_2p_{3/2}$ peak but it is not observable since the intensity of Cr is low. For Mo (Figure 5.1.1.4 (c)), no peaks representative of oxides are present. The intensities increase as the sputtering time increases but become saturated after 1000 s.

In summary, the microstructure characterization reveals that the as-sprayed coating exhibits an amorphous alloy matrix, nanocrystalline phases such as Fe_2C, Cr_7C_3, $M_{23}C_6$, Cr_2B, and a native oxide film on the surface that mainly consist of Fe_2O_3 and Cr_2O_3.

5.1.2. Electrochemical Properties in Seawater

LSV curves of CS, Ni-P, and Ni-P/TiO_2 and their fitting parameters based on the Tafel fitting were shown in Figure 5.5 and Table 5.1. Figure 5.5 gives that the coated samples have a higher corrosion potential (E_0) as well as low exchange current density (I_0), and thus they are much nobler in oxidizing or aggressive environments when compared to CS. Effects of TiO_2 can be clarified by comparing the curves of Ni-P and Ni-P/TiO_2. Moreover, Ranganatha and Abdel Aal explained the role of TiO_2 nanoparticles as a corrosion inhibitor through two mechanisms [91, 92]: Firstly, TiO_2 nanoparticles act as a physical barrier to prevent localized corrosion at the surface of the Ni coating layer. As shown in Figure 5.1, numerous cluster boundaries are observed in surface morphologies, which are a potential pathway for electrolyte penetration. In this context, the nanoparticles can efficiently suppress the localized corrosion in cluster boundaries or defects. Secondly, TiO_2 acts as a cathode, while Ni acts as an anode because the corrosion potential of TiO_2 is notably more positive than that of Ni, so the passivity of Ni-P alloys are reinforced. Moreover, reinforcement of Ni-P matrix by the spatial dispersion

nanoparticles induces greater hardness. Novakovic reported that for low concentration of TiO_2 nanoparticle in bath (< 2 g/L) induces higher hardness by incorporation of Ni and Ni_3P matrix with TiO_2 nanoparticles [81]. In other words, the fine nanoparticles enhances the integrity of the coating by hindering the movement of dislocation.

From the microstructure analysis result, equivalent circuit models for CS and the coatings have been established as shown in Figure 5.6. Traditionally, metals and alloys exhibit Randle's circuit model (Figure 5.6(a)). This model composed of solution resistance (R_s), charge transfer resistance (R_{ct}), and double layer constant phase element (CPE_{dl}). For an ideally flat surface (i.e., polished metals), CPE_{dl} has usually n=1 where n is exponent value. In contrast, the Lyons and Brandon's model (Figure 5.6(b)) has been adopted for the heat-treated coatings because there is pre-oxidized NiO layer exist at the topmost surfaces. This model composed of R_s, pore resistance (R_{po}), and oxide capacitance (CPE_c). CPE_c is related to the capacitance of a top oxide coating. The impedance of CPE (Z_{CPE}) can be given as follows:

$$Z_{CPE} = \frac{1}{-Q(i\omega)^n} \tag{5.1}$$

where Q is the constant independent of the frequency relating to each capacitor, i is the imaginary number, ω is the angular frequency. The AC responses of the coatings are displayed in Figure 5.7 and the fitting parameters are enlisted in Table 5.2. The R_s values of the AC responses were approximately 15 $\Omega \cdot cm^2$ which is a typical value for 3.5 wt.% NaCl solution. The diameters of semi-circles of the plots approximately gives that the corrosion resistivity of the materials can be enlisted as follows: Ni-P/TiO_2, Ni-P, and CS. This signifies the nanoparticles make the coating resist Cl^- containing solution. In addition, C_{dl} of the samples are given as 59.3, 0.876, and 1.28 $\mu F/cm^2$ for CS, Ni-P and Ni-P/TiO_2, respectively. This implies that the metallic parts of the coatings or the substrates, i.e., Ni-P or Fe, are comparatively less exposed to the solution. Two semi-circle region in Ni-P and Ni-P/TiO_2 indicates the presence of NiO; the electrochemical properties of NiO/electrolyte and Ni-P/electrolyte are revealed. The data point at the lowest frequency gives the instructive information on the electrochemical stability of Ni-P/TiO_2 which is at least one-order higher than that of Ni-P. Thus, compared to the CS, Ni-P and Ni-P/TiO_2 behaves as a capacitor, which inhibits the penetration of electrolytes and aggressive ions more efficiently with good coating quality. The corrosion resistance of Ni-P and Ni-P/TiO_2 is 15 and 150 times higher, respectively, than that of CS indicating that the anodic polarization is efficiently suppressed. This indicates a low C_{dl}, and the electron accumulation at the metal/electrolyte interface is inhibited leading to surface activation. Additionally, the exponent of CPE_{dl}, n_{dl}, for the coatings is closed

to 1 while that of the as-polished sample is 0.782 indicating capacitor behavior of the coatings. The presence of TiO_2 leads to high R_{ct}, low C_{dl} and n_{dl} close to 1 compared to CS and Ni-P. Effects of heat treatment on the EIS results are caused by the formation of crystalline Ni and Ni_3P and mainly the oxide layer at the surface. This can be explained by the role of TiO_2 during corrosion process, which is previously discussed [91, 92] as shown in Figure 5.8. In Figure 5.8(a), boundaries of Ni-P clusters play a role as electrolyte penetration path. However, TiO_2 nanoparticles are spatially dispersed in Ni-P matrix, the structure of matrix is randomly oriented and TiO_2 obstruct the penetration of the electrolyte as shown in Figure 5.8(b).

Corrosion behavior in seawater of Fe-based AMC is displayed in Figure 5.9. The LSV curves of CS and Fe-based AMC are compared. Compared to that of CS, E_0 of Fe-based AMC is shifted to more positive direction and the i_0 is shift to large value. This is because Fe-based AMC is susceptible to corrosion in seawater since it has much wider surface area than CS. Similar trend is observable in EIS results, shown in Figure 5.10. Equivalent circuit model for CS and Fe-based AMC is Randle's circuit model since interface structure of both alloys are simple metal/electrolyte interface. In similar, those of LSV curves, the corrosion resistance of Fe-based AMC is less than that of CS because of large surface area according to the diameter of the semi-circles. As shown in Figure 5.11, R_{ct} of Fe-based AMC is less than that of CS (Figure 5.11(a)) meaning oxidation of metallic species in Fe-based AMC is activated in this electrolyte. Larger C_{dl} indicates the surface area of Fe-based AMC. Also, relatively low n_{dl} is due to intrinsic surface roughness and defects. Therefore, in terms of electrochemical properties, Fe-based AMC is not effective for corrosive environment such as seawater environments. Zheng's study on erosion behavior of 304 SS and Fe-based AMC also shows that Fe-based AMC is much corrosive in static NaCl solution [68]. However, Fe-based AMC is usually used in erosion environments or high-temperature conditions. Thus, its performance in high-temperature condition will be evaluated in the following sections.

5.1.3. Electrochemical Properties in High-temperature and Pressure Water

In the previous sections, the effects of TiO_2 nanoparticles on the corrosion behavior of CS, Ni-P and Ni-P/TiO_2 in seawater was discussed in agreement with the microstructure characterization and the other previous works. Now, the performance of Ni-P and Ni-P/TiO_2 as an anti-corrosion barrier for CSs which are extremely susceptible to corrosion in alkaline water at 125, 150, and 175 °C will be demonstrated.

LSV curves of the samples at elevated temperature are plotted as shown in Figure 5.12 and the best-fit parameters and those results Table 5.3. At 125 °C, E_0 of the samples can be enlisted as CS < Ni-P < Ni-P/TiO_2. This indicates that the coatings show noble state and this effect is stimulated by TiO_2

nanoparticles (Figure 5.12(a)). As E_0 shifts to positive direction, I_0 decreases meaning that Ni-P/TiO_2 is the most corrosion resistive in these environments. Polarization resistance (R_p) values show that the corrosion resistance of Ni-P/TiO_2 coating is 8 and 4 times higher than those of CS and Ni-P. Similar trend is observable at 150 ºC. The coatings have positive E_0 and low I_0 meaning that they are effectively suppress corrosion where FAC is favored. In this condition, the corrosion rate of Ni-P/TiO_2 is 80 and 3 times lower than the others according to R_p. Thus, it can be concluded that at 150 ºC, Ni-P/TiO_2 can be an adequate countermeasure. However, at 175 ºC, E_0 of the samples is almost same and I_0 of CS, Ni-P, and Ni-P/TiO_2 show not much difference. And, I_0 of Ni-P is less than Ni-P/TiO_2 meaning the effect of spatially dispersed TiO_2 is diminished. This indicates that at the temperature 175 ºC, the predominant electrode kinetic becomes diffusion controlled rather than activation controlled. The metal loss or corrosion rate of CS and the coatings is displayed in Figure 5.13. In this graph, it can be observed that the corrosion rate of the metals are dominated by i_0 at 125 and 150 ºC but by i_{lim} at 175 ºC. And, according to the corrosion rate of Ni-P and Ni-P/TiO_2, TiO_2 induces negative effect on corrosion at 125 and 150 ºC. This is due to TiO_2 induces galvanic corrosion for Ni-P matrix in the early stage of corrosion.

The equivalent circuit models of CS, Ni-P, and Ni-P/TiO_2 under high-temperature condition is established as previously shown in Figure 5.6 and the AC responses of the samples under 10 mV perturbation are displayed in different temperature: 125 (Figure 5.14), 150 (Figure 5.15), and Figure (5.C). The best-fit fitting parameters are listed in Table 5.4. All of the samples consist of two semi-circle regions likewise to the corrosion behavior in seawater. At 125 ºC (Figure 5.14), the diffusion behavior is not observable so only semi-circle regions appears in all frequency ranges. The $R_{po} + R_{ct}$ of CS, Ni-P and Ni-P/TiO_2 are 0.181, 1.485 and 1.554 kΩ·cm^2, respectively, indicating that Ni-P/TiO_2 is much corrosion resistive in this temperature. Likewise, the CPE_{dl} of Ni-P/TiO_2 is smaller than Ni-P. And, there was no significant difference at CPE_C for two coatings. In the Bode plots (Figure 5.14(b)), it can be seen that the bulk resistance of Ni-P is higher than that of CS and Ni-P/TiO_2. In the Bode phase plots, it can be seen that the Warburg modulus which appears to be 45º line in the Nyquist plot is not observable thus the electrode kinetics in this temperature is activation controlled. Furthermore, in 150 ºC (Figure 5.15), the corrosion resistance of CS, Ni-P and Ni-P/TiO_2 is 0.114, 1.100, and 1.884 kΩ·cm^2. This is in a good agreement with general information on corrosion behavior of CS. In addition, the Warburg elements appears for Ni/NiO implying the diffusion of electroactive species according to Figure 5.15(c). The system where the mass transport is dominant is irreversible so it means the destructive electrochemical reaction is observable at Ni-P surface. Contrarily, Ni-P/TiO_2 remains as a catalyst. However, Figure 5.15(c) denotes that the both catalyst is under the primarily influenced by the mass transport rather than the charge transfer while CS keeps its electrochemical properties. Figure 5.16 delivers that the electrocatalytic activity of Ni-P/TiO_2 is faded away. In this manner, the loss of electrocatalytic activity of Ni-P/TiO_2 is mainly caused by mass transport rather than electrode kinetics so the process is irreversible according to Figure 5.16(b) and Figure 5.16(c).

5.1.4. Performance in FAC Simulation Condition

To evaluate FAC behavior of CS and LAS, after the FAC simulation experiments at 150 ºC, weight loss of CS (A516 Gr.60) and LAS (A335 P22) was measured and surface morphologies were analyzed by SEM as shown in Figure 5.17. Generally, 150 ºC is known as FAC favored temperature due to synergetic effects of Fe_3O_4 solubility and mass transport of soluble species [2-5]. As shown in Figure 5.17(a), CS exhibits approximately 4 times higher weight loss compared to P22 indicating Cr and Mo enhance passivity in the high-temperature flowing water condition. Figure 5.17(b) gives surface morphology of CS. The surface is covered spinel-like oxide with composition of approximately 96 wt.% Fe and 4 wt.% O. Likewise to CS, P22 also exhibits surface, which is covered by spinel-like oxide (Figure 5.17(c)). And, 2-3 wt.% Cr and 1 wt.% Mo are observable which is in good agreement with that of substrate. Thus, it is hard to find their differences in surface morphology according to the SEM images.

Figure 5.18 illustrates CX morphologies and EDS analysis results of CS and P22 after the test. In case of CS, approximately 200 nm thickness oxide is formed, and the oxide has porosity. It is generally known that the oxide layer formed on CS where FAC favored condition is Fe_3O_4 which can be also confirmed by EDS results. In case of P22, two oxide layer structure appears. The structure of the outer oxide is polyhedral and that of the inner oxide is compact and uniform. According to EDS, the chemical composition of the outer oxide is estimated as Fe_3O_4, and enrichment of Cr is observable for the inner oxide. For the detailed chemical analysis, STXM and XAS is employed.

STXM images and XAS spectrum of CS and P22 on Fe L-edge energy range are displayed in Figure 5.19. In Figure 5.19(a), STXM morphology of CS is displayed. Number indicate XAS analysis points in the following figure. At the region 1, the oxide layer is visible. In case of P22 (Figure 5.19(b)), it exhibits two oxide layers: spinel as topmost oxide and relatively compact oxide below it. As shown in Figure 5.19(c), for each region, XAS spectrum is constructed. The spectrum were compared to the reference Fe_2O_3 and Fe_3O_4 spectrum [6]. Generally, the Fe L_3-edge for oxides exhibit a double peak structure. For Fe^{2+} the first peak of the double is higher than the second peak while for Fe^{3+} the second peak of the double is higher than the first peak [116, 117]. For L_2-edge, Fe^{2+} exhibits three peaks while Fe^{3+} exhibits two peaks. Fe_3O_4 is an inverse spinel with all Fe^{2+} occupying the octahedral sites, half of the Fe^{3+} occupying the tetrahedral and the remaining Fe^{3+} occupying octahedral sites thus is composed of 1/3 Fe^{2+} - 2/3 Fe^{3+} [118]. Therefore, its L_3-edge is more like that of an Fe^{3+} species. In region 1, both CS and P22 possess more intense second peak (at *ca.* 708.8 eV) than first peak (at *ca.* 709.8 eV). And, in L_2-edge, only two peaks appear meaning Fe^{3+} is dominant. However, their spectrum is not correctly well-matched with the reference Fe_2O_3 spectrum. Early conjecture is that the passive oxide is mixture

of Fe oxides such as Fe_2O_3, Fe_3O_4, and FeO rather single phase oxide even for CS. In addition, hydroxide shoulder (at *ca.* 711.2 eV) is observable only for CS. Similar tendency is observable for region 2. From the shape and the intensity of peaks at L_3- and L_2-edges, oxidation state is Fe^{3+} rather than Fe^{2+} but the shape of the spectrum does not match the reference Fe_2O_3, either. Like the topmost oxide, the bulk oxide also is composed of various oxides. The hydroxide shoulder is also found for CS indicating the oxide layer is not compact and protective.

Here, the intensity ratio of two peaks of L_3-edge of Fe is quantified. Since the first peak of L_3-edge is predominated by Fe^{3+} ions, the intensity ratio of first peak to second peak can be interpreted as indirect indication of the chemical composition of oxidation state. For CS, the ratio is 0.892 while that of P22 is 0.905 in the region 1 (spinel region). This indicates that the spinel of P22 contains more Fe^{3+} ions in its oxide [116]. Thus it can be concluded that P22 contains more Fe_2O_3 in the spinel region. However, in the region 2 (oxide layer region), the intensity ratio of CS is 0.949 and that of P22 is 0.950. That is, the chemical composition of Fe^{2+} ions increase along with depth. Since the dissolution of Fe_3O_4 is much severe than Fe_2O_3, it can be concluded that the surface of P22 undergoes severe dissolution of Fe_3O_4 but it does not critical affects the metal loss. This also explains why the hydroxide shoulder only appears for CS in the XAS spectrum since the dissolution process of Fe_3O_4 is closely related to the hydroxide formation. In region 3 and 4, metallic Fe spectrum appears for both alloys.

A STXM image and XAS spectrum of P22 on Cr L-edge energy range are displayed in Figure 5.20. Unlike to the Fe L-edge images and spectrum, those of Cr L-edge exhibits low resolution (for Figure 4a) and signal-to-noise ratio (for Figure 4b) due to chemical composition of alloy (*ca.* 2.25 wt.%). Therefore, it was arduous to differentiate region 1, 2, 3, 4 and pick up peaks. Instead, oxide layer and substrate region is picked for the XAS analysis. In the oxide region, two peaks appear at both L_3- and L_2-edge energy range while, in substrate region, single peak appears. The spectra of reference Cr_2O_3 presents a richer structure, with shoulders and unresolved multiplets. And, that of metallic Cr presents rather smooth, broad features with an asymmetric tail towards higher photon energy [119]. Even though signal-to-noise ratio of the spectrum is quiet low, it is understandable that Cr exists as Cr^{3+} states in both topmost and bulk oxide regions i.e., Cr_2O_3. Subramanian's work on FAC behavior of carbon steels and low alloy steels suggested that Cr was not observable on 2.25Cr-1Mo [118]. In our study, however, Cr exists in the passive oxide layer in form of Cr_2O_3. Nevertheless, enrichment of Cr and formation of Cr_2O_3 layer was not observable.

Corrosion rate of CS, Ni-P, and Ni-P/TiO_2 with temperature variation is compared in Figure 5.21. In Figure 5.21(a), the instructive information is achievable: firstly, CS is severely corroded at temperature 150 ^oC and secondary, the corrosion resistance of the coatings especially Ni-P/TiO_2 is the most effective at 150 ^oC. The corrosion rate of Ni-P and Ni-P/TiO_2 coating show huge difference at 150 ^oC. It seems the corrosion rate of Ni-P follows a bell-shaped curve likewise to CS. In short, the spatial

dispersion of TiO_2 into Ni-P coating is not functional at 125 and 175 ºC. This tendency is more clearly observable in Figure 5.21(b), which shows a corrosion rate without that of CS. The formation of Fe_3O_4 and NiO induces the slight weight gain at 125 ºC because the test was performed in an oxidizing condition. Thus, adherent oxides may be formed at the surface of CS and the coatings.

Figure 5.22 illustrates the microstructure evolution for the surfaces of CS, Ni-P, and Ni-P/TiO_2 using SEM. Figures 5.20(a), (b), and (c) gives the surface morphologies CS at 125 ºC, 150 ºC, and 175 ºC, respectively. From the chemical analysis, wt.% on overall surface gives that the formed oxide is Fe_3O_4 according to the EDS analysis. At 125 and 150 ºC, thick flim-like oxide is formed but at 175 ºC it is not observable indicating the reinforcement of passivity. Surface morphologies of the Ni-P after the tests are given in Figures 5.20(d), (e), and (f) at 125 ºC, 150 ºC, and 175 ºC, consecutively. It can be confirmed that surface morphologies after exposure to 125 ºC (Figure 5.22(d)) and 175 ºC (Figure 5.22(f)) keeps similarity with the as-plated coating. However, severe peeling of the top surface is observable when the coating is exposed to 150 ºC (Figure 5.22(e)). As previously discussed in Figure 5.21(b), Ni-P shows severe weight loss compared to Ni-P/TiO_2 coating at 150 ºC. The major portion of this weight loses is originated from the detachment of the top surface especially NiO. Furthermore, the region where the detachment occurs has porous structures, which means alloy elements are dissolved into the bulk water during the test. In other hands, Ni-P/TiO_2 does not represent detachment during the tests (Figures 5.20(g), (h), and (i)), indicating that the nanoparticles play a substation role in the test conditions. As with Ni-P, the microstructures after the 125 ºC (Figure 5.22(g)) and 175 ºC (Figure 5.22(i)) tests have a similarity. At both 125 and 175 ºC. microstructure of Ni-P/TiO_2 coating show similarity with that of the as-plated sate. While Ni-P shows the detachment of the oxide film at 150 ºC, the surface detachment of NiO is not observable in Figure 5.22(h). This indicates that the spatial dispersion of TiO_2 nanoparticles in Ni-P matrix enhances passivity.

Figure 5.23 gives the TEM CX morphologies of the coatings after the tests at 150 ºC. Figure 5.23(a) displays the STEM morphologies and the corresponding chemical elements mapping data for CX view of the region where NiO is not detached for Ni-P coating. Underneath the NiO layer, small porosity is observable. EDS mapping confirms that Ni is depleted at this region. The top NiO region does not reveal any degradation process. Thus, it can be concluded that the dissolution of Ni into Ni^{2+} ions or destructive electrochemical reaction including hydrolysis occurs at the interfaces. Thus, it can be assumed that NiO is detached owing to the formation of a porous structure at the interface. Figure 5.23(b) clearly shows that there is severe dissolution Ni species into bulk water then, finally, NiO is detached from the surface. Thus, this mechanism is originated from the water penetration into the microchannels of NiO, and at the metal/oxide water interface, metallic Ni transformed into soluble species (e.g., Ni^{2+} or $Ni(OH)_2$). This enables the formation of porous structure between NiO and Ni-P matrix eventually losing chemical bonding. Contrarily, the heterostructure of Ni-P/TiO_2 maintains its

passivity after the immersion, as shown in Figure 5.23(c). Ni-depleted zone does not appear according to EDS mapping images on Ni and O. This is due to the electrochemical property of TiO_2 and Ni-P coupling as previously discussed in the previous sections.

The corrosion behavior of CS is well-known based on the electrochemistry and hydrolysis of Fe_3O_4. Corrosion of CS at the elevate temperature without DO and other oxidizing agents is known as follows which is attributed from two simultaneous reaction [6]:

$$Fe + 2H_2O \rightarrow Fe(OH)_2 + H_2 \quad (5.2)$$

$$3Fe(OH)_2 \rightarrow Fe_3O_4 + H_2 + 2H_2O \quad (5.3)$$

Sweeton and Bae studied the dissolution of Fe_3O_4 into flowing bulk water in HCl and KOH condition between 50 °C to 300 °C with H_2 at 1 atm at 25 °C. The dissolution process is known as follows [7]:

$$1/3\,Fe_3O_4 + (2-b)H^+ + 1/3\,H_2 \rightarrow Fe(OH)_b^{(2-b)^+} + (4/3-b)H_2O \quad (5.4)$$

where, b = 0, 1, 2, and 3. Furthermore, Dooley suggested the corrosion behavior of CS in simulated NPPs chemistry with the equilibrium between soluble species and Fe hydroxides as follows [120]:

$$Fe \rightarrow Fe^2 + 2e^- \quad (5.5)$$

$$2H_2O + 2e^- \rightarrow 2OH^- + H_2 \quad (5.6)$$

$$Fe^2 + nOH^- \leftrightarrow Fe(OH)_n^{2-n} \quad (5.7)$$

where, b = 0, 1, 2. The corrosion rate of CS is generally dominated by Equation 5.5 and 5.6 and the rate of reaction increases rapidly as temperature approaches to 175 °C. Thus, enhancement of passivity occurs as temperature increases. This induces the formation of film-like oxide at 175 °C. In addition, Equation 5.4 gives a common description of the formation of porous Fe_3O_4 layer on CS due to hydrolysis. Thus, it the bell-shaped curves where the peak is 150 °C is induced from the synergetic effects of electrochemical reaction of Fe species and mass transport since the mass transport of

hydroxide species is controlled by temperature above 150 ºC.

For the bell-shaped curve of Fe species, the electrode kinetics at the elevated temperature should be discussed. When there is a concentration difference between bulk and surface electrolyte, the electrode kinetics can be described as follows:

$$i = i_0 \left(1 - \frac{i}{i_{lim}}\right) \exp\left[-\frac{(1-\alpha)nF}{RT}(E - E_{rev})\right] \quad (5.8)$$

where i is the current density of the system, i_0 is the exchange current density, i_{lim} is the limiting current density, α is the unitless change transfer number (usually, 0.5), n is the charge on the ion, F is the Faraday constant, E is the driving force for the reaction, and E_{rev} is the reversible potential. i_{lim} can be defined as follows:

$$i_{lim} = -\frac{nFDc_b}{d} \quad (5.9)$$

where D is the diffusion coefficient, cb is the ion concentration in the bulk electrolyte, and d is the diffusion layer thickness. Since the i_{lim} is predominated by the diffusion coefficient, it can be concluded that at the certain temperature above (usually 150 ºC), the dominant kinetic of Fe corrosion become diffusion controlled. In contrast, at the certain temperature below, due to the dissolution of Fe species, the kinetic will be activation controlled. In the flowing electrolyte, i_{lim} can be redefined as follows [121]:

$$i_{lim} = 0.0791 \times n \times F \times c_b \times U^{0.7} \times \left(\frac{R}{V}\right)^{-0.3} \left(\frac{V}{D}\right)^{-0.644} \quad (5.10)$$

where U is the peripheral velocity, R is the electrode radius, W is the angular velocity, V is the kinematic viscosity. From the equation, diffusion layer thickness can be redefined [121]:

$$d = 12.64 \times U^{-0.7} \times R^{0.3} \times D^{0.356} \times V^{0.344} \quad (5.11)$$

This states that when the flow velocity exceeds 5 m/sec, the change in diffusion layer thickness is negligibly small as shown in Figure 5.24.

To describe the corrosion behavior of Ni-P and Ni-P/TiO_2 coatings, the works from Tremaine and Ziemniak are introduces which includes the hydrolysis behavior of NiO at the elevated temperature in variety pH condition. Where pH is 9.3 at 150 ºC, the molality of Ni^{2+} at the ion saturated solution is almost saturated compared to other hydroxides, but as the temperature increases up to 200 ºC, the molality of $Ni(OH)_3^-$ significantly increases. This explains that the dissolution of Ni^{2+}, which is ionized from NiO, is dominated at 150 ºC [56]. The active reactions of the hydrolysis of NiO in deoxygenated ammonium and sodium hydroxide solutions are known as follows [59]:

Below 149ºC, a hydrous NiO phase controls the dissolution reaction equilibrium via

$$\beta - Ni(OH)_2 + 2H^+(aq) \leftrightarrow Ni^{2+}(aq) + 2H_2O \quad (5.12)$$

Above 149 ºC, but below 247 ºC, busenite NiO controls the dissolution reaction equilibrium via

$$NiO(s) + 2H^+(aq) \leftrightarrow Ni^{2+}(aq) + H_2O \quad (5.13)$$

Thus, near 150 ºC, the pre-oxidized element may undergo the dissolution reaction equilibrium via

$$\beta - Ni(OH)_2 \leftrightarrow Ni^{2+} \leftrightarrow NiO \quad (5.14)$$

According to the phase diagram, the thermodynamic favored phase in Ni-H_2O system is NiO at temperature 125 – 175 ºC. Thus, in the observation severe corrosion at the metal/oxide interface is due to the oxidation of Ni to Ni^{2+} to form NiO. The mechanism of the enhanced corrosion resistance of Ni-P/TiO_2 coating is the substantial role owing to electrochemical property of TiO_2 is a galvanic coupling between anodic Ni-P and cathodic TiO_2 [91, 92, 122]. Since TiO_2 provides anodic protection for Ni-P matrix, the nanoparticles stimulate the formation of passive layer (NiO) thus ECP of the system moves toward positive direction. Thus, localized corrosion is inhibited. Thus, Ni system becomes stable as it locates in passive region. In addition, Ashassi-Sorkhabi and Chen found that the spatially dispersed

nanoparticles induce the formation of spherical shape clusters. Thus, the penetration of aggressive electrolyte is effectively supressed [106, 122]. Therefore, spatial dispersion of the nanoparticle obstruct the corrosion behavior of Ni-P coating in both physical and chemical way.

Figure 5.25 gives the schematic diagram of the corrosion behavior of various Ni system in flowing condition. Zeller and Medway investigated the corrosion behavior of Ni system in alkaline solution such as NaOH and KOH. They found that when Ni is exposed to the alkaline condition, Ni/NiO/$Ni(OH)_2$, NiOOH/water structures are formed in the static condition, as shown in Figure 5.25(a) [57, 60]. This indicates that there is hydrolysis of NiO occurs at the metal/environment interface. In this study, the complex structures are not observable indicating that neither $Ni(OH)_2$ nor NiOOH is deposited at the oxide/water interfaces.

Compared to static condition corrosion, the corrosion in flowing water is displayed in Figure 5.25(b) and (c). In case of Ni-P, the system continuously dissolved into flowing bulk water by forming NiO and $Ni(OH)_2$. The flowing water induces severe mass transport of Ni^{2+} ions into the water thus severe corrosion occurs at temperature 150 ºC. However, when TiO_2 nanoparticles are incorporated in Ni-P matrix, NiO becomes fully stabilized due to anodic protection since TiO_2 play a role as a cathode and Ni play a roles as a anode [91, 92, 122]. To be concluded, the thermodynamic stability of NiO thin film is achieved by the anodic protection between active Ni-P and noble TiO_2 nanoparticles. Thus, the dissolution of Ni-P/TiO_2 matrix is suppressed due to the anodic protection as the ions are directly oxidized at the interface. Therefore, the Ni-P/TiO_2 can be a promising solution to mitigate FAC of CS under high-temperature flowing water condition. However, when there is a continuous dissolution of Ni from Ni-P matrix, accumulation of P in the localized area is expected. Phosphate have been widely applied as a water treatment additive in numerous power plants including fossil and nuclear. It controls the pH and buffer against development of acidic or caustic condition. But in 1970s, phosphates were largely discontinued due to SCC and wastage problem [123]. Regardless of these issues, the formation of localized phosphate would be permissible because recently application of Ni plating repair technique for pressure vessel or steam generator tube is added in ASME code section XI [124].

From here, FAC simulation behavior of Fe-based AMC will be discussed. The change in the weight of the samples is displayed in Figure 5.21. The metal losses were calculated by dividing the weight losses by the surface area, 8 cm^2. The error bars represent the deviation from four samples for each of the tests. Figure 4 shows that at approximately 150 °C, corrosion rate of Fe-based AMC exhibit a slightly positive weight change, i.e., a weight gain. The weight gain of the metallic materials can be ascribed to oxidation. Thus, it can be concluded that alloy elements including Fe, Cr, and Mo oxidized during the tests. However, in contrast with other temperatures, the samples decreased in weight at 150 °C.

In Figure 5.26, the surface of the coated samples after the tests is displayed along with the chemical analysis data of the matrix from EDS. To clearly show the morphology of the oxide covering the surface of the coating, we show the flat surface. In Figure 5.26(a), neither oxide scales nor polyhedral oxide crystals can be observed on the surface. As a slight increase in the weight is observed, as shown in Figure 5.21, it can be concluded that the coating was oxidized due to oxygen diffusion into the bulk matrix. According to the EDS analysis, the samples immersed at 150 °C (Figure 5.26(b)) exhibit scale-like oxides on the surface that cover approximately 50% of the surface area. The EDS analysis also shows a slight increase in the O contents compared to the sample immersed at 125 °C; however, proposing a clear explanation for this is currently difficult. Similar to the samples heated at 150 °C, scale-like oxide formation is also observable for the coating immersed at 175 °C, which covers a much smaller surface area compared to that of the sample heated at 150 °C (Figure 5.26(c)). In contrast, polyhedral oxides formed for the samples at 200 °C (Figure 5.26(d)). The chemical composition of the polyhedral oxide was unable to be determined by the EDS analysis, but it is expected to be AB_2O_4 (spinel), mainly $FeCr_2O_4$, while few other metals or metalloids elements are present.

For the following analysis, we chose two experimental conditions, namely, immersion at 150 and 200 °C because the prepared coating is proposed as a corrosion barrier in carbon steels, which undergo severe corrosion at 150 °C. Therefore, an in-depth discussion of their performance is needed. In addition, the formation of the polyhedral oxides, which is estimated as $FeCr_2O_4$ spinel oxides, only appears at 200 °C. It is interesting to note that the spinel usually forms when the protective internal oxide is present. Therefore, XPS and FETEM analyses were carried out for the 150 and 200 °C samples.

Figure 5.27 and Figure 5.28 illustrated the XPS spectra of the samples after the FAC simulation tests at 150 and 200 ºC, respectively. In Figure 5.27(a), it is found that Fe species are observable at 0 secs sputtering while Cr and Mo are not observable in Figure 5.27(b), and Figure 5.27(c). It explains that the composition of the oxide at the oxide-water interface is mainly Fe species. As sputtering time increases, evolution of Fe spectrum is observable for Fe. In case of Cr (Figure 5.27(b)), the broad Cr_2O_3 peak near 577 eV is observable and, likewise to Fe, evolution of Cr peak is observable after 1010 s of sputtering. However, Mo is not observable until 20 secs of sputtering but after 350 secs of sputtering, metallic Mo appears. In case of the samples immersed at 200 ºC, the evolution of peaks at oxide-water interface is observable for not only Fe (Figure 5.28(a)) but Cr (Figure 5.28(b)). Furthermore, metallic Fe peak is not clearly observable until 1010 s of sputtering. This tendency is same for Cr. In case of Mo, it is hard to find clear spectra (Figure 5.28(c)).

TEM images of the CX morphologies of the samples immersed at 150 °C and 200 °C are displayed in Figure 5.29 and Figure 5.30, respectively. In Figure 5.29, an oxide layer approximately 200 nm in thickness with spherical oxide precipitates can be observed for the 150 °C sample. According to the chemical analysis, The bulk oxide is composed of mainly Fe with remarkable contents of Cr, and

W. Small dot shaped Fe-Mo rich phase is observable which is assumed to be Mo-substituted Fe_3O_4.

For the sample immersed at 200 °C (Figure 5.30), three oxide layers appear: octahedral oxide crystals at the topmost surface (Fe_3O_4), compact Cr-rich oxide at the intermediate layer, and the amorphous bulk oxide layer. The chemical analysis confirms that the main components of the spinel is Fe_3O_4; the thickness of the intermediate Cr-rich oxide layer is 60 nm, and a bulk oxide layer is present. Also, the bulk oxide remains as amorphous thus in high-temperature water, Fe-based AMC keeps its original crystal structure.

This indicates that the passivation behavior of the Fe-based AMC highly depends on the oxidation behavior of Cr. Since Cr_2O_3 is known as a protective oxide, weight gain occurs during the erosion–corrosion tests. However, according to the TEM images of the samples immersed at 150 °C (Figure 5.29(a)), compact and uniform oxides near the oxide/water interface or metal/oxide interface are not observable. Instead, Fe–Mo intermetallic compounds are spatially dispersed in the bulk matrix. In addition, the oxide formed at 150 °C is much thicker than that formed at 200 °C. Zeng's work on the effects of metallic nanoparticles on the oxidation behavior of alloys revealed that the existence of nanosized metallic nanoparticles provides a potential path for O_2 diffusion [125]. Since the nanosized intermetallic compounds are formed in the bulk matrix, these compounds provide an O_2 diffusion path; thus, oxidation of the metallic species at the metal/oxide interface may continuously occur. In contrast, at 200 °C, three oxides were found: $FeCr_2O_4$ spinel at the surface, Cr-rich oxide (Cr_2O_3) in the intermediate layer, and a bulk oxide layer with an amorphous structure. At 200 °C, a compact and uniform Cr_2O_3 layer is formed; thus, the diffusion of O_2 along the defects was successfully hindered. The most outstanding advantage of metallic glasses is known to be its corrosion resistance due to its defect-free structure. Therefore, as shown in Figure 11 (e), amorphous oxides successfully obstruct the penetration of O_2.

The electron microscopy and XPS results show that the Fe-based AMC exhibit Cr_2O_3 as a passive oxide layer in different forms at 150 and 200 °C. Different morphologies of the passive oxide layers are highly related to the thermodynamic properties of the metal oxides, including Fe_3O_4, Cr_2O_3, and $FeCr_2O_4$. XPS analysis on the post-test samples immersed at 150 and 200 ºC gives that the formation of minor species such as metallic oxides and hydroxides definitely occurs

To calculate the solubility of Cr under hydrothermal alkaline conditions, Ziemniak's work on the solubility and phase behavior of Cr(III) oxides in hydrothermal alkaline media is adopted [126]. In his work, the solubility of Cr(III) oxides under hydrothermal conditions (T > 60 °C) was calculated based on the Cr(III) oxide dissolution reaction as follows:

$$\mathrm{CrOOH(s) + (3-n)H^+ \rightleftarrows Cr(OH)_n^{(3-n)} + (2-n)H_2O} \quad (5.15)$$

where *n* refers to the state of hydrolysis and may take on the values 0–6. However, unlike the case of the solubility of Fe, that of Cr is not highly dependent on temperature. Specifically, at both 150 °C and 200 °C, Cr_2O_3 can remain as a passive oxide layer since it does not severely hydrolyze (e.g., $CrOH)_3$) or dissolve. $FeCr_2O_4$ can exist as a product of chemical reaction with Fe species. Instead, based on the knowledge of Cr(III) ion hydrolysis, Ziemniak argued that ferrous chromite may be expected to dissolve in near neutral pH aqueous solutions by the following reaction [126]:

$$\mathrm{FeCr_2O_4(s) + 2H_2O + 2H^+ \rightleftarrows Fe^{2+} + 2Cr(OH)_3} \quad (5.16)$$

From the available thermodynamic data, the standard Gibbs free energy change (ΔG^0) was obtained as follows [126]:

$$\mathrm{\Delta G^0(J/mol) = -73097 + 423.73T} \quad (5.17)$$

where T is the temperature (K). It is known that thermodynamically stable solid phase of Cr(III) oxide is expected to dissolved in high temperature solution via the reaction [126]:

$$\mathrm{CrO(OH)(s) + 3H^+ \rightleftarrows Cr^3 + 2H_2O} \quad (5.18)$$

Furthermore in the temperature range including 150 and 200 °C, a second dissolution reaction needs to be considered [126]:

$$\mathrm{Cr(OH)_3 \cdot 3H_2O + 3H^+ \rightleftarrows Cr^3 + 6H_2O} \quad (5.19)$$

The dissolved Cr(III) ion is stabilized by forming hydroxocomplexes. Thus, for temperature above 60°C, the overall Cr(III) oxide dissolution reaction becomes the following sequence:

$$\mathrm{CrOOH(s) + (3-n)H^+ \rightleftarrows Cr(OH)_n^{(3-n)+} + (2-n)H_2O} \quad (5.20)$$

where n is the state of the hydrolysis. Therefore, as temperature increases, the dissolution of Fe^{2+} and Cr^{3+} accelerates according to the Equation (4).

At 200 °C, $FeCr_2O_4$ remains as a stable oxide at the oxide/water interfaces since the formation reaction of $FeCr_2O_4$ is as follows [127]:

$$\mathrm{Fe + 1/2\,O_2 + Cr_2O_3 = FeCr_2O_4} \quad (5.21)$$

Even if the DO concentration during the experiment was maintained at less than 1 ppb, that amount of DO is enough to simulate Equation 8. In brief, at 150 °C, thermodynamic equilibrium phase in Fe-Cr-H_2O system are Fe_3O_4, $FeCr_2O_4$. Even with DO, less than 1 ppb, is enough to stimulate those chemical reactions. Furthermore, the dissolution rate of Fe_3O_4 and $FeCr_2O_4$ is relatively higher than the condition when only Cr_2O_3 remains. However, because of the presence of nanosized Fe–Mo intermetallic compounds, oxygen diffuses into the metal/oxide interfaces. Therefore, continuous oxidation occurs for the Fe-based AMC. In contrast, at 200 °C, the dissolution of Fe_3O_4 and $FeCr_2O_4$ is not thermodynamically favored. Furthermore, Cr_2O_3 dissolves only negligibly. Thus, the protective oxide layer forms at the oxide/water interface. In addition, $FeCr_2O_4$ spinel is formed at the topmost oxide via the chemical reaction with Fe and Cr_2O_3. Therefore, it can be concluded that the Fe-based AMC can be utilized for high-temperature erosion–corrosion resistant coatings owing to its outstanding passivity.

.

5.1.5. Performance in FAC Condition

The thickness change during the FAC experiments are displayed in Figure 5.31. UT was employed to measure the thickness of CS, LAS, Ni-P/TiO_2 coated CS, and Fe-based AMC coated CS elbow pipeline. After 21 days of immersion at dearated 150 °C flowing water, the thickness was measured. Commonly, intrados show much severe corrosion behavior than extrados. Study from El-Gammal that investigate flow profiles in 90° elbow found that significantly accelerates along the intrados due the favorable pressure gradient [71]. In case of CS, there was significant thickness reduction in both intrados and extrados and at point 3, the thickness reduction is much higher (Figure

5.31(a)). This is because there is acceleration flow at elbow point. In case of LAS (P22), thickness was barely changed (Figure 5.31(b)). This indicates that P22 is noble in this condition due to the formation of Cr-rich oxide at the surface. In case of Ni-P/TiO_2, there was significant thickness reduction at position 3 of intrados. Likewise, thickness reduction at extrados is observable. This is assumed to be there is peeling-off of coating layer (Figure 5.31(c)). However, likewise to FAC simulation results, Fe-based AMC show increase in thickness in intrados indicating that thickness gain due to oxidation (Figure 5.31(d)). To investigate the morphology of the tested pipeline, photography and SEM were employed.

Figure 5.32 illustrated the photography of cut samples after 21 days of immersion. From top to bottom, CS, Ni-P/TiO_2, Fe-based AMC, and P22 are aligned. In case of CS, corroded surface appears with reddish brown colored oxide mainly Fe_3O_4. All the surface is corroded uniformly. In case of Ni-P/TiO_2, severely corroded surface is observable at intrados. This well matches with the result from UT in Figure 5.31. In case of Fe-based AMC, reddish brown colored oxide is observable along with intrados in elbow position indicating severe corrosion at intrados. Thus, it can be assumed that thickness gain at intrados is due to the formation of Fe oxides. However, P22 does not show corroded surface indicating the stability of P22.

Surface and CX morphologies of the pipe samples are analyzed from Figure 5.33 to Figure 5.36. The position of the analysis is 3 (center of the UT analysis). Figure 5.33 displays the morphologies of CS. As indicated in Figure 5.33(a), Figure 5.33(b, c) are the extrados and Figure 5.33(d,e) are intrados, respectively. At the extrados, porous Fe_3O_4 layer is formed and CX analysis gives that there is severe porosity. Similar tendency is observable for the intrados. Surface is covered by thick oxide layer and CX gives that there is severe porosity, which is formed during the hydrolysis of Fe species. In case of P22 (Figure 5.34), the extrados surface is covered by relatively porous oxides (Figure 5.34(b) but there is no significant porosity according to CX analysis (Figure 5.34(c)). The thickness oxide reduces compared to that of CS. In the intrados, the surface reveals orange-peel shape oxide (Figure 5.34(d)) and likewise to the other side, the CX reveals that there is no significant porosity (Figure 5.34(e)). The different morphology of P22 at the intrados and the extrados is originated from flow profile. Since the intrados has more fast velocity, there is more significant dissolution of the oxide occurs. In case of Ni-P/TiO2 coatings, the surface is covered by Ni-P/TiO_2 coatings in both intrados and extrados (Figure 5.35(b) and (d)). However, according to the CX analysis the coating layer is barely visible (Figure 5.35(c) and (e). This indicates that the coating is detached during the FAC test and this well matches with the result of Figure 5.31(c). In case of Fe-based AMC, the surface is well covered by the coating layer at both intrados and extrados (Figure 5.36(b) and (d)). And, the coating layer is observable for both side according to CX analysis (Figure 5.36(c) and (e)). This confirms that Fe-based AMC is resistive even in high-temperature flowing condition.

Finally, the measurement results from the UT and the post mortem analysis is compared as

shown in Figure 5.37. During the post mortem measurement, the error is set to 1 %. In this figure, the scatters in left indicates the UT results, and the right ones indicate the post mortem measurement. In all samples, CS (Figure 5.37(a)), P22 (Figure 5.37(b)), Ni-P/TiO2 (Figure 5.37(c)), and Fe-based AMC (Figure 5.37(d)), significant difference between two measurement techniques is not observable. Thus, it can be concluded that the performance evaluation in the FAC condition is quiet reliable.

5.2. Performance of the E-C Resistive Alloys

5.2.1. Microstructure and Chemical Analysis

To confirm the chemical contents of the alloys, spark emission spectroscopy was employed as shown in Table 5.5. From the result, the chemistry of the alloys well matches with the ratio of feedstock materials. FRA 1 exhibits 2.180 wt.% Cr, 1.000 wt.% Mo, and 0.096 wt.% of C. FRA 2 exhibits 3.165 wt.% of Cr, 0.495 wt.% of Mo, and 0.094 wt.% of C. And MFRA exhibits 4.185 wt.% of Cr, and 0.101 wt.% of C. Impurity elements such as P and S was less than 0.003 wt.%. Crucible material, Cu, was not observable. Thus, purity of the alloy is verified. Microstructure of the alloys observed by OM is enlisted in Figure 5.38. The surfaces were etched according to E407-07. The heat treatment history of P22 is normalizing and tempering. According to Hideaki, the microstructure of normalized and tempered P22 is bainite and the results is in good agreement [128]. However, the microstructure near the surface is ferrite rather than bainite. This is due to decarburization during heat-treatment procedure. Microstructure of FRA 1 resembles that of P22. With bainite base, some ferritie is observable (Figure 5.38(b)). And at the surface, the portion of ferrite increases due to the decarburization process. In case of FRA 2, also bainite structure is observable but the portion of bainite decreases as Cr content increases (Figure 5.38(c)). As Mo is eliminated from the alloy (Figure 5.38(d)), the structure becomes a complex of acicular ferrite and bainite. This is because Mo makes more strong impacts on bainite formation.

5.2.2. Mechanical Properties

Vicker's hardness results of the alloys are enlisted in Figure 5.39. For each alloy, 10 points for surface, intermediate, and bulk regions are measured. For FRA 1, the hardness from the surface scatters since the mixture of ferrite and bainite exists. However, as the portion of ferrite decreases in intermediate and bulk region, the hardness is in good agreement with commercial P22. Similar trend is observable for FRA 2 but hardness in intermediate and bulk region slight decreased since the portion of bainite decrease. In case MFRA, hardness at surface region slightly increases but that of bulk region decreases less than 200 HV. This is originated from the portion of bainite decreases.

In stress-strain curves (Figure 5.40), the trend is that YS and UTS of the alloys are comparably

similar. YS of the alloys are 348.2, 372.4, 350.2 MPa for FRA 1, FRA 2, MFRA, respectively. ASTM requirement for A335 P22 in YS is known as 210 MPa. And, UTS for the alloys are 443.3, 462.8, and 446.4 MPa. But elongation decreases in order of FRA 1 – FRA 2 – MFRA. Reduction in elongation is originated from the reduction in bainite portion in microstructure. However, all the criteria satisfy ASTM standards for P22.

According to Fadel's work, the effect of these elements, such as Cr, Mn and Mo, on the transformation behavior is of the particular interest in this steel grades [129]. They make a huge impact on the formation of proeutectodie ferrite. If the ferrite is transformed, austenite grains is decorated then bainite formation is disabled. In other words, if there is proeutectodie ferrite, acicular ferrite intergranular nucleation becomes dominant. Cr, Mn, and Mo is known as to prevent the formation of proeutectodie ferrite and pealite thus hardenability of the steel increases.

5.2.2. Electrochemical Properties in Seawater

In Figure 5.41, LSV results of FRA 1, FRA 2 and MFRA in 3.5 wt.% NaCl are displayed. Regardless of the chemistry of the alloys, the LSV curves have a similarity in E_0 and I_0. This is because 3.5 wt.% NaCl solution is aggressive solution thus general corrosion occurs rather than pitting corrosion. Since E-C is a type of general corrosion rather than localized corrosion, it is expected that the alloys will possess sufficient corrosion resistance in simulated secondary water chemistry. Figure 5.42 illustrates the AC responses of the alloys in 3.5 wt.% solution. Unlike to the trend in Figure 5.41, FRA 2 shows susceptibility to corrosion than the others. This is because there would be threshold Cr and Mo contents for corrosion resistance in 3.5 wt.% NaCl solution. In Nyquist plots (Figure 5.42(a)), the circuit model was Randle's circuit model thus there is single oxide at the metal/water interface. Small diameter of FRA 2 indicates poor corrosion resistance. This tendency is also observable in Bode plots (Figure 5.42(b)). Thus, it is noticeable that the modification of Cr and Mo contents for LAS make a impact on corrosion resistance in seawater.

5.2.3. Performance in FAC Simulation Condition

After the FAC simulation experiments, the corrosion rate of the samples were calculated based on the weight loss, surface area, and immersion time as shown in Figure 42 In Figure 5.43(a), the corrosion rate of CS, P22, FRA 1, FRA 2, and MFRA is plotted with calculated result from Ducreux's model. The corrosion rate of the Cr and Mo containing alloys are less than that of CS and the result is in good agreement with Decruex's model.

In Figure 5.43(b), the corrosion rate of the alloys without CS is illustrated. Theoretically, the

corrosion rate of P22 and that of FRA 1 should be identical however P22 shows less corrosion rate. The different corrosion rate in two alloys are due to the presence of Si in P22 and galvanic coupling between cementite (Fe_3C) and ferrite. Ishitsuka reported that when Si exists in the alloy, it forms a protective amorphous-SiO_2 film at the surface which reduces the oxidation rate considerably [130]. Also, Nam reported that for pearlite structure, there is a galvanic coupling which occurred at cementite and ferrite phases [15]. The corrosion rate of FRA 1, FRA 2, and MFRA follows Ducreux's model. That of FRA 1 and MFRA is almost identical and that of FRA 2 is the smallest. This result indicates that not only Cr and Mo but also other alloy elements affects FAC rate, Mo plays a role during FAC rate, and Mo can be substituted by Cr.

SEM images on the surface after the FAC simulation tests are illustrated in Figure 5.44. The surface morphology of P22 (Figure 5.44(a)) exhibits some oxide scales but the number of the oxide scale decreases in that of FRA 1 (Figure 5.44(b)). Thus, weight differences in P22 and FRA 1 may arise from formation of oxide scales. In case of FRA 2 (Figure 5.44(c)) and MFRA (Figure 5.44(d)), those oxide scales are not observable. Only polishing scratches are observable thus the oxidation mechanism of Cr and/or Mo containing alloys is internal oxidation. To investigate FAC behavior of the alloys, TEM is employed as shown in following figures.

From Figure 5.45 to Figure 5.48, they illustrates CX images of P22, FRA 1, FRA 2, and MFRA and yellow dot lines indicate EDS line profile region for the corresponding chemical analysis result. In the EDS results, chemical composition of Ga and C is omitted since they are residual due to TEM sampling process. In case of P22, three oxide layers are observable in Figure 5.45(a): oxide scale at the topmost location, thin compact oxide which can be clearly seen in Figure 5.45(b), and bulk oxide region. The EDS line on relatively low magnitude shows that the oxides are composed of Fe and O. Since the ratio of Fe and O is close to 3:4, the chemistry of oxide is assumed to be Fe_3O_4. According to the EDS profile on high magnitude image, the enrichment of Cr in the compact oxide is observable. Thus, the oxide layer structure of P22 is seemed to be Fe_3O_4 scale – Cr-enriched compact oxide – bulk Fe_3O_4 layer.

In Figure 5.46(a), the overall oxide structure is illustrated and the structure resembles that of P22. The overall oxide chemistry is assumed to be Fe_3O_4 based on the ratio of Fe and O. And, enrichment of Cr is observable as shown in Figure 5.46(b). Thus, likewise to P22, the oxide layer structure is Cr-enriched compact oxide – bulk Fe_3O_4.

In Figure 5.47(a), the oxide structure of FRA 1 is shown. Likewise to the other alloys, two oxide layer is observable: thin and compact oxide as topmost oxide and bulk oxide layer. However, void appears at the interface between two oxide layers. The chemical composition of the oxide layers appears to be Fe_3O_4 and there is enrichment of Cr in the topmost oxide (Figure 5.47(b)). Since 0.5 wt.% Mo is

in the alloy, the presence of void indicate that local corrosion resistance of Mo-containing alloy may be hindered due to high-temperature flowing water. And as Cr contents increases, homogenous distribution of Cr in the oxide layers arises.

In MFRA, the oxide layer structure resembles that of FRA 2. Along with the depth, Cr is also homogenously distributed as shown in Figure 5.48(a)). At the topmost oxide layer, enrichment of Cr is observable (Figure 5.48(b)). However, any void does not appear at the oxide interface.

From the CX analysis, it can be concluded that Cr and/or Mo containing LASs have bi-layer oxide structure with Cr-enriched topmost oxide and Fe_3O_4 bulk oxide. In Figure 5.49, this trend can be clearly observable. In Figure 5.49(a), the enrichment of Cr at the outer layer can be clearly observable. The Cr content in the inner layer is relatively smaller than that of Cr in metal. Likewise to P22, FRA 1 (Figure 5.49(b)), the enrichment of Cr in the outer layer is seen. As Cr increases in metal (Figure 5.49(c)), the both enrichment in the outer oxide and the inner oxide is observable. And, the similar trend is shown in MFRA (Figure 5.49(d)). This indicates that increase in Cr contents in steels induces higher Cr contents in both oxides. To investigate the detailed chemistry and crystal structure of the oxide layers, electron DPs were analyzed based on HRTEM measurement as shown in Figure 5.50 and Figure 5.51.

Figure 5.50 displays the electron DPs of the Cr-enriched topmost oxide layer of P22 (Figure 5.50(a)), FRA 1 (Figure 5.50(b)), FRA 2 (Figure 5.50(c)) and MFRA (Figure 5.51(d)). In the patterns, amorphous halos appear thus the Cr-enriched layers are amorphous Fe_3O_4 with Cr substitution. But the bulk oxides reveal Fe_3O_4 structure as enlisted in Table 5.6 and Figure 5.51. In Table 6, miller indices and reference d-spacing data of Fe_3O_4 and those of the alloys are given. From the DP pattern images, the strongest intensity was chosen and they are (111), (220), (311), (400), (511), and (440). In case of P22, average d-spacing distortion ratio is -0.329 %. And that of FRA 1, FRA 2, and MFRA is -0.567 %, -0.694 %, and -0.815 %, respectively. The compression of crystal structure is due to Cr substitution in Fe_3O_4 structure. According to Manjanna's work, there is a slight decrease in unit-cell values with Cr-substitution in Fe_2O_3 and Fe_3O_4 due to relatively smaller ionic radii of Cr^{3+} [131-133]. Liang reported reduction in crystal size of Cr-substituted Fe_3O_4 and stoichiometry of Cr ion as Cr^{3+} [134]. For Cr cations in $Fe_{3-x}Cr_xO_4$, their K-edge positions in XAS are also quite close to those of Cr^{3+} in Cr_2O_3 and $FeCr_2O_4$, but far from those of CrO^3, and Cr metal. The peak profiles of $Fe_{3-x}Cr_xO_4$ are also similar to that of spinel $FeCr_2O_4$ containing octahedra Cr^{3+}. These two evidences indicate that Cr cations in $Fe_{3-x}Cr_xO_4$ are mainly Cr^{3+}.

Figure 5.52 illustrated chemical composition of Cr in the oxide layers. As shown in Figure 5.52(a), the composition of Cr in the outer oxide is the highest for FRA 2 followed by MFRA, FRA 1 and P22. Since the corrosion rate of FRA 2 is the smallest, FAC behavior is dominated by Cr contents of outer oxide layers. As previously explained, the Cr contents of the inner oxides is proportional to

change in d-spacing. To evaluate the correlation between the corrosion rate and the Cr contents, that of the oxides is divided by that of the metal as shown in Figure 5.51(b). The Cr contents of the outer oxides is smallest for P22, and that of FRA 1 and MFRA is similar, and the largest for FRA 2. Since the corrosion rate of FRA 1 and MFRA is similar, it can be concluded that the chemical composition of Cr in an outer oxide determines the FAC behavior. And, that of P22 does not follows this trend, may other elements such as Si may make influence on FAC behavior.

Evolution of oxide layers of Fe-Cr alloy in alkaline environment was reported by Jiang [135]. The OH^- from the solution reacts firstly with selectively dissolved Fe in the outer passive film layer. Plenty of nucleation sites lead to the formation of the Fe oxide island and eventually passive layer as follows:

$$Fe^{2+} + 2OH^- \rightarrow Fe(OH)_2 \quad (5.22)$$

$$Fe(OH)_2 + \frac{1}{2}O_2 + H_2O \rightarrow Fe(OH)_3 \quad (5.23)$$

Since the outer oxide layer disables the direct interaction between the dissolved Fe species and hydroxide ions, the ions penetrate into the oxide layer and they are chemically contact with Cr in the metal. The in situ Fe-Cr oxide inner layer then forms:

$$Cr^{3+} + 3OH^- \rightarrow Cr(OH)_3 \quad (5.24)$$

The relatively low Cr content in the passive film and large number of particle boundaries facilitate the transport of Cr through passive film. Due to the hindering of the inner oxide layer with contact to H_2O, the following reaction occurs:

$$2Cr(OH)_3 \rightarrow Cr_2O_3 + 3H_2O \quad (5.25)$$

Similar tendency will be found since Cr_2O_3 is more stable in PWR condition rather than $Cr(OH)_3$ [136]. After long-time passivation, a stable passive film forms on the steel with the amorphous outer layer consists of Fe_2O_3 and $FeOOH_3$ and the crystalline inner layer $FeO\text{-}Cr_2O_3$.

In high-temperature alkaline water, the corrosion behavior of Fe and Cr is determined by thermodynamics. According to Ziemniak's serious work on solubility of Fe and Cr oxides in high-temperature alkaline water, the corrosion behavior of Fe and Cr is known as follows [10]. By means of magnetite solubility studies conducted in sodium hydroxide with varying level of dissolved hydrogen, Tremaine and Leblanc quantified the redox equilibrium:

$$Fe(OH)_2(aq) + H_2O \leftrightarrow Fe(OH)_3(aq) + \frac{1}{2}H_2(g) \quad (5.26)$$

By means of Fe_3O_4 solubility studies conducted in sodium hydroxide with varying level of dissolved hydrogen, Tremaine and Leblanc quantified the redox equilibrium. The dissolved Cr^{3+} is stabilized by forming hydroxocomplexes in high-temperature alkaline water [126]. That is, Cr^{3+} ion is surrounded by six H_2O molecules in octahedral symmetry. Multiple steps of dissociation of these complexes occurs as follows:

$$Cr^3 + 3H_2O \rightarrow Cr(OH)^{2+} + H^+ \quad (5.27)$$

$$Cr(OH)^{2+} + H_2O \rightarrow Cr(OH)_2^+ + H^+ \quad (5.28)$$

$$Cr(OH)_2^+ + H_2O \rightarrow Cr(OH)_3(aq) + H^+ \quad (5.29)$$

$$Cr(OH)_3(aq) + H_2O \rightarrow Cr(OH)_4^- + H^+ \quad (5.30)$$

Thus, for temperature above approximately 60 ºC, the overall Cr^{3+} oxide dissolution reaction becomes the following sequences since:

$$Cr(OOH)(s) + (3 - n)H^+ \rightarrow Cr(OH)_n^{(3-n)+} + (2 - n)H_2O \quad (5.31)$$

However, based on summaries of room temperature equilibria, it may be concluded that only hydrostatic states corresponding to n >= 3 need to be considered when analyzing behavior of Cr^{3+} in neutral and alkaline pH solution. As shown in 5.48, thermodynamically favored reaction of Cr^{3+} in alkaline pH solution is known as follows [126]:

$$CrO(OH)(s) + H_2O \rightarrow Cr(OH)_2(aq) \quad (5.32)$$

Diffusion through the oxide layer at high temperature is by short circuit routes, such as micro-pores and grain boundaries, rather than the lattice. In deaerated condition, the inward diffusion of oxidized species occurs by diffusion of either water molecules or oxygen ions or hydroxide ions along the short circuit routes [34, 35]. Therefore, in high-temperature flowing water, FAC behavior of LASs can be determined as 3-step process as shown in Figure 5.54:

1. The OH^- from the solution reacts firstly with selectively dissolved Fe in the outer passive film layer then plenty of nucleation sites lead to the precipitation of Fe oxides and the formation of passive particles
2. Since the continuous layer hinders the exposure of the inner layer to H_2O in the solution, Cr^{3+} dissolved into the Fe oxide layer
3. Continuous passivation to form the compact two layers with the amorphous and the crystalline Cr substituted Fe oxides
4. Since the solubility of Cr species is far less than that of Fe species, there is a continuous dissolution at the outer amorphous layer. This induces enrichment of Cr in the outer layer thus the higher Cr content reinforces the passivity of the steels [36].

5.3. Performance Evaluation of the Developed Materials

Figure 5.55 illustrated the performance of the developed materials in FAC simulation tests at 150 ºC. In this study, two commercial alloys (CS, LAS), three E-C resistive coatings (Ni-P, Ni-P/TiO_2, Fe-based AMC), and three E-C resistive alloys (FRA 1, FRA 2, MFRA) are tested in various E-C conditions using multiple instruments. As shown in graphs, CS is extremely susceptible to the E-C, thus LAS replaces its position but LAS still also possess unsolved problems including weldability, mechanical property, and price. According to the results, Ni-P/TiO_2 coating and Fe-based AMC can be promising candidate since their corrosion rate is comparable to P22. However, the result from FAC tests gave that Ni-P/TiO_2 coating is not applicable for high flow rate or erosion condition due to its low mechanical property. In case of E-C resistive alloys, all the materials reveal comparable corrosion rate with the commercial LAS. This confirms that the result well matches will Ducreux's model. Even without Mo, E-C is suppressed by higher Cr rate thus MFRA can be a promising alternative for secondary system of NPPs. Figure 5.56 gives the comparison of the corrosion rate with EDF CIROCO loop data, Ducreux's high and low flow rate model, and the result from this study [37]. In the loop test,

various tests were conducted in low, high flow rate in single and two-phase flow with different steam quality (X in the graph). One phase flow tests were conducted at pH 9.0, DO concentration < 1 ppb, and temperature was 180 and 175 ºC for single- and two-phase flow, respectively. Reference Cr content (= 0.04 wt.%) is originated from the chemical composition of Cr of U 490. Ducreux defined the reference value since his data showed that reduction in FAC rate had been observable above 0.04 wt.% Cr. FAC rate was measured by thin layer activation by using ^{56}Co as a radionuclide surface marker. The result from this study is in the range of low and high Ducreux's model confirming the validity of this study. Since it is unable to locate Ni-P/TiO_2 coating and Fe-based AMC due to weight gain, the position of Ni-P is located. According to the result, Ni-P coating is equal to 0.6 wt.% Cr containing steel. E-C resistive alloys reveal 1/50 times lower corrosion rate compare to reference steel.

Table 5.1. LSV fitting parameters of the CS, Ni-P and Ni-P/TiO_2 in seawater condition

Sample	**E_{corr} (V_{SCE})**	**I_{corr} ($\mu A/cm^2$)**	**R_p ($\Omega \cdot cm$)**
CS (A516 Gr.60)	-0.720	16.6	1570
Ni-P	-0.451	2.50	20883
Ni-P/TiO_2	-0.382	0.385	105750

Table 5.2. EIS fitting parameters of the CS, Ni-P and Ni-P/TiO_2 in seawater condition

Sample	R_{po} ($\Omega \cdot cm^2$)	R_{ct} ($\Omega \cdot cm^2$)	CPE_c		CPE_{dl}		C_{dl} ($\mu F/cm^2$)
			Q_{ox} ($\mu F \cdot s^{(n-1)} \cdot cm^{-2}$)	n_c	Q_{dl} ($\mu F \cdot s^{(n-1)} \cdot cm^{-2}$)	n_{dl}	
CS (A516 Gr.60)		1230			104.99	0.782	59.338
Ni-P	1059	19287	15.34	0.749	1.4416	0.878	0.87629
Ni-P-TiO_2	1557	196010	6.5902	0.837	1.522	0.877	1.2845

Table 5.3. LSV fitting parameters of the CS, Ni-P and Ni-P/TiO_2 in high-temperature water

Test Temperature (°C)	Specimen	E_0 (mV_{SHE})	I_0 (A/cm^2)	I_{lim} (A/cm^2)	R_p ($\Omega \cdot cm^2$)
125	CS (A516 Gr.60)	-725	5.30×10^{-5}		492
	Ni-P	-653	2.50×10^{-5}		1041
	Ni-P-TiO_2	-554	6.66×10^{-5}		3920
150	CS (A516 Gr.60)	-774	1.89×10^{-5}		137
	Ni-P	-665	6.54×10^{-5}		3991
	Ni-P-TiO_2	-620	2.36×10^{-5}		11000
175	CS (A516 Gr.60)	-838	4.77×10^{-5}	3.13×10^{-5}	546
	Ni-P	-853	1.66×10^{-5}	2.66×10^{-5}	1565
	Ni-P-TiO_2	-852	2.02×10^{-5}	2.05×10^{-6}	1291

Table 5.4. EIS fitting parameters of the CS, Ni-P and Ni-P/TiO_2 in high-temperature water with different temperature

Parameters	R_{po} ($\Omega \cdot cm^2$)	R_{ct} ($\Omega \cdot cm^2$)	W_S		CPE_c	CPE_{dl}	
			R	T		Q_{dl} ($\mu F \cdot s^{(n-1)} \cdot cm^{-2}$)	n_{dl}
125 ºC							
CS	50.78	130.2	3110	12.87	0.49517	2652.4	0.54652
Ni-P	38.85	1447	5615	0.100	0.41653	351.44	0.54834
Ni-P-TiO_2	49.57	1505	954.9	15.07	0.41477	251.7	0.68005
150 ºC							
CS	71.96	42.08	2233	42.71	0.37299	3058.4	0.64978
Ni-P	38.3	1062	16679	26.62	0.35252	355.31	0.49489
Ni-P-TiO_2	57.52	1827	2183	17.71	0.362727	294.7	0.64587
175 ºC							
CS	12.12	151.0	7185	0.24791	0.96448	2578.3	0.52469
Ni-P	51.79	134	8764	92.59	0.34564	134.82	0.66365
Ni-P-TiO_2	19.26	199.7	7727	62.68	1.0424	248.06	0.64827

Table 5.5. Spark emission spectroscopy results of chemical composition of the alloys

	C	Si	Mn	P	S	Cr	Mo	Ni	Cu	Fe
FRA 1	0.096	0.008	0.010	0.002	0.002	2.180	1.000	0.004	-	96.70
FRA 2	0.094	0.014	0.011	0.002	0.002	3.165	0.495	0.004	-	96.21
MFRA	0.101	0.021	0.013	0.002	0.003	4.185	0.024	0.005	-	95.65

Table 5.6. Miller indices, d-spacing, and distortion rate of the alloys and the reference

JCPDS 019-0629 (Fe_3O_4)		**P22**		**FRA 1**		**FRA 2**		**MFRA**	
(hkl)	d-spacing (A)	d-spacing (A)	Distortion Rate (%)	d-spacing (A)	Distortion Rate (%)	d-spacing (A)	Distortion Rate (%)	d-spacing (A)	Distortion Rate (%)
(111)	4.852	4.8400	-0.247	4.8370	-0.309	4.7870	-1.340	4.7990	-1.092
(220)	2.9670	2.9500	-0.573	2.9620	-0.169	2.9540	-0.438	2.9480	-0.640
(311)	2.5320	2.5270	-0.197	2.5120	-0.790	2.5080	-0.948	2.5160	-0.632
(400)	2.0993	2.0950	-0.205	2.0830	-0.776	2.0920	-0.348	2.0820	-0.824
(511)	1.6158	1.6140	-0.111	1.6140	-0.111	1.6020	-0.854	1.6030	-0.792
(440)	1.4845	1.4750	-0.640	1.4660	-1.246	1.4810	-0.236	1.4710	-0.909
		Average (%)	-0.329	Average (%)	-0.567	Average (%)	-0.694	Average (%)	-0.815

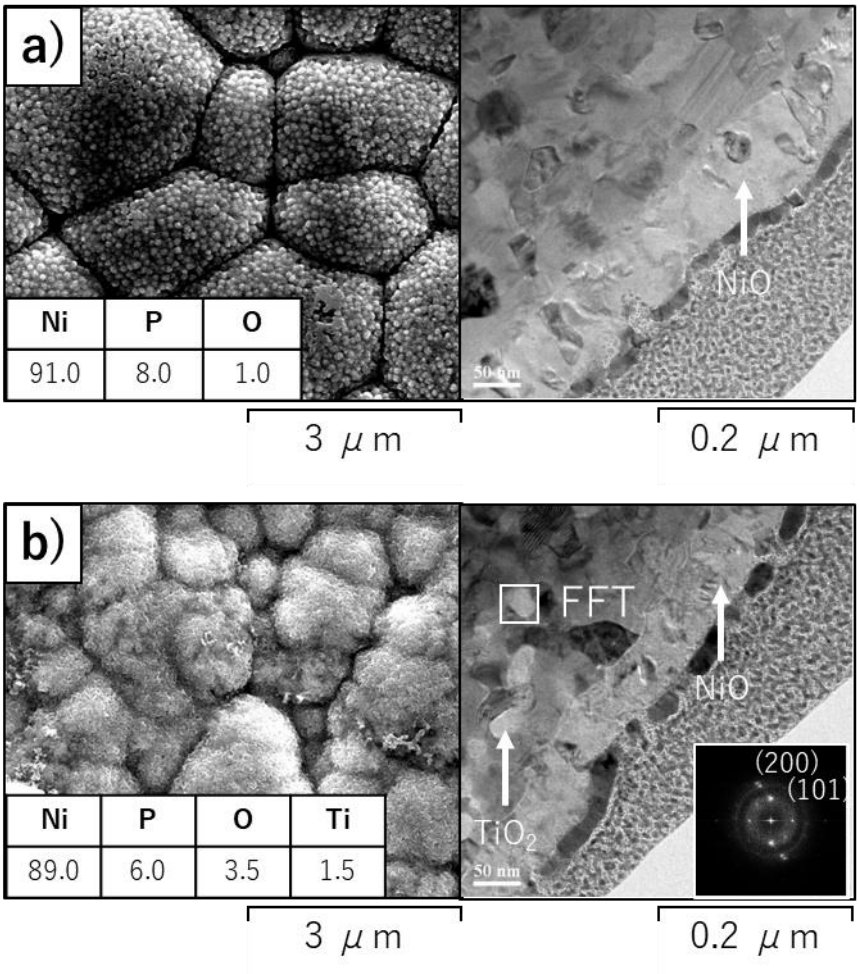

Figure 5.1. SEM surface and TEM CX morphologies of the coating: (a) Ni-P and (b) Ni-P/TiO_2

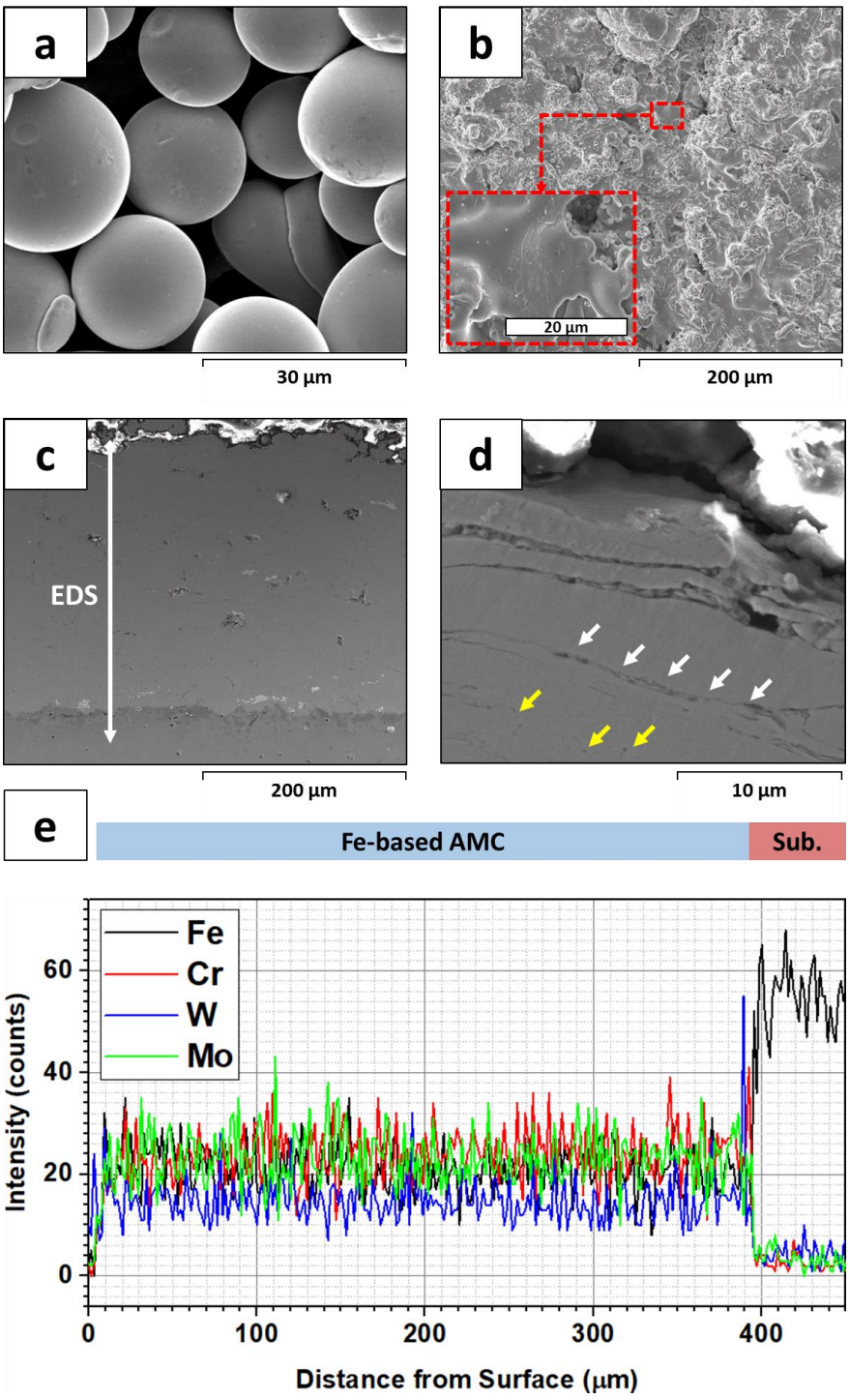

Figure 5.2. SEM morphologies of Fe-based AMC: (a) feedstock powder, (b) surface, (c, d) CX with indication of porosity by white and yellow arrows, and (e) EDS line profiles indicated in (c).

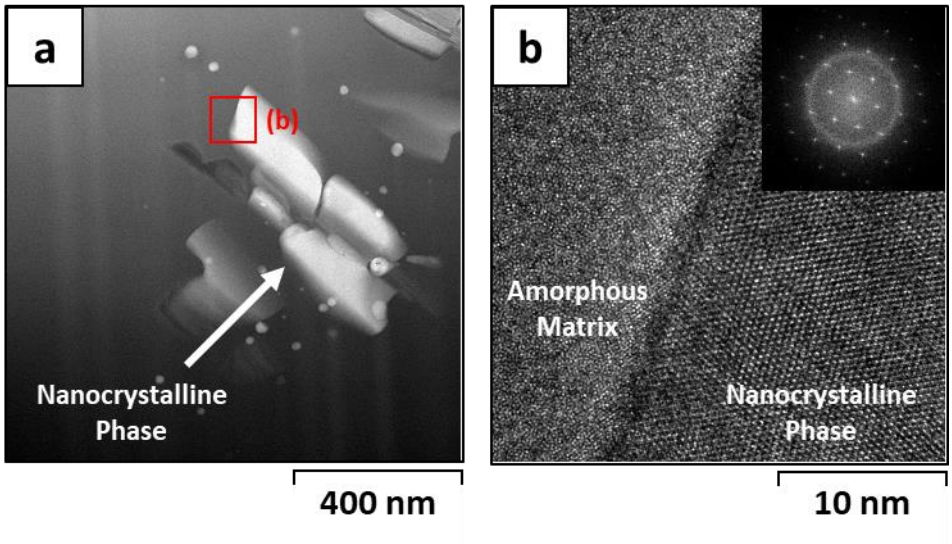

Figure 5.3. TEM morphologies of Fe-based AMC: (a) STEM and (b) HRTEM nanocrystalline and amorphous matrix morphology of Fe-based AMC with electron DP

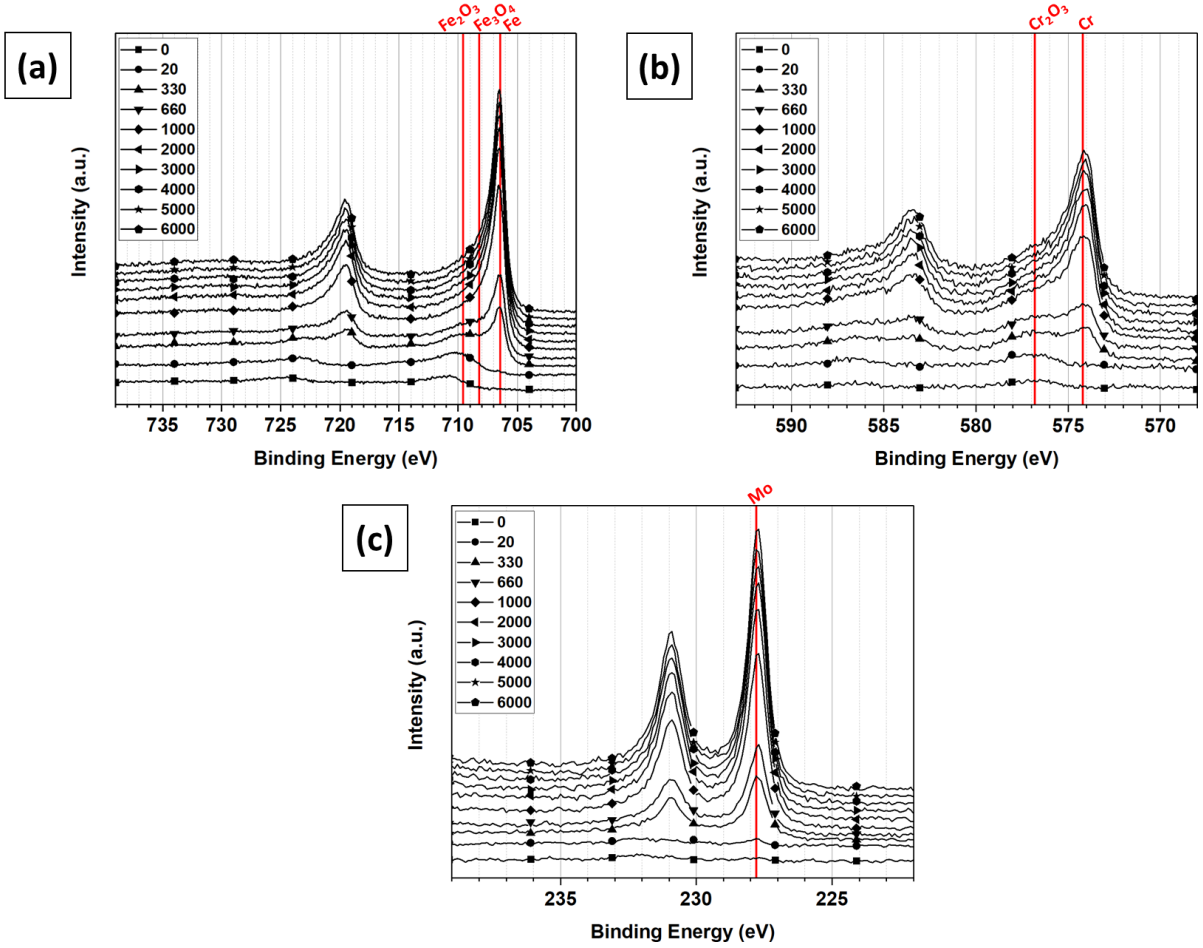

Figure 5.4. Depth-profiled XPS spectra of as-sprayed Fe-based AMC: (a) Fe, (b) Cr, and (c) Mo

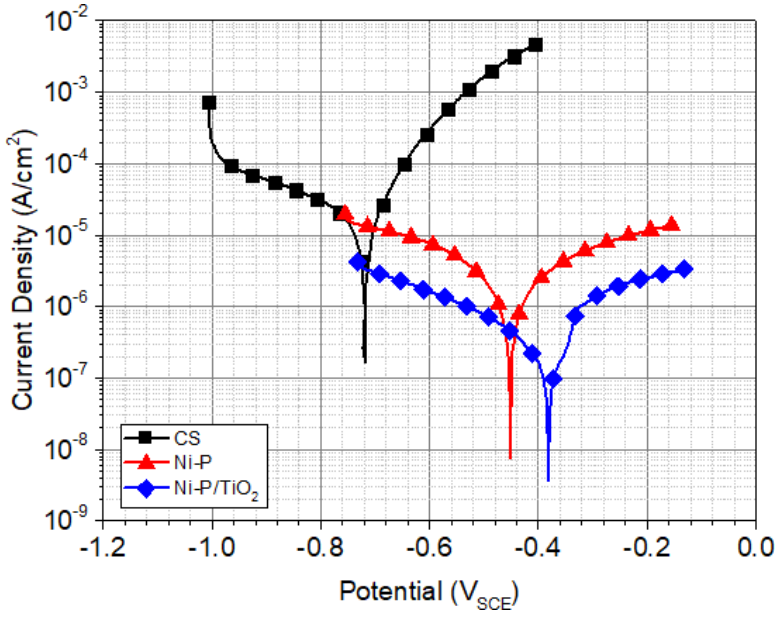

Figure 5.5. LSV results of CS, Ni-P, and Ni-P/TiO_2 in seawater condition

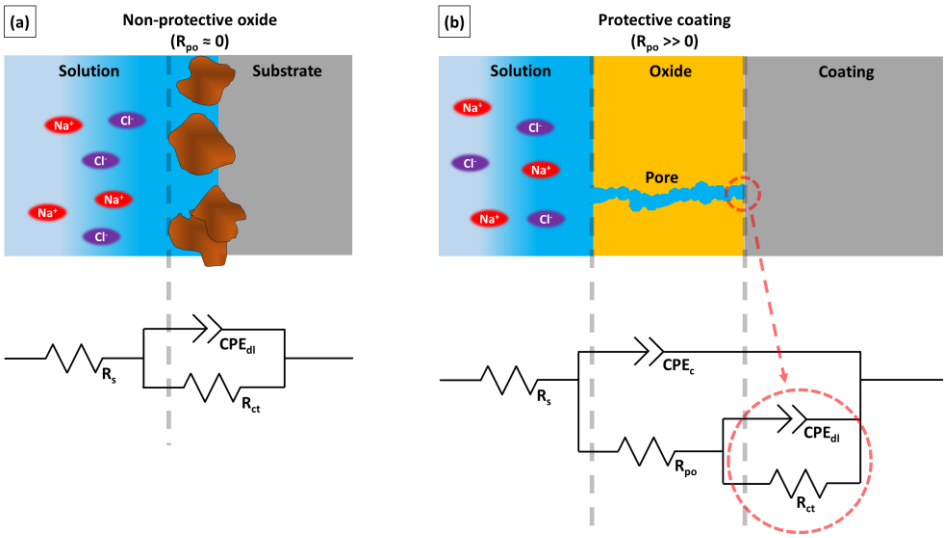

Figure 5.6. Equivalent circuit model for (a) CS and (b) Ni-P, Ni-P/TiO_2

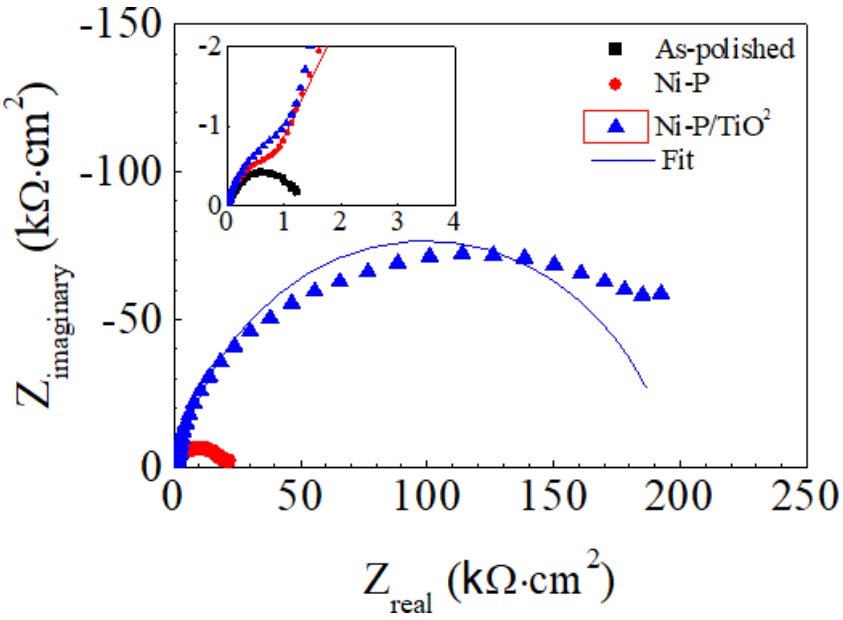

Figure 5.7. EIS results of CS, Ni-P, and Ni-P/TiO_2 in seawater condition

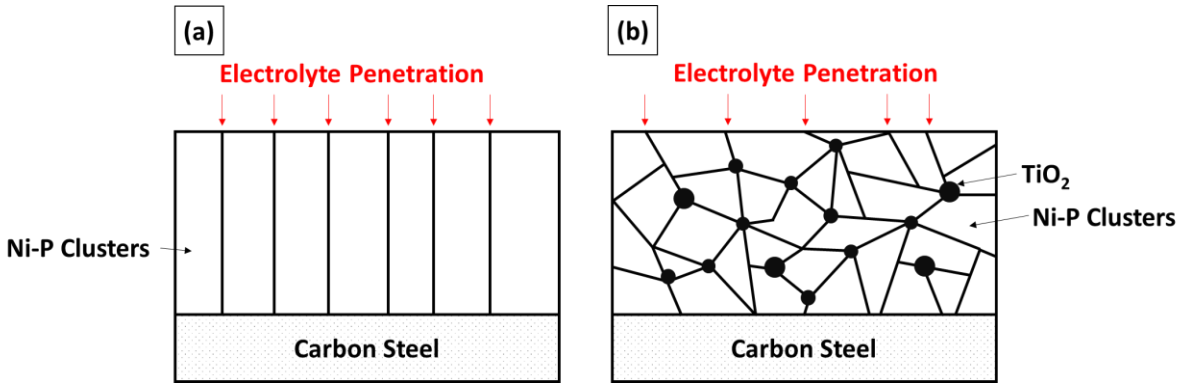

Figure 5.8. Schematic diagram on the corrosion process of ENP coatings with and without nanoparticles: (a) Ni-P coating, (b) Ni-P/TiO_2 coating

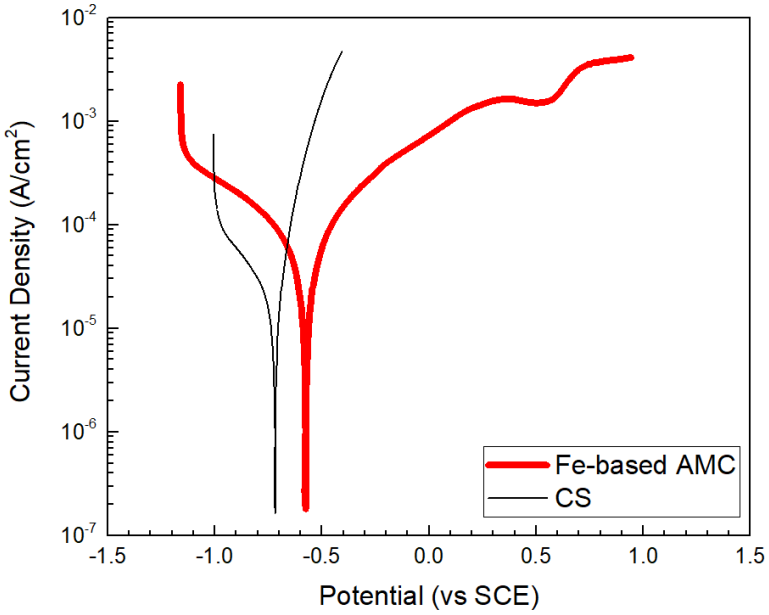

Figure 5.9. LSV results of CS and Fe-based AMC in seawater condition

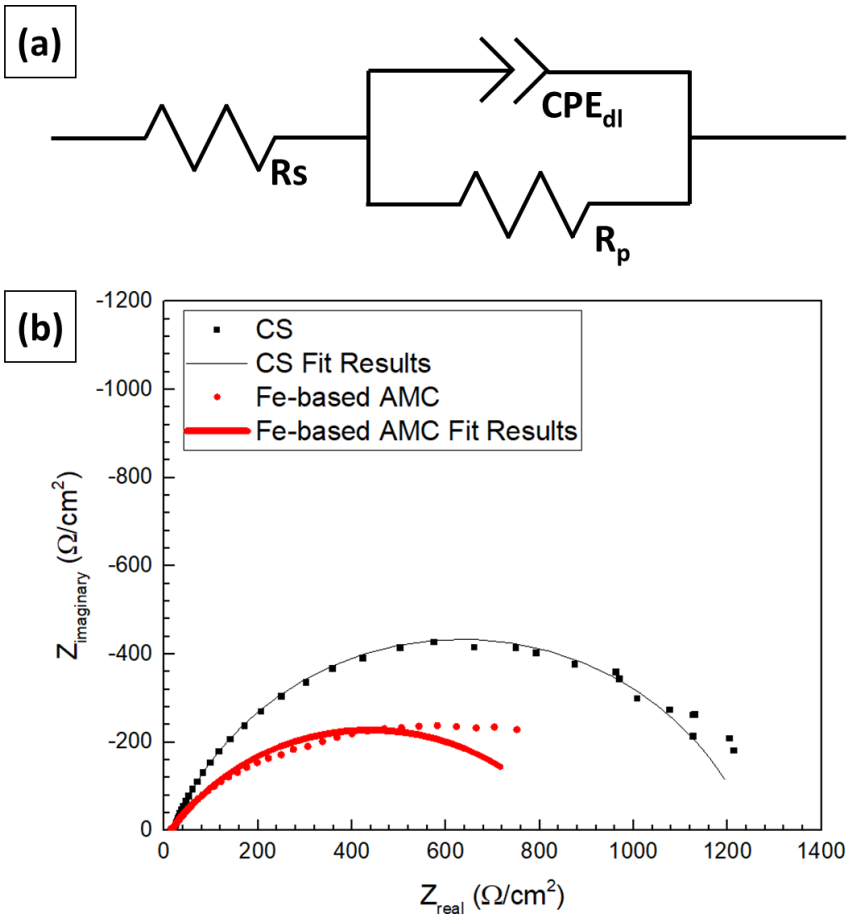

Figure 5.10. EIS results of CS and Fe-based AMC in seawater condition: (a) equivalent circuit model, (b) Nyquist plots

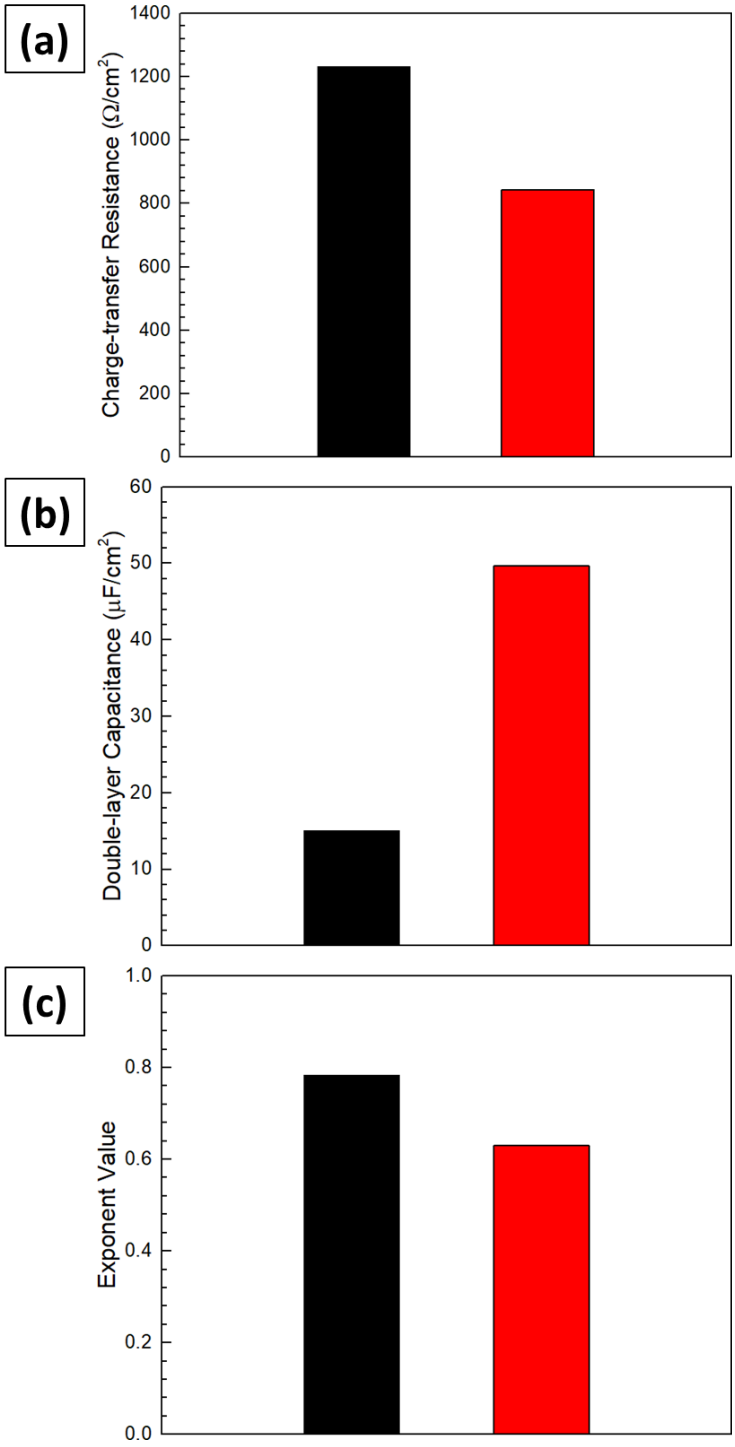

Figure 5.11. Fitting parameters of CS and Fe-based AMC after EIS tests in seawater: (a) R_{ct}, (b) C_{dl}, and (c) n_{dl}

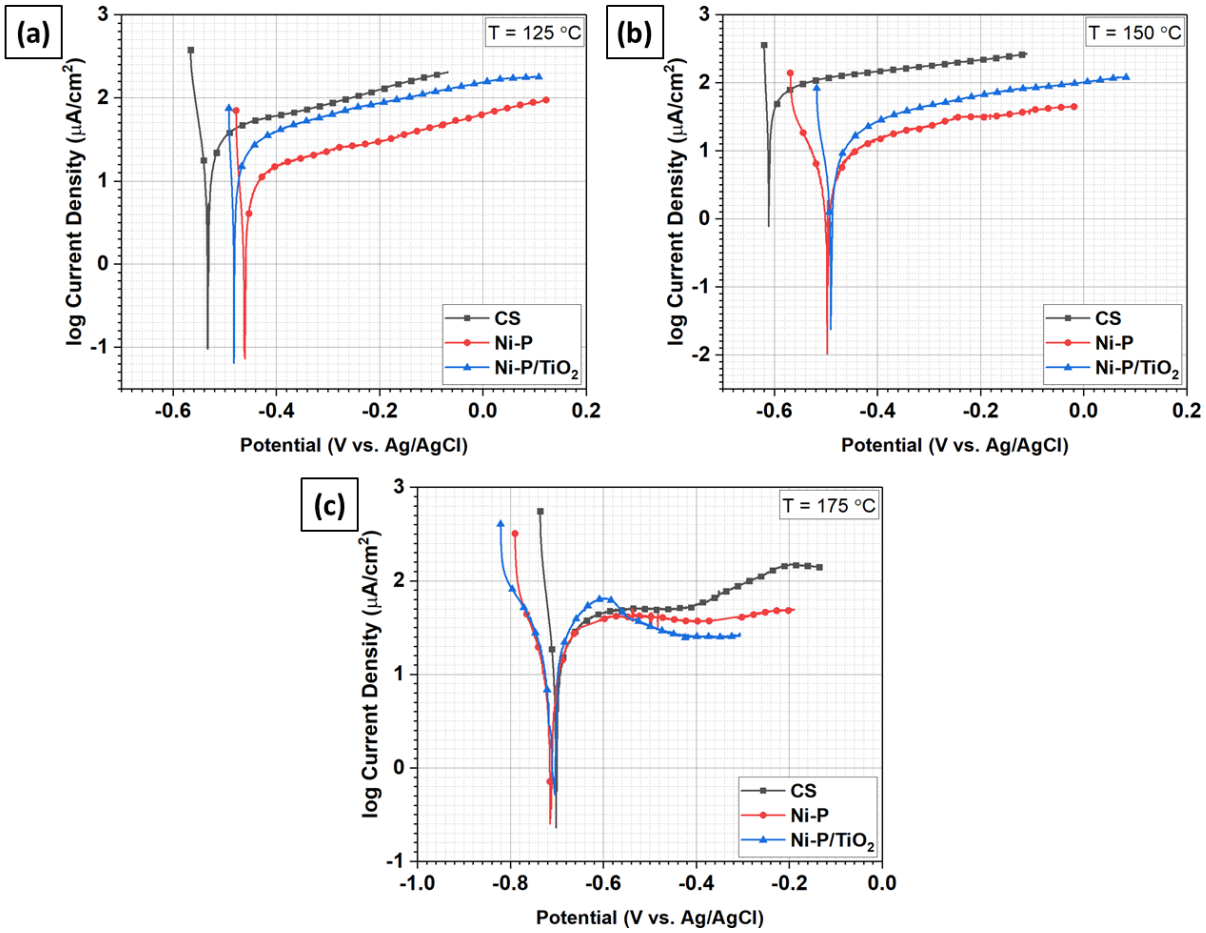

Figure 5.12. LSV results of CS, Ni-P, and Ni-P/TiO_2 at deaerated (a) 125, (b) 150, (c) 175 ºC, 8 MPa, and pH_{25} 9.3 water condition

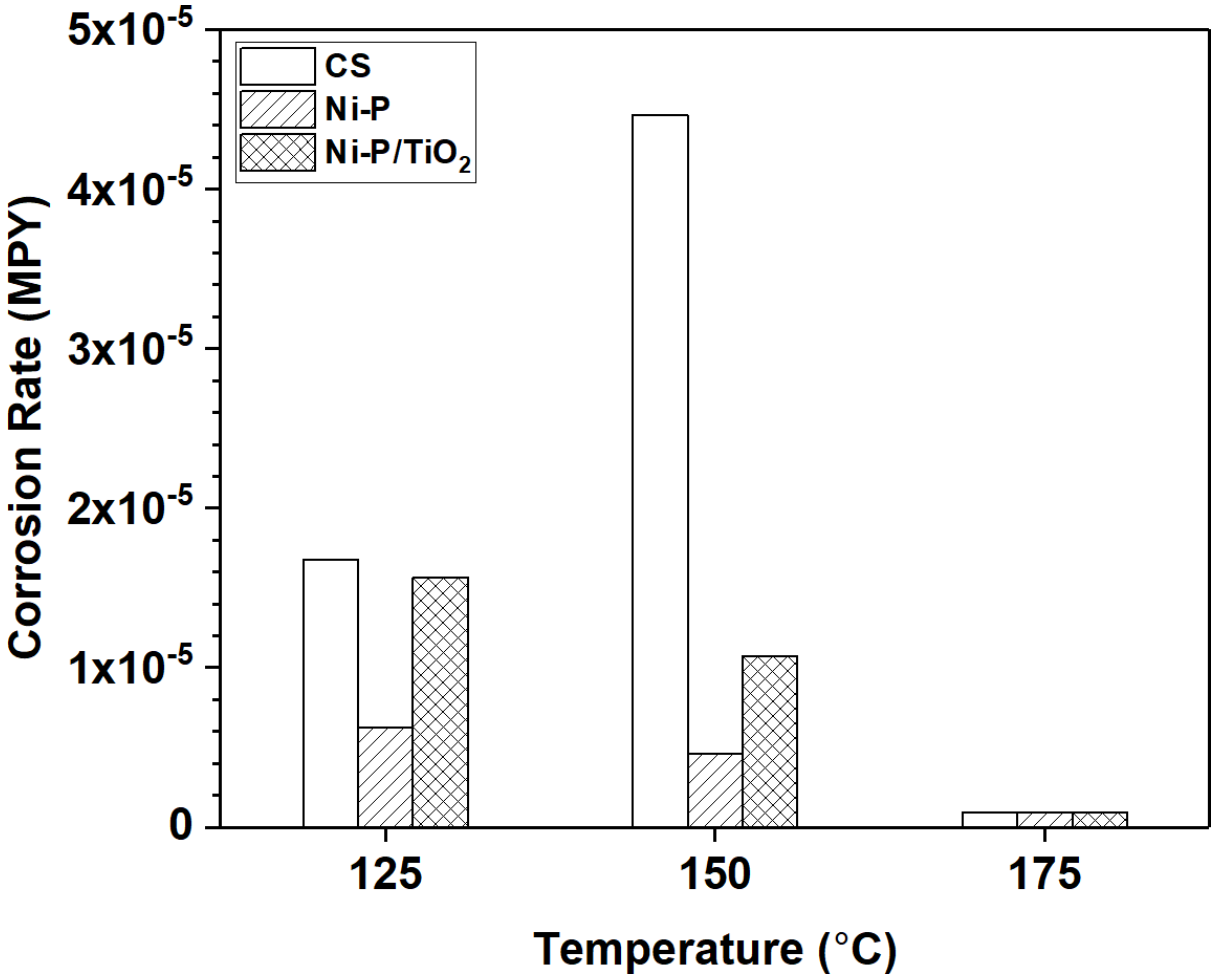

Figure 5.13. Corrosion rate of CS, Ni-P, and Ni-P/TiO_2 at deaerated (a) 125, (b) 150, (c) 175 °C, 8 MPa, and pH_{25} 9.3 water condition]

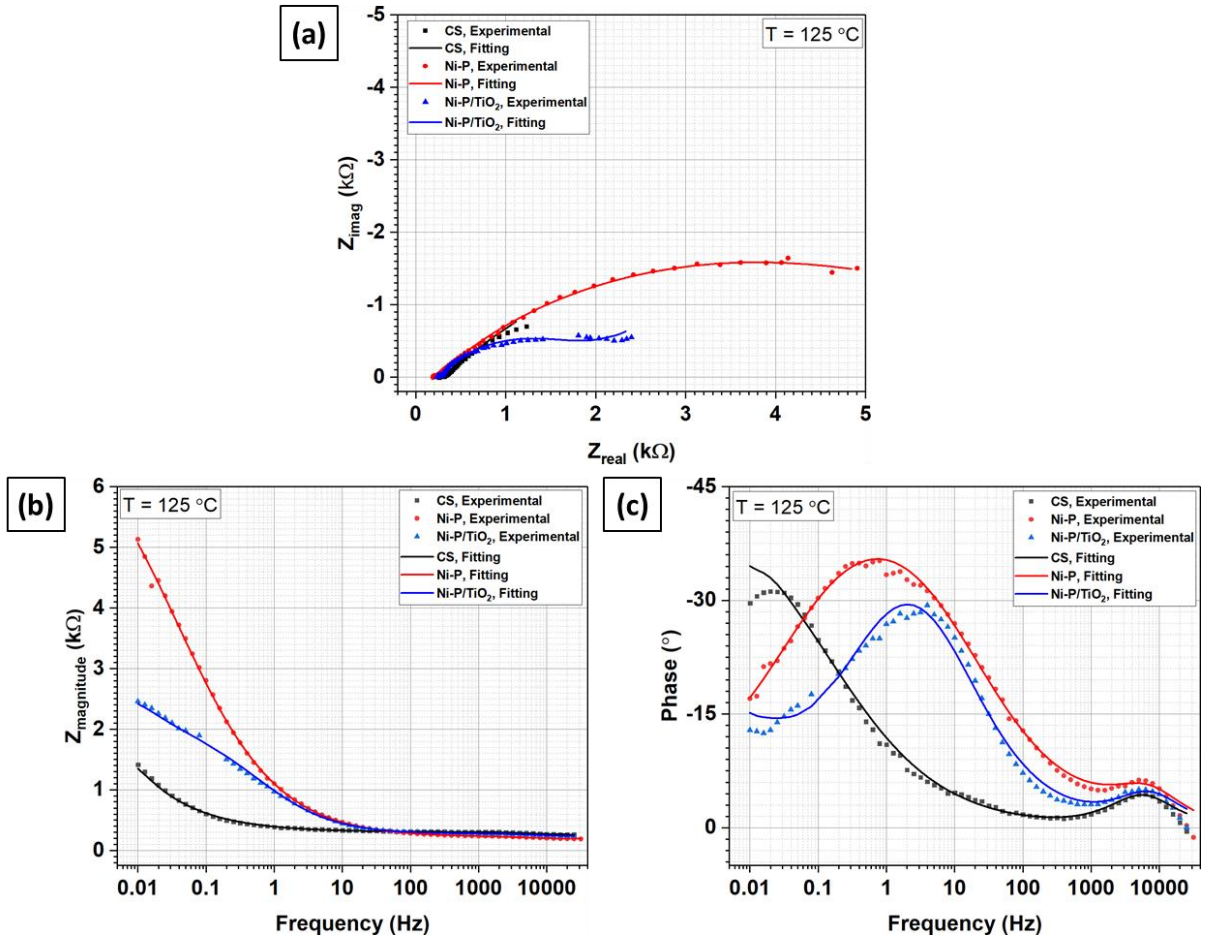

Figure 5.14. EIS results of CS, Ni-P, and Ni-P/TiO_2 deaerated pH_{25} 9.3 water condition at 125 °C: (a) Nyquist, (b, c) Bode plots.

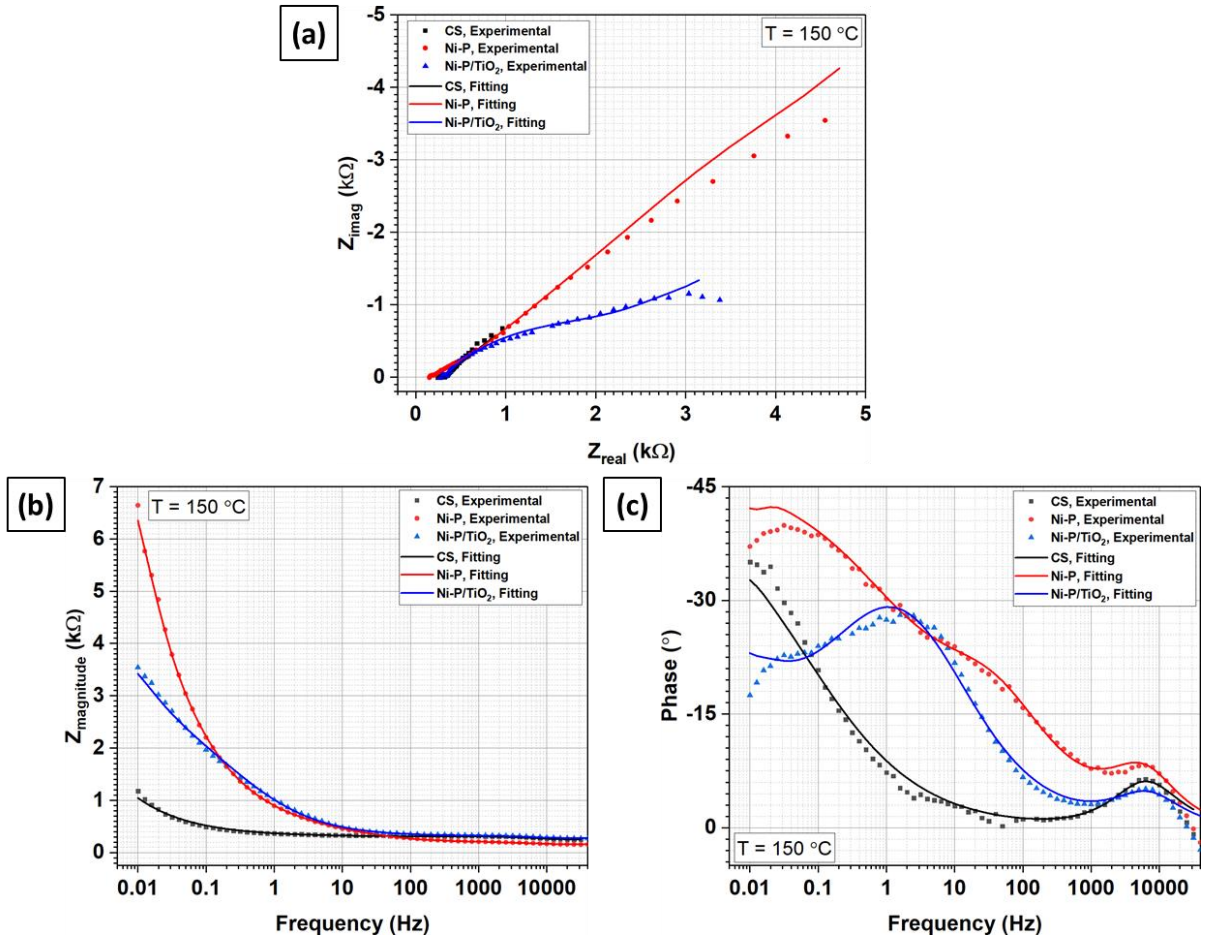

Figure 5.15. EIS results of CS, Ni-P, and Ni-P/TiO_2 deaerated pH_{25} 9.3 water condition at 150 °C: (a) Nyquist, (b, c) Bode plots.

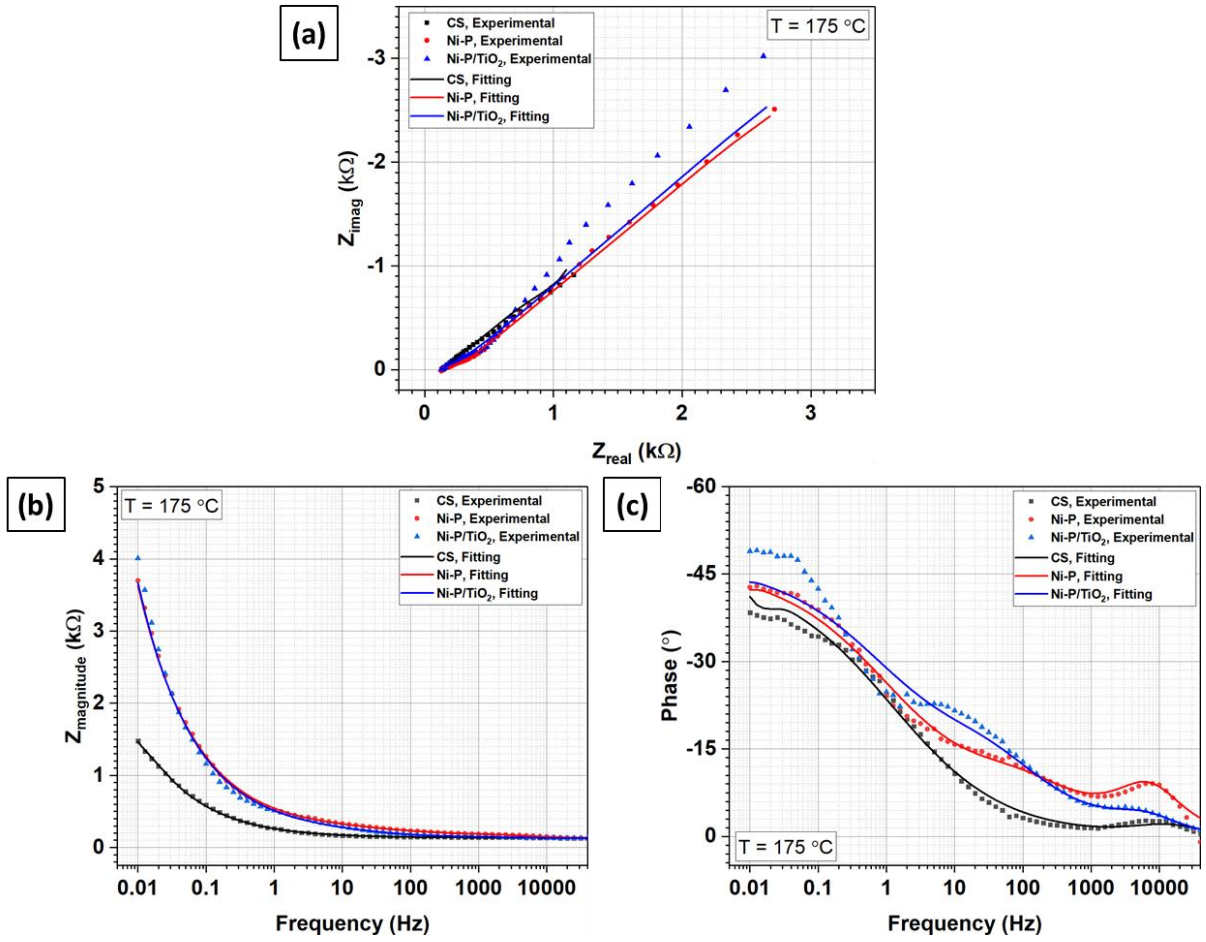

Figure 5.16. EIS results of CS, Ni-P, and Ni-P/TiO_2 deaerated pH_{25} 9.3 water condition at 175 °C: (a) Nyquist, (b, c) Bode plots.

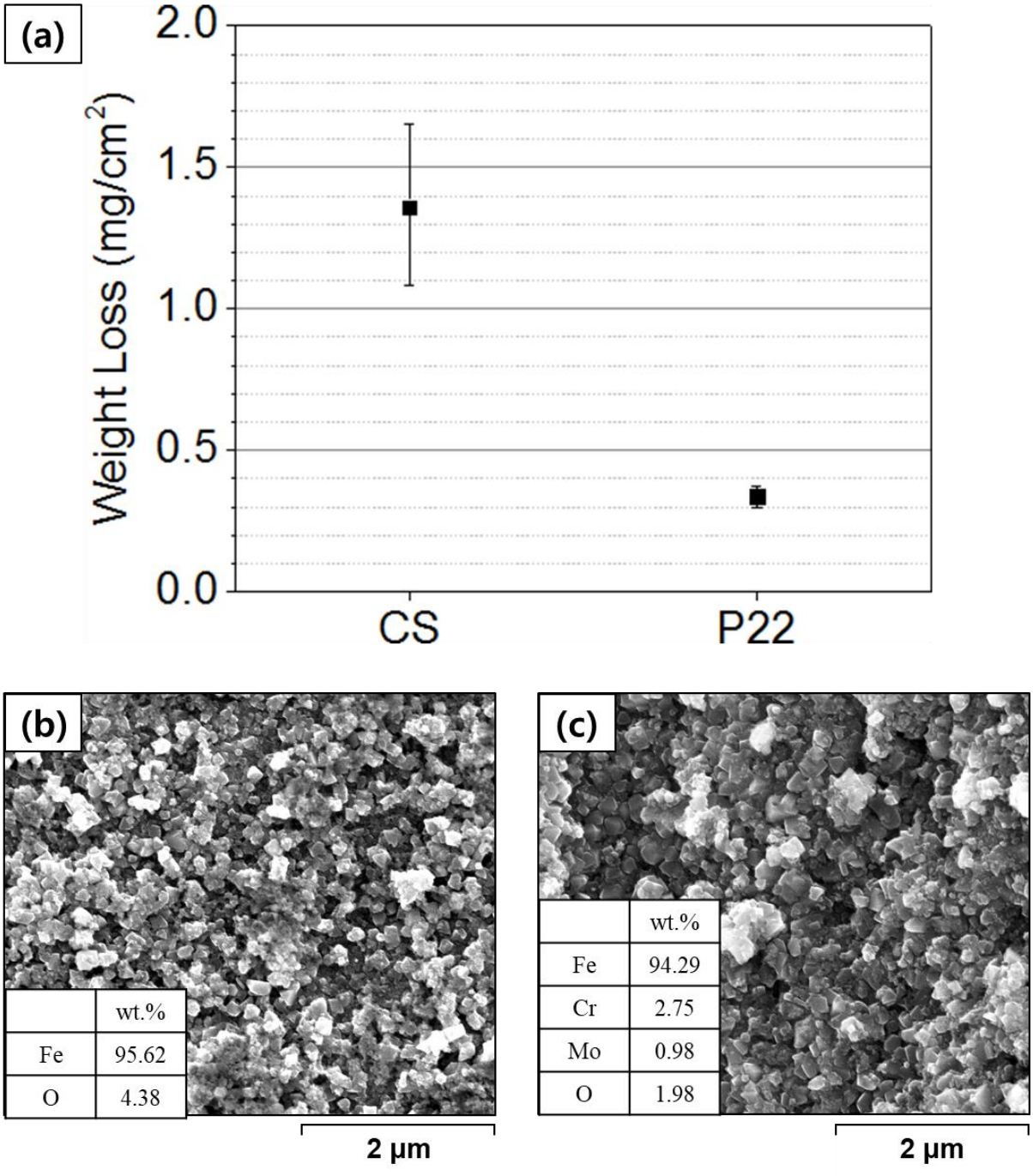

Figure 5.17. FAC simulation results of CS and P22 after 14 days of immersion at 150 °C: (a) weight loss, and SEM surface morphology of (b) CS and (c) P22

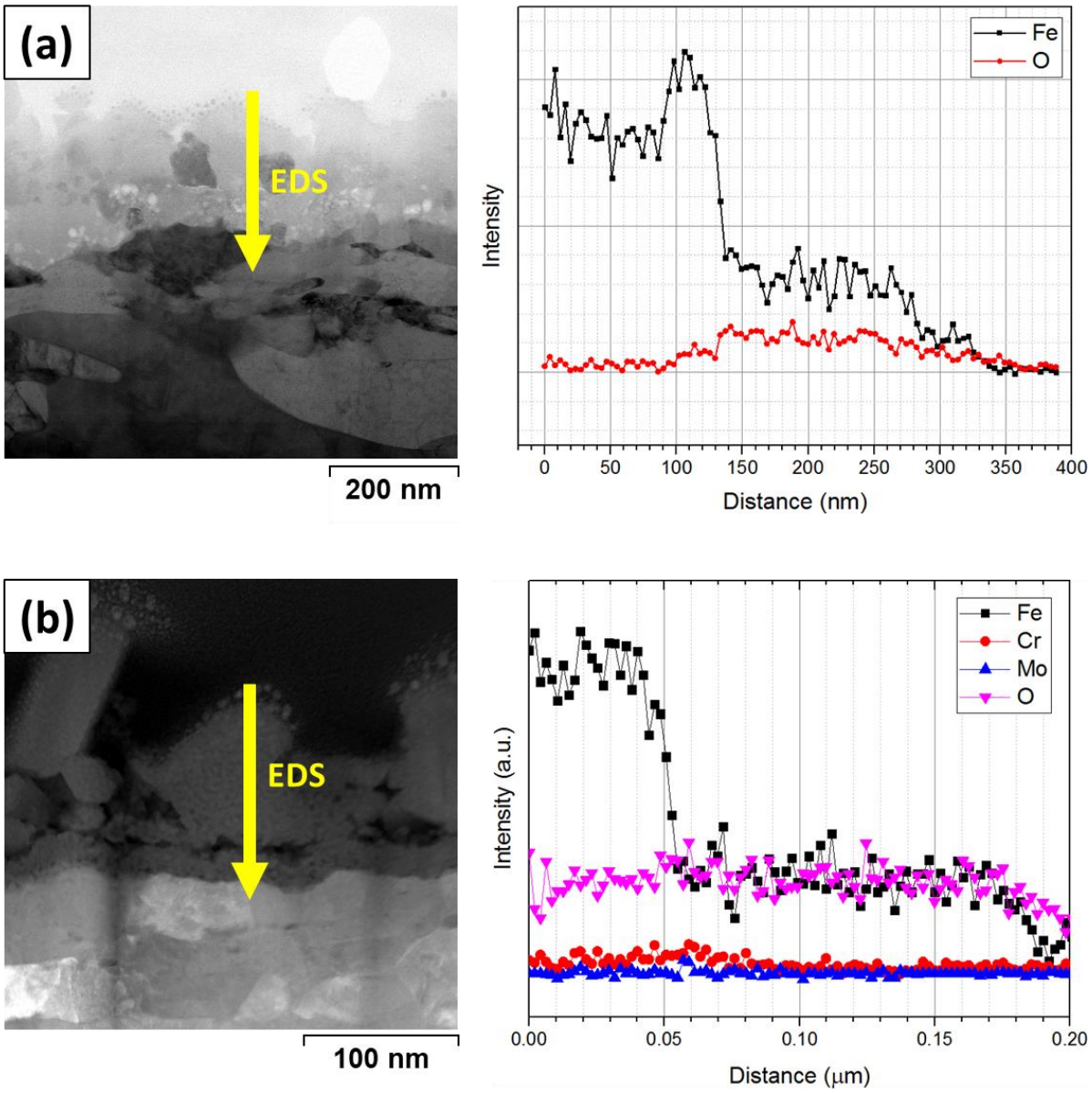

Figure 5.18. TEM CX morphology of (a) CS and (b) P22 after 14 days of immersion at 150 °C with EDS chemical analysis on yellow arrows

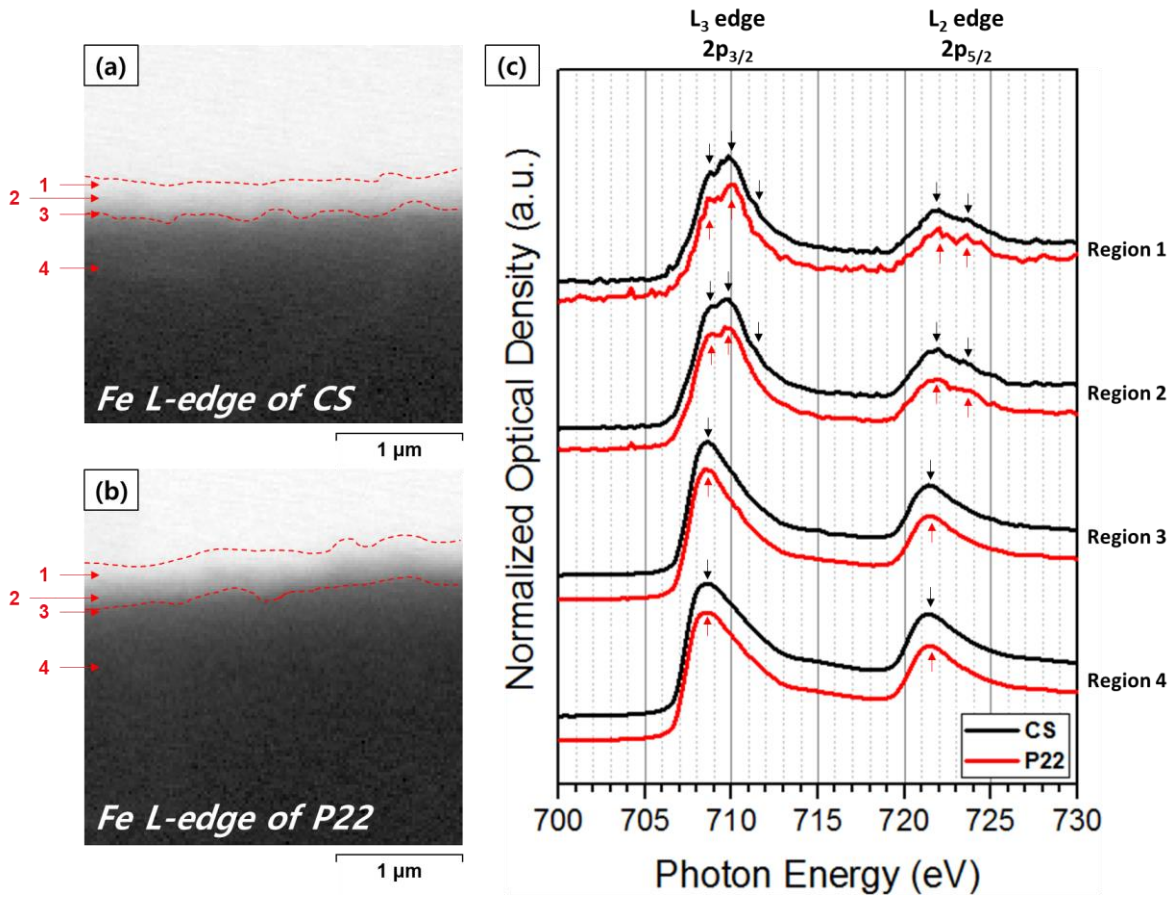

Figure 5.19. STXM morphology and XAS spectra of CS and P22 after FAC simulation test at 150 °C: STXM morphology of (a) CS, (b) P22, and (c) XAS spectra in different regions

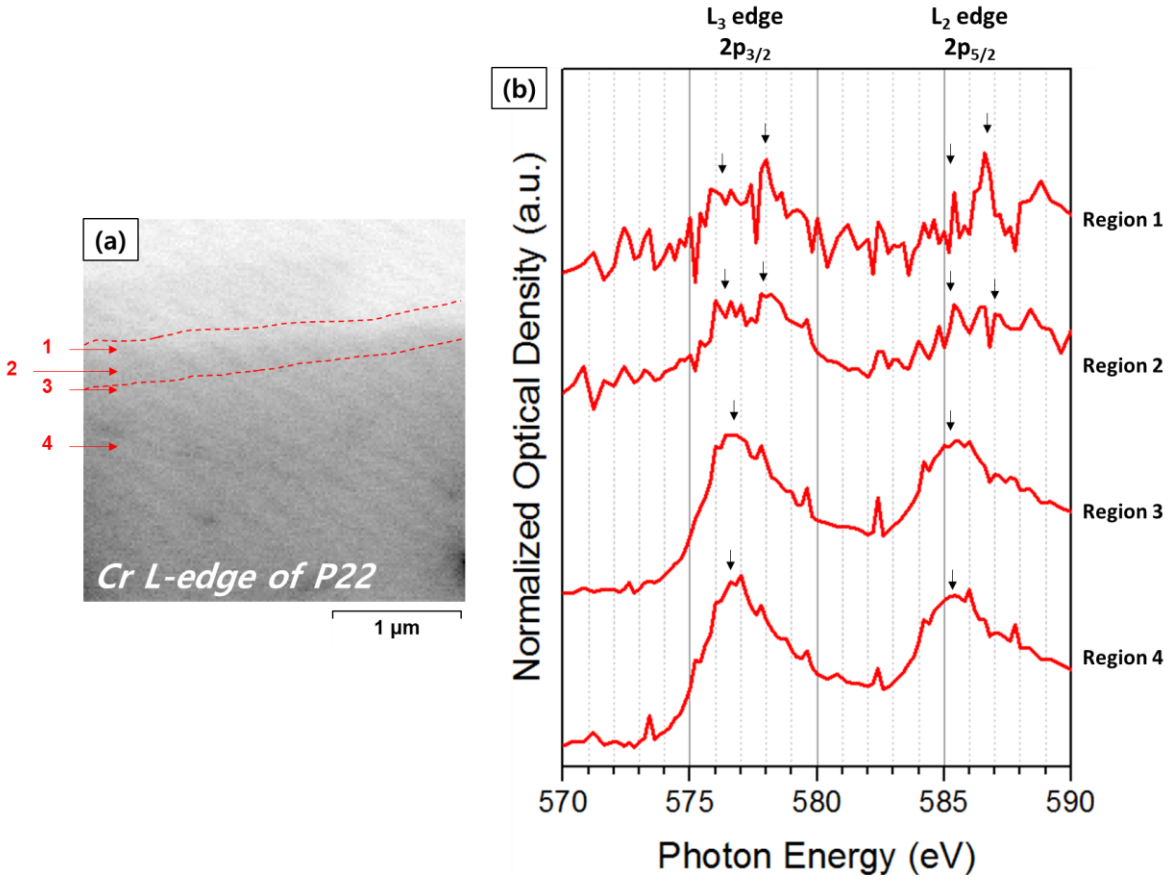

Figure 5.20. STXM morphology and XAS spectra of P22 after FAC simulation test at 150 °C: STXM morphology of (a) P22, and (b) XAS spectra in different regions

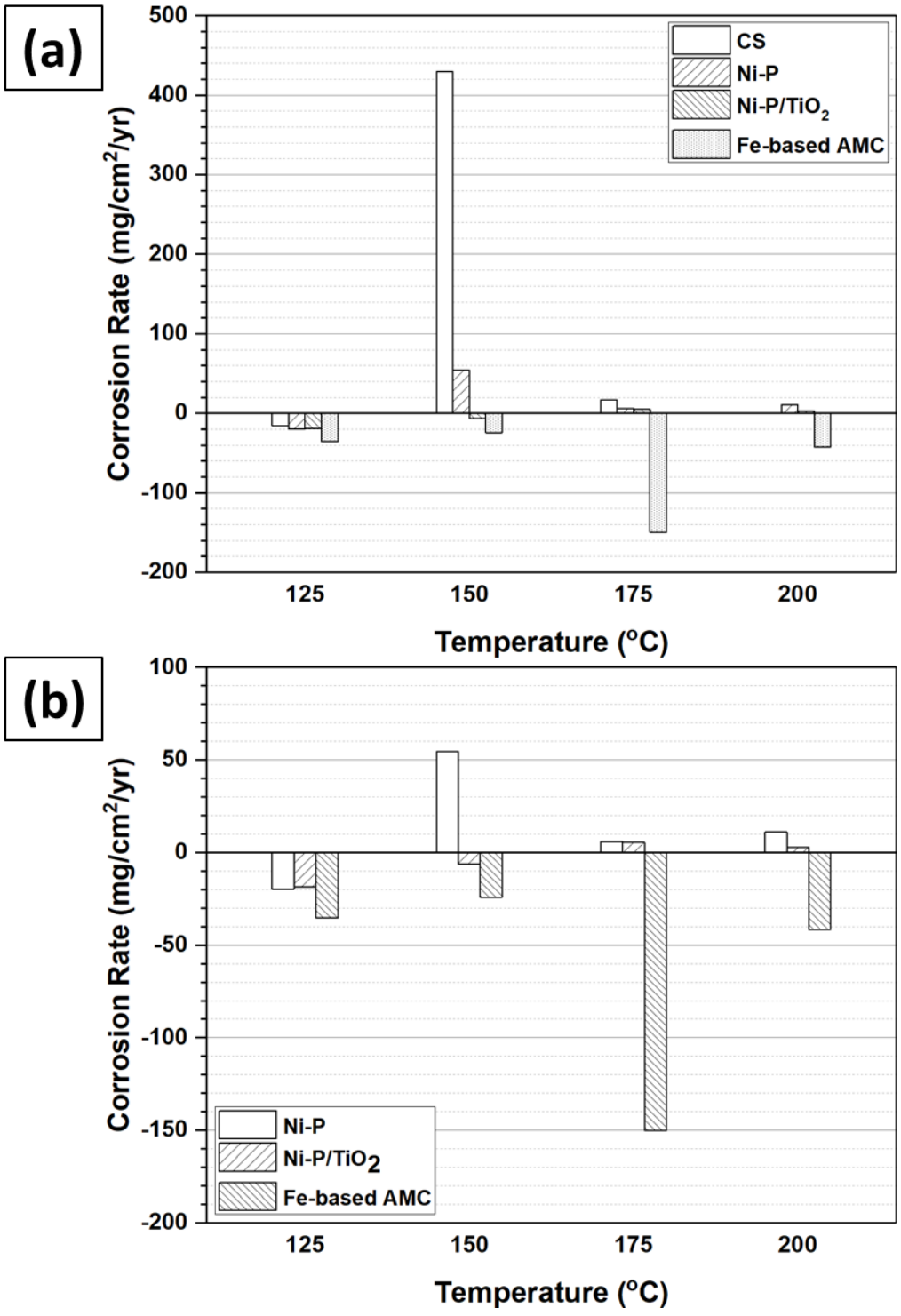

Figure 5.21. Corrosion rate of Ni-P, Ni-P/TiO_2 and Fe-based AMC at deaerated 125, 150, 175 and 200 °C, 8 MPa, and pH_{25} 9.3 water condition after 2 weeks of immersion (a) with and (b) without that of CS

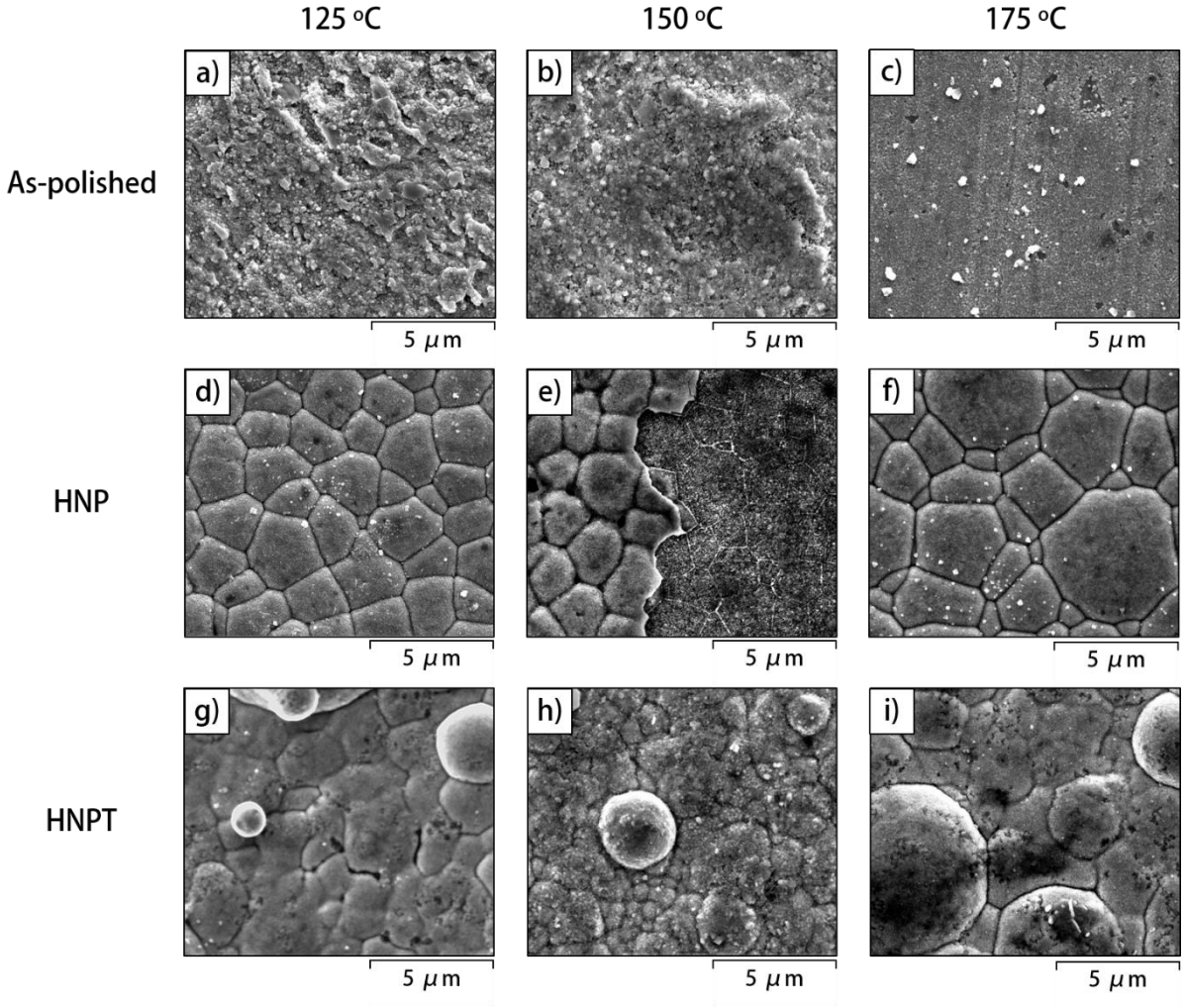

Figure 5.22. SEM surface morphologies of (a,b,c) CS, (d,e,f) Ni-P, and (g,h,i) Ni-P/TiO_2 after the FAC simulation experiments with temperature variation [55]

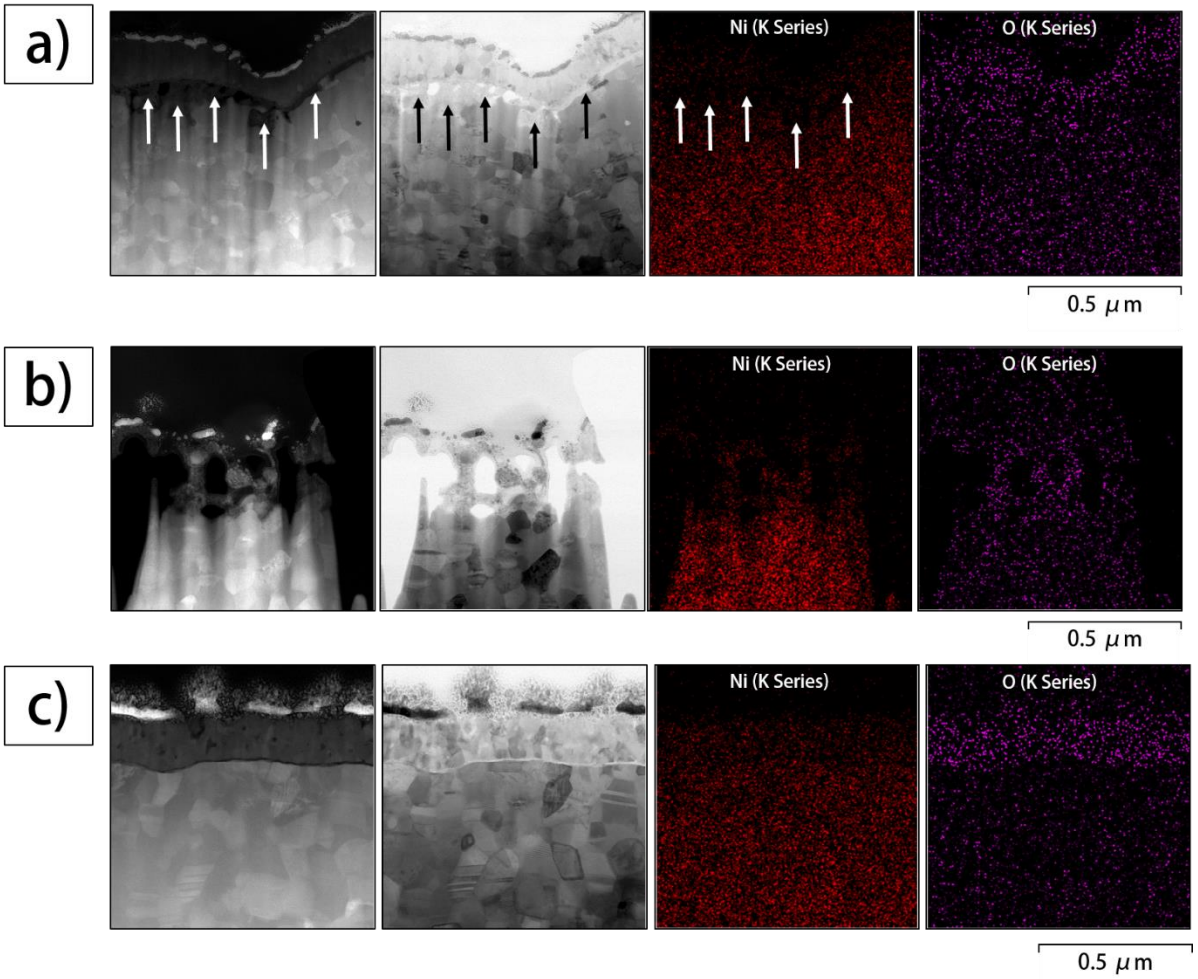

Figure 5.23. TEM CX morphologies of the Ni-P and Ni-P/TiO_2 after the immersion at 150 °C. (a) STEM morphologies on the NiO/Ni-P interfaces corresponding chemical elements mappings. The white arrows indicate Ni-depleted zones. (b) STEM morphologies on the NiO-detached area with the chemical elements mappings. (c) STEM morphologies on the Ni-P/TiO_2 with the EDS mappings [55]

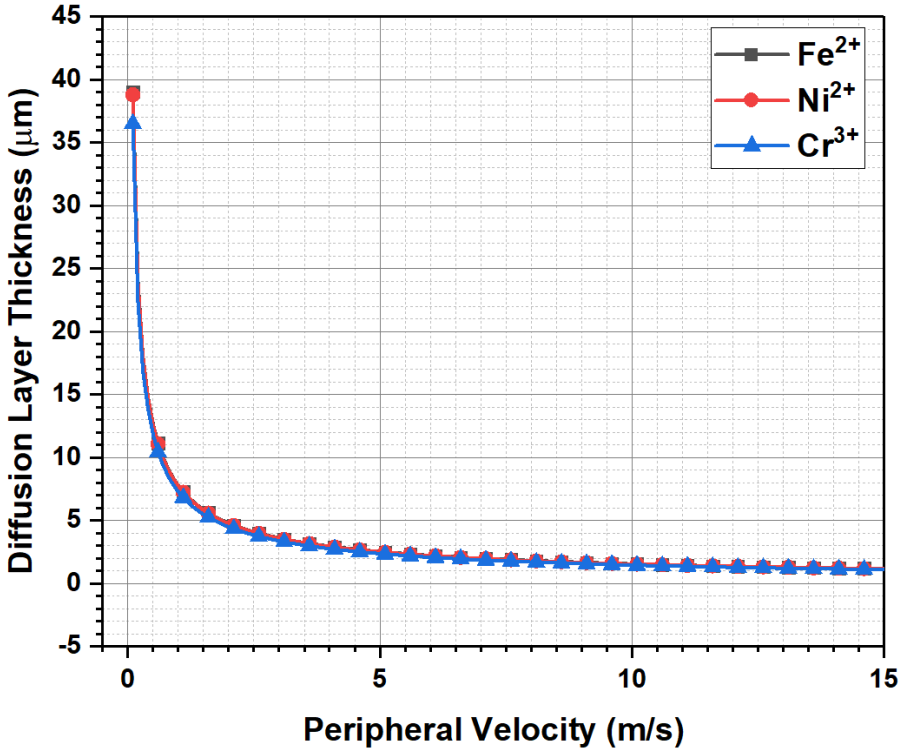

Figure 5.24. Effects of peripheral velocity on the diffusion layer thickness of the metallic species.

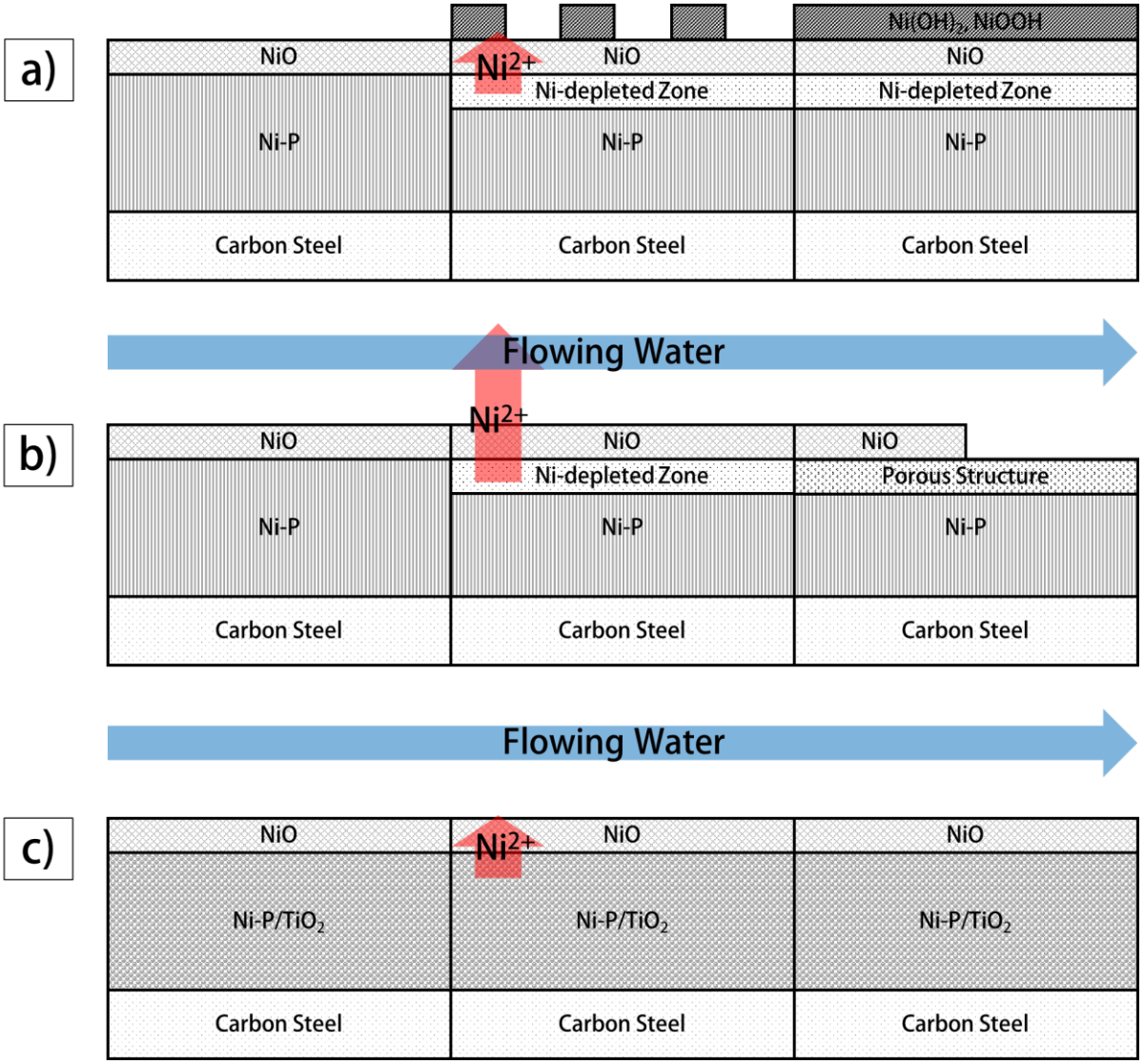

Figure 5.25. The FAC mechanism of Ni-P alloys and Ni-P/TiO_2 under static and flowing conditions. (a) Previous studies on the hydroxide formation of Ni-P alloys under static condition. FAC behavior of (b) Ni-P and (c) Ni-P/TiO_2 at 150°C in this study [55].

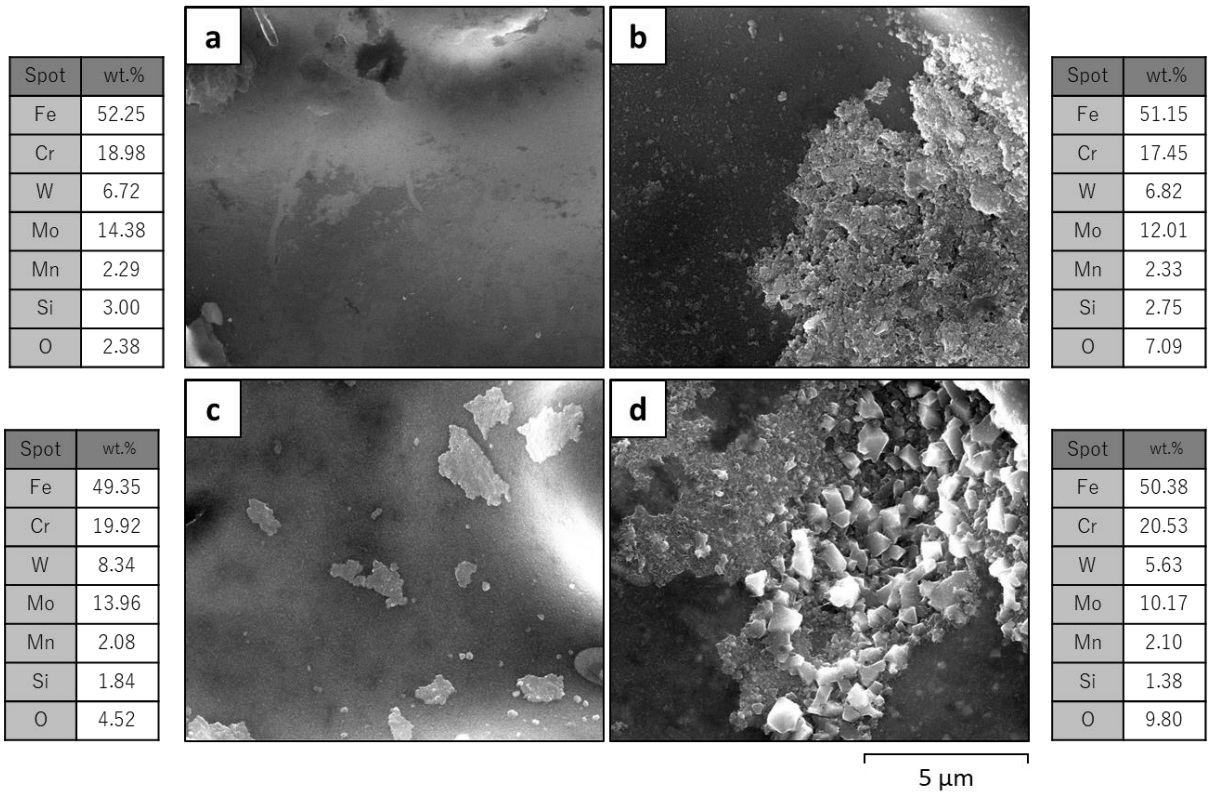

Spot	wt.%
Fe	52.25
Cr	18.98
W	6.72
Mo	14.38
Mn	2.29
Si	3.00
O	2.38

Spot	wt.%
Fe	51.15
Cr	17.45
W	6.82
Mo	12.01
Mn	2.33
Si	2.75
O	7.09

Spot	wt.%
Fe	49.35
Cr	19.92
W	8.34
Mo	13.96
Mn	2.08
Si	1.84
O	4.52

Spot	wt.%
Fe	50.38
Cr	20.53
W	5.63
Mo	10.17
Mn	2.10
Si	1.38
O	9.80

Figure 5.26. SEM surface morphologies of Fe-based AMC after the FAC simulation experiments at (a) 125, (b) 150, (c) 175, and (d) 200 ºC

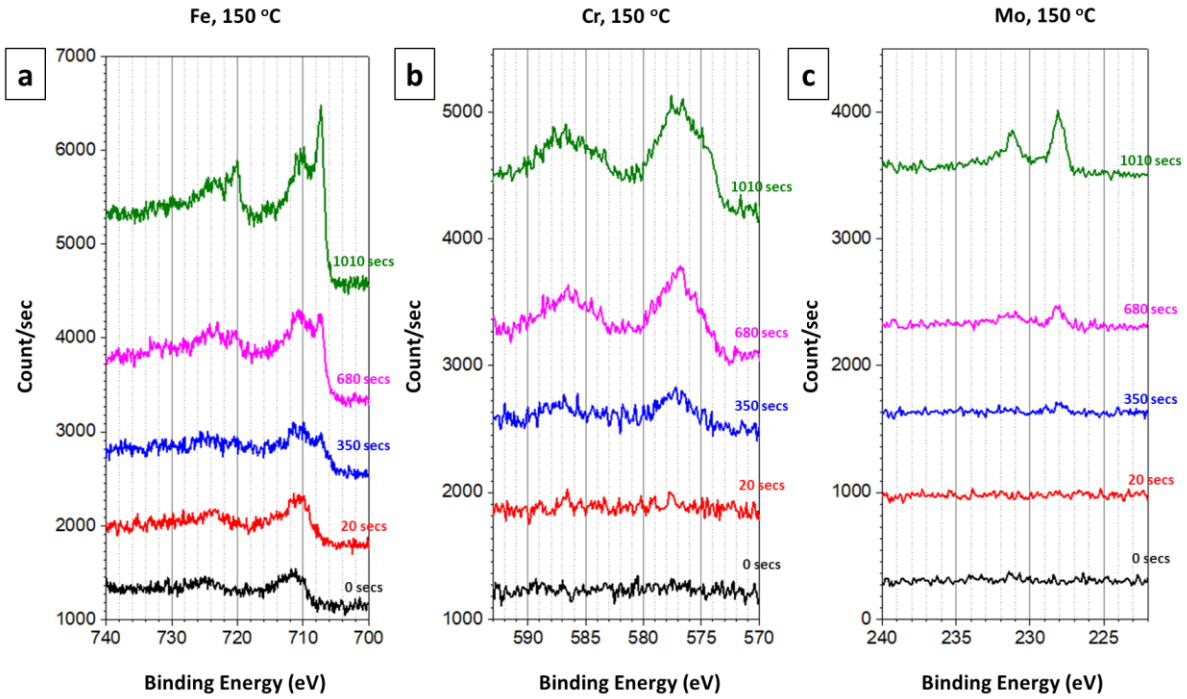

Figure 5.27. XPS depth profiling results of Fe-based AMC after the FAC simulation experiments at 150 ºC: (a) Fe, (b) Cr, and (c) Mo

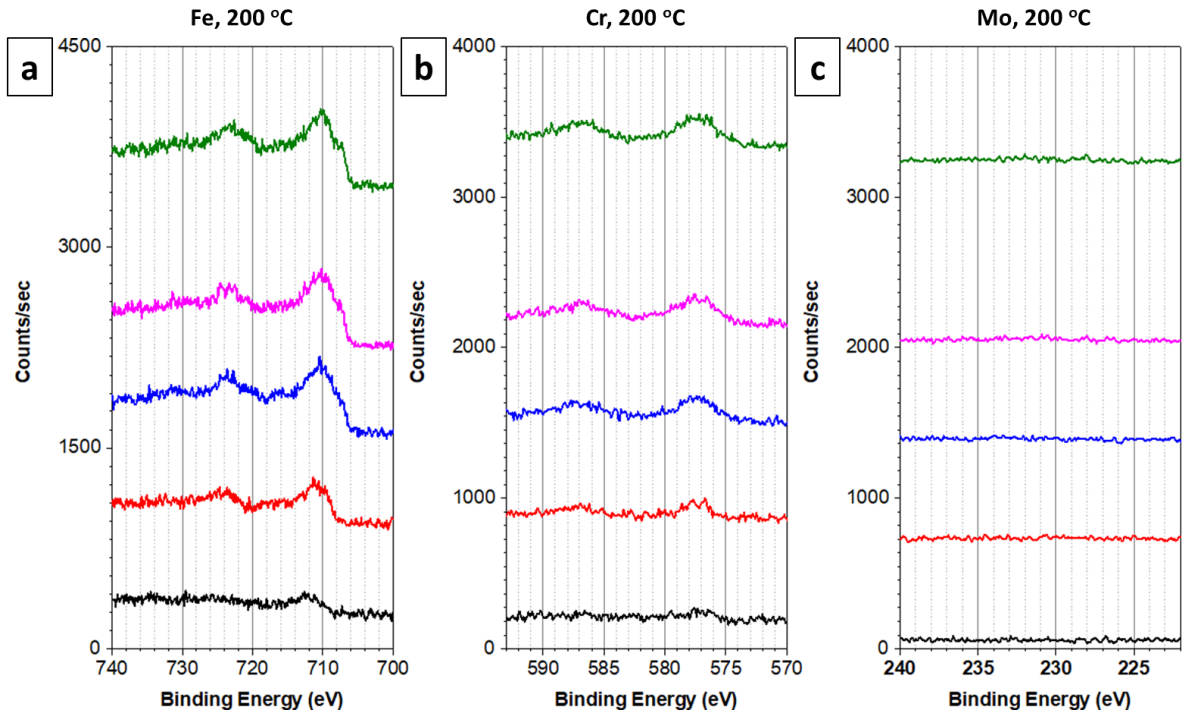

Figure 5.28. XPS depth profiling results of Fe-based AMC after the FAC simulation experiments at 200 °C: (a) Fe, (b) Cr, and (c) Mo

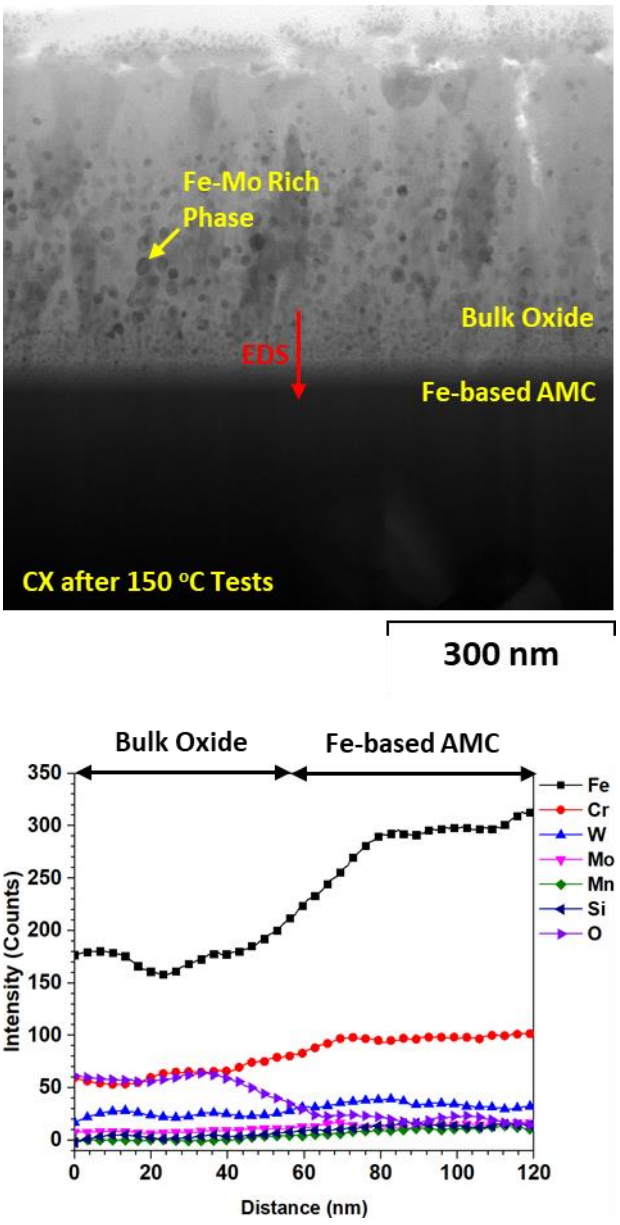

Figure 5.29.TEM analysis results for the samples immersed at 150 °C. The position of chemical composition analysis is indicated in the CX morphologies.

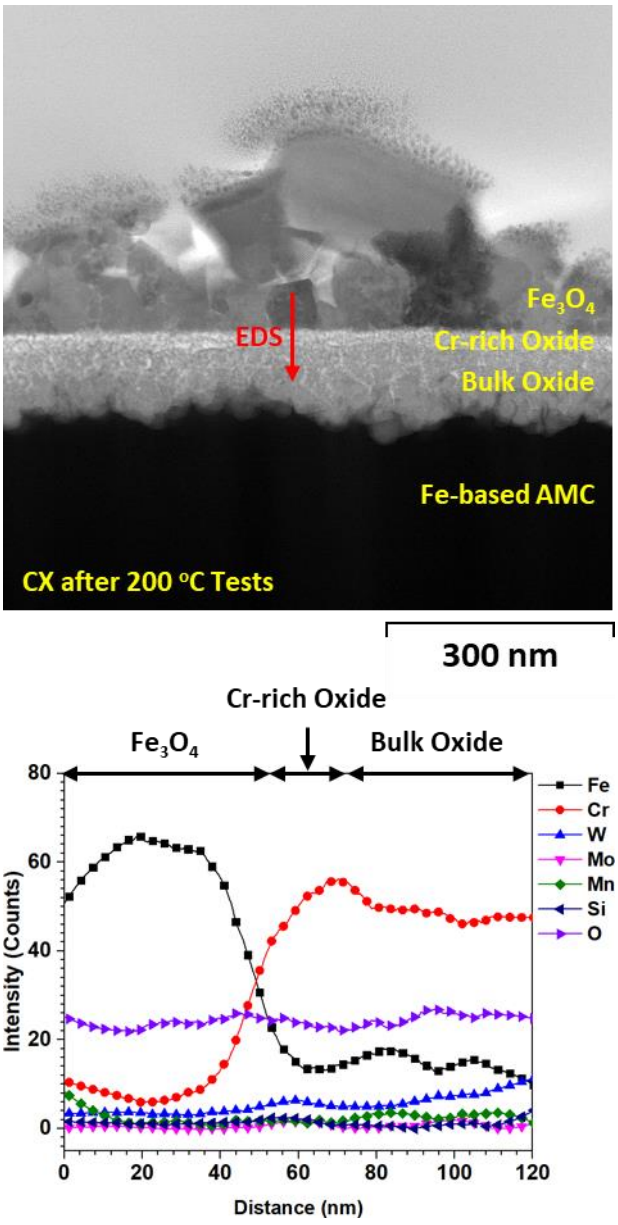

Figure 5.30.TEM analysis results for the samples immersed at 200 °C. The position of chemical composition analysis is indicated in the CX morphologies.

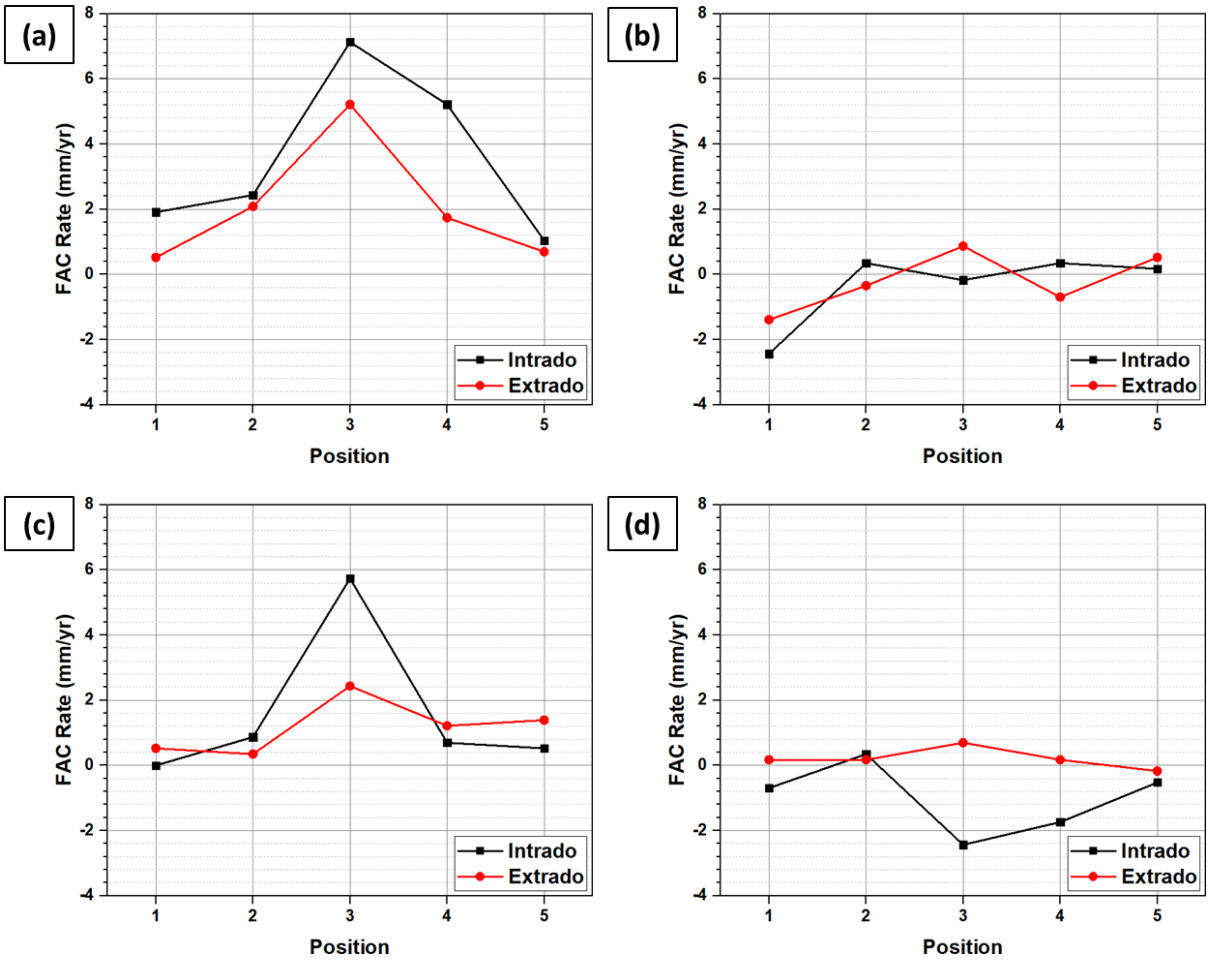

Figure 5.31. UT results of (a) CS, (b) P22, (c) Ni-P/TiO_2 and (d) Fe-based AMC after 21 days of immersion under 5.7 m/sec of 150 ºC flowing deaerated water at pH 9.3

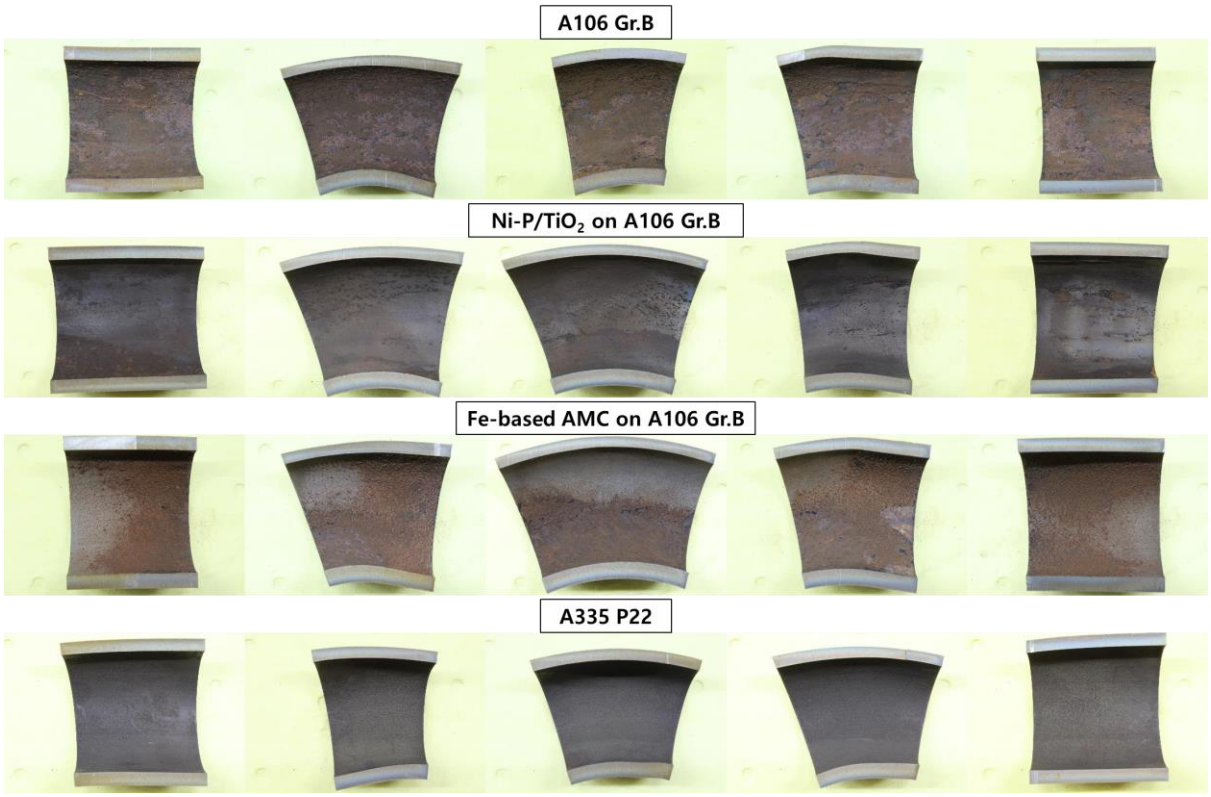

Figure 5.32. Photography of the cut samples after the FAC experiments

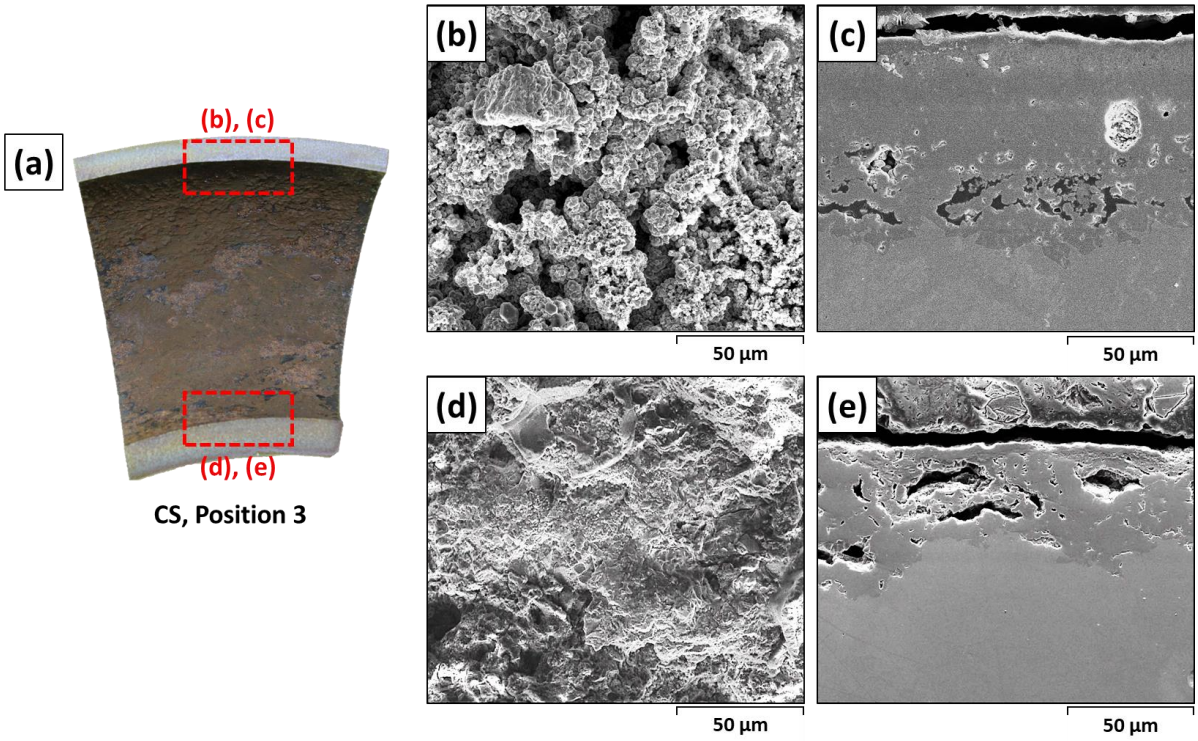

Figure 5.33. SEM surface and CX morphologies of CS at (a, b) intrados and (c, d) extrados at the position 3

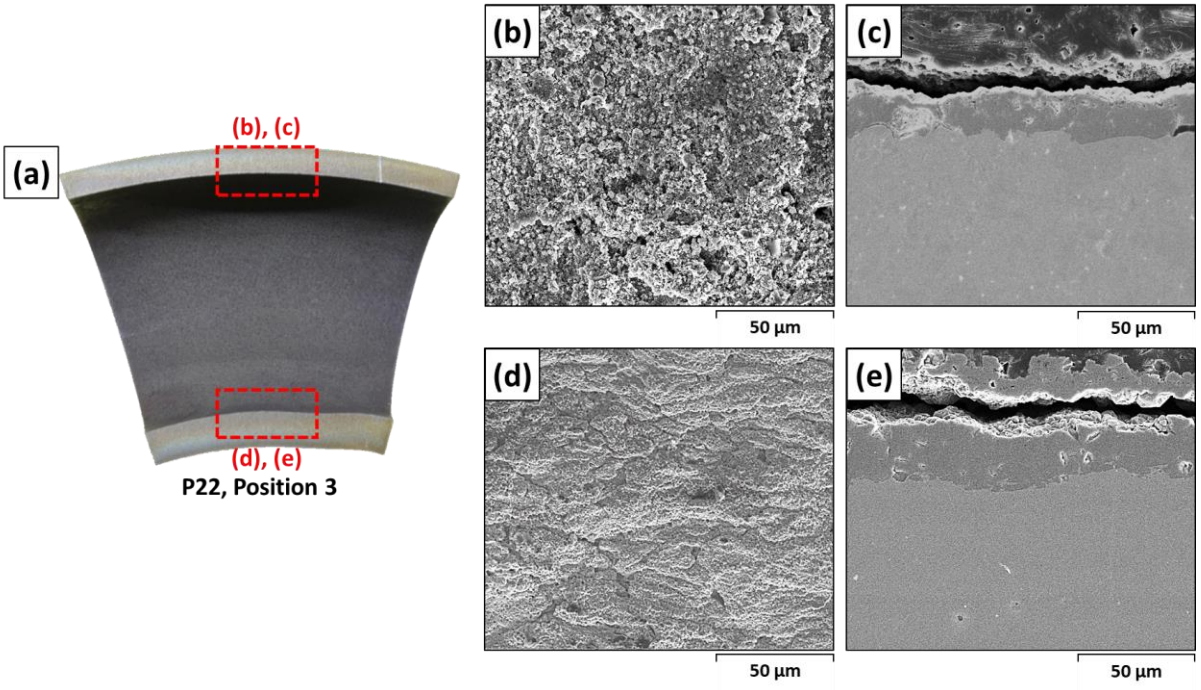

Figure 5.34. SEM surface and CX morphologies of P22 at (a, b) intrados and (c, d) extrados at the position 3

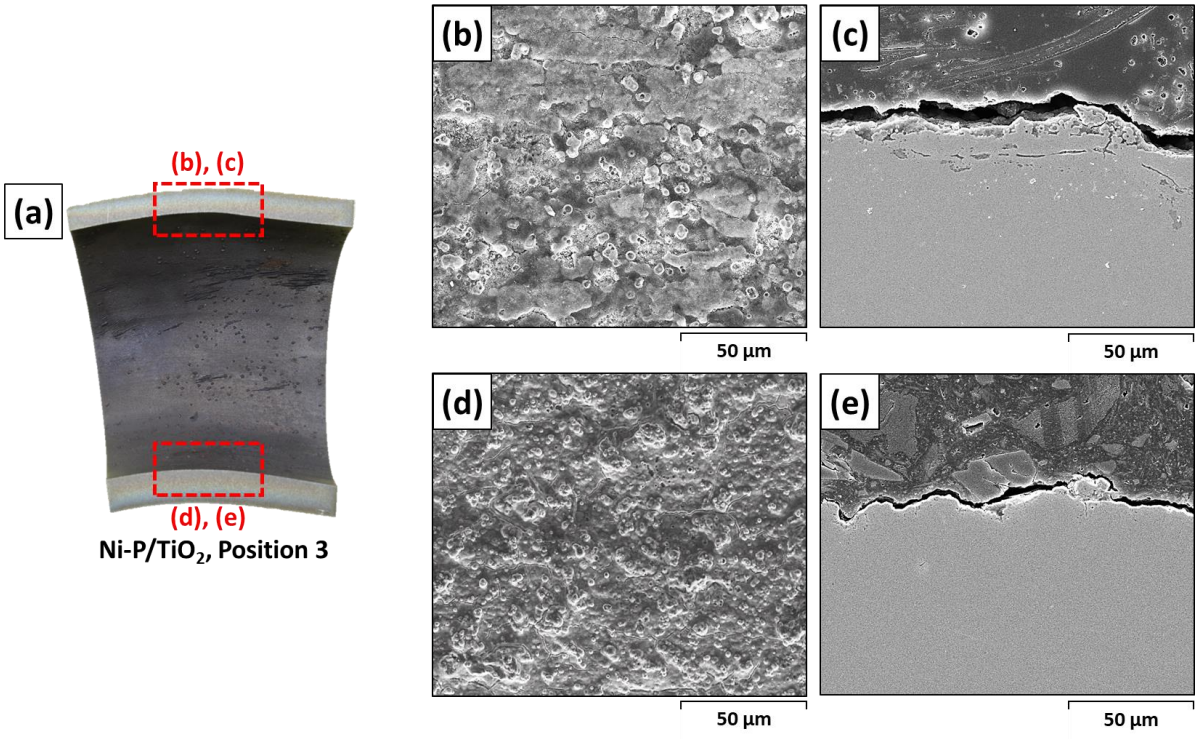

Figure 5.35. SEM surface and CX morphologies of Ni-P/TiO_2 at (a, b) intrados and (c, d) extrados at the position 3

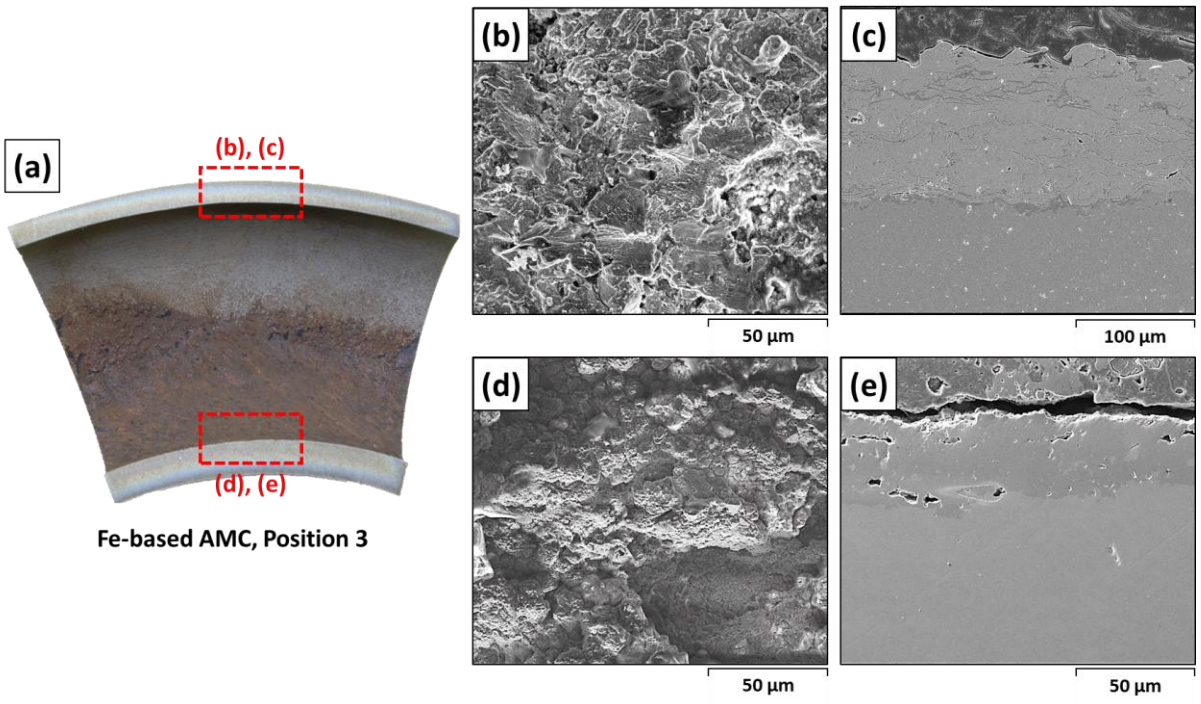

Figure 5.36. SEM surface and CX morphologies of Fe-based AMC at (a, b) intrados and (c, d) extrados at the position 3

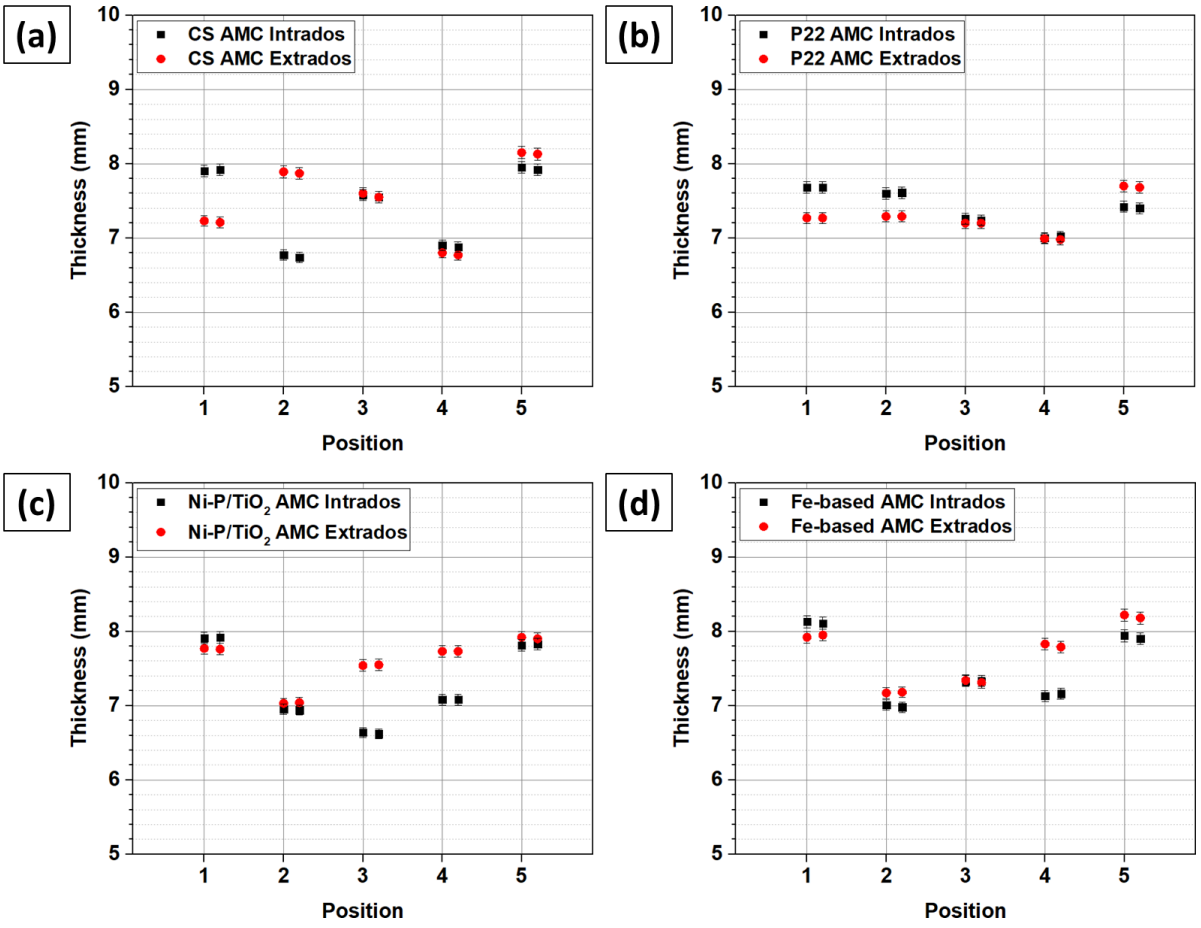

Figure 5.37. The comparison between UT thickness measurement data (after 3 weeks of immersion) and the post mortem thickness measurement data: (a) CS, (b) P22, (c) Ni-P/TiO_2, and (d) Fe-based AMC. In the same position, the left scatters indicate the UT results, and the right scatters indicate the post mortem measurement.

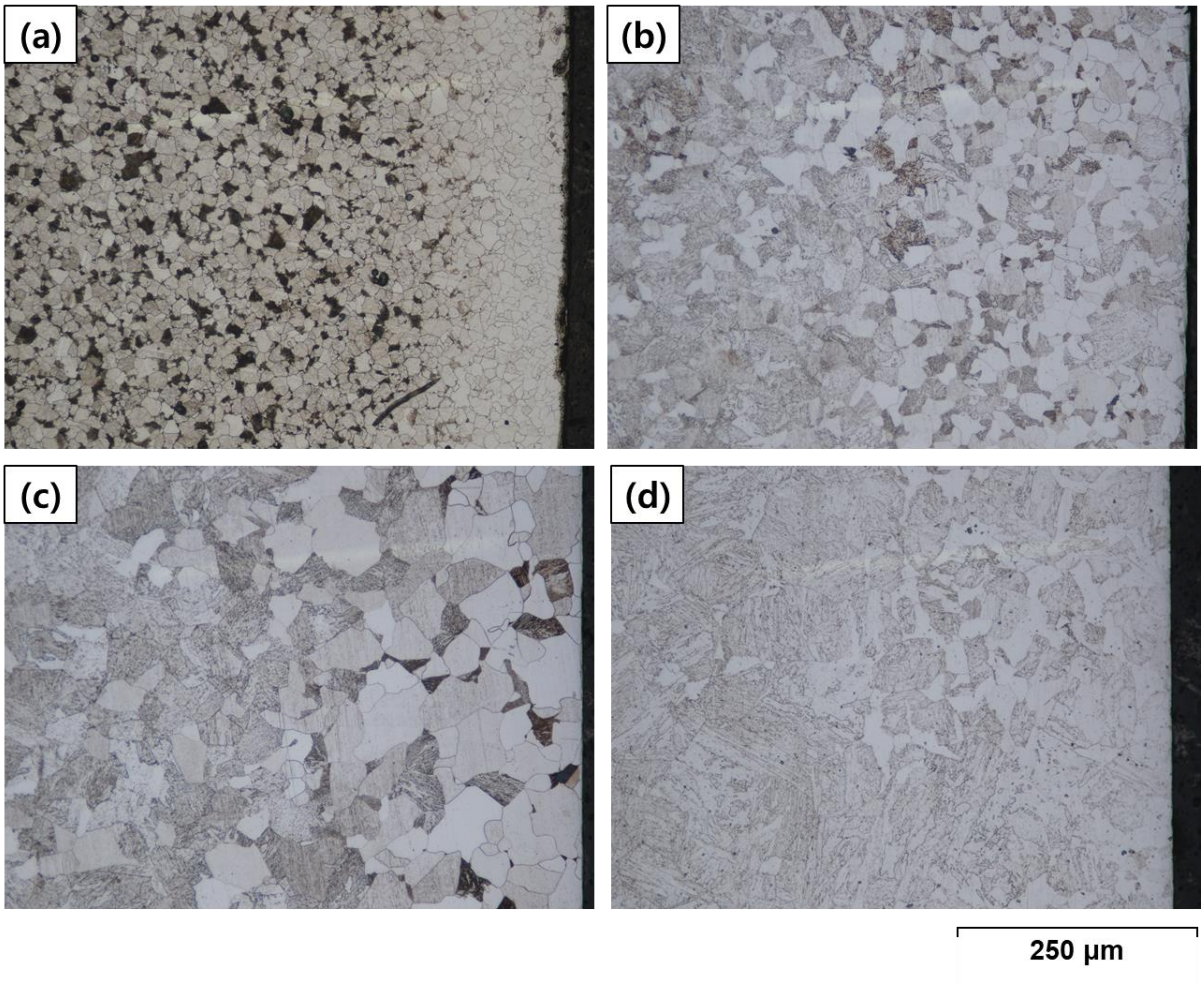

Figure 5.38. Microstructure of (a) P22, (b) FRA1, (c) FRA2, and (d) MFRA in surface region

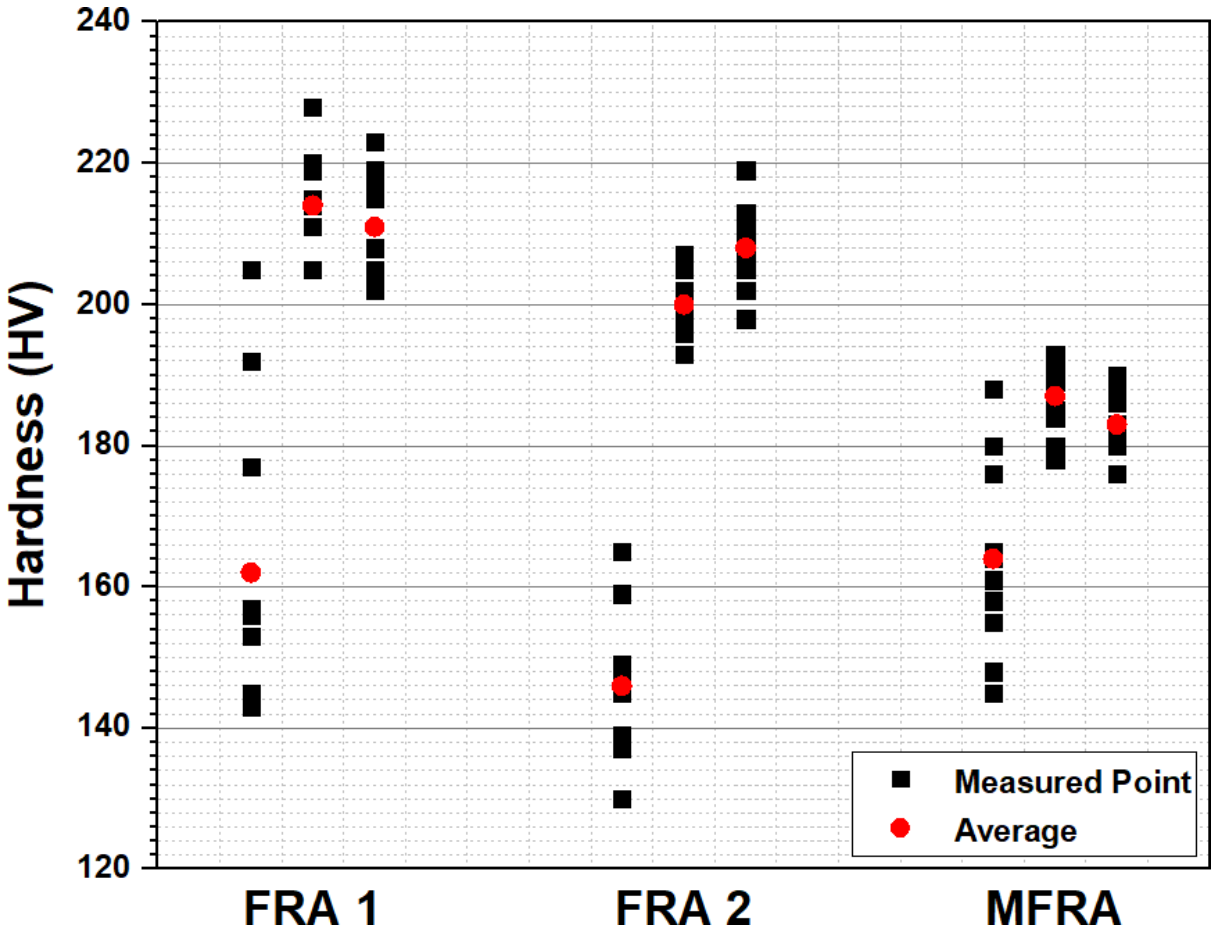

Figure 5.39. Vicker's hardness measurement results of the alloys – black scatters are measured points and red scatters are average of the region

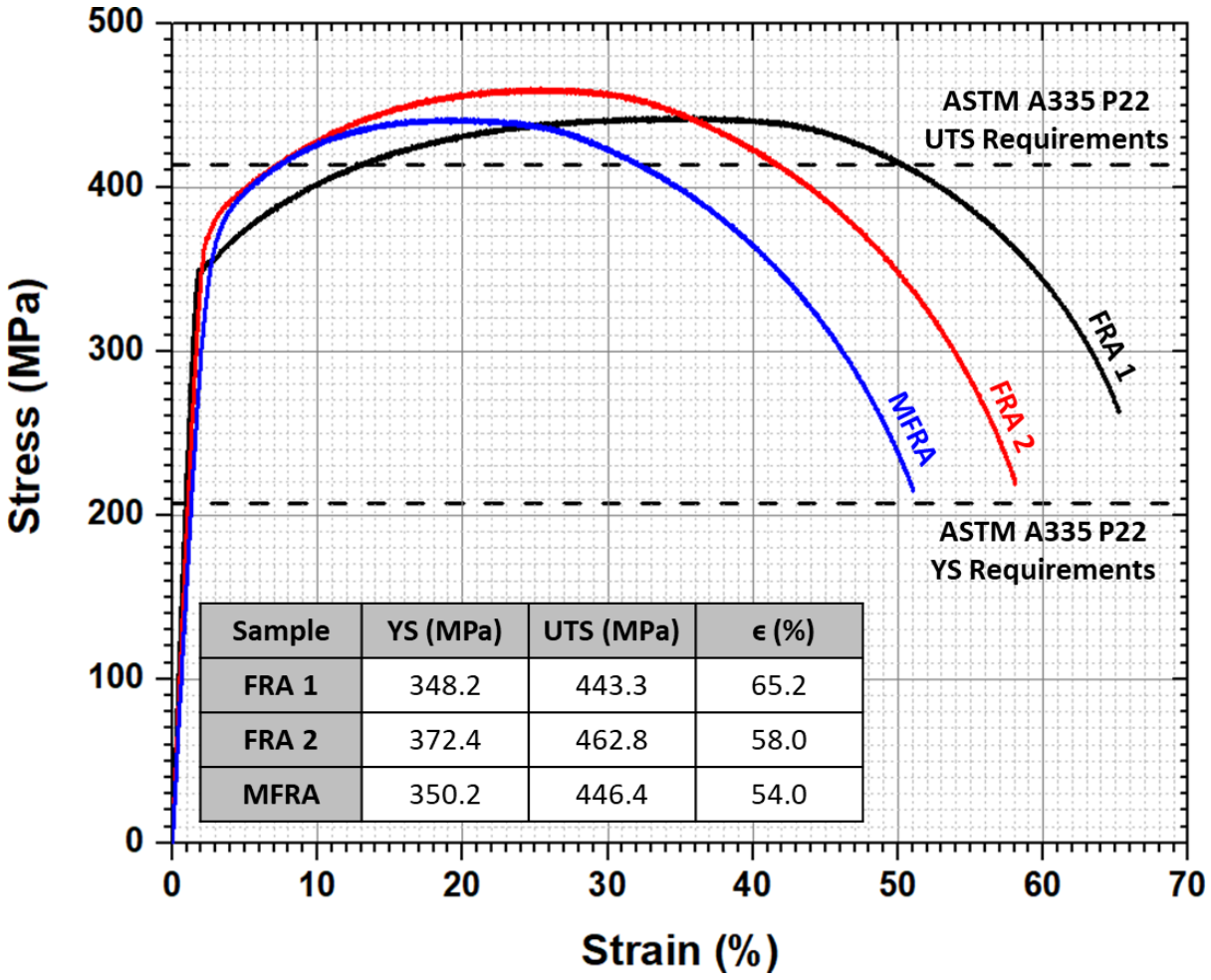

Sample	YS (MPa)	UTS (MPa)	ϵ (%)
FRA 1	348.2	443.3	65.2
FRA 2	372.4	462.8	58.0
MFRA	350.2	446.4	54.0

Figure 5.40. Tensile test results of the alloys and the parameters

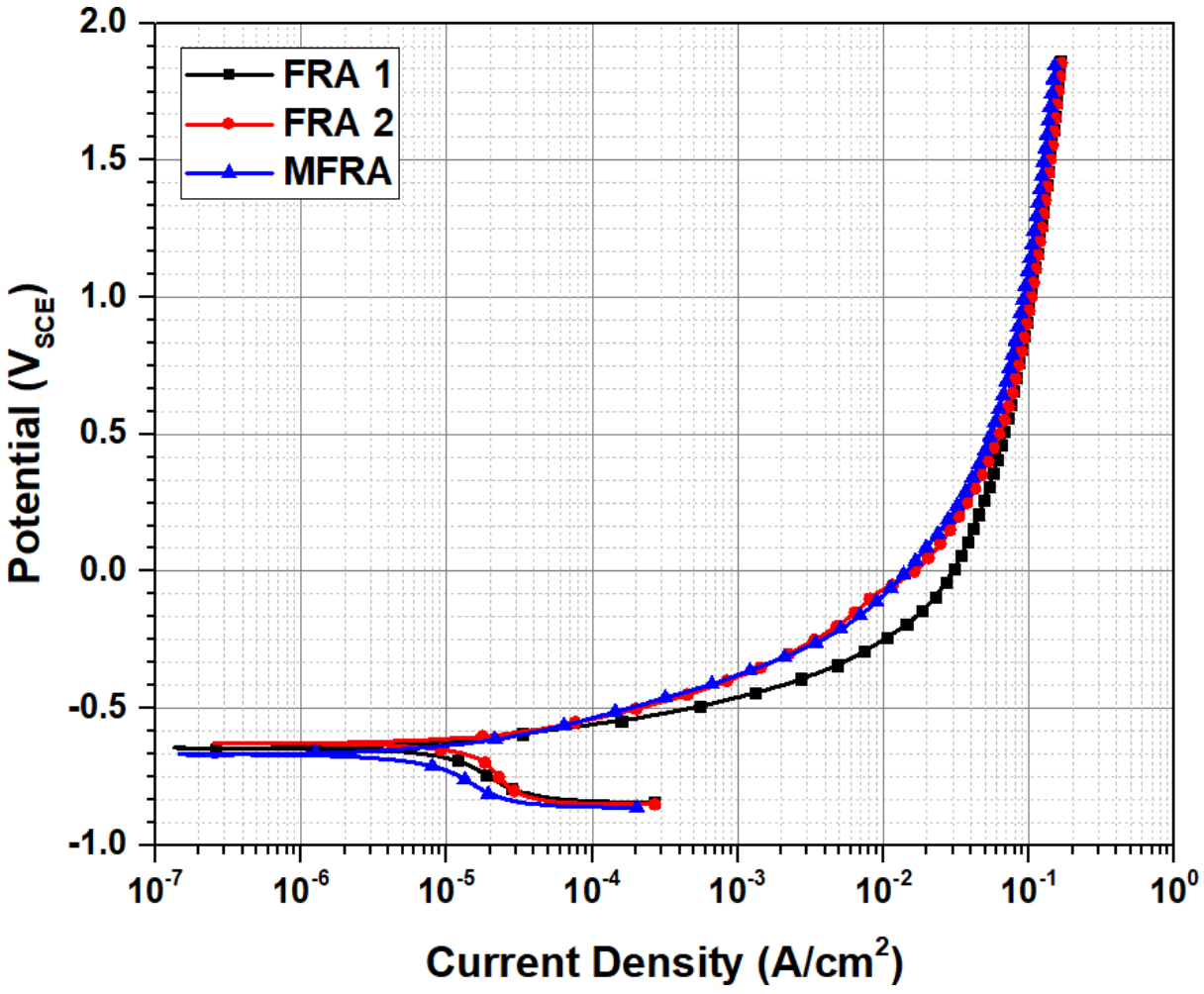

Figure 5.41. LSV results of FRA1, FRA2 and MFRA in seawater condition

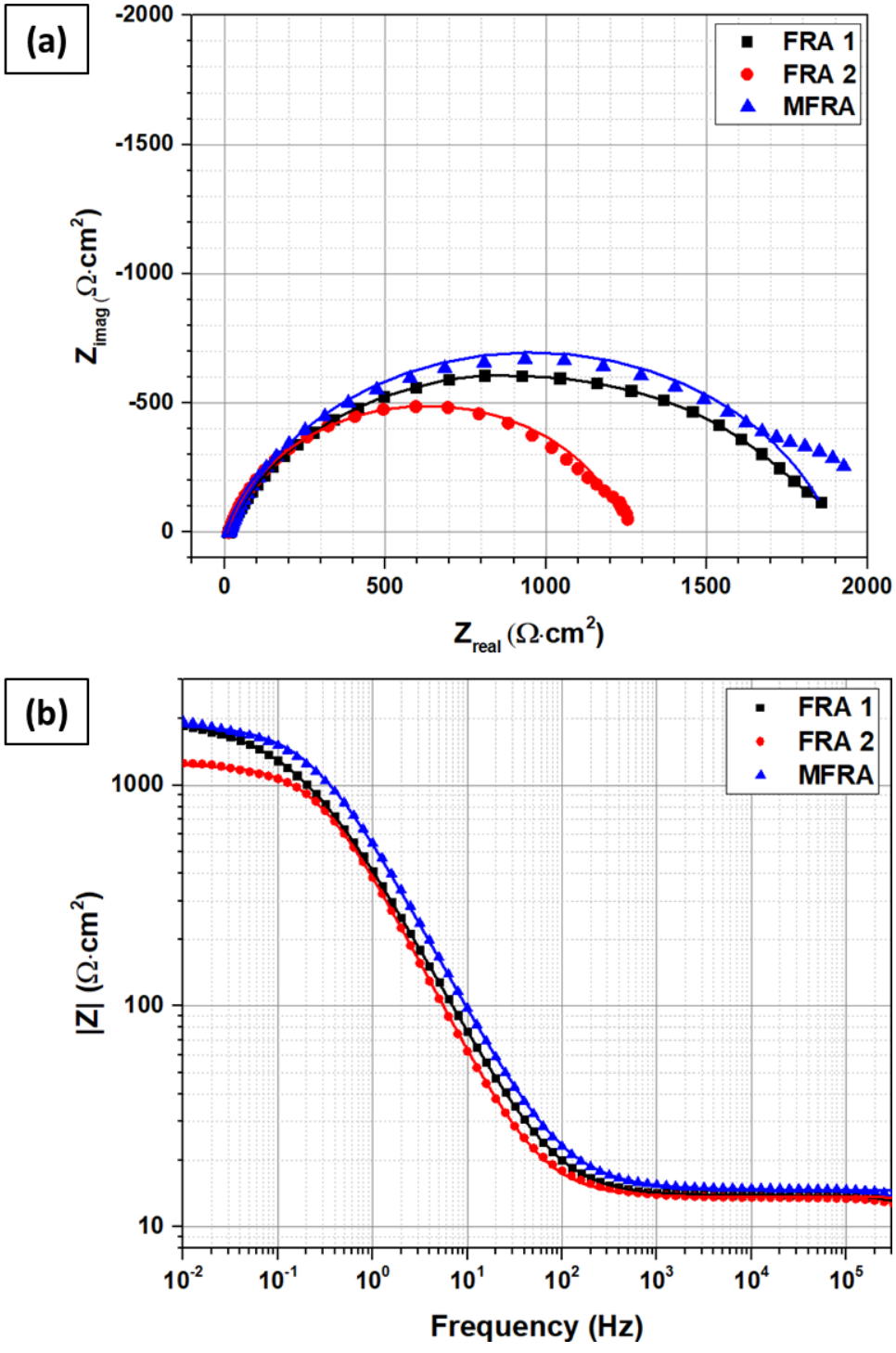

Figure 5.42. EIS results of FRA1, FRA2 and MFRA in seawater condition: (a) Nyquist plots (b) Bode plots

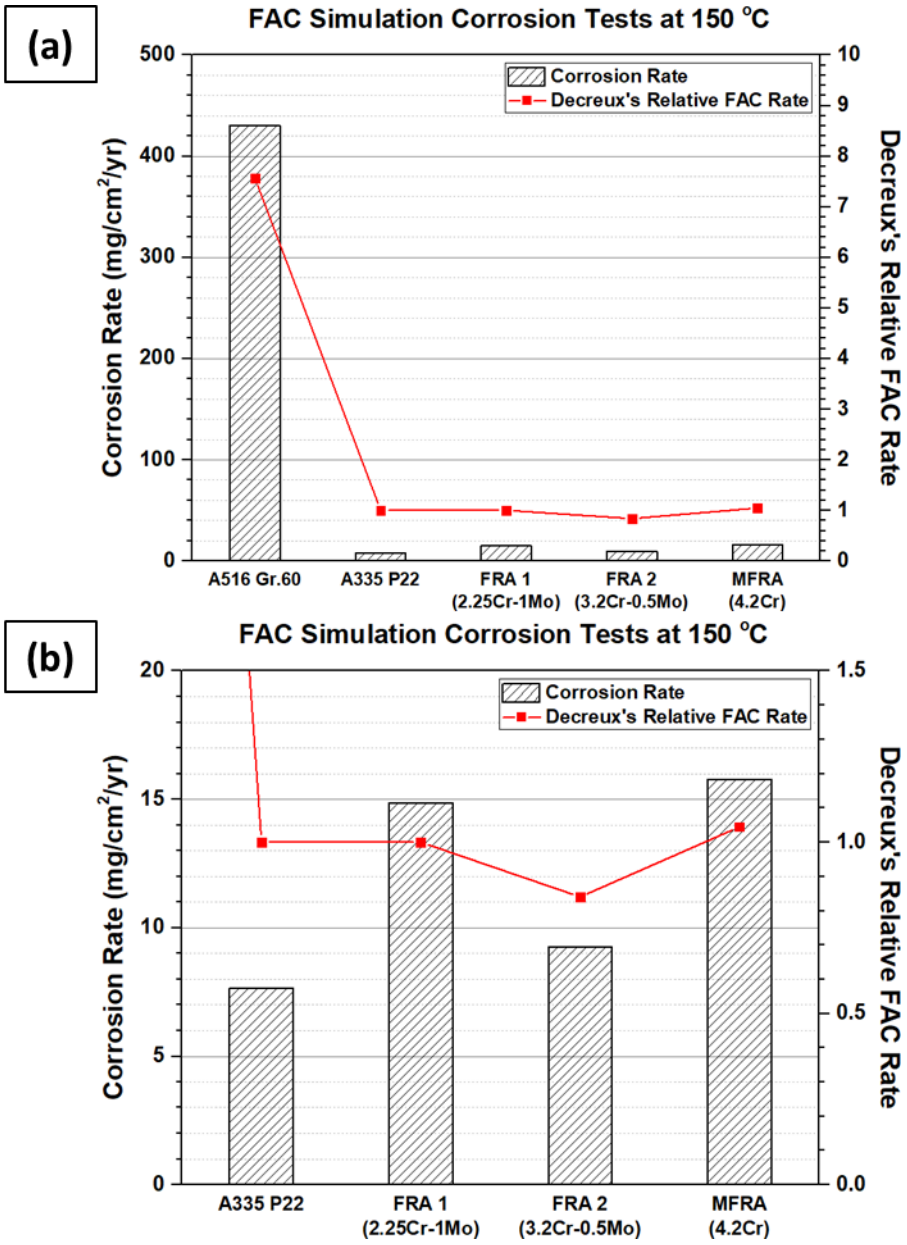

Figure 5.43. Weight loss of CS, P22, FRA 1, FRA 2, MFRA after FAC simulation tests at deaerated 150 °C, 10 MPa, and pH_{25} 9.3 water for 14 days (a) with and (b) without that of CS

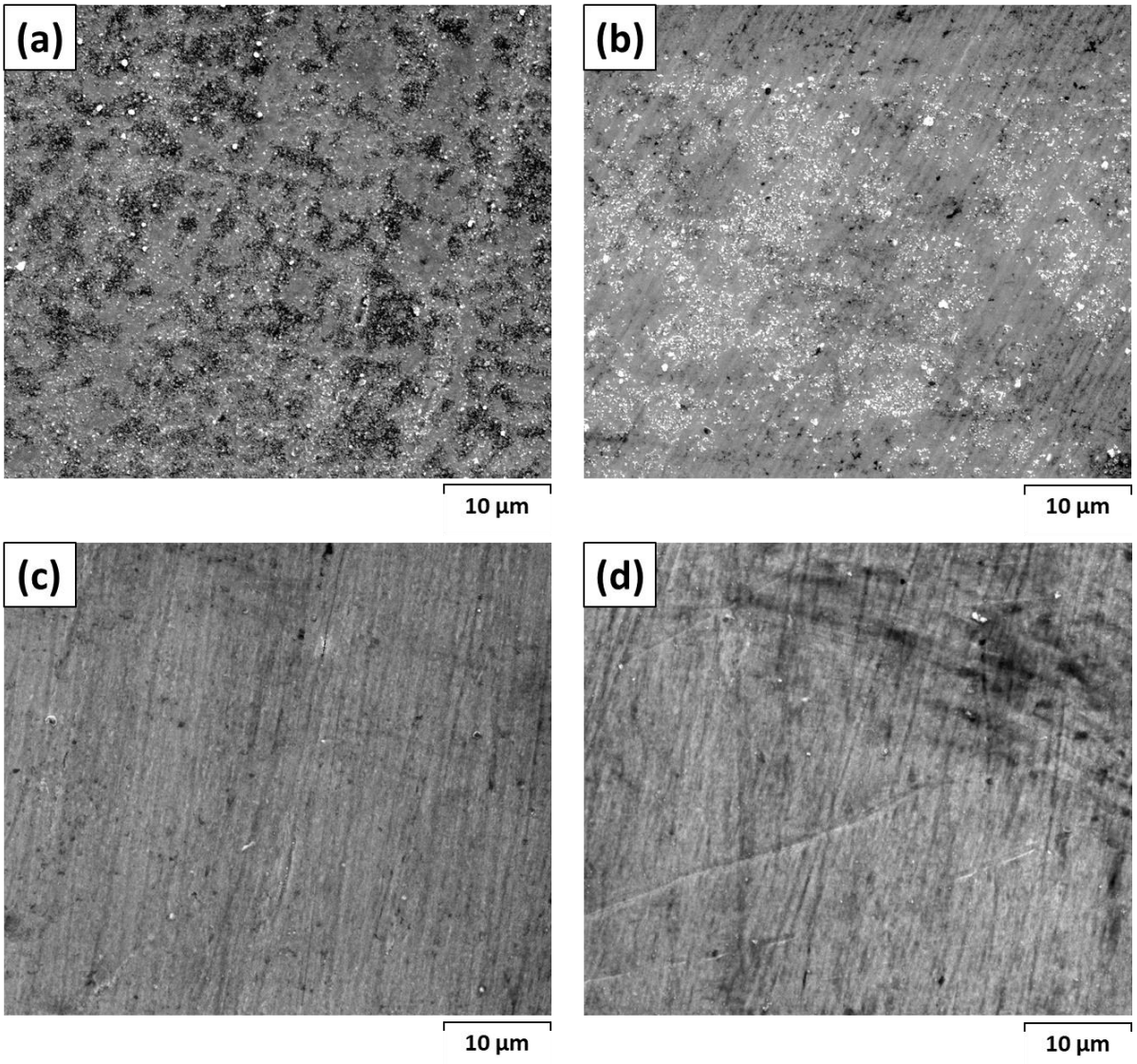

Figure 5.44. SEM surface morphologies and EDS results of (a) P22, (b) FRA 1, (c) FRA 2, and (d) MFRA after FAC simulation tests at deaerated 150 °C, 10 MPa, and pH_{25} 9.3 water for 14 days

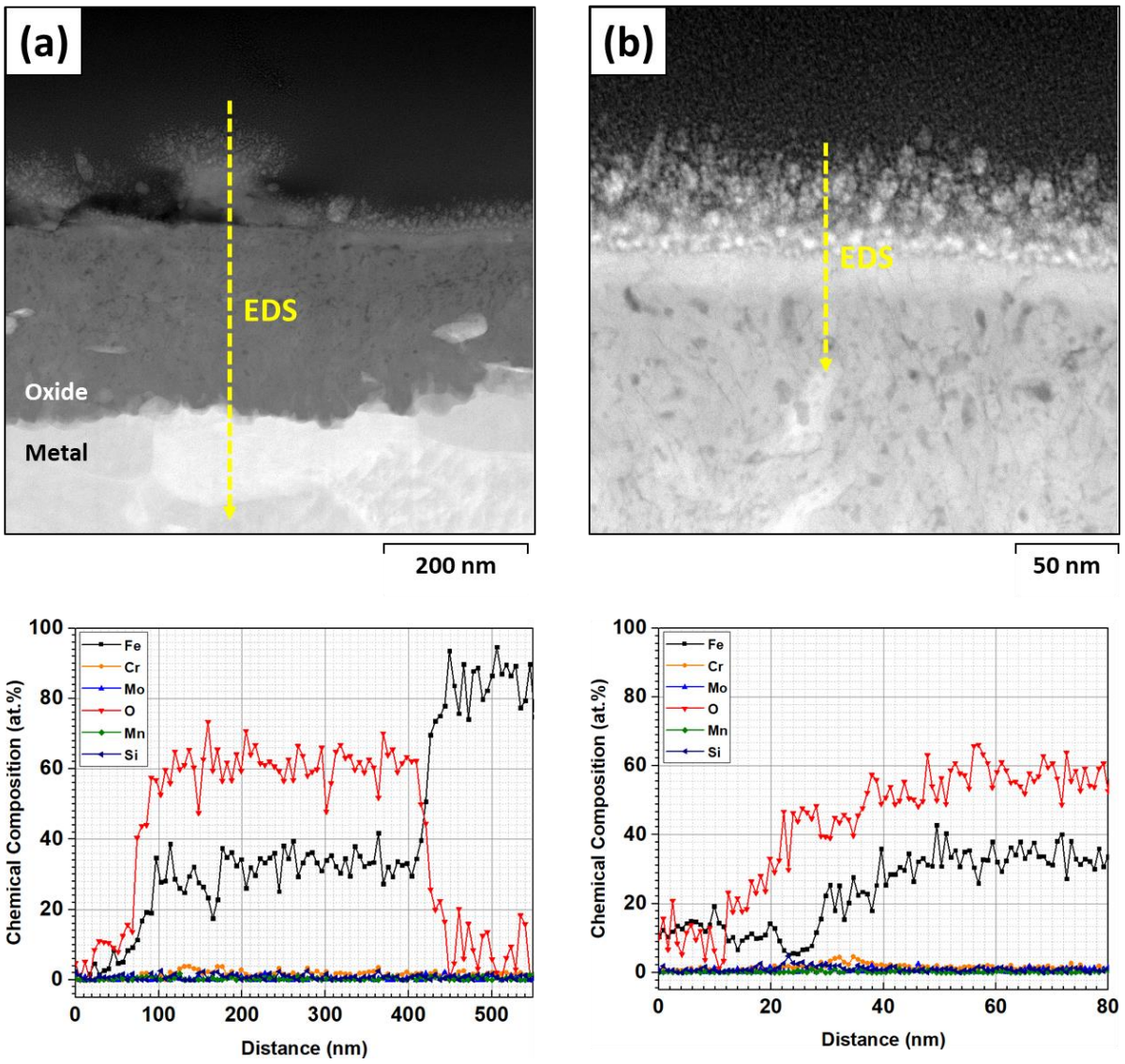

Figure 5.45. STEM CX morphologies and EDS results of P22: (a) overall oxide, (b) topmost oxide

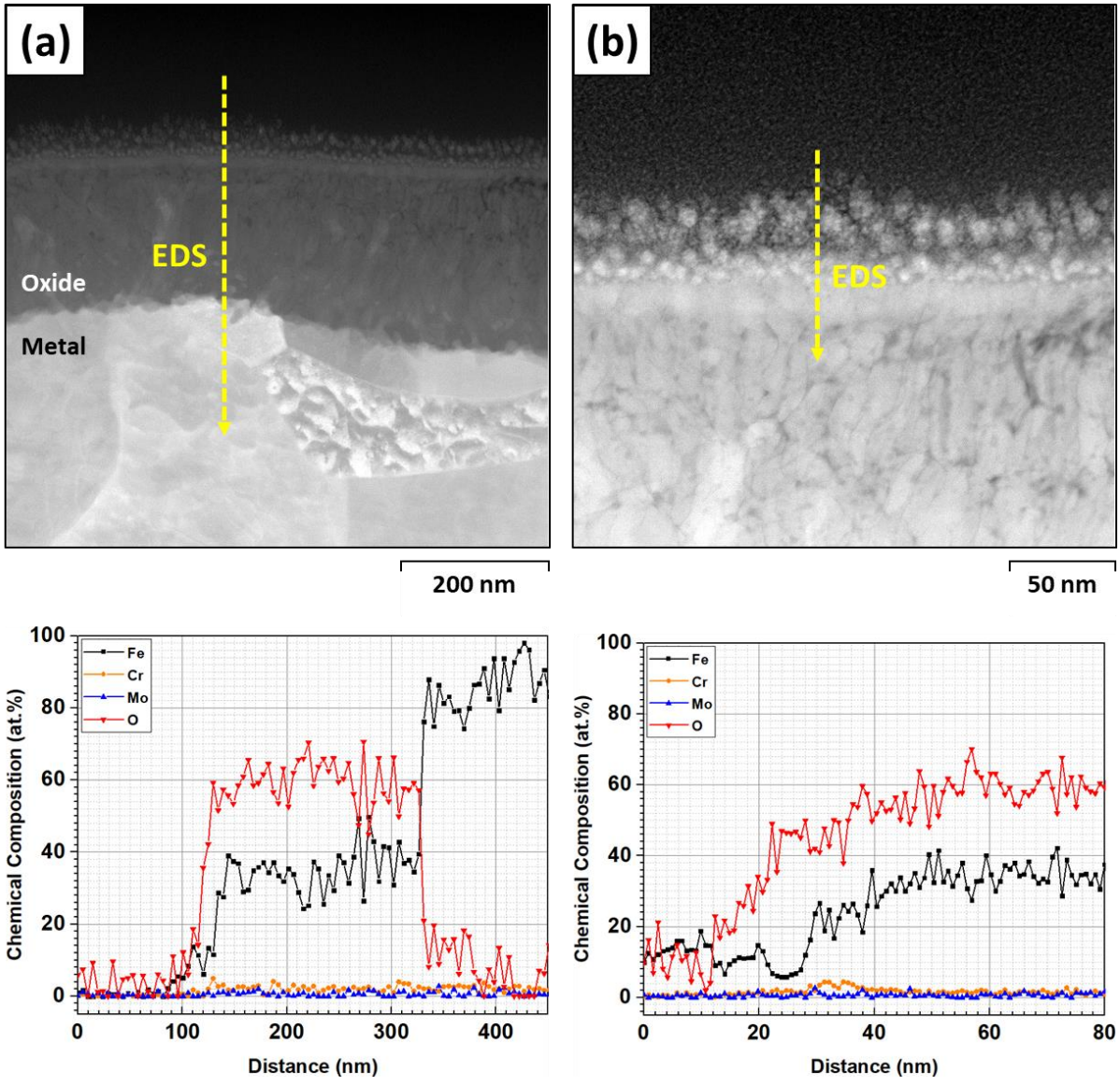

Figure 5.46. STEM CX morphologies and EDS results of FRA 1: (a) overall oxide, (b) topmost oxide

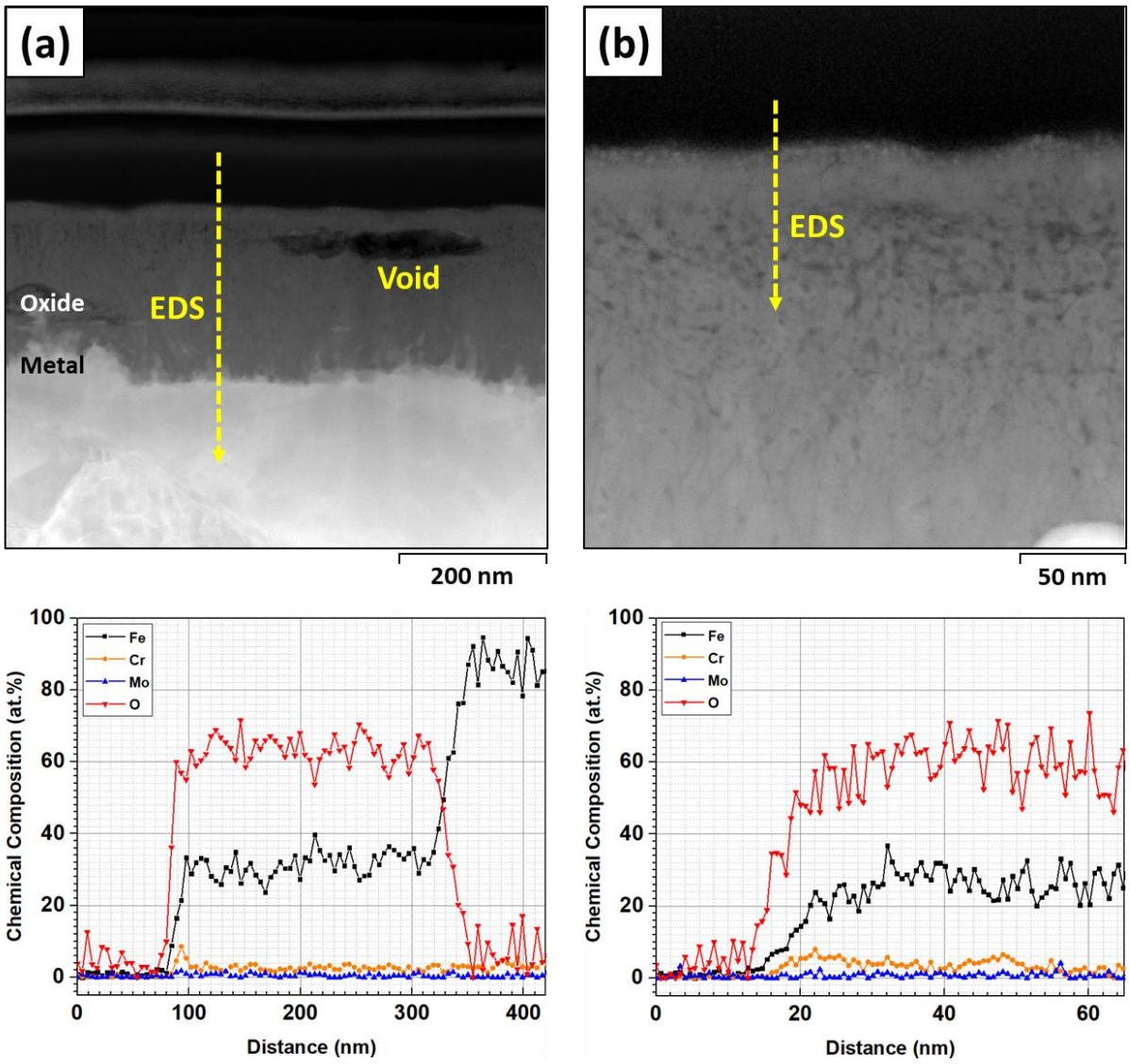

Figure 5.47. STEM CX morphologies and EDS results of FRA 2: (a) overall oxide, (b) topmost oxide

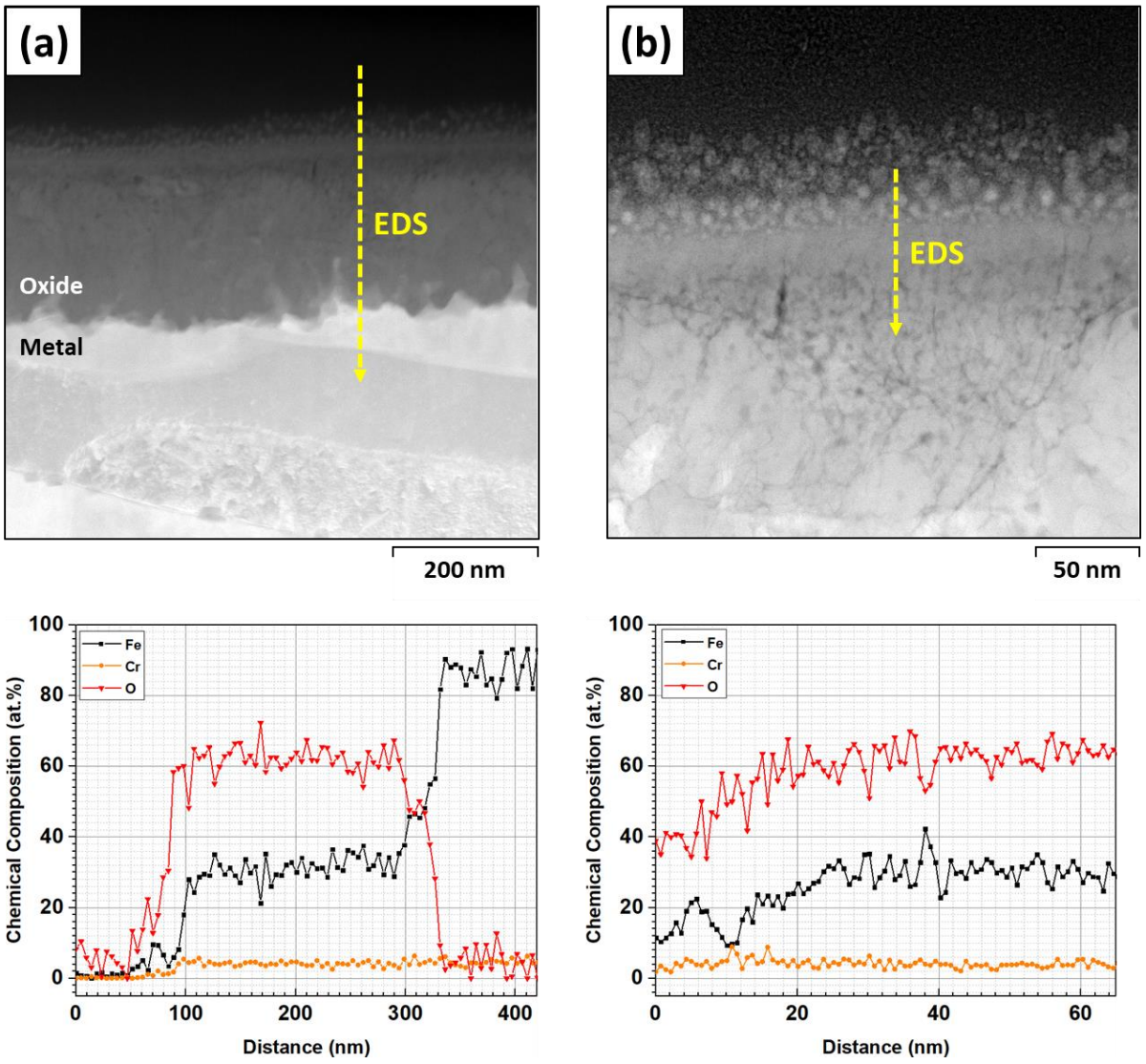

Figure 5.48. STEM CX morphologies and EDS results of MFRA: (a) overall oxide, (b) topmost oxide

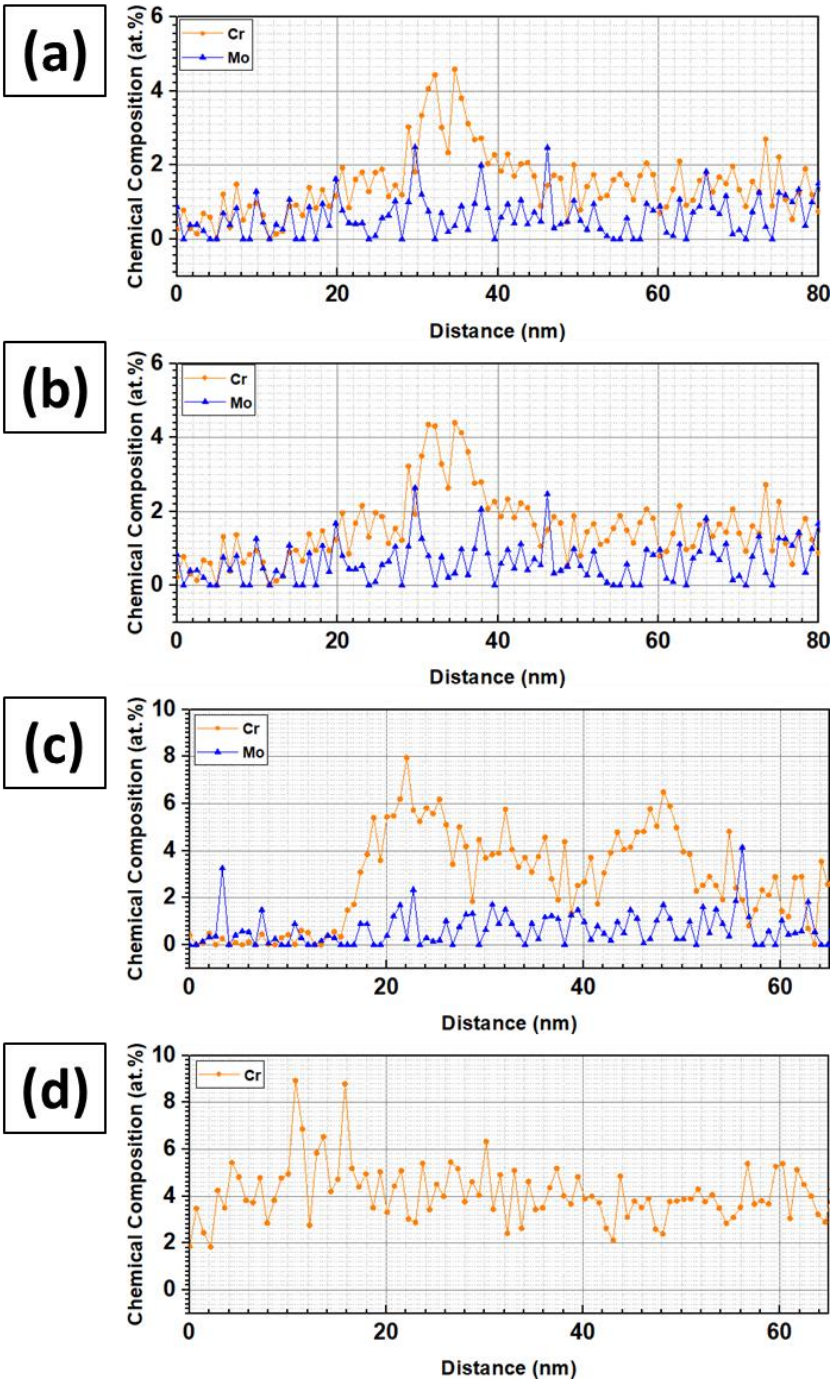

Figure 5.49. Enlarged EDS chemical composition of Cr and Mo of the alloys: (a) P22, (b) FRA 1, (c) FRA 2, and (d) MFRA

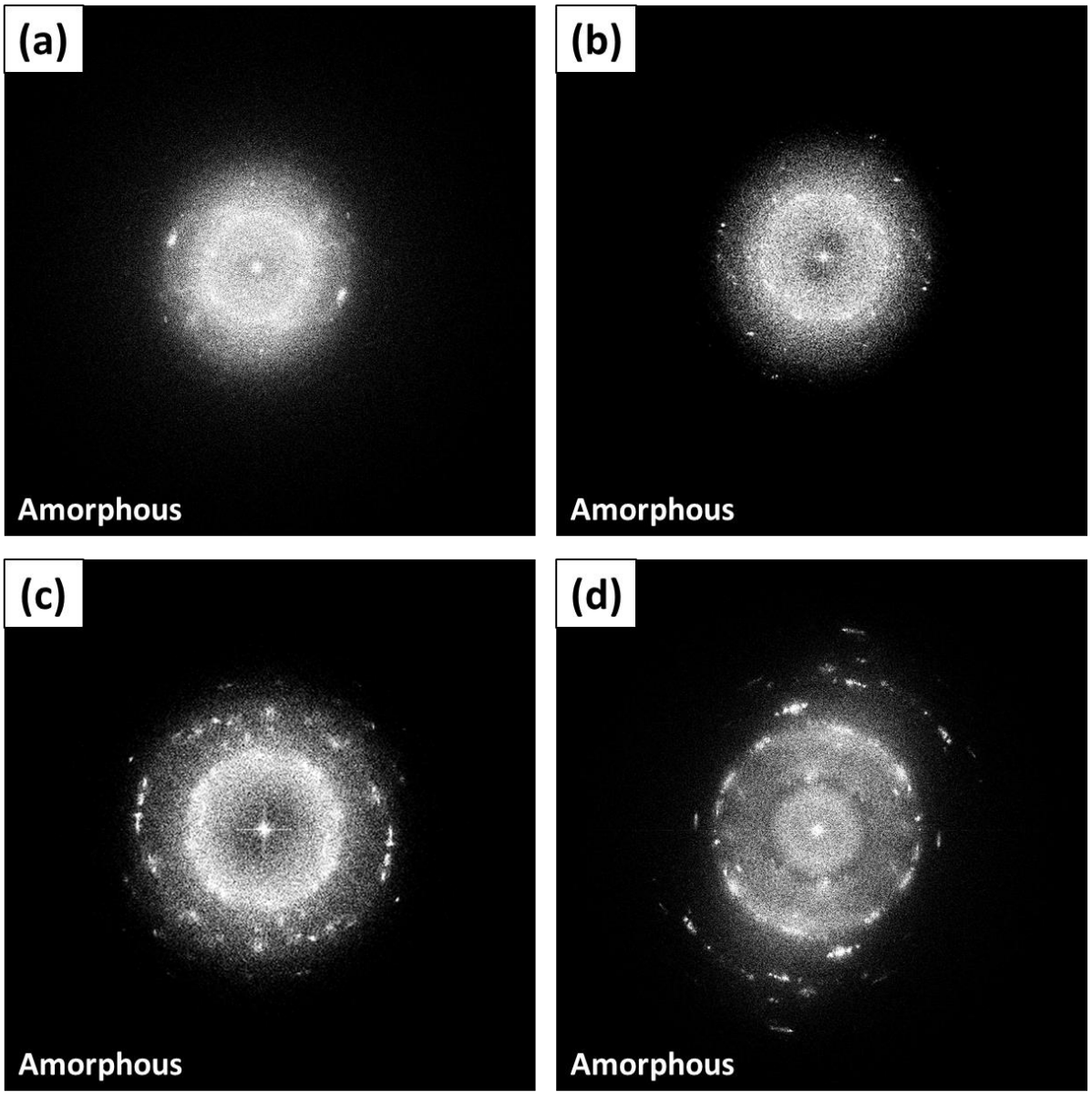

Figure 5.50. Electron DP on the compact oxide layer of the alloys: (a) P22, (b) FRA 1, (c) FRA 2, and (d) MFRA

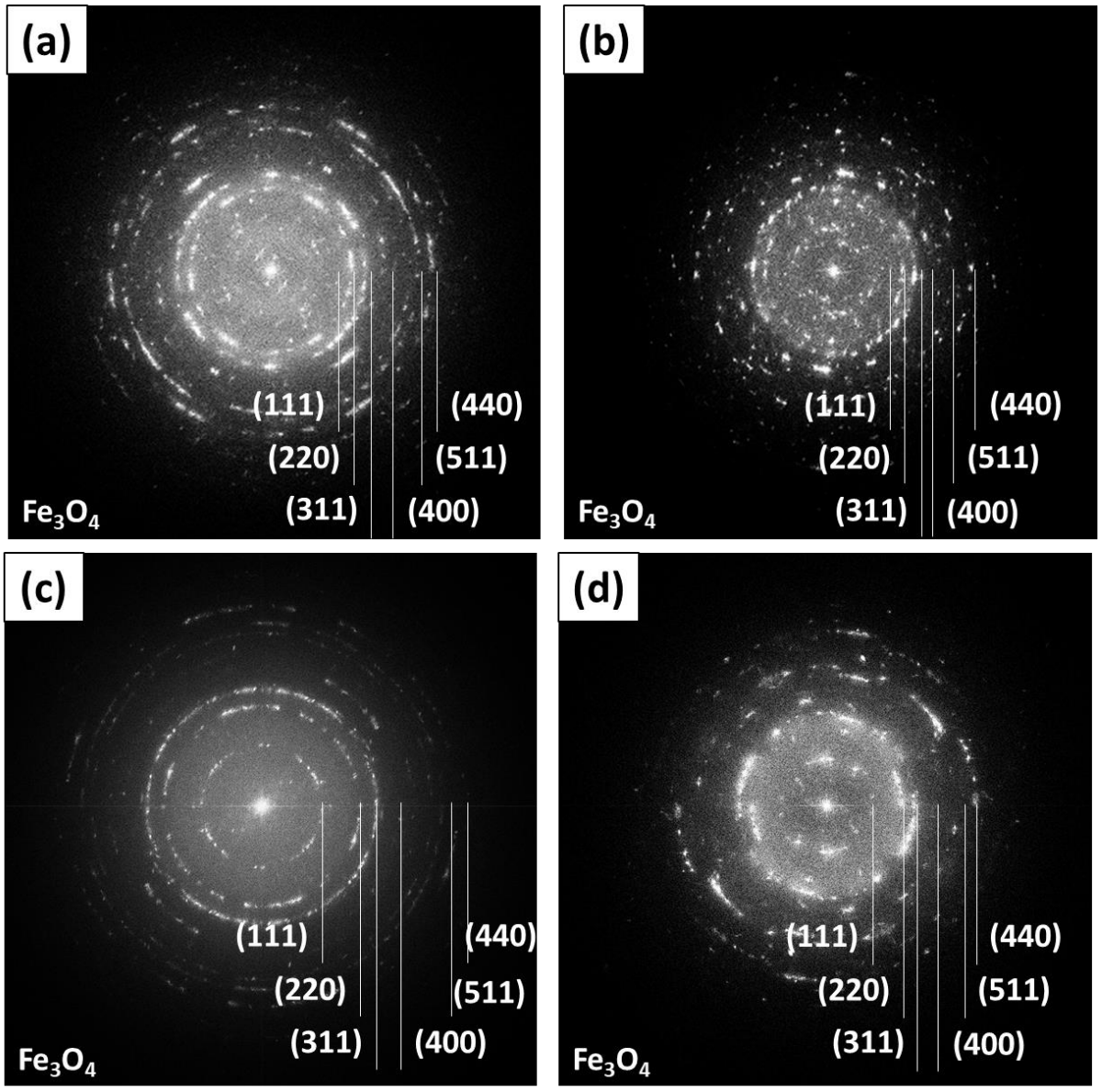

Figure 5.51. Electron DP on the bulk oxide of the alloys: (a) P22, (b) FRA 1, (c) FRA 2, and (d) MFRA

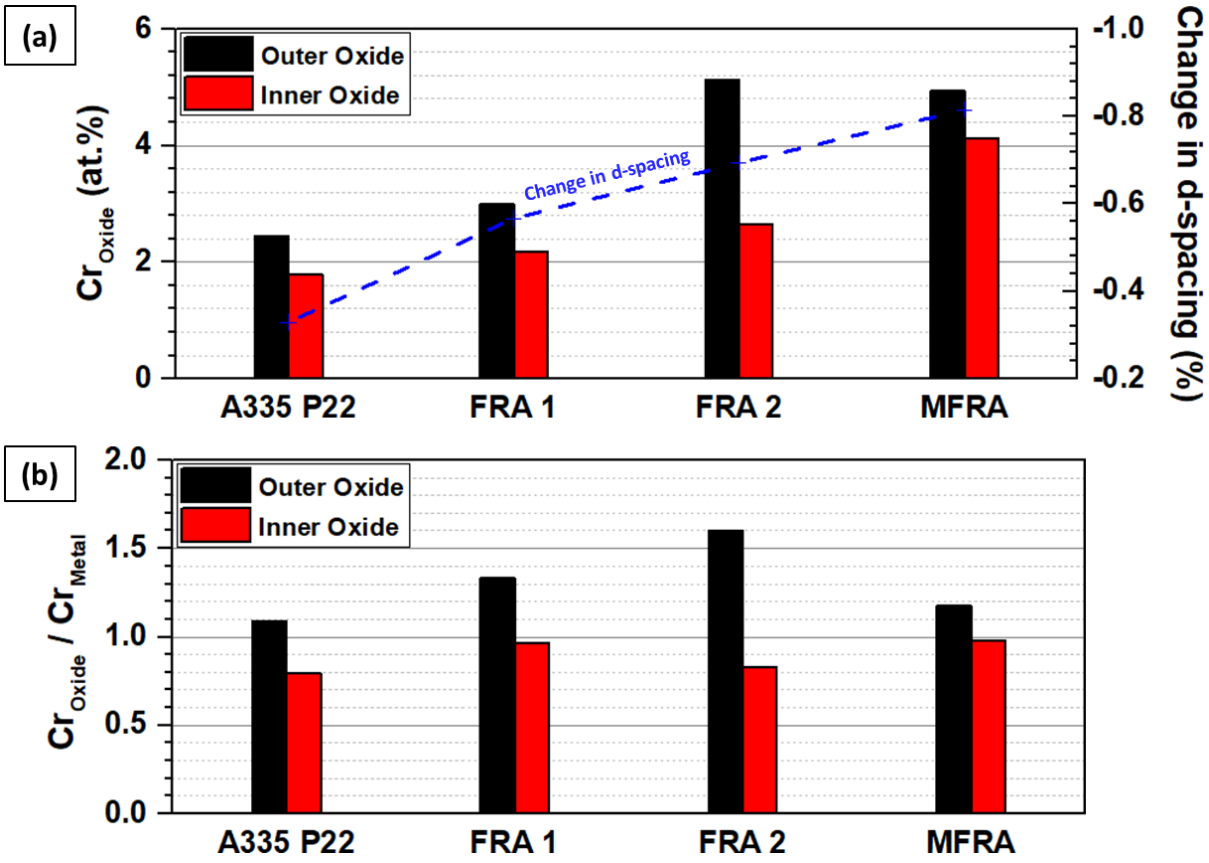

Figure 5.52. (a) Cr contents in the oxides of P22, FRA 1, FRA 2, and MFRA and their correlation with change in d-spacing, (b) the ratio of Cr contents in the oxide and the metals of P22, FRA 1, FRA 2, and MFRA

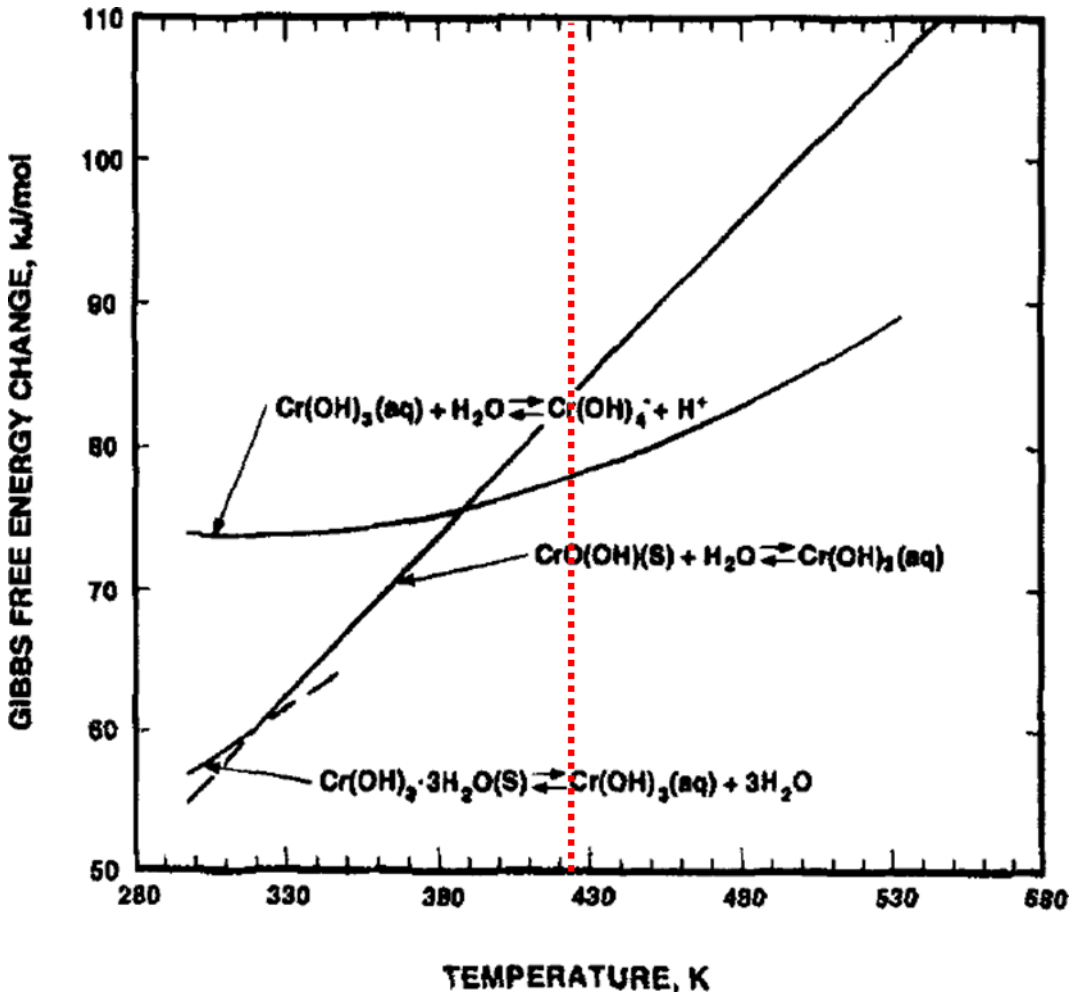

Figure 5.53. Gibbs free energy change during the oxidation of Cr species in high temperature water [126]

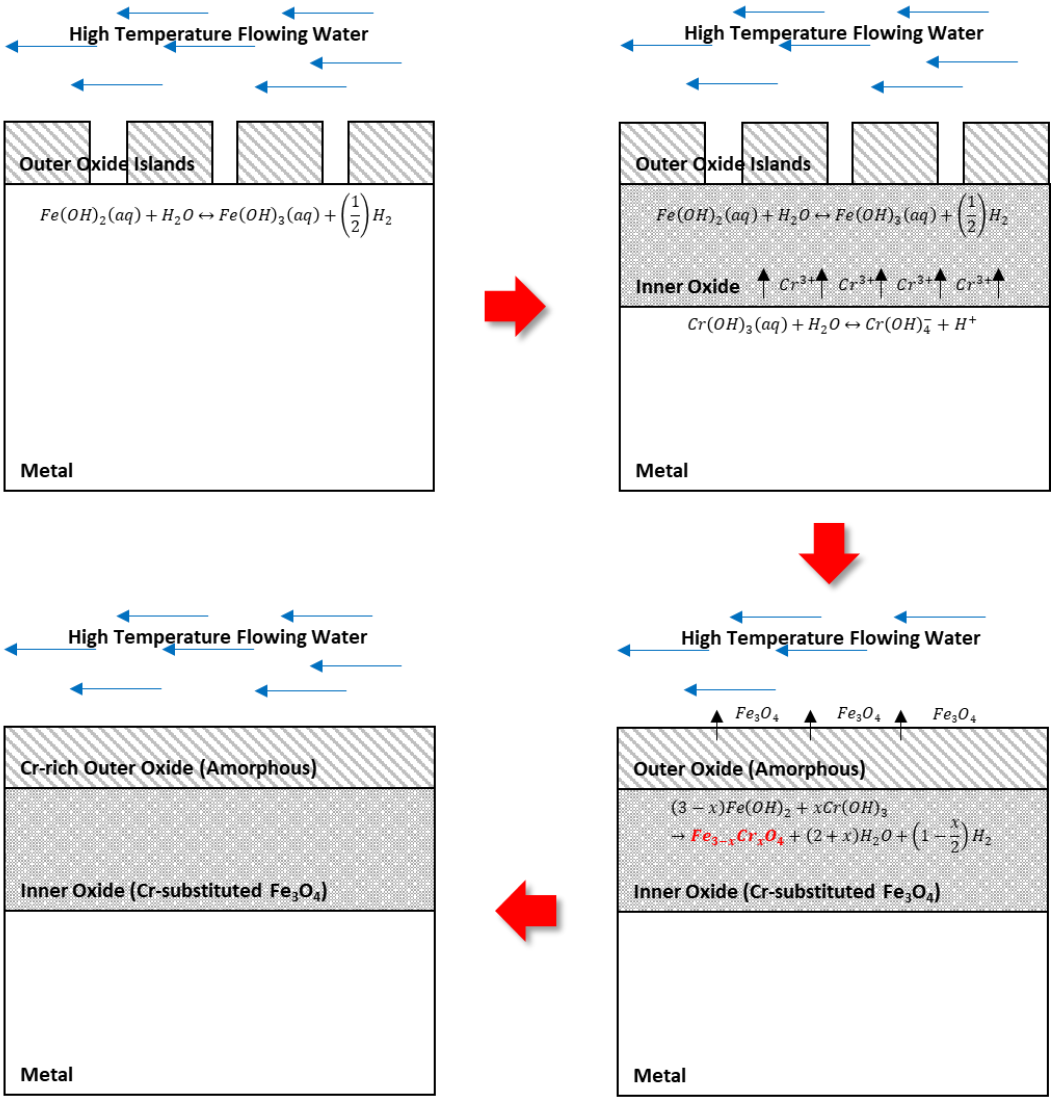

Figure 5.54. FAC mechanism of LAS with different Cr and Mo contents in high-temperature flowing water

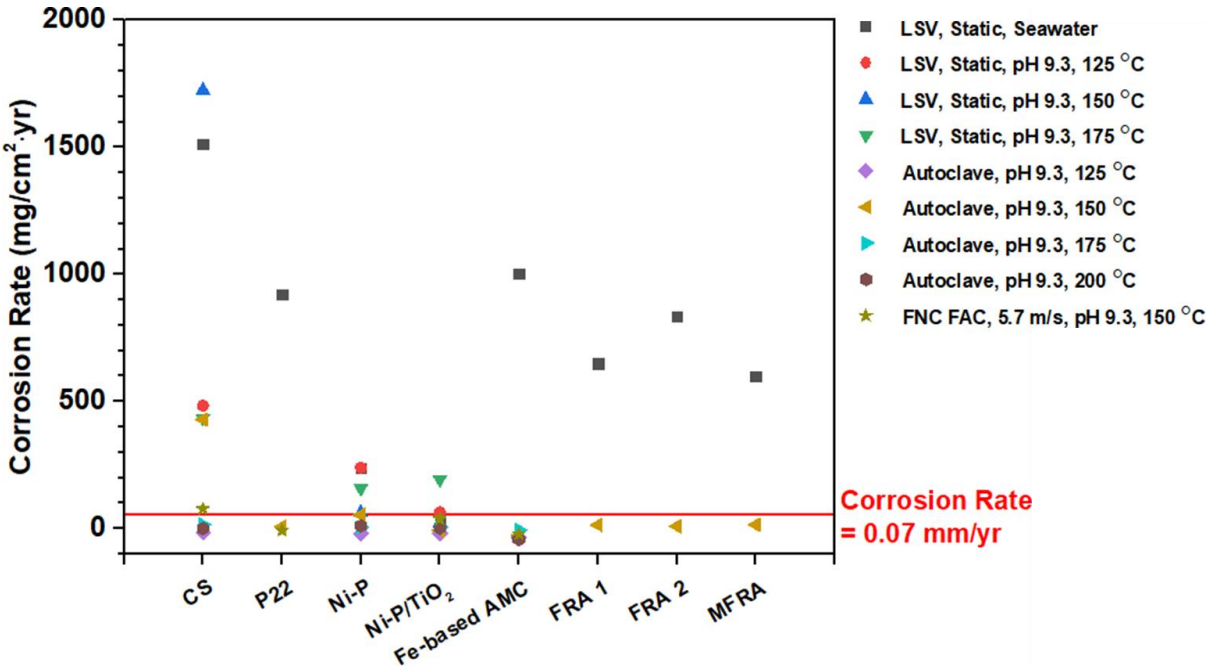

Figure 5.55. The corrosion rate of the commercial alloys, the E-C resistive coatings and alloys in FAC favored condition

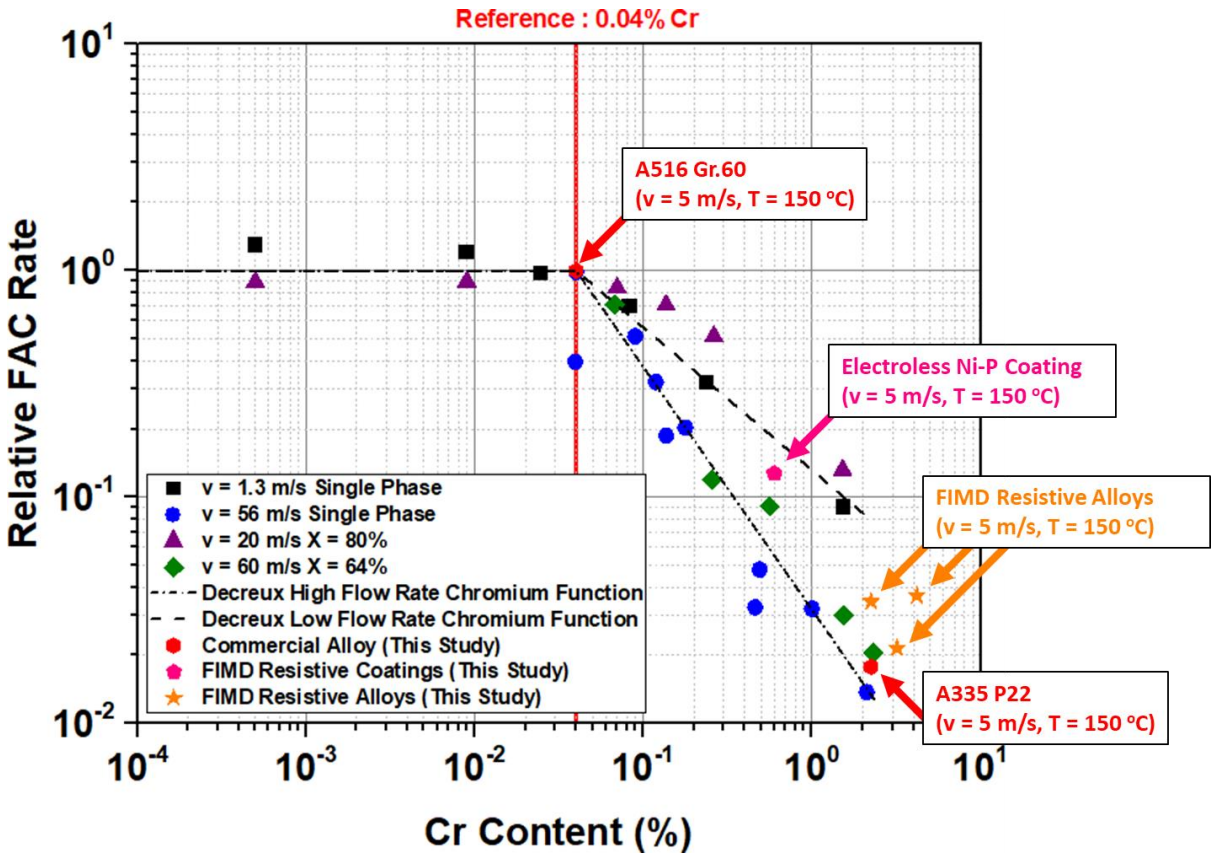

Figure 5.56. Comparison with Decrreux's high and low flow rate model and EDF CIROCO experimental data (Reproduced from [37])

VI. CONCLUSION

In this study, to mitigate or prevent FAC, resistive coatings (Ni-P/TiO_2 and Fe-based AMC) and alloys (FRA 1, FRA 2, and MFRA) have been designed and manufactured and their performance is evaluated by multiple techniques.

- FAC behavior of CS and LAS is investigated under various condition. In FAC simulation condition with different temperature variations, it can be concluded that the susceptibility of CS is due to the formation of porous magnetite, which could be easily dissolved into flowing water. Contrarily, LAS forms Cr-substituted magnetite layer at the interface thus it can successfully resist to E-C
- To design FAC resistive coatings, thermodynamic stability, and corrosion-, erosion, and wear-resistance of materials have been considered. As candidate materials, Ni-P/TiO_2 coating and Fe-based AMC is chosen.
- In seawater condition, Ni-P/TiO_2 coating shows remarkable corrosion resistance compared to CS and Ni-P due to the galvanic coupling between Ni-P bulk matrix and noble TiO_2 nanoparticles. However, Fe-based AMC is susceptible to seawater corrosion due to intrinsic surface area, defects, and morphology.
- In simulated secondary water chemistry, electrochemical behavior of Ni-P/TiO_2 is also remarkable compared to Ni-P at 150 ^oC. However, at 125 and 175 ^oC, Ni-P coating also possesses excellent corrosion resistance. This is due to the electrochemical property of TiO_2 is not activated at those temperature.
- FAC simulation tests are performed using secondary water chemistry control system and a magne-drive installed autoclave system. The test conditions are: temperature 125-150 ^oC, < 1 ppb DO, pH 9.3, ETA controlled. CS follows bell-shaped curves where the peak corrosion rate is 150 ^oC. The corrosion rate of LAS is 1/9 of CS. Ni-P and Ni-P/TiO_2 coating are effectively suppress the corrosion but, at 150 ^oC, the peeling-off of the oxide is observable for Ni-P while Ni-P/TiO_2 is stable. The CX morphologies confirms that this is due to galvanic coupling between Ni-P and TiO_2 nanoparticles. Fe-based AMC shows weight gain in all temperature due to the formation of thick oxide.
- FAC simulation results of FRA 1, FRA 2, and MFRA show that the corrosion rate follows Ducreux's model. This confirms that Cr could substitute Mo. All the alloy possesses two-layer oxide structure: Cr-rich amorphous outer layer and Cr-substituted bulk oxide layer. Since Cr contents at the outer oxide layer determines corrosion rate, it can be concluded that MFRA can be a good countermeasure for commercial LAS. However, degradation in mechanical property

especially hardness and elongation presents in MFRA.

- UT results from CS, LAS, and coated 90 ºC experiments show that severe corrosion is observable especially at intrados of CS, and Ni-P/TiO_2. Morphologies confirms that this is due to severe corrosion at intrados. However, P22 and Fe-based AMC is not corroded under 5.7 m/s flow condition. Thus, Fe-based AMC is effective in erosion favored condition.

VII. SUMMARY

Structural materials in secondary system of commercial NPPs undergoes severe degradation so called E-C. Many studies have substantially studied its form, mechanism, and case study to understand and acknowledge its fundamental but still clear countermeasures have not been developed. These days, E-C is being managed by NDE and commercial software but it is unable to solve materials challenge.

In this study, various E-C resistive coatings and alloys are developed and their performance is evaluated in simulated secondary water chemistry. As candidate materials, ENP Ni-P/TiO_2, and Fe-based AMC are chosen owing to their excellence corrosion and wear resistance. Also, based on Ducreux's relative FAC model, three FRAs are designed with different Cr and Mo contents. The model inspired that Mo can be substituted by higher Cr rate. In simulated secondary water chemistry, Ni-P/TiO_2 coating shows better corrosion resistance than Ni-P due to galvanic coupling between Ni-P matrix and the nanoparticle. However, it is not corrosion resistive according to high flow rate FAC test. In case of Fe-based AMC, it is not corrosion resistive in seawater condition but its performance in FAC condition is promising. Three FRAs show outstanding FAC resistance in simulated secondary water chemistry. As Cr content increases, the Cr content in the oxide layer increases. Until now, the chemistry of the oxide is known as $FeCr_2O_4$ but microstructure and chemical analysis gives that the chemistry of the oxide is Cr-substituted Fe_3O_4. Also, the role of Mo in alkaline water chemistry is not clearly observed but it aids the passivity of FRAs.

Based on this study, it is able to replace commercial alloys -both CS and LAS- in operating NPPs since the replacement of material is relatively not time- and energy-consuming compared to the modification of water chemistry factor. Also, the findings in this study especially corrosion behavior of various alloys (Ni, Fe-Cr-Mo, *etc.*) in high-temperature flowing water can be either directly or indirectly expand a viewpoint on the materials degradation in coolant transportation system.

VIII. REFERENCES

[1] S. J. Zinkle and G. S. Was, "Materials challenges in nuclear energy," *Acta Materialia,* vol. 61, no. 3, pp. 735-758, 2// 2013.

[2] I. S. Kim, M. V. D. Helm, and R. G. Ballinger, "Flow induced material degradation in power plant secondary systems - a review," *Journal of the Korean Nuclear Society,* vol. 30, no. 2, pp. 148-163, 1998.

[3] B. Poulson, "Predicting and Preventing Flow Accelerated Corrosion in Nuclear Power Plant," *International Journal of Nuclear Energy,* vol. 2014, p. 23, 2014, Art. no. 423295.

[4] V. Kain, S. Roychowdhury, P. Ahmedabadi, and D. K. Barua, "Flow accelerated corrosion: Experience from examination of components from nuclear power plants," *Engineering Failure Analysis,* vol. 18, no. 8, pp. 2028-2041, 2011/12/01/ 2011.

[5] H. M. Crockett and J. S. Horowitz, "Erosion in Nuclear Piping Systems," *Journal of Pressure Vessel Technology,* vol. 132, no. 2, pp. 024501-024501-3, 2010.

[6] S. Trevin, "7 - Flow accelerated corrosion (FAC) in nuclear power plant components," in *Nuclear Corrosion Science and Engineering*, D. Féron, Ed.: Woodhead Publishing, 2012, pp. 186-229.

[7] F. H. Sweeton and C. F. Baes Jr, "The solubility of magnetite and hydrolysis of ferrous ion in aqueous solutions at elevated temperatures," *The Journal of Chemical Thermodynamics,* vol. 2, no. 4, pp. 479-500, 7// 1970.

[8] P. Tremaine and J. LeBlanc, "The solubility of magnetite and the hydrolysis and oxidation of Fe2+ in water to 300°C," (in English), *Journal of Solution Chemistry,* vol. 9, no. 6, pp. 415-442, 1980/06/01 1980.

[9] P. R. Tremaine, R. V. Masscow, and G. R. Shierman, "A calculation of gibbs free energies for ferrous ions and the solubility of magnetite in H2O and D2O to 300°C," *Thermochimica Acta,* vol. 19, no. 3, pp. 287-300, 1977/06/01 1977.

[10] S. E. Ziemniak, M. E. Jones, and K. E. S. Combs, "Magnetite solubility and phase stability in alkaline media at elevated temperatures," *Journal of Solution Chemistry,* journal article vol. 24, no. 9, pp. 837-877, 1995.

[11] J. W. Kim, S. H. Lee, and C. Y. Park, "Experimental evaluation of the effect of local wall thinning on the failure pressure of elbows," *Nuclear Engineering and Design,* vol. 239, no. 12, pp. 2737-2746, 12// 2009.

[12] H. K. Seo, "Characteristics and evaluation techniques about cavitation and flashing on the nuclear power plants piping system," *Corrosion Science and Technology,* vol. 11, no. 1, pp. 20-25, 2012.

[13] S.-M. Hong *et al.*, "Cavitation erosion behavior of SA 106B carbon steel after treatment of the melt with nano-sized TiC particles," *Tribology International,* vol. 92, pp. 585-594, 2015/12/01/

2015.

[14] T. Shakouchi, K. Kinoshita, K. Tsujimoto, and T. Ando, "Flow-Accelerated Corrosion in Pipe Wall Downstream of Orifice for Water and Air-Water Bubble Flows," *Journal of Flow Control, Measurement & Visualization,* vol. 04, pp. 93-103, 2016.

[15] W. C. Nam, "Liquid Droplet Impingement Erosion Mechanism of Low-Alloy Steels in the Secondary Side of Pressurized Water Reactors," Ph. D., School of Energy Systems Engineering, Seoul National University, 2015.

[16] S. Uchida, M. Naitoh, H. Okada, T. Ohira, S. Koshizuka, and D. H. Lister, "Verification and Validation of Evaluation Procedures for Local Wall Thinning Due to Flow-Accelerated Corrosion and Liquid Droplet Impingement," *Nuclear Technology,* vol. 178, no. 3, pp. 280-297, 2012/06/01 2012.

[17] V. Kain, "Flow Accelerated Corrosion: Forms, Mechanisms and Case Studies," *Procedia Engineering,* vol. 86, pp. 576-588, 2014/01/01 2014.

[18] B. Villien, Y. Zheng, and D. Lister, "The scalloping phenomenon and its significance in flow-assisted-corrosion," presented at the Twenty Sixth Annual CNS-CNA Student Conference, Toronto, Ontario, Canada, 2018.

[19] P. Madasamy, H. Subramanian, T. V. Krishna Mohan, S. Velmurugan, E. Natarajan, and S. V. Narasimhan, "Experimental determination of flow accelerated corrosion in bend and straight sections of carbon steel primary coolant feeder pipes in pressurised heavy water reactor system," *Corrosion Engineering, Science and Technology,* vol. 46, no. 4, pp. 346-352, 2011/06/01 2011.

[20] Y. S. Lee, S. H. Lee, and K. M. Hwang, "Cause Analysis of Flow Accelerated Corrosion and Erosion-Corrosion Cases in Korea Nuclear Power Plants," *Corrosion Science and Technology,* vol. 15, no. 4, pp. 182-188, 2016.

[21] H. Kyeong Mo, "Cause Analysis for the Wall Thinning and Leakage of a Small Bore Piping Downstream of an Orifice " *Corrosion Science and Technology,* vol. 12, no. 5, pp. 227-232, 2013.

[22] J. L. Singh *et al.*, "Flow accelerated corrosion of carbon steel feeder pipes from pressurized heavy water reactors," *Journal of Nuclear Materials,* vol. 429, no. 1, pp. 226-232, 2012/10/01/ 2012.

[23] K. Fujiwara, M. Domae, K. Yoneda, F. Inada, T. Ohira, and K. Hisamune, "Correlation of flow accelerated corrosion rate with iron solubility," *Nuclear Engineering and Design,* vol. 241, no. 11, pp. 4482-4486, 11// 2011.

[24] H. J. Kim and K. H. Kim, "Intuitional experiment and numerical analysis of flow characteristics affected by flow accelerated corrosion in elbow pipe system," *Nuclear Engineering and Design,* vol. 301, pp. 183-188, 5// 2016.

[25] V. Kain, S. Roychowdhury, T. Mathew, and A. Bhandakkar, "Flow accelerated corrosion and its control measures for the secondary circuit pipelines in Indian nuclear power plants," *Journal of Nuclear Materials,* vol. 383, no. 1–2, pp. 86-91, 12/15/ 2008.

[26] B. Poulson, "Advances in understanding hydrodynamic effects on corrosion," *Corrosion Science,* Article vol. 35, no. 1-4, pp. 655-661, 1993.

[27] D. H. Moed, S. Weerakul, D. H. Lister, N. Leaukosol, L. C. Rietveld, and A. R. D. Verliefde, "Effect of Ethanolamine, Ammonia, Acetic Acid, and Formic Acid on Two-Phase Flow Accelerated Corrosion in Steam–Water Cycles," *Industrial & Engineering Chemistry Research,* vol. 54, no. 36, pp. 8963-8970, 2015/09/16 2015.

[28] I. H. Rhee, H. Jung, and D. Cho, "Evaluation of pH Control Agents Influencing on Corrosion of Carbon Steel in Secondary Water Chemistry Condition of Pressurized Water Reactor," *Nuclear Engineering and Technology,* vol. 46, no. 3, pp. 431-438, 6// 2014.

[29] S. Nasrazadani, A. Reid, J. Stevens, R. Theimer, and B. Fellers, "Comparison of DBU, NH_3, DMA, ETA, and morpholine interactions with ferrous chloride solution and carbon steel surfaces," in *15th International Conference on Environmental Degradation of Materials in Nuclear Power Systems-Water Reactors 2011*, 2011, vol. 3, pp. 1759-1776.

[30] D. H. Lister, L. Liu, and A. D. Feicht, "A fundamental study of flow-accelerated corrosion in feedwater systems," *Power Plant Chemistry,* vol. 10, no. 11, pp. 659-667, 2008.

[31] K. M. K. Eun Hee Lee, Hong Pyo Kim, Dong Jin Kim, "Effect of Cr on Flow Accelerated Corrosion of Carbon Steel," *Corrosion Science and Technology,* vol. 14, no. 1, pp. 25 - 32, 2015.

[32] K. Fujiwara, M. Domae, K. Yoneda, and F. Inada, "Model of physico-chemical effect on flow accelerated corrosion in power plant," *Corrosion Science,* vol. 53, no. 11, pp. 3526-3533, 2011.

[33] J. H. Moon, H. H. Chung, K. W. Sung, U. C. Kim, and J. S. Rho, "Dependency of single-phase FAC of carbon and low-alloy steels for NPP system piping on pH, orifice distance and material," *Nuclear Engineering and Technology,* vol. 37, no. 4, pp. 375-384, 2005.

[34] Y. F. Cheng and F. R. Steward, "Corrosion of carbon steels in high-temperature water studied by electrochemical techniques," *Corrosion Science,* vol. 46, no. 10, pp. 2405-2420, 2004/10/01/ 2004.

[35] Y. F. Cheng, J. Bullerwell, and F. R. Steward, "Electrochemical investigation of the corrosion behavior of chromium-modified carbon steels in water," *Electrochimica Acta,* vol. 48, no. 11, pp. 1521-1530, 2003/05/15/ 2003.

[36] B. Chexal, J. Horowitz, and B. Dooley, "Flow-accelerated corrosion in power plants. Revision 1,"; Electric Power Research Inst., Palo Alto, CA (United States);Electricite de France (France);Siemens AG Power Generation (Germany)EPRI-TR--106611-R1; Other: ON: UN99003340; TRN: AHC29927%%2 United States Other: ON: UN99003340; TRN: AHC29927%%2 EPRI Distribution Center, 207 Coggins Drive, PO Box 23205, Pleasant Hill,

CA 94523 (United States) OSTI English, 1998.

[37] E.-M. Pavageau, "Residual Chromium Effects on Flow-Accelerated Corrosion of Carbon Steel," Electric Power Research Institute, Electric Power Research Institute2006.

[38] H. D. Y. Kyeong Mo, Lee, "A Study on the Thermal Hydraulic Analysis and B-Scan Inspection for LDIE Degradation of Carbon Steel Piping in a Nuclear Plant " *Corrosion Science and Technology,* vol. 11, no. 6, pp. 218-224, 2012.

[39] G. A. Zhang, L. Zeng, H. L. Huang, and X. P. Guo, "A study of flow accelerated corrosion at elbow of carbon steel pipeline by array electrode and computational fluid dynamics simulation," *Corrosion Science,* vol. 77, no. 0, pp. 334-341, 12// 2013.

[40] K. H. Ryu, I. S. Hwang, and J. H. Kim, "Development of wall thinning screening system and its application to a commercial nuclear power plant," *Nuclear Engineering and Design,* vol. 265, no. 0, pp. 591-598, 12// 2013.

[41] K. H. Ryu *et al.*, "Online monitoring method using Equipotential Switching Direct Current potential drop for piping wall loss by flow accelerated corrosion," *Nuclear Engineering and Design,* Article vol. 240, no. 3, pp. 468-472, 2010.

[42] K. H. Ryu *et al.*, "Screening method for piping wall loss by flow accelerated corrosion," *Nuclear Engineering and Design,* vol. 238, no. 12, pp. 3263-3268, 12// 2008.

[43] H. Subramanian *et al.*, "Thin layer activation for probing flow accelerated corrosion of carbon steel," *Corrosion Science,* vol. 54, pp. 45-51, 2012.

[44] I. Betova, M. Bojinov, and T. Saario, "Predictive Modelling of Flow-accelerated Corrosion - Unresolved Problems and Issues," 2009.

[45] B. Poulson, "Complexities in predicting erosion corrosion," *Wear,* vol. 233–235, pp. 497-504, 12// 1999.

[46] T. Satoh, Y. Shao, W. G. Cook, D. H. Lister, and S. Uchida, "Flow-Assisted Corrosion of Carbon Steel under Neutral Water Conditions," *Corrosion,* vol. 63, no. 8, pp. 770-780, 2007/08/01 2007.

[47] S. Fyfitch, "5.04 - Corrosion and Stress Corrosion Cracking of Ni-Base Alloys," in *Comprehensive Nuclear Materials*, R. J. M. Konings, Ed. Oxford: Elsevier, 2012, pp. 69-92.

[48] A. M. D. Munson, "Flow-Accelerated Corrosion Investigation of Trace Chromium," EPRI, Palo Alto, CA2003.

[49] G. O. Ilevbare and G. T. Burstein, "The role of alloyed molybdenum in the inhibition of pitting corrosion in stainless steels," *Corrosion Science,* vol. 43, no. 3, pp. 485-513, 3// 2001.

[50] R. F. A. Jargelius-Pettersson and B. G. Pound, "Examination of the Role of Molybdenum in Passivation of Stainless Steels Using AC Impedance Spectroscopy," *Journal of The Electrochemical Society,* vol. 145, no. 5, pp. 1462-1469, May 1, 1998 1998.

[51] K. Sugimoto and Y. Sawada, "The role of molybdenum additions to austenitic stainless steels in the inhibition of pitting in acid chloride solutions," *Corrosion Science,* vol. 17, no. 5, pp.

425-445, 1977/01/01 1977.

[52] J. R. Galvele, J. B. Lumsden, and R. W. Staehle, "Effect of Molybdenum on the Pitting Potential of High Purity 18% Cr Ferritic Stainless Steels," *Journal of The Electrochemical Society,* vol. 125, no. 8, pp. 1204-1208, August 1, 1978 1978.

[53] R. C. Newman, "The dissolution and passivation kinetics of stainless alloys containing molybdenum—II. Dissolution kinetics in artificial pits," *Corrosion Science,* vol. 25, no. 5, pp. 341-350, 1985/01/01 1985.

[54] S. Kou, *Welding Metallurgy*. Hoboken, New Jersey: John Wiley & Sons, 2003.

[55] S. Kim, J. W. Kim, and J. H. Kim, "Enhancement of corrosion resistance in carbon steels using nickel-phosphorous/titanium dioxide nanocomposite coatings under high-temperature flowing water," *Journal of Alloys and Compounds,* vol. 698, pp. 267-275, 3/25/ 2017.

[56] P. R. Tremaine and J. C. Leblanc, "The solubility of nickel oxide and hydrolysis of Ni2+ in water to 573 K," *The Journal of Chemical Thermodynamics,* vol. 12, no. 6, pp. 521-538, 6// 1980.

[57] R. L. Z. III and L. S. Jr., "Effects of Phosphorus on Corrosion Resistance of Electroless Nickel in 50% Sodium Hydroxide," *Corrosion,* vol. 50, no. 6, pp. 457-467, 1994.

[58] J. Kang, Y. Yang, and H. Shao, "Comparing the anodic reactions of Ni and Ni–P amorphous alloy in alkaline solution," *Corrosion Science,* vol. 51, no. 9, pp. 1907-1913, 9// 2009.

[59] S. E. Ziemniak and M. A. Goyette, "Nickel(II) Oxide Solubility and Phase Stability in High Temperature Aqueous Solutions," (in English), *Journal of Solution Chemistry,* vol. 33, no. 9, pp. 1135-1159, 2004/09/01 2004.

[60] S. L. Medway, C. A. Lucas, A. Kowal, R. J. Nichols, and D. Johnson, "In situ studies of the oxidation of nickel electrodes in alkaline solution," *Journal of Electroanalytical Chemistry,* vol. 587, no. 1, pp. 172-181, 2/1/ 2006.

[61] M. J. Duarte *et al.*, "Crystallization, phase evolution and corrosion of Fe-based metallic glasses: An atomic-scale structural and chemical characterization study," *Acta Materialia,* vol. 71, pp. 20-30, 6// 2014.

[62] J. E. Gao *et al.*, "Fe-based bulk metallic glass composites without any metalloid elements," *Acta Materialia,* vol. 61, no. 9, pp. 3214-3223, 5// 2013.

[63] P. F. Gostin, S. Oswald, L. Schultz, and A. Gebert, "Acid corrosion process of Fe-based bulk metallic glass," *Corrosion Science,* vol. 62, pp. 112-121, 9// 2012.

[64] W. J. Botta, J. E. Berger, C. S. Kiminami, V. Roche, R. P. Nogueira, and C. Bolfarini, "Corrosion resistance of Fe-based amorphous alloys," *Journal of Alloys and Compounds,* vol. 586, Supplement 1, pp. S105-S110, 2/15/ 2014.

[65] S. D. Zhang, W. L. Zhang, S. G. Wang, X. J. Gu, and J. Q. Wang, "Characterisation of three-dimensional porosity in an Fe-based amorphous coating and its correlation with corrosion

behaviour," *Corrosion Science,* vol. 93, pp. 211-221, 4// 2015.

[66] C. A. C. Souza, D. V. Ribeiro, and C. S. Kiminami, "Corrosion resistance of Fe-Cr-based amorphous alloys: An overview," *Journal of Non-Crystalline Solids,* vol. 442, pp. 56-66, 6/15/ 2016.

[67] W.-H. Liu, F.-S. Shieu, and W.-T. Hsiao, "Enhancement of wear and corrosion resistance of iron-based hard coatings deposited by high-velocity oxygen fuel (HVOF) thermal spraying," *Surface and Coatings Technology,* vol. 249, pp. 24-41, 6/25/ 2014.

[68] Z. B. Zheng, Y. G. Zheng, W. H. Sun, and J. Q. Wang, "Erosion–corrosion of HVOF-sprayed Fe-based amorphous metallic coating under impingement by a sand-containing NaCl solution," *Corrosion Science,* vol. 76, pp. 337-347, 11// 2013.

[69] Z. B. Zheng, Y. G. Zheng, W. H. Sun, and J. Q. Wang, "Effect of applied potential on passivation and erosion–corrosion of a Fe-based amorphous metallic coating under slurry impingement," *Corrosion Science,* vol. 82, pp. 115-124, 5// 2014.

[70] Y. Wang *et al.*, "Corrosion and erosion–corrosion behaviour of activated combustion high-velocity air fuel sprayed Fe-based amorphous coatings in chloride-containing solutions," *Corrosion Science,* vol. 98, pp. 339-353, 9// 2015.

[71] M. El-Gammal, H. Mazhar, J. S. Cotton, C. Shefski, J. Pietralik, and C. Y. Ching, "The hydrodynamic effects of single-phase flow on flow accelerated corrosion in a 90-degree elbow," *Nuclear Engineering and Design,* vol. 240, no. 6, pp. 1589-1598, 6// 2010.

[72] K. S. Jung and K. W. Sung, *Magnetite: Electrochemical properties and its role on flow accelerated corrosion* (Magnetite: Sturcture, Properties and Applications). 2011, pp. 261-296.

[73] S. Uchida, M. Naitoh, H. Okada, Y. Uehara, and S. Koshizuka, "Evaluation of flow accelerated corrosion by coupled analysis of corrosion and flow dynamics. Relationship of oxide film thickness, hematite/magnetite ratio, ECP and wall thinning rate," *Nuclear Engineering and Design,* vol. 241, no. 11, pp. 4585-4593, 2011/11/01/ 2011.

[74] Y. Wang *et al.*, "Duplex Ni–P–ZrO_2/Ni–P electroless coating on stainless steel," *Journal of Alloys and Compounds,* vol. 630, pp. 189-194, 5/5/ 2015.

[75] C. Yanhai, C. Hengyang, H. Dongtai, Z. Yong, and Z. Zhencai, "Effect of PTFE Addition on the Properties of Electroless Ni-Cu-P-PTFE Deposits," *Rare Metal Materials and Engineering,* vol. 43, no. 5, pp. 1025-1030, 5// 2014.

[76] B. Panja and P. Sahoo, "Friction performance of electroless Ni-P coatings in alkaline medium and optimization of coating parameters," *Procedia Engineering,* vol. 97, pp. 47-55, // 2014.

[77] P. Makkar, R. C. Agarwala, and V. Agarwala, "Wear characteristics of mechanically milled TiO_2 nanoparticles incorporated in electroless Ni–P coatings," *Advanced Powder Technology,* vol. 25, no. 5, pp. 1653-1660, 9// 2014.

[78] S. H. K. J-H. Huh, J.H. Chu, S.Y. Kim, J.H. Kim and S-Y. Kwon, "Enhancement of seawater

corrosion resistance in copper using acetone-derived graphene coating," *Nanoscale Res Lett,* vol. 6, pp. 4379-4386, 2014.

[79] P. Makkar, R. C. Agarwala, and V. Agarwala, "Chemical synthesis of TiO_2 nanoparticles and their inclusion in Ni–P electroless coatings," *Ceramics International,* vol. 39, no. 8, pp. 9003-9008, 12// 2013.

[80] M. Momenzadeh and S. Sanjabi, "The effect of TiO_2 nanoparticle codeposition on microstructure and corrosion resistance of electroless Ni-P coating," *Materials and Corrosion,* vol. 63, no. 7, pp. 614-619, 2012.

[81] J. Novakovic and P. Vassiliou, "Vacuum thermal treated electroless NiP–TiO_2 composite coatings," *Electrochimica Acta,* vol. 54, no. 9, pp. 2499-2503, 3/30/ 2009.

[82] Y. Wang *et al.*, "Slurry erosion–corrosion behaviour of high-velocity oxy-fuel (HVOF) sprayed Fe-based amorphous metallic coatings for marine pump in sand-containing NaCl solutions," *Corrosion Science,* vol. 53, no. 10, pp. 3177-3185, 2011/10/01/ 2011.

[83] A. Faghri and Y. Zhang, *Transport Phenomena in Multiphase System*. Elsevier: Elsevier, 2006.

[84] A. F. Kanta, V. Vitry, and F. Delaunois, "Wear and corrosion resistance behaviours of autocatalytic electroless plating," *Journal of Alloys and Compounds,* vol. 486, no. 1–2, pp. L21-L23, 11/3/ 2009.

[85] D. D. N. Singh and R. Ghosh, "Electroless nickel–phosphorus coatings to protect steel reinforcement bars from chloride induced corrosion," *Surface and Coatings Technology,* vol. 201, no. 1–2, pp. 90-101, 9/12/ 2006.

[86] J. Sudagar, J. Lian, and W. Sha, "Electroless nickel, alloy, composite and nano coatings – A critical review," *Journal of Alloys and Compounds,* vol. 571, pp. 183-204, 9/15/ 2013.

[87] A. Abdel Aal, "Hard and corrosion resistant nanocomposite coating for Al alloy," *Materials Science and Engineering: A,* vol. 474, no. 1–2, pp. 181-187, 2/15/ 2008.

[88] S. Zhang, Q. Li, X. Yang, X. Zhong, Y. Dai, and F. Luo, "Corrosion resistance of AZ91D magnesium alloy with electroless plating pretreatment and Ni–TiO_2 composite coating," *Materials Characterization,* vol. 61, no. 3, pp. 269-276, 3// 2010.

[89] N. Veronovski, P. Andreozzi, C. La Mesa, and M. Sfiligoj-Smole, "Stable TiO_2 dispersions for nanocoating preparation," *Surface and Coatings Technology,* vol. 204, no. 9–10, pp. 1445-1451, 1/25/ 2010.

[90] Y.-B. Tang *et al.*, "Incorporation of Graphenes in Nanostructured TiO_2 Films via Molecular Grafting for Dye-Sensitized Solar Cell Application," *ACS Nano,* vol. 4, no. 6, pp. 3482-3488, 2010/06/22 2010.

[91] S. Ranganatha, T. V. Venkatesha, and K. Vathsala, "Development of electroless Ni–Zn–P/nano-TiO_2 composite coatings and their properties," *Applied Surface Science,* vol. 256, no. 24, pp. 7377-7383, 10/1/ 2010.

[92] A. Abdel Aal, H. B. Hassan, and M. Abdel Rahim, "Nanostructured Ni–P–TiO_2 composite coatings for electrocatalytic oxidation of small organic molecules," *Journal of Electroanalytical Chemistry,* vol. 619, pp. 17-25, 2008.

[93] H. Yun, J. Li, H.-B. Chen, and C.-J. Lin, "A study on the N-, S- and Cl-modified nano-TiO_2 coatings for corrosion protection of stainless steel," *Electrochimica Acta,* vol. 52, no. 24, pp. 6679-6685, 8/1/ 2007.

[94] J. Novakovic, P. Vassiliou, K. Samara, and T. Argyropoulos, "Electroless NiP–TiO_2 composite coatings: Their production and properties," *Surface and Coatings Technology,* vol. 201, no. 3–4, pp. 895-901, 10/5/ 2006.

[95] P. Makkar, D. D. Mishra, R. C. Agarwala, and V. Agarwala, "A novel electroless plating of Ni–P–Al–ZrO_2 nanocomposite coatings and their properties," *Ceramics International,* vol. 40, no. 8, Part A, pp. 12013-12021, 9// 2014.

[96] R. Arghavanian and N. Parvini-Ahmadi, "The effect of co-electrodeposited ZrO_2 particles on the microstructure and corrosion resistance of Ni coatings," (in English), *Journal of Solid State Electrochemistry,* vol. 15, no. 10, pp. 2199-2204, 2011/10/01 2011.

[97] D. Gutsev, M. Antonov, I. Hussainova, and A. Y. Grigoriev, "Effect of SiO_2 and PTFE additives on dry sliding of NiP electroless coating," *Tribology International,* vol. 65, pp. 295-302, 9// 2013.

[98] M. H. Allahyarzadeh, M. Aliofkhazraei, A. R. S. Rouhaghdam, and V. Torabinejad, "Electrodeposition of Ni–W–Al_2O_3 nanocomposite coating with functionally graded microstructure," *Journal of Alloys and Compounds,* vol. 666, pp. 217-226, 5/5/ 2016.

[99] S. Karthikeyan and B. Ramamoorthy, "Effect of reducing agent and nano Al_2O_3 particles on the properties of electroless Ni–P coating," *Applied Surface Science,* vol. 307, no. 0, pp. 654-660, 7/15/ 2014.

[100] C. Ma, F. Wu, Y. Ning, F. Xia, and Y. Liu, "Effect of heat treatment on structures and corrosion characteristics of electroless Ni–P–SiC nanocomposite coatings," *Ceramics International,* vol. 40, no. 7, Part A, pp. 9279-9284, 8// 2014.

[101] J. A. Calderón, J. E. Henao, and M. A. Gómez, "Erosion–corrosion resistance of Ni composite coatings with embedded SiC nanoparticles," *Electrochimica Acta,* vol. 124, no. 0, pp. 190-198, 4/1/ 2014.

[102] F. Kılıç, H. Gül, S. Aslan, A. Alp, and H. Akbulut, "Effect of CTAB concentration in the electrolyte on the tribological properties of nanoparticle SiC reinforced Ni metal matrix composite (MMC) coatings produced by electrodeposition," *Colloids and Surfaces A: Physicochemical and Engineering Aspects,* vol. 419, no. 0, pp. 53-60, 2/20/ 2013.

[103] A. Farzaneh, M. Mohammadi, M. Ehteshamzadeh, and F. Mohammadi, "Electrochemical and structural properties of electroless Ni-P-SiC nanocomposite coatings," *Applied Surface Science,*

vol. 276, no. 0, pp. 697-704, 7/1/ 2013.

[104] I. R. Mafi and C. Dehghanian, "Comparison of the coating properties and corrosion rates in electroless Ni–P/PTFE composites prepared by different types of surfactants," *Applied Surface Science,* vol. 257, no. 20, pp. 8653-8658, 8/1/ 2011.

[105] M. H. Sadhir, M. Saranya, M. Aravind, A. Srinivasan, A. Siddharthan, and N. Rajendran, "Comparison of in situ and ex situ reduced graphene oxide reinforced electroless nickel phosphorus nanocomposite coating," *Applied Surface Science,* vol. 320, pp. 171-176, 2014.

[106] H. Ashassi-Sorkhabi, "Corrosion resistance enhancement of electroless Ni–P coating by incorporation of ultrasonically dispersed diamond nanoparticles," *Corrosion Science,* vol. 77, pp. 185-193, 2013.

[107] X. H. Chen *et al.*, "Dry friction and wear characteristics of nickel/carbon nanotube electroless composite deposits," *Tribology International,* vol. 39, no. 1, pp. 22-28, 1// 2006.

[108] S. Kundu, S. K. Das, and P. Sahoo, "Properties of Electroless Nickel at Elevated Temperature-a Review," *Procedia Engineering,* vol. 97, pp. 1698-1706, // 2014.

[109] J. H. Kim and I. S. Hwang, "Electroless nickel-plating for the PWSCC mitigation of nickel-base alloys in nuclear power plants," *Nuclear Engineering and Design,* Article vol. 238, no. 10, pp. 2529-2535, 2008.

[110] E. Turunen *et al.*, "On the role of particle state and deposition procedure on mechanical, tribological and dielectric response of high velocity oxy-fuel sprayed alumina coatings," *Materials Science and Engineering: A,* vol. 415, no. 1, pp. 1-11, 2006/01/15/ 2006.

[111] J. E. B. Randles, "Kinetics of rapid electrode reactions," *Discussions of the Faraday Society,* 10.1039/DF9470100011 vol. 1, no. 0, pp. 11-19, 1947.

[112] K. Suttiponparnit, J. Jiang, M. Sahu, S. Suvachittanont, T. Charinpanitkul, and P. Biswas, "Role of Surface Area, Primary Particle Size, and Crystal Phase on Titanium Dioxide Nanoparticle Dispersion Properties," *Nanoscale Res Lett,* vol. 6, no. 1, p. 27, 2011.

[113] T. Hentschel, D. Isheim, R. Kirchheim, F. Müller, and H. Kreye, "Nanocrystalline Ni–3.6 at.% P and its transformation sequence studied by atom-probe field-ion microscopy," *Acta Materialia,* vol. 48, no. 4, pp. 933-941, 2/25/ 2000.

[114] K.-H. Hur, J.-H. Jeong, and D. Lee, "Microstructures and crystallization of electroless Ni-P deposits," (in English), *Journal of Materials Science,* vol. 25, no. 5, pp. 2573-2584, 1990/05/01 1990.

[115] Y. Wang, S. L. Jiang, Y. G. Zheng, W. Ke, W. H. Sun, and J. Q. Wang, "Effect of porosity sealing treatments on the corrosion resistance of high-velocity oxy-fuel (HVOF)-sprayed Fe-based amorphous metallic coatings," *Surface and Coatings Technology,* vol. 206, no. 6, pp. 1307-1318, 12/15/ 2011.

[116] A. Michelin, E. Drouet, E. Foy, J. J. Dynes, D. Neff, and P. Dillmann, "Investigation at the

nanometre scale on the corrosion mechanisms of archaeological ferrous artefacts by STXM," *Journal of Analytical Atomic Spectrometry,* 10.1039/C2JA30250K vol. 28, no. 1, pp. 59-66, 2013.

[117] L. A. J. Garvie, A. J. Craven, and R. Brydson, "Use of electron-energy loss near-edge fine structure in the study of minerals," *American Mineralogist,* vol. 79, no. 5-6, pp. 411-425, 1994.

[118] V. Subramanian *et al.*, "Electrochemical characterization of oxide formed on chromium containing mild steel alloys in LiOH medium," *Materials Chemistry and Physics,* vol. 145, no. 3, pp. 499-509, 2014/06/16/ 2014.

[119] L. Soriano *et al.*, "Chemical analysis of passivated and oxidized layers on FeCr and FeTi alloys by soft x-ray absorption spectroscopy," *Surface and Interface Analysis,* vol. 20, no. 1, pp. 21-26, 1993.

[120] R. B. Dooley and V. K. Chexal, "Flow-accelerated corrosion of pressure vessels in fossil plants," *International Journal of Pressure Vessels and Piping,* vol. 77, no. 2–3, pp. 85-90, 2// 2000.

[121] R. Walker and N. S. Holt, "Determination of the nernst diffusion layer thickness in the hydroson agitation tank," *Surface Technology,* vol. 22, no. 2, pp. 165-174, 1984/06/01/ 1984.

[122] X. H. Chen, C. S. Chen, H. N. Xiao, F. Q. Cheng, G. Zhang, and G. J. Yi, "Corrosion behavior of carbon nanotubes–Ni composite coating," *Surface and Coatings Technology,* vol. 191, no. 2–3, pp. 351-356, 2/21/ 2005.

[123] K. Fruzzetti, "Pressurized Water Reactor Secondary Water Chemistry Guidelines – Revision 6," Electric Power Research Institute, Electric Power Research Institute2004.

[124] V. I. W. G. o. R. o. R. P. C. International Atomic Energy Agency, "Corrosion and erosion aspects in pressure boundary components of light water reactors," International Atomic Energy Agency (IAEA)1990, Available: http://inis.iaea.org/search/search.aspx?orig_q=RN:22038332.

[125] Z. Zeng, K. Natesan, Z. Cai, and S. B. Darling, "The role of metal nanoparticles and nanonetworks in alloy degradation," *Nat Mater,* 10.1038/nmat2227 vol. 7, no. 8, pp. 641-646, 08//print 2008.

[126] S. E. Ziemniak, M. E. Jones, and K. E. S. Combs, "Solubility and Phase Behavior of Cr(III) Oxides in Alkaline Media at Elevated Temperatures," *Journal of Solution Chemistry,* journal article vol. 27, no. 1, pp. 33-66, 1998.

[127] S. E. Ziemniak, L. M. Anovitz, R. A. Castelli, and W. D. Porter, "Thermodynamics of Cr2O3, FeCr2O4, ZnCr2O4, and CoCr2O4," *The Journal of Chemical Thermodynamics,* vol. 39, no. 11, pp. 1474-1492, 11// 2007.

[128] T. W. Hideaki Kushima, Masaharu Murata, Kazushige Kamihira, Hideo Tanaka, Kazuhiro Kimura, "Metallographic Atlas for 2.25Cr-1Mo Steels and Degradation due to Long-term Service at the Elevated Temperatures," in *ECCC Creep Conference*, London, 2005.

[129] A. Fadel, D. Glišić, N. Radović, and D. Drobnjak, "Influence of Cr, Mn and Mo Addition on Structure and Properties of V Microalloyed Medium Carbon Steels," *Journal of Materials Science & Technology,* vol. 28, no. 11, pp. 1053-1058, 2012/11/01/ 2012.

[130] T. Ishitsuka, Y. Inoue, and H. Ogawa, "Effect of Silicon on the Steam Oxidation Resistance of a 9%Cr Heat Resistant Steel," *Oxidation of Metals,* vol. 61, no. 1, pp. 125-142, 2004/02/01 2004.

[131] J. Manjanna and G. Venkateswaran, "Dissolution of chromium-substituted iron oxides in V(II) formulations," *Hydrometallurgy,* vol. 61, no. 1, pp. 45-63, 2001/06/01/ 2001.

[132] U. Schwertmann, U. Gasser, and H. Sticher, "Chromium-for-iron substitution in synthetic goethites," *Geochimica et Cosmochimica Acta,* vol. 53, no. 6, pp. 1293-1297, 1989/06/01/ 1989.

[133] R. D. Shannon, "Revised effective ionic radii and systematic studies of interatomic distances in halides and chalcogenides," *Acta Crystallographica Section A,* vol. 32, no. 5, pp. 751-767, 1976/09/01 1976.

[134] X. Liang *et al.*, "The application of chromium substituted magnetite as heterogeneous Fenton catalyst for the degradation of aqueous cationic and anionic dyes," *Chemical Engineering Journal,* vol. 191, pp. 177-184, 2012/05/15/ 2012.

[135] J.-y. Jiang *et al.*, "The Passive Film Growth Mechanism of New Corrosion-Resistant Steel Rebar in Simulated Concrete Pore Solution: Nanometer Structure and Electrochemical Study," vol. 10, no. 4, p. 412, 2017.

[136] T. Fukumura and K. Arioka, "Influence Of Ethanol Amine Injection On Flow Accelerated Corrosion Of PWR Secondary System," *Journal of Materials Science & Technology,* 2009.

IX. ACKNOWLEDGEMENTS

Firstly, I would like to express my sincere gratitude to my advisor Prof. Ji Hyun Kim for the continuous support of my Ph. D. study and related research, for his patience, motivation, and immense knowledge. His guidance helped me in all the time of research and writing of this thesis. I could not have imagined having a better advisor and mentor for my Ph. D. study.

Besides my advisor, I would like to thank the rest of my thesis committee: Prof. In Cheol Bang, Prof. Soon-Yong Kwon, Prof. Chi Bum Bahn, and Dr. Young-Jin Kim, for their insightful comments and encouragement, but also for the hard question which incented me to widen my research from various perspectives.

I thank my fellow UNIMAT labmates in for the simulation discussions, for uncountable days we were working together, and for all the fun we have had in the last 10 years.

I also would like to thank my parents, and relative for supporting me spiritually throughout writing this thesis and my life in general.

Last but not the least, I would like to thank my lovely wife, Dr. Eunae Kim, for believing in me in both joyful and harsh times. She stood by me through all my travails, my absences, my fits of pique and impatience. She gave me support and help, discussed ideas and prevented several wrong turns.

감사의 글

먼저 연구자로서 첫 발을 디딜 수 있고, 또한 연구를 진행하는 과정에서 혜안으로 저를 이끌어 주신 저의 지도 교수님, 김지현 교수님께 지난 몇 년간의 감사를 이 기회를 빌어 전해드립니다. 많이 내색 하진 않으셨지만, 저에게 많이 기대도 하셨을 것이며 또한 실망한 경우도 많을 것이라고 생각합니다. 늘 좋은 학생이 아닌 좋은 제자가 될 수 있도록 노력하였지만, 많이 부족했던 것 같습니다. 이제 연구자로서 시작하는 이 시점에, 늘 그 가르침을 잊지 않도록 하겠습니다.

저의 학위 논문 심사에 참석해 주신, 방인철 교수님, 권순용 교수님, 반치범 교수님, 그리고 김영진 박사님께도 감사드립니다. 많이 부족한 학위 논문이지만 심사 하는 과정에서 주신 의견은 저의 연구를 뒤돌아 보고 다듬는 데 있어서 시금석과 같았습니다. 방인철 교수님께서는 학부와 대학원 과정 간에 원자력에 관한 다양한 기초 지식을 많이 전달해 주셨습니다. 권순용 교수님은 학부 과정에서 재료 공학 및 과학에 관한 강의와 부식 실험의 기초에 관해 많이 배울 수 있게 해주셨습니다. 반치범 교수님은 처음 미국 아르곤 국립 연구소에서 뵐 때부터 많이 도와 주셨고, 연구 과제 진행 중에도 많은 도움을 주셨습니다. 마지막으로 김영진 박사님은 원자력 재료 전반에 관한 많은 멘토링을 해주셨습니다. 이에 심사 위원 분들께도 다시 한번 감사드립니다. 그리고, 심사 위원은 아니셨지만 지난 몇 년간 아르곤 국립 연구소에서 저를 많이 지도해주신 박창용 박사님께도 감사의 말씀을 전해드립니다.

이 논문이 완성되기까지 저의 사랑스러운 아내이자 동료로써 많은 도움을 준 김은애 박사(우내)에게도 감사와 사랑의 말을 남깁니다. 보잘것없는 저를 믿어주고, 기쁠 때나 슬플 때나 항상 저의 옆에 지켜 서서 늘 용기를 낼 수 있도록 해주었습니다. 지금까지 같이 해온 시간은 그리 길지 않았지만 앞으로 남은 인생을 같이 살아가고 그 동안에도 많이 싸우지만(?) 서로 늘 아껴줄 수 있도록 하겠습니다. 다만, 침대에서 계속 내 자리를 침범하지는 않았으면 좋겠습니다. 그리고 겨울에도 선풍기 켜서 미안합니다.

제가 이때까지 크는 동안 저를 키우시느라 많이 고생하셨을 부모님, 특히 어머니께도 감사 말씀 드립니다. 30년의 세월 동안 사람 구실 하는 사람 하나 만드는 것이 쉽지 않으셨을 텐데 이제 열심히 효도하도록 하겠습니다. 직장 생활 하시랴, 저 키우시랴 고생 많이 하셨고, 하시고 싶은 것 많이 못 하셨는데 이제 하고 싶은 것 하시면서 사시면 좋겠습니다. 또 제가 어릴 때 많이 돌봐 주신 삼촌, 숙모님, 이모님들과 이모부님들,

그리고 마지막으로 이제는 하늘 나라에 계시는 외할아버지, 외할머니께도 감사드립니다. 손자와 손자의 아내가 같이 박사 되는 것을 보셨으면 많이 좋아하셨을 텐데 아쉽습니다. 최근 많은 시간을 보내진 못하지만 사촌들도 각자의 길을 잘 걸어갔으면 좋겠습니다.

애지중지 키우신 딸을 데려가서 많이 아쉬우셨을(?) 장인어른, 장모님께도 감사드립니다. 가진 것도 없이 결혼하겠다고 하여 내심 많이 걱정하셨을 테지만 앞으로 아내와 가족을 책임지는 사위로, 가장으로 열심히 살도록 하겠습니다. 그리고 늘 하나라도 더 챙겨 주시는 이모, 이모부님도 감사합니다. 든든한 처남 선익이도 앞으로 진로, 계획대로 잘 풀렸으면 좋겠습니다.

어떻게 보면 가족보다 더 많은 시간을 함께 했던 우리 원자력 재료 연구실 식구들에게도 감사의 글을 남깁니다. 좋은 일도 많았고, 서로 섭섭했던 일도 많았지만 앞으로 사회에 나가서 결국 힘이 되는 것은 같은 연구실 사람들이라 생각합니다. 좋은 선배 혹은 후배는 아니었지만 그런 사람이 될 수 있도록 늘 노력하겠습니다. 저를 원자력 재료 연구의 세계로 납치 해오신 상훈이 형, 한국에서나 미국에서나 저를 술독으로 인도하신 종진이 형과 시선이 누나, 짧은 시간이었지만 함께 했던 정석이 형, 영원한 동안 좡좡 주앙이 형, 늘 웃는 얼굴로 고집이 센 경준이 형과 형수님께 감사합니다. 이런 좋은 선배님들 덕분에 저는 원자력 재료 연구의 늪에 빠질 수 있었습니다. 그리고 2차 계통과 코팅의 쓴 맛을 같이 봤던 정원이 형, 좋은 과학자인 상일, 위스콘신 시골에서 농사를 짓고 있는지 연구를 하고 있는지 모르겠지만 정말 10년간 많은 일을 함께 겪은, 또 논문 실적이 부러운 태호, 원자력 동기이자 시카고 동행자 큘 브로커 광범, 승모근으로 연구하는 우리 든든한 랩장 승창, 차세대 원전을 이끌어갈 정현, 컴퓨터 파괴자 태용, 정말 고생 많이 하는 윤주, 그리고 마찬가지로 늘 웃는 얼굴(?)로 살아가던 꿀빵맨 인영, 돌아온 준혁이와 천둥벌거숭이 정환이 까지 좋은 동료이자 선배로써 살고 싶었지만 그렇지 못한 것 같아 미안하고 또 감사합니다. 마지막으로, 이렇게 인연이 될지 몰랐으나, 앞으로 많은 시간을 함께할 기동이형에게는 이 자리를 빌어서 다시 감사드립니다.

그리고, 제 인생에서 잊을 수 없는 시간을 함께한 친구들에게도 감사의 말을 전합니다. 늘 우정과 의리의 중요성을 우리에게 각인시키는 허세쟁이 재형, 10년을 봐도 아직 무슨 생각인지 감도 안 잡히는 신선놀음 도현, 좋은 회사 창업해서 우리의 재무를 책임질 선필, 우리보다 강아지가 중요한 태민, 마찬가지로 박사 학위 하느라 고생 많은 정민, 일본에서 외화벌이하는 실명을 까먹은 바우, 그리고 다른 친구들에게도 고맙고 앞으로도 자주 보면서 소주 한 잔 하면 좋겠습니다. 또 잊을 수 없는 1학년 1학기를 함께한 영철, 용혁, 범철 그리고 찬호, 성철, 보철, 지훈, 승욱, 지훈, 지수, 종원, 상걸, 상흠도

각자의 길을 잘 걸어갔으면 좋겠습니다. 또한, UNIST 원자력 동기, 선배, 후배들인 경모, 관윤, 인국, 영신, 성보, 현석, 한이 형, 태우 형, 욱제, 철민, 태원과 다른 대학교의 많은 대학원생 분들에게도 감사드립니다. 앞으로 서로 힘든 일이 있을 때 힘이 되어주면 좋겠습니다. 준호 형은 이렇게 인연이 닿을 줄 몰랐지만 앞으로도 이전처럼 많은 추억을 만들어 갑시다.

마지막으로, 이 학위 논문이 완성될 수 있도록 배려해주신 재료연구소 재료안전평가본부의 본부장님을 비롯한 많은 분들, 특히 원자력공인검사단과 접합기술연구실의 단장님, 실장님, 박사님들, 선생님들께 이 자리를 빌어 죄송하다는 말씀과 감사하다는 말씀을 전합니다. 첫 직장으로 너무 과분하게 좋은 곳으로 오게 된 것 같지만 제가 앞으로 잘 할 수 있음을 믿어 주셨기에 이러한 기회를 주셨다 생각하고 열심히 하도록 하겠습니다.

이 밖에도 많은 분들이 저에게 귀감이 되셨고, 영감을 주셨습니다. 비록 보잘것없는 하나의 박사 학위 논문이지만 그 과정에서 많이 배울 수 있었고 또한 제가 부족하다는 것을 알 수 있는 인생의 큰 경험이었습니다. 이제 앞으로 한 명의 박사로 제 삶을 시작하게 된 이 시점에서 지금까지 받아온 많은 사랑과 배려를 다시 다른 사람들에게 돌려줄 수 있도록 열심히 살겠습니다.

2019년 1월 4일

김승현 드림